

Pulse Shaping for Terahertz Communications

by

Mohamed Shehata

Master's of Electrical Engineering (Electrical Communications and Electronics),
Al-Azhar University, Cairo, Egypt, 2013

Bachelor of Electrical Engineering (Electrical Communications and Electronics),
Al-Azhar University, Cairo, Egypt, 2006

Thesis submitted for the degree of

Doctor of Philosophy

in

School of Electrical & Electronic Engineering
Faculty of Engineering, Computer & Mathematical Sciences
The University of Adelaide

November, 2022

Supervisors:

Prof. Withawat Withayachumnankul, School of Electrical & Electronic Engineering, The University of Adelaide, Australia

A/Prof. Ke Wang, School of Engineering, Royal Melbourne Institute of Technology (RMIT University), Australia



© 2022
Mohamed Shehata
All Rights Reserved



Contents

Contents	iii
Abstract	vii
Originality Declaration	ix
Acknowledgments	xi
Publications	xv
List of Figures	xvii
Chapter 1. Introduction	1
1.1 Current Frequency Allocation Plan	3
1.2 Vision and Roadmap for Future Wireless Networks	4
1.3 Emerging Terahertz Technology and Its Applications	5
1.4 Variants of Terahertz Transceivers	6
1.5 Overview of Terahertz Communications	10
1.6 Research Motivation and Challenges	13
1.7 Dissertation Scope, Contribution and Outline	15
Chapter 2. Terahertz Communications and Pulse Shaping	17
2.1 Introduction	19
2.2 Implementation Techniques and Challenges	22
2.3 IEEE 802.15.3d-Compliant Communications	25
2.4 Existing Pulse Shapes in Terahertz Communications	28
2.5 Time-Jittering in Terahertz Communications	31
2.6 Overview of Terahertz Transceiver Architectures	36
2.7 Demonstration of Terahertz Communications	41
2.8 Summary	46

Chapter 3. IEEE 802.15.3d-Compliant Pulse Shaping	47
3.1 Introduction	49
3.2 IEEE 802.15.3d Spectrum Analysis Framework	51
3.2.1 Spectral Compliance Metric	53
3.2.2 Spectral Radiation Efficiency Metric	54
3.3 Proposed Waveform	55
3.3.1 Comparison of the Waveforms' Spectra	58
3.3.2 Waveform Design Optimisation	58
3.4 Experiment and Results	62
3.5 Impact of Receiver Nonlinearity	70
3.6 Conclusion	72
Chapter 4. Timing-Jitter Tolerant Nyquist Pulse for Terahertz Communications	75
4.1 Introduction	77
4.2 Proposed Nyquist Pulse Shape	79
4.3 Inter-Symbol Interference Analysis	82
4.4 Experimental Results and Analysis	86
4.5 Conclusion	89
Chapter 5. Carrierless Terahertz Amplitude and Phase Modulation	91
5.1 Introduction	93
5.2 CAP Modulation versus I-Q Mixing	95
5.3 Experimental Setup	98
5.4 System Performance and Analyses	102
5.4.1 System Performance	102
5.4.2 Linear and Nonlinear Impairments	104
5.4.3 Signal-to-Noise Ratio Analysis	106
5.4.4 Transceiver Complexity Analysis	111
5.5 Conclusion	113
Chapter 6. Signal Generation and Processing in Terahertz Communications	115
6.1 Introduction	117

6.2	Optical Frequency Tuning of Terahertz Signals	118
6.2.1	Principle of Operation	119
6.2.2	Simulation Results and Analysis	124
6.3	Terahertz Pulse Shaping using Microwave-Photonics	126
6.3.1	Principle of Operation	126
6.3.2	Experiment	129
6.4	Low-Complexity Equalisation for MIMO SC-FDMA	132
6.4.1	MIMO SC-FDMA: System Model Review	133
6.4.2	Proposed FDE-ZF Algorithm	135
6.4.3	Simulation Results and Analysis	137
6.5	Volterra Filters for Nonlinearity Mitigation	139
6.5.1	Experimental Setup and Results	139
6.6	Conclusion	143
Chapter 7. Summary and Outlook		145
7.1	Conclusion	147
7.2	Future Outlook	148
Bibliography		151
Biography		173

Abstract

Over the last two decades, terahertz communications has emerged to unleash the potential of the electromagnetic spectrum beyond 100 GHz. The rapid development in this area has derived benefits from the state-of-the-art breakthroughs in terahertz technology. However, employing this technology to terahertz communications applications comes with a number of interrelated technical challenges, which tend to ceil the overall performance of terahertz communications systems. On a fundamental level, the information-bearing waveforms routed over these systems are power-limited due to the inherently low radiation levels of currently available terahertz transmitters and the availability of terahertz amplifiers. In addition, globally adopted wireless standards introduce additional spectral power and bandwidth constraints to these waveforms. Hence, the prudent utilisation of the permissible regulatory emission power raises a key challenge. Another important challenge is the reliable decoding of these waveforms after wireless transmission. At the receiver front-end, the signal-to-noise ratio of terahertz signals becomes severely low, making them highly sensitive to time-jittering and hence, prone to decoding errors, especially at high baudrates. Further to that, simplifying the transceivers architectures in future wireless communications without sacrificing the high throughput is another fundamental design challenge, which is usually foreseen as an implicit urging necessity for nontraditional waveforms with high spectral efficiency. Concurrently, there is a pressing need for hardware-based computationally efficient signal processing techniques. This challenge is driven by high bit rates available from terahertz communications, leading to an increased latency in digital post-processing. Despite their importance, the aforementioned design challenges remain under-investigated. Therefore, specifically designed waveforms and systems able to sustain in such severe transmission conditions are sought after.

To this end, the main research theme of this dissertation focuses on pulse shaping in terahertz communications. Specifically, two pulse shapes are proposed based on the Lorentzian pulse. The first pulse shape, referred to here as the logarithmic Lorentzian pulse, fully complies with the spectral constraints imposed by the IEEE Standard for terahertz communications and possesses a close-to-unity spectral radiation efficiency. The spectrum of this pulse is designed based on the partial overlap of two logarithmic Lorentzian spectra spaced apart by the desired bandwidth, leading to a flat, i.e.,

frequency-invariant, in-band spectrum and controllable out-of-band suppression. Consequently, an additional degree of freedom is granted to this pulse in order to flexibly control the inter-band interference and hence, adapt to different multi-band transmission scenarios. Validated by rigorous experiments, this pulse shape shows a potential to support terahertz signalling with a limited emission power and stringent spectral constraints, compared to the conventional pulse shapes. Under the same experimental conditions, a proposed variant of this pulse is designed and tested. The modified pulse shows a high tolerance over a wide range of the time-jittering at the receiver side. This outcome further emphasises the vital role of pulse shaping for terahertz communications. Furthermore, the optical communications-inspired carrierless amplitude and phase modulation technique is adopted to terahertz communications. Experimental results show that this technique is a spectrally efficient orthogonal pulse shaping and modulation contender that can significantly simplify the architecture of terahertz transceivers for the sixth generation (6G) terahertz communications systems and, at the same time, achieve a high throughput.

Signal processing techniques for terahertz communications constitute a supplementary research theme in this dissertation. In this part, a microwave photonics-based pulse shaping technique for multi-band terahertz communications is proposed and experimentally demonstrated. Volterra nonlinear filters are also employed to compensate for the dispersion and high nonlinearity of photonics-based terahertz communications systems with optical and wireless transmission. Additionally, a low complexity equalisation technique for multiple-input multiple output single-carrier terahertz communications is proposed and simulated using experimental measurements for the indoor terahertz channel frequency response.

The adoption of the concepts and contributions presented throughout this dissertation can significantly improve the performance of existing terahertz communications systems. Additionally, the proposed pulse shapes establish the foundations for further development of other terahertz-specific waveforms and can be used as informing guidelines for the design and development of terahertz communications systems with high spectral power efficiency as well as robustness to time-jittering under the limited power emission levels offered by current terahertz technology. Moreover, the signal processing techniques presented in this dissertation can potentially cope up with the high data rate requirements of terahertz communications.

Originality Declaration

I certify that this work contains no material which has been accepted for the award of any other degree or diploma in my name, in any university or other tertiary institution and, to the best of my knowledge and belief, contains no material previously published or written by another person, except where due reference has been made in the text. In addition, I certify that no part of this work will, in the future, be used in a submission in my name, for any other degree or diploma in any university or other tertiary institution without the prior approval of the University of Adelaide and where applicable, any partner institution responsible for the joint-award of this degree.

I give consent to this copy of the thesis, when deposited in the University Library, being available for loan, photocopying, and dissemination through the library digital thesis collection, subject to the provisions of the Copyright Act 1968.

I also give permission for the digital version of my thesis to be made available on the web, via the University's digital research repository, the Library Search and also through web search engines, unless permission has been granted by the University to restrict access for a period of time.

Signed _____

10 April 2023

Date

Acknowledgments

First and foremost, I would like to sincerely thank ALLAH for giving me the strength, wisdom and ability to complete my PhD journey. Without any of His blessings, none of my achievements would have been possible. “My Lord, increase me in knowledge.” Amen.

I would like to express my deepest gratitude to my parents who sparked my mind by teaching me math and sciences since my early childhood. I never forgot the great efforts they did until I could solve the first math problem by myself back in 1993; to calculate $475/15$ using long division.

I am extremely grateful to my esteemed supervisor, A/Prof. Withawat Withayachumnankul for his invaluable advice, continuous support, kindness and patience during my PhD study. Professor Withawat never saved any effort to support me in many practical ways. Back in late 2018, he took me on when I was a fresh Ph.D student who had no idea what terahertz communications is about. He introduced me not only to this field, but also to his wide network of professionals and experts. Also, he tirelessly guided me through my research, especially during the hard times when I had to manage many responsibilities. His immense expertise in the field of terahertz communications provided me with invaluable insights into my research. Our weekly meetings were the kitchen where ideas were born, inspired, discussed, sorted out and ultimately polished in order to make the most of these meetings. Due to a lack of sufficient hands-on experience at the beginning, I showed a relatively slow progress in some laboratory-based activities. I must confess that, it was his excellent leadership that took me out of my comfort zone and put me on the right research track. He used to tell me: “If you want to be the best, you must offer the best”. His approach in challenging and questioning my research ideas motivated me to be more sceptical, rigorous and thorough when it comes to scientific research. He would thoroughly review my manuscripts and give me very critical review comments to further improve the technical aspects of my research and, thanks to his eagle eye, my writing as well. Apart from that, his high-level integrity, self-denial and humbleness are some of the most salient ethics I learned from him. For these and many other reasons, I always feel too shy to call such a giant scientist by his name without saying Prof.

Acknowledgments

A/Prof. Ke (Desmond) Wang, my co-supervisor and an outstanding scholar, has also contributed a lot to my PhD journey. His extensive knowledge and understanding in the fields of optical and wireless communications as well as his generosity in sharing that knowledge were vital to my birth and progress as a researcher. He was always open to suggestions, questions and discussions at any time. He also encouraged me to go back to the fundamentals whenever I fell short of understanding any underlying principle. He would point out to the gaps in my knowledge very gently with extreme politeness. In the meantime, he did not hesitate to support me whenever I wanted to challenge conventional concepts and techniques. His constructive feedback has been a great motivation towards the completion of my PhD dissertation. I cannot forget how warmly he welcomed me as a visiting student in RMIT University when I wanted to learn from his expertise in optics. On top of that, I will always remember the beautiful words he said to me in order to encourage me and take me right out of the blue. These words expressed the amount of trust he put in my capabilities during the tough times when I was about to lose my self-confidence. The remarkable positivity of A/Prof. Desmond made my mind transparent to almost any of his comments on my research progress. I owe him so much for his golden advice regarding my career development plans. These unforgettable situations are as important as the formal academic support. Both helped me keep going and maintain my balance, and this is invaluable.

During my candidature I received extensive support from different people from both inside Australia and overseas. As soon as I have arrived this country, I have been surrounded by amazing people. I was warmly welcomed into the University of Adelaide, the city of Adelaide and my big Aussie family; Australia. No one hesitated to give me a hand whenever I came across obstacles that appeared insurmountable. Because there is no much room to say thank you to many people, here are some special mentions.

To my colleagues, Dr. Xiaolong You, Ms. Panisa Dechwechprasit, Mr. Harrison Lees, Mr. Bryce Chung, Mr. Stephen Li and Mr. Sakib Quader, I truly enjoyed our group meetings and comprehensive discussions about many aspects of terahertz communications. I appreciate all of you for providing the much-needed stress relief through our casual chats at the laboratory, kitchen area and other places that witnessed our gathering. I would like to especially thank Dr. Wendy S.-L. Lee for introducing me to our terahertz engineering laboratory (THEL), and Dr. Wei Jie Gao for sharing some of his thesis writing tips. A special note of appreciation goes to Dr. Daniel Headland

who gave me the first hand-on experience in setting up, testing and using key terahertz communications equipment. Thank you everyone.

I also acknowledge the staff of the School, IT officers, workshop colleagues for all their assistance throughout my candidature, including Prof. Nelson Tansu, Prof. Christophe Fumeaux, Assoc. Prof. Wen L. Soong, Dr. Hong Gunn Chew, Ms. Franca Guest, Ms. Antoinette Brincat, Ms. Jodie Schluter, Mr. Danny Di Giacomo, Mr. Bradon Pullen, and Mr. David Bowler, to mention a few. I am also grateful for the friends I have made at the University of Adelaide, who in one way or another supported me throughout this journey, including Dr. Md Saiful Islam and Dr. Jakeya Sultana.

I am also thankful for the financial assistance granted by the School of Electrical and Electronic Engineering in The University of Adelaide, which allowed me to attend international conferences to present my work and learn from really brilliant minds in the field of terahertz communications. I would like to acknowledge The University of Adelaide for providing me with the Adelaide Scholarship International and for extending this scholarship, I would like to thank The Government of South Australia for granting me financial support during the COVID19 crisis.

From the industry, I would like to thank Mr. Steve Karandais, Mr. Timothy Lee and Mr. Danny Tan from Keysight Technologies Australia Pty Ltd. for providing me with the necessary hands-on training on state-of-the-art instrumentation systems for 6G communications. I am also grateful for the SmartSAT Cooperative Research Centre (SmartSAT CRC) for granting me a top-up PhD scholarship.

Also, I would like to take this opportunity to express my gratitude to my collaborators, and actually success partners, in Osaka University, Japan. Many of the measurements presented in this dissertation were carried out by them. Thank you Prof. Tadao Nagatsuma, Assoc. Prof. Masayuki Fujita, and Assoc. Prof. Julian Webber for providing me with your invaluable insight and suggestions which aided my research.

Last but not least, my heartfelt gratitude goes to my wife, Rana, whose unconditional love and encouragement supported me during all the tough times I went through. Her patience, understanding and appreciation of my hectic research life nurtured me to be who I am today. Indeed, she is my best friend. Thank you for everything that you have done for me, without which I would not be able to survive and keep going in this life. I sincerely ask ALLAH to help me treasure our relationship forever.

Publications

Journals

SHEHATA M., WANG-K., AND WITHAYACHUMNANKUL-W. (2022). Carrierless amplitude and phase modulation for terahertz communications. (*Under review*).

SHEHATA M., WANG-K., WEBBER-J., MASAYUKI-F., NAGATSUMA-T., AND WITHAYACHUMNANKUL-W. (2022). Timing-jitter tolerant Nyquist pulse for terahertz communications, *IEEE/OSA Journal of Lightwave Technology, A Special Issue on Optical Systems and Technologies for 6G Mobile Networks*, 40(2), pp. 557–564.

SHEHATA M., WANG-K., WEBBER-J., MASAYUKI-F., NAGATSUMA-T., AND WITHAYACHUMNANKUL-W. (2021). IEEE 802.15.3d-compliant waveforms for terahertz wireless communications, *IEEE/OSA Journal of Lightwave Technology, A Special Issue on Microwave Photonics*, 39(24), pp. 7748–7760.

Conferences

SHEHATA M., WANG-K., WEBBER-J., MASAYUKI-F., NAGATSUMA-T. AND WITHAYACHUMNANKUL-W. (2022). Mitigating the Timing-Jitter in Terahertz Communications via Nyquist Pulse Shaping, *The 2023 Optical Fiber Communication Conference*, California, USA. (*Accepted*)

SHEHATA M., WANG-K., AND WITHAYACHUMNANKUL W. (2022). Mitigating The Nonlinearity of Radio-over-Fiber Terahertz Systems, *47-th International Conference on Infrared, Millimeter, and Terahertz Waves*, Delft, The Netherlands.

SHEHATA M., WANG-K., AND WITHAYACHUMNANKUL W. (2022). Carrierless I-Q Mixing For Terahertz Communications, *47-th International Conference on Infrared, Millimeter, and Terahertz Waves*, Delft, The Netherlands.

SHEHATA M., WANG-K., AND WITHAYACHUMNANKUL W. (2021). Terahertz Pulse Shaping using Microwave-Photonic Delay Line Filters, *46-th International Conference on Infrared, Millimeter, and Terahertz Waves*, Sichuan, China P. R. (**Keynote Talk**)

- SHEHATA M., WANG-K., WEBBER-J., MASAYUKI-F., NAGATSUMA-T. AND WITHAYACHUMNANKUL-W.** (2021). Waveforms with High Spectral Efficiency for Terahertz Communications, *46-th International Conference on Infrared, Millimeter, and Terahertz Waves*, Sichuan, China P. R.
- SHEHATA M., WANG-K. AND WITHAYACHUMNANKUL-W.** (2021). Low-Complexity Zero-Forcing Equalization for MIMO SC-FDMA Terahertz Communications, *The 2021 Fourth International Workshop on Mobile Terahertz Systems*, Essen, Germany.
- SHEHATA M., WANG-K. AND WITHAYACHUMNANKUL-W.** (2020). Photonic Generation of Sub-Terahertz Signals using Self Phase Modulation in Highly Nonlinear Fibres, *2020 Conference on Lasers and Electro-Optics Pacific Rim*, Sydney, NSW, Australia.
- SHEHATA M., WANG-K., WEBBER-J., MASAYUKI-F., NAGATSUMA-T. AND WITHAYACHUMNANKUL-W.** (2020). Pulse Shaping for IEEE 802.15.3d Standard Compliant Wireless Links in the 300 GHz Band, *The 2020 Third International Workshop on Mobile Terahertz Systems*, Essen, Germany.

List of Figures

1.1	Edholm’s law of data traffic growth	4
1.2	Connectivity map of hybrid-access heterogeneous networks in future communications systems	5
1.3	Electromagnetic spectrum	6
1.4	Variants of semiconductor-based terahertz technology developed for wireless communications applications	9
1.5	Atmospheric attenuation of terahertz waves in terrestrial outdoor links .	12
1.6	Dissertation outline	15
<hr/>		
2.1	Example of terahertz pulse shaping techniques using free-space optics .	23
2.2	The spectral emission mask of the first channelisation scheme in the IEEE 802.15.3d and its inverse Fourier transform	27
2.3	Estimated lower bound of the time-jittering range versus the symbol rate	35
2.4	Photonics- and electronics-based implementation of terahertz transceiver architectures for the generation of quadrature amplitude modulated (QAM) terahertz signals	37
2.5	Common terahertz transceiver architectures for the generation of quadrature amplitude modulated (QAM) terahertz signals	39
2.6	Schematic showing the experimental setup of the terahertz over fibre system	42
2.7	Measured error performance with and without single mode fibre transmission	44
2.8	Transmission of a 4k video signal over a photonics-based terahertz communications system with combined optical and wireless transmission . .	45
<hr/>		
3.1	Distribution of the PSD over the sub-bands of spectral emission mask defined by the IEEE 802.15.3d Standard for the first channelisation scheme	57
3.2	Simulated baseband spectra of the three considered waveforms	59

List of Figures

3.3	Design optimisation metrics of the three considered waveforms	60
3.4	Three waveforms obtained from the optimal parameters to comply with the IEEE spectral emission mask	61
3.5	Impact of hard truncation on the stop-band attenuation of the RC, BTRC and the proposed waveforms	62
3.6	Experimental setup of the terahertz photonic communications link based on photomixing	63
3.7	The measured UTC-PD terahertz output power versus its photo-current	64
3.8	Signals and spectra at the receiver side for OOK modulation	66
3.9	Signals and spectra at the receiver side for BPSK modulation	67
3.10	Measured optical-terahertz response of the UTC-PD and the end-to-end response of the photonic-terahertz system	68
3.11	Measured bit error rate performance of the proposed waveforms as compared to the RC and the BTRC waveforms	69
3.12	Measured input-output response of the photonic-terahertz transmitter active and passive components	71
3.13	Evolution of the received IEEE 802.15.3d signal spectrum with the transmitter-receiver antenna separation	72
—————		
4.1	Simulated baseband spectra of the three considered waveforms	79
4.2	Eye diagrams of a binary-phase modulated sequence of 2^{10} symbols length	80
4.3	Simulated time domain baseband waveforms	81
4.4	Probability of bit error performance resulting from the timing-offset-induced inter-symbol interference	84
4.5	Time-bandwidth product and effective signal-to-noise ratio versus the roll-off factor, α	85
4.6	Block diagram of the experimental setup including the receiver processing	87
4.7	Bit error rate performance versus the normalised timing-offset of the received waveforms at two different values of the emitted terahertz power	88
—————		
5.1	Comparison of sinusoidal carrier-based versus carrierless <i>I-Q</i> mixing . .	96

5.2	Experimental setup of the M -ary CAP photonics-terahertz system	99
5.3	Measured bit error rate performance of three QAM-equivalent CAP modulation schemes	103
5.4	Linear and nonlinear distortions of the terahertz photonic system	106
5.5	Received terahertz power as a function of distance at different photo-currents based on Eq. (5.9)	108
5.6	Simulated bit error rate performance of CAP and QAM modulation schemes in an AWGN channel	110

6.1	Schematic diagram of the proposed photonics-based terahertz voltage controlled oscillator	120
6.2	Performance of the system proposed in Fig. 6.1	123
6.3	Time and frequency domain performance of the proposed sub-terahertz photonic signal generator	125
6.4	Schematic diagram of the proposed microwave photonic-assisted multi-band terahertz filter	128
6.5	Design and optimisation of the microwave photonic filter frequency response	129
6.6	Experimental setup and measurement of the photonics-based multi-band terahertz filter	131
6.7	Block diagram of a typical 2×2 MIMO SC-FDMA system	134
6.8	Comparison of the accuracy and complexity of the ZF and the proposed equalisers in noiseless channels	138
6.9	Bit error rate performance of the 2×2 MIMO SC-FDMA system	138
6.10	Schematic diagram of the nonlinear photonic-terahertz system	140
6.11	Nonlinear distortion and memory effects introduced by the terahertz-photonic system in Fig. 6.10 at a photo-current of 1 mA and a Tx-Rx antenna separation of 6 cm	141
6.12	Nonlinear distortion and memory effects introduced by the terahertz-photonic system in Fig. 6.10 at a photo-current of 3 mA and a Tx-Rx antenna separation of 1 cm	142

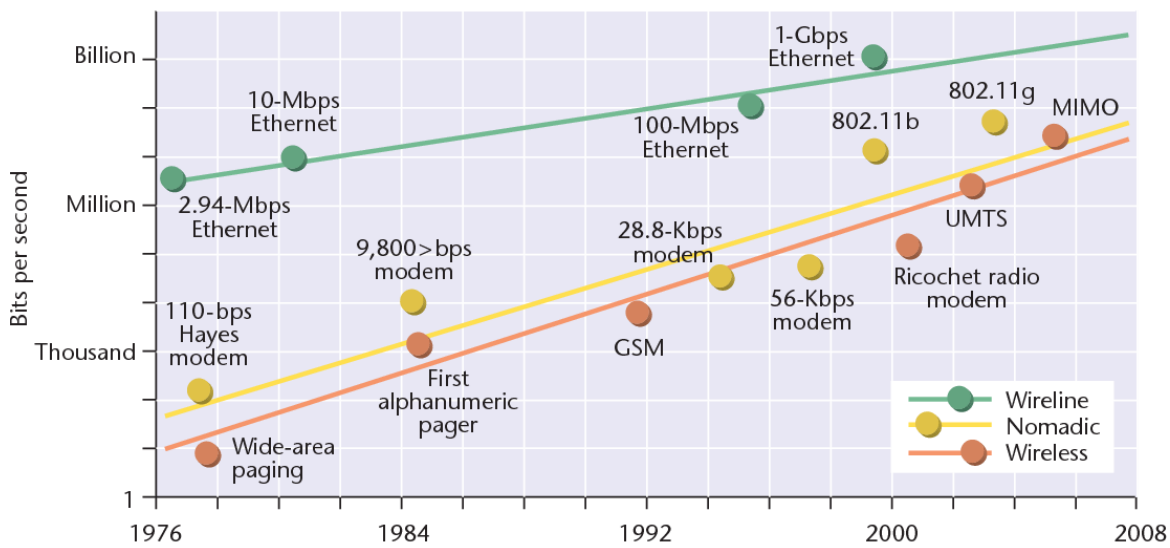
TERAHERTZ radiation is a facet of the electromagnetic spectrum adjacent to the microwave and infrared bands. The unique characteristics of this part of the spectrum continues to uncover a multitude of applications, from molecular imaging to space communications. With the endlessly increasing demands for wireless connectivity, this part of the spectrum emerges as a promising solution to the foreseen shortage of regulated radio frequency (RF) spectral resources in the near future. This chapter presents a brief summary of the progress in the field of terahertz wireless communications. First, the upcoming challenges of existing wireless communications systems are highlighted, and the future trends in wireless services are overviewed. Second, terahertz technology is presented as a key enabler of these services, together with its most salient variants, opportunities and limitations. The last part of this chapter presents the motivation behind this research and outlines the structure and major contributions of this dissertation.

1.1 Current Frequency Allocation Plan

Continuously growing public interests in software applications developed for social networking have stimulated a corresponding increase in the image and video-rich information content on the internet. Based on long-term observations conducted over a period of 25 years, Edholm (Cherry 2004) was the first to trace the evolution of the average growth rate of the data traffic routed through high speed – short range wireless communications networks as shown in Fig. 1.1. In 2004, Edholm's law empirically predicted that the network traffic worldwide increases linearly. Inspired by Edholm's law, more accurate data traffic forecasts were conducted by telecommunications equipment providers (Cisco & its Affiliates 2015) in order to verify and extrapolate this observation. The reliability of CISCO forecast reports relies on data traffic measurements extracted from communications devices equipped with data traffic monitoring capabilities. The measurements validate Edholm's model and estimate that the data traffic generated by the wireless end-users doubles almost every 18 months. Extrapolating Edholm's law, it is foreseen that the wireless access at data rates of 5-10 Gbit/s/user will be inevitably required by 2030. Consequently, the overall data traffic consumption is expected to increase by several orders of magnitude by the end of this decade.

Currently, the 60 GHz millimetre wave systems can support wireless transmission up to 7 Gbit/s (Mackay et al. 2022), and the peak transmission rate of fifth-generation (5G) links is only 10 Gbit/s. However, day-by-day increasing demands for reliable high-speed wireless services are expected to rapidly approach the capacity of 5G communications networks in the near future. In addition, the spectral resources for wireless communications are limited such that, in the current frequency allocation plan, there is no continuous bandwidth larger than 10 GHz available below 100 GHz (Tekbiyık et al. 2019). These demands are unlikely to be fulfilled without ongoing vigorous research on next-generation wireless networks, namely, 6G. Therefore, a progress in the development of beyond-fifth-generation (B5G) and 6G wireless communications networks has been accelerating over the past decade. This progress have been achieved by the research efforts dedicated in search for tremendously high transmission capacities as well as enabling technologies. Consequently, there is pressing need to push the carrier frequencies beyond the millimetre wave band to cope up with the users' activities on wireless networks by increasing the channel capacities and reducing the routing latency. To that end, exploring to the next frontier of the electromagnetic spectrum using new core technologies is indispensable.

1.2 Vision and Roadmap for Future Wireless Networks



© 2007 IEEE

Figure 1.1. Edholm's law of data traffic growth. Evolution of the nominal data rate for wireline, nomadic, and wireless technologies. Adapted from (Baker 2007).

1.2 Vision and Roadmap for Future Wireless Networks

New paradigms are foreseen for 6G networks (Chowdhury et al. 2020), such as supporting 8K-360° video streaming, machine-to-machine (M2M) communications, holographic tele-presence and wireless power transfer. Compared to 5G, 6G wireless communications is expected to achieve a broader geographical coverage and incorporate a wide range of applications, from chip-to-chip communications to satellite-terrestrial links (Ji et al. 2021). It is also expected that 6G communications will act as a central hub that could potentially interconnect heterogeneous physical layer technologies such as visible light communications (VLC) links and radio-over-fibre (RoF) links as well as millimetre wave wireless links (Borges et al. 2021). Such a multi-level integration will be required to support different applications such as cloud computing, radar and navigation, control, sensing and imaging (Ji et al. 2021). To smartly control the exchange of gigantic data traffic among these heterogeneous structures, various supporting technologies will be employed, such as machine learning, which will be required for real-time network self-awareness and -management (Chowdhury et al. 2020). To that end, the availability of spectral resources, together with enabling technologies, is crucial to the realisation of the roadmap envisaged for 6G communications. It is foreseen that, in 6G communications (Ji et al. 2021), the nominal transmission rate will range from 100 Gbit/s to

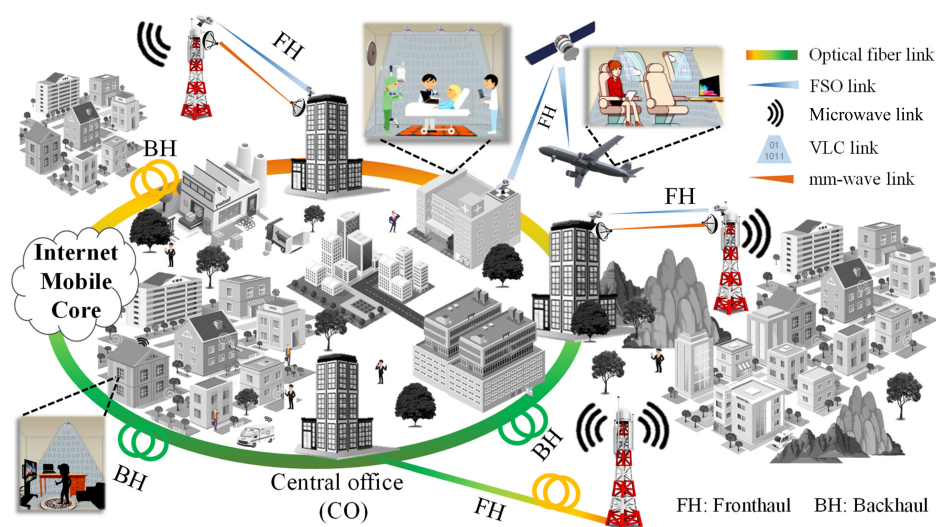


Figure 1.2. Connectivity map of hybrid-access heterogeneous networks in future communications systems. (Reproduced from (Borges et al. 2021), *Applied Sciences; an mdpi open access journal*)

about 1 Tbit/s, and a latency as low as 1 μ s (Lee et al. 2020), which is not achievable using neither existing microwave nor millimetre wave wireless systems.

1.3 Emerging Terahertz Technology and Its Applications

Terahertz radiation refers to electromagnetic waves in the frequency range from 100 GHz to 10 THz. In terms of the wavelength, the terahertz band is defined from a wavelength of 3 mm to 30 μ m. This definition overlaps the millimetre wave band, which ranges from 30 GHz to 300 GHz, and incorporates the sub-millimetre wave region, from 300 GHz to 3 THz (Wiltse 1984). In addition, at its high frequency edge, the terahertz band overlaps the far infrared region, which is defined from 3 to 20 THz (Vatansever & Hamblin 2012). Apart from the technical definitions, Fig. 1.3 shows that the terahertz band is halfway between the microwave and the visible bands of the electromagnetic spectrum, without sharp boundaries at the edges of both bands.

Owing to its unique and highly desirable properties, the feasibility of employing terahertz radiation to a wide range of applications has been experimentally demonstrated during the last two decades. For instance, terahertz waves are transparent to materials that are opaque at visible and near-infrared frequencies (Moriwaki et al. 2017, Kanda

1.4 Variants of Terahertz Transceivers

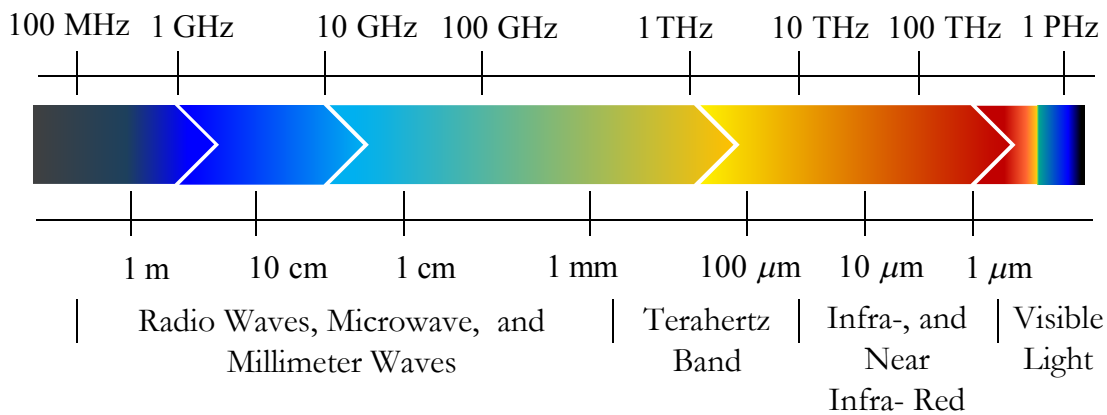


Figure 1.3. Electromagnetic spectrum. The terahertz frequency regime within the electromagnetic spectrum is shown here with its overlap with the microwave and infrared regions.

et al. 2017, Suzuki et al. 2016). Due to the low photon energies at terahertz frequencies, terahertz radiation is non-ionising and hence, poses no threat to biological tissues exposed to the typical radiation levels of terahertz time-domain spectroscopy (THz-TDS) systems (Fitzgerald et al. 2002). These properties are useful for non-destructive medical imaging and sensing applications (Withayachumnankul et al. 2007). The absorption spectra of a wide variety of materials exhibit high responsivity to terahertz radiation (Naftaly & Miles 2007), which resonates with the need to characterise these materials at terahertz frequencies. Terahertz technology can also support ultra-broadband wireless communications, which is one of the most salient applications of terahertz technology (Dhillon et al. 2017) for the unprecedented data rates associated with terahertz carrier frequencies. Such unique characteristics would not have been uncovered without development of the technologies required for generating and detecting terahertz waves.

1.4 Variants of Terahertz Transceivers

The development of compact radiation-efficient terahertz sources for practical applications has been an active research topic in the field of terahertz engineering and sciences (Dhillon et al. 2017). Currently, there are several variants of low-power terahertz technology that can be employed in wireless communications applications. The terahertz radiation emitted by these sources can be classified into two broad categories, namely, the impulse-radiation mode and the continuous-wave (CW) radiation mode. Each of these two radiation modes has its own generation and detection techniques as well as its unique application scenarios.

In the impulse radiation mode, terahertz waves are emitted in the form of short-duration energy bursts that typically last for a few pico-seconds (Degert et al. 2012). Due to the time-frequency duality, the spectra of such ultra-short pulses span a wide frequency range; from a few GHz, and up to several THz (Degert et al. 2012). Such an ultra-broad bandwidth makes the emitted terahertz waves prone to the non-ideal atmospheric propagation conditions, especially the high power loss in outdoor environments due to water-vapour absorption (Song & Nagatsuma 2011), (Shams et al. 2016), (Kallfass et al. 2015).

Photo-conductive antennas (PCAs) have been the most established variant of terahertz technology that can be used to generate and detect impulse terahertz waves (Bacon et al. 2021). A major functional drawback of PCAs is the requirement for high-bias voltage, which can exceed 100 V (Bacon et al. 2021), making these devices impractical for handheld communications equipment. Importantly, the data rates that can be achieved using currently-available PCA-based transmitters are, so far, as low as a few hundreds of MByte/s (Systems 2022). This is because PCAs are optically pumped using low repetition rate femto-second laser sources to generate terahertz pulses at the same rates. However, such low data rates makes PCA-based communications lagging behind the increasing demands for broadband applications, which have been driving the innovations in the 6G roadmap. Nonetheless, when operated in the receiving mode, PCAs can be used as high-speed terahertz detectors at data rates up to 640 Gbit/s (Yu et al. 2015*b*).

In the CW mode, terahertz radiation is emitted as a sinusoidal wave, which has a limited spectral spread around a well-defined frequency in the terahertz band. Therefore, such type of terahertz radiation is commonly used for narrowband carrier-based wireless communications. Resonant tunnelling diodes (RTDs) is an electronic variant of semiconductor-based terahertz technology, which can be used to generate and CW terahertz waves (Asada & Suzuki 2021). These devices can also be used to detect CW terahertz radiation, either coherently (Yu et al. 2020), or non-coherently (Webber et al. 2019). A major limitation of RTDs is that these devices can only oscillate at unstable discrete operational frequencies (Oshima et al. 2017). However, for practical communications applications, it is highly desirable that terahertz sources are continuously tunable over a large bandwidth. Tunable RTDs have been developed to overcome this limitation and hence, extend their usability for wireless communications applications (Kitagawa et al. 2016). Additionally, being electronic device, RTD-based transmitters are incompatible

1.4 Variants of Terahertz Transceivers

with microwave-photonic (MWP) techniques. For RTD-based transmitters to support these techniques, the baseband signals need to be electro-optic-modulated before being processed using MWP techniques and subsequently photo-detected, which makes the transmitter architecture rather complicated (Webber et al. 2019).

High-speed photo-diodes (PDs) is another semiconductor-based variant of terahertz technology that can be used to generate CW terahertz radiation based on photo-mixing (Seddon et al. 2022). In photo-mixing, two independent optical sources, with two different frequencies, are combined and optically modulated before being applied to a high-responsivity photo-diode for optical-to-terahertz down-conversion. One of the powerful advantages offered by these techniques is their seamless integrability to radio-over-fibre (RoF) optical networks (Shams et al. 2016). This particular feature intersects with one of the foreseen goals in the roadmap of future hybrid access networks. Importantly, this integration makes it possible to apply MWP techniques to terahertz signals for all-optical signal processing (Shams et al. 2016) and distribution purposes (Shams et al. 2015), (Gonzalez-Guerrero et al. 2018). Another benefit that can be gained from employing photonics technologies to terahertz communications is to extend the reach of terahertz signals in order to enable wireless access by end-users and exchange gigantic data volumes over short range links such as home broadband. Thanks to the parallel development of integrated terahertz photonics (Withayachumnankul et al. 2018), the potentials of terahertz technology for wireless communications applications are gradually unleashed.

Examples of PDs especially developed for high-speed photo-mixing include positive-intrinsic-negative photo-diodes (PIN-PDs) (Ali et al. 2020), (Castro et al. 2019) and uni-travelling carrier PDs (UTC-PDs) (Ito et al. 2004), (Piels & Bowers 2014). Compared to UTC-PDs, currently-available PIN-PDs emit higher terahertz power at frequencies below 170 GHz (Nellen et al. 2019). However, at frequencies from 170 GHz to 350 GHz, the UTC-PDs are more efficient terahertz emitters than the PIN-PDs. To put into perspective, the UTC-PD can typically emit $56 \mu\text{W}$ at about 300 GHz, whereas the PIN-PD power drops to about $35 \mu\text{W}$ at the same frequency. For frequencies higher than 300 GHz, the output power levels of both emitters are almost identical, except for a subtle difference of about $2 \mu\text{W}$ at 1 THz. Being the most efficient photonics-based terahertz emitter in the 220-330 GHz band, the UTC-PD is the most widely adopted choice for experimental demonstrations on wireless communications. However, one of the major limitation of UTC-PDs is their rather limited power which is typically

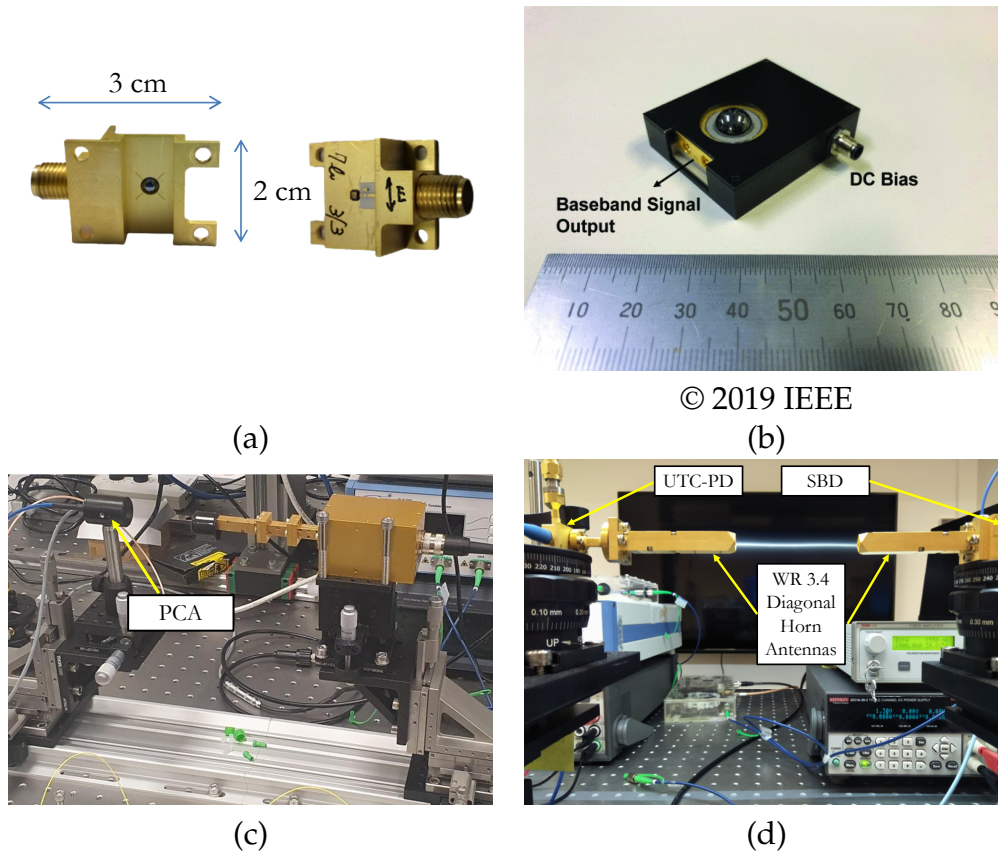


Figure 1.4. Variants of semiconductor-based terahertz technology developed for wireless communications applications. (a) Photo for a packaged resonant tunnelling diode that oscillates at 200 GHz. (b) Fermi-level managed barrier diode (FMBD) (Nagatsuma et al. 2019). (c) Photoconductive antenna (PCA) with an integrated silicon focusing lens. (d) A terahertz link comprising a uni-travelling carrier photo-diode (UTC-PD) and a Schottky-barrier diode (SBD) operating in the 220-330 GHz band. The components in (a), (c) and (d) are at The University of Adelaide.

as low as 1 mW (Song et al. 2012). Although relatively low, this power is useful for close-proximity wireless applications (Dhillon et al. 2017).

Similar to other wireless communications, modulated CW terahertz signals can be detected either coherently or non-coherently, i.e., envelope detection (Nagatsuma & Carpintero 2015). In coherent detection, the received terahertz signal is down-converted from the terahertz band to an intermediate frequency (IF) using a local oscillator and a sub-harmonic mixer (SHM) (Nagatsuma & Carpintero 2015). This technique is usually required when the terahertz signal is both amplitude- and phase-modulated. However, with simple amplitude-only modulation schemes, such as the on-off keying (OOK) and double sideband with carrier (DSB+C) binary phase shift keying (BPSK) schemes, envelope detection is a less-complex and more power-efficient alternative. Both the

1.5 Overview of Terahertz Communications

Table 1.1. Sample use cases of different variants of terahertz technology for communications.

	Technology (Tx+Rx)	Frequency (GHz)	Data Rate (Gbit/s)	Modu- lation
(Yu et al. 2015 <i>b</i>)	UTC-PD + PCA	Carrierless (IR)	640	OOK
(Jia et al. 2018 <i>a</i>)	UTC-PD + SHM	400	106	16-QAM
(Nagatsuma et al. 2013)	UTC-PD + SBD	300	48	OOK
(Nishida et al. 2019)	UTC-PD + RTD	343.2	30	ASK
(Webber et al. 2019)	RTD + RTD	340	10	OOK
(Oshima et al. 2017)	RTD + SBD	500, 800	2×28	OOK
(Minoofar et al. 2021)	PIN-PD + SHM	300	4	QPSK

RTD and the Schottky-barrier-diode (SBD) are highly-nonlinear terahertz envelope detectors. However, the input power-output voltage response of RTDs is highly nonlinear compared to SBDs (Shiode et al. 2011). In addition, whilst the sensitivity of typical RTDs is typically 30 dB higher than that of SBDs (Shiode et al. 2011), SBDs are more power-efficient as they are essentially zero-bias detectors. Another device that has been recently developed for terahertz envelope detection is the Fermi-level managed barrier diode (FMBD) (Nagatsuma et al. 2019). This device outperforms the SBD in terms of the detection sensitivity and the noise equivalent power. Yet, the heterodyne (Ito & Ishibashi 2018) and homodyne (Roser et al. 1992) detection performance of the FMBD has not been investigated.

Over the last two decades, various experiential demonstrations have been reported in the design and development of high-speed wireless communications systems using different variants of terahertz technology. Table 1.1 shows that, terahertz communications systems have been experimentally demonstrated using different combinations of terahertz technology variants at the transmitter and receiver sides. The performance of each system depends mainly on this particular combination (Yu et al. 2015*b*).

1.5 Overview of Terahertz Communications

Using terahertz waves for wireless communications has been considered as a promising solution that can meet the foreseen demands for ultra-broadband wireless connectivity and terahertz technology is a key enabler for these demands (Petrov et al. 2020), (Ji et al. 2021). Based on Shannon's theory, the capacity of a band-limited communications channel increases with its bandwidth and the transmitted signal power (Shannon 1948). In terms of the bandwidth, the terahertz band offers ample spectral resources such that, theoretically, the average throughput can be as high as 10 Gbit/s/GHz (Schneider

et al. 2012). However, practically, the transparency of terahertz wave propagation through a water-vapour filled atmosphere is limited to certain discontinuous spectral windows. The frequency range from 220 GHz to 330 GHz, which is commonly known as the WR-3.4 band and also known as the low terahertz band, is the largest transmission window with the minimum attenuation under different atmospheric conditions as shown in Fig. 1.5 (Song & Nagatsuma 2011). Therefore, the majority of previous demonstrations on terahertz communications have focused on this part of the terahertz spectrum (Shams et al. 2016), (Seeds 2014b). Concurrently, different spectral windows in the terahertz band are explored and progressively regulated. This is to ensure the authorised access to different parts of the terahertz spectrum and secure harmonious and interference-free operation of future wireless communications. In addition, conformity of the developed products/services to globally adopted standards is also indispensable phase in the development phase of such an emerging generation of wireless communications networks (R. E. & Spencer 2010). This is to ensure the interoperability of products developed by different manufacturers. In relation to that, in 2017, the IEEE Standards Association (IEEE-SA) approved the first worldwide standard to regulate wireless communications at terahertz frequencies. The final release of this standard, officially called the IEEE 802.15.3d-2017 Standard, specifies the physical (PHY) layer for the operation of point-to-point terahertz band communication networks (P2P-TBCN) up to 100 Gbps (IEEE 2017). Additionally, in February 2019, the U.S Federal Communications Commission has released the first report on licensing the spectrum from 95 GHz to 3 THz for experiments on terahertz signalling (FCC 2019).

It is challenging to approach Shannon's capacity limits based on the power levels of currently-available terahertz emitters (Schneider et al. 2012). On top of that, the propagation of terahertz waves is also prone to free-space path loss (FSPL) (Schneider et al. 2012), which can be modelled by the Friis gain formula as follows:

$$P_{\text{Rx}} = P_{\text{Tx}} \frac{G_{\text{Tx}} G_{\text{Rx}} c^2}{(4\pi d f)^2}, \quad (1.1)$$

where P_{Tx} is the transmitted terahertz power, P_{Rx} is the terahertz power at the receiver front-end, d is the Tx-Rx separation, f is the terahertz frequency, and $c = 3 \times 10^8$ m/s is the speed of light in the free space. As can be seen in Eq. (1.1), due to their dependence on frequency, terahertz waves suffer from a severely high FSPL. Considering two 25 dBi gain antennas separated by a moderate transmission distance of 10 m, the FSPL ranges from about 49.29 dB to 52.8 dB in the 220–330 GHz band. If not compensated,

1.5 Overview of Terahertz Communications

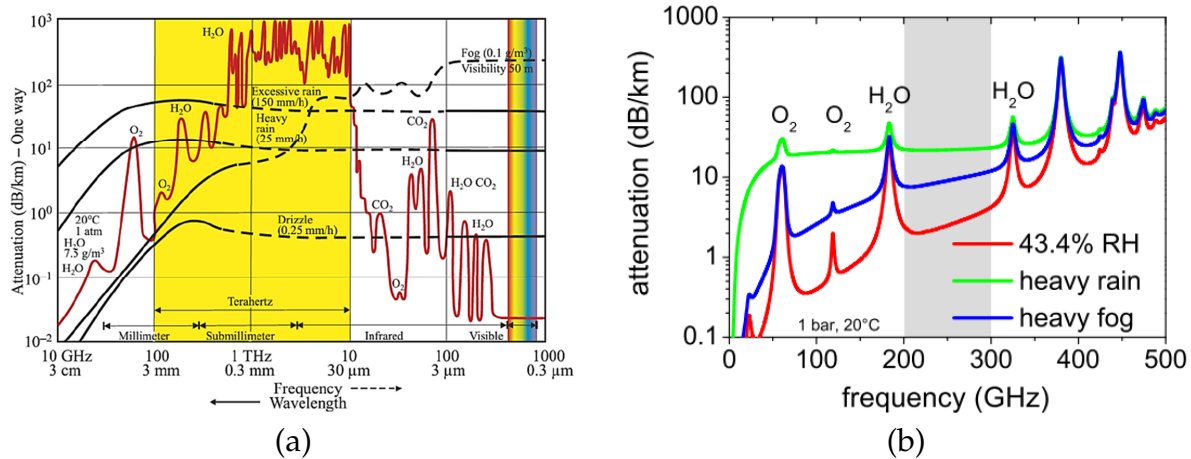


Figure 1.5. Atmospheric attenuation of terahertz waves in terrestrial outdoor links. (a) Attenuation of the Earth atmosphere from radio frequencies to the visible band (*Reproduced from Versita (Rogalski & Sizov 2011) under a CC-BY-NC-ND open access license*). (b) Attenuation in the terahertz band (*Reproduced from (Kallfass et al. 2015) with permission from Springer Nature*).

such a high power loss can significantly reduce the signal-to-noise ratio (SNR) at the receiver front-end and hence, deteriorate the BER performance. This power loss can be compensated using focusing Teflon lens (Ducournau et al. 2015), which can reduce the FSPL to 0 dB, and/or high-gain terahertz antennas (Castro et al. 2020) (Liu et al. 2021). Alternatively, coherent detection techniques can be used to improve the receiver sensitivity by up to 35 dB when the received power is as low as -30 dBm (Yu et al. 2020). Without these power-loss compensation techniques, the maximum wireless reach of terahertz signals would range from less than 1 mm (Hirata & Hirokawa 2018) to a few tens of centimetres (Song 2019).

Another important challenge is the high directionality of terahertz antennas, which allows only line-of-sight (LoS) propagation paths. However, recently, it has been experimentally proven that, even if the terahertz waves propagate from the Tx to the Rx via a non-LoS (NLoS) paths with obstructions, still high quality links can be established (Ma et al. 2018). In (Sheikh et al. 2020), a 3-D ray-tracing approach has been developed to evaluate the channel capacity in a realistic office room environment around 300 GHz. These research efforts highlight the potential of using terahertz technology in typical indoor wireless communications applications in the 300 GHz band. Therefore, in (Petrov et al. 2018), a road-map for the deployment of terahertz Ethernet links for indoor environments has been proposed.

To overcome the aforementioned limitations and hence, push terahertz communications towards the Shannon's capacity limits, several concepts and techniques have been introduced to the area of terahertz communications. Many of these techniques are essentially inspired by concepts and experimental demonstrations that have proven practically feasible during the development of the 5G wireless networks, such as polarisation division multiplexing (PDM) (Oshima et al. 2017), (Nagatsuma et al. 2013) and multiple-input multiple-output (MIMO) multiplexing (Cheng et al. 2019). Nonetheless, without signal processing, the realisability and reliability of such advanced transmission techniques are not necessarily guaranteed.

1.6 Research Motivation and Challenges

The field of terahertz communications is multi-disciplinary and relies on the parallel advancement of various inter-related fields such as terahertz technology, passive and active integrated terahertz devices as well as wireless communications. Together, these fields are all indispensable for the realisation of practical terahertz communications systems. Of particular importance is the field of signal processing, which is crucial to the development terahertz communications systems that show high resilience to the transmission impairments and non-ideal characteristics of key terahertz devices. Despite their immaturity, the transmission performance of current experimental demonstrations on terahertz communications would have been further limited without employing signal processing techniques. Admittedly, the lack of these techniques is one of the key factors that made the progress in terahertz communications relatively slack. To that end, the parallel advancement of the field of signal processing for terahertz communications is essential to put the practical application of terahertz technology in place and unleash its full potential.

Designing waveforms, or equivalently, pulse shapes, that can meet specific requirements and/or challenges is, so far, one of the under-investigated applications of signal processing in the field of terahertz communications. It is noteworthy that, to date, experimental demonstrations on terahertz communications still rely on conventional pulse shapes, which do not necessarily meet the requirements and challenges that are specific to this field. Independently, classical approaches for the waveform design and processing in terahertz communications have been theoretically suggested without being experimentally investigated. Therefore, it is of paramount importance to thoroughly

1.6 Research Motivation and Challenges

investigate the specific requirements of practical terahertz communications systems in order to develop waveforms and signal processing techniques that can meet these requirements. Motivated by these considerations, the main aim of this dissertation is to showcase a number of pulse shapes and computationally-efficient signal processing techniques through a number of contributions distributed over seven chapters. These contributions are validated through a series of experimental demonstrations, using photonics-based terahertz communications systems as well as rigorous simulations.

1.7 Dissertation Scope, Contribution and Outline

The general scope of this dissertation focuses on short-range high-speed CW terahertz wireless communications systems. Specifically, this dissertation aims to improve the transmission performance and simplify the design of photonics-based terahertz communications systems in the WR-3.4 band through pulse shaping and signal processing techniques. This dissertation comprises seven chapters in total, including three chapters of original contributions to the field of terahertz communications. The dissertation structure is visually represented in Fig. 1.6, and the technical contents of each chapter are as follows:

Chapter 1 - Introduction presents the background knowledge required to understand the context of terahertz communications and its underlying technology. The motivation behind the research contributions presented in this dissertation is also discussed.

Chapter 2 - Terahertz Communications and Pulse Shaping presents the background knowledge required to establish the context of narrowband pulse shaping for terahertz communications. Additionally, the temporal and spectral properties of two Nyquist pulse shapes, namely, the raised-cosine (RC) pulse and the better-than RC pulse, are

Background	Chapter 1	Introduction
	Chapter 2	Terahertz Communications and Pulse Shaping
Pulse Shaping	Chapter 3	IEEE 802.15.3d-Compliant Pulse Shaping
	Chapter 4	Timing-Jitter Tolerant Nyquist Pulse for Terahertz Communications
	Chapter 5	Carrierless Terahertz Amplitude and Phase Modulation
Signal Processing	Chapter 6	Signal Generation and Processing in Terahertz Communications
Conclusion	Chapter 7	Summary and Outlook

Figure 1.6. Dissertation outline. The chapters are divided into 4 major parts as background, pulse shaping, wireless transmission and digital signal processing (DSP).

revised. Key challenges in the implementation of signal processing techniques for terahertz communications are also presented in this chapter.

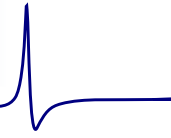
Chapter 3 - Original Contribution presents a non-Nyquist waveform that fully complies with the spectral constraints defined in the IEEE 802.15.3d Standard with a close-to-100% spectral power efficiency (SPE). The proposed waveform, which outperforms the conventional RC and BTRC waveforms in terms of the SPE and the bit error rate performance, also possesses two degrees of freedom that can be used to control its temporal and spectral properties for flexible spectral interference management. To the best of our knowledge, there has been no other pulse shape designs for the IEEE 802.15.3d Standard. Therefore, the proposed waveform, together with the developed analytical framework, would be an asset in terahertz communications, particularly for wireless-channel multiplexing. The content of this Chapter is published in (Shehata et al. 2021).

Chapter 4 - Original Contribution presents a Nyquist pulse that is highly tolerant to the timing-jitter. The proposed pulse shape, which is a modified form of the pulse shape presented in Chapter 3, satisfies the Nyquist criterion for inter-symbol interference (ISI)-free signalling and compared with the RC and BTRC pulses. In addition, the transmission performance of this pulse shape outperforms the conventional RC pulse as well as the BTRC pulses. The content of this Chapter is published in (Shehata et al. 2022c)

Chapter 5 - Original Contribution introduces the concept of carrierless amplitude and phase modulation to terahertz communications for the first time, to the best of our knowledge. This modulation technique is experimentally demonstrated using a typical photonic-based terahertz communications system with combined optical and wireless transmission. The content of this chapter has been submitted for publication (Shehata et al. 2022a).

Chapter 6 - Signal Generation and Processing in Terahertz Communications. This part presents pulse shaping and signal processing techniques that are particularly useful for further development of terahertz communications systems. These techniques aim at the generation, processing and shaping the spectra of terahertz signals in the optical and baseband domains. The proposed techniques are computationally-efficient and their implementation is potentially simple.

Chapter 7 - Summary and outlook concludes the dissertation and provides an outlook for future developments based on the proposed contributions.



Terahertz Communications and Pulse Shaping



THIS chapter presents a literature review and key challenges that arise from transmission impairments usually encountered in terahertz communications with an emphasis on the aspects relevant to the scope of this dissertation. Firstly, a general overview of the challenges and performance limitations associated with current terahertz communications systems is presented. The remaining sections in this Chapter overview transmission impairments in terahertz communications, with spotlights on the existing possible solutions and their limitations. Finally, the potential challenges facing the signal processing are discussed in light of applications to the terahertz regime.

2.1 Introduction

In communications systems, the waveforms are the ultimate result of signal processing at the transmitter side before emission over-the-air (OTA) via the transmitter's antenna in wireless communications (Yazar & Arslan 2020), or distribution over optical fibres in optical communications (Seeds 2014a). These waveforms determine many of the physical resources required by the communications system, including the computational resources, bandwidth, power budget as well as generation and detection techniques (Yazar & Arslan 2020). In terahertz communications, the transceiver architecture impacts the choice of the signalling waveform (Gustavsson et al. 2021) and vice versa (Shehata et al. 2022a). It is foreseen that, such a mutual dependence will be more complicated in future 6G communications systems as multiple waveforms for different standards may be required to coexist in a single transmitted OTA frame (Yazar & Arslan 2020). Furthermore, multi-purpose waveforms might be shared among heterogeneous 6G applications, such as joint communications and sensing (Mao et al. 2021), (Wild et al. 2021). Therefore, the waveform design is a core process in the development of the physical layer (PHY) of communications systems (Yazar & Arslan 2020). In relation to this, several waveforms have been suggested as potential contenders for 6G terahertz communications (Tarboush et al. 2022), (Song & Lee 2022), (Yazar & Arslan 2020). In principle, most of these waveforms, which were originally developed for 5G applications, can be considered as potentially transferable contenders that need to be adapted to the beyond-5G (B5G) and 6G requirements. At least, conceptually, automated machine learning techniques can be employed to dynamically adapt these waveforms to various requirements using parameter assignment and optimisation techniques (Yazar & Arslan 2019), (Yazar & Arslan 2020). However, a multitude of practical considerations, particularly, the energy efficiency (Song & Lee 2022), should be rigorously considered when designing, selecting and/or comparing different candidate waveforms for 6G terahertz communications (Tarboush et al. 2022), (Choi 2021).

On the most fundamental level, terahertz radiation emitted by currently available variants of terahertz technology is power-limited. This radiation can be classified into two broad categories, namely, impulse-like waves and continuous-wave (CW) signals as discussed in Section 1.4. Each of these two waveform types has its own generation techniques as well as temporal and spectral characteristics, which determine its unique application scenarios. For instance, owing to their ultra-short spread in the time-domain, impulse-like terahertz waves are valuable for electromagnetic field measurements with

pico second resolution. However, the ultra-broad bandwidth of this waveform type makes it susceptible to the non-ideal atmospheric propagation conditions and hence, impractical for communications applications. On the other hand, the limited spectral spread of CW terahertz waveforms is a highly desired feature for spectral sharing by multiple users communicating over a single wireless channel with limited spectral resources. To date, the majority of experimental demonstrations on terahertz wireless communications are based on CW terahertz technology variants. In CW terahertz communications, waveforms can be further divided into two broad categories, namely, single carrier (SC) waveforms (Xin et al. 2021) and multi-carrier (MC) waveforms (Berardinelli et al. 2021). Several variants of both waveform types have been suggested and theoretically compared in the context of terahertz communications (Nguyen et al. 2022), (Tarboush et al. 2022), (Schram et al. 2020). Therefore, this chapter focuses on reshaping the spectra of CW terahertz waveforms for several requirements demanded by terahertz communications as will be detailed later in this chapter.

The waveforms that result from the orthogonal frequency division multiplexing (OFDM) of simple SC waveforms is one of the most salient examples that have been considered as potential candidates for CW terahertz communications (Berardinelli et al. 2021). In practice, the OFDM is the only MC candidate waveform that has been experimentally demonstrated in terahertz communications. For example, in (Mingming et al. 2019), a full OFDM-based terahertz communications system with combined optical and wireless transmission has been experimentally demonstrated. However, the implementation of real-time terahertz OFDM systems could be prohibitively complex, especially at high baudrates (Tarboush et al. 2022). This is mainly due to the need for a discrete Fourier transform (DFT) module and its inverse at the receiver and transmitter sides, respectively. Indeed, in (Takiguchi 2017a) and (Takiguchi 2017b), a terahertz OFDM system was experimentally demonstrated using a photonic integrated circuit (PIC), which process in real-time. This PIC, which was used to implement a 4-point discrete Fourier transform (DFT) in real-time only at the receiver side, resulted in an effective data rate of 40 Gbit/s. However, using offline DSP at the transmitter and receiver sides, a 512-point OFDM-based terahertz communications system has been experimentally demonstrated with combined optical and wireless transmission at a data rate of 59 Gbit/s (Hermelo et al. 2017). In addition to these implementation challenges, there is a broad agreement that various modifications should be introduced to OFDM-based waveforms before they can be adopted for terahertz communications (Nguyen et al. 2022), (Zhang et al. 2020), (Tarboush et al. 2022). These modifications include enhancing

the spectral efficiency, reducing the out-of-band (OOB) emissions and minimising the peak-to-average power ratio (PAPR) (Tarboush et al. 2022). To reduce the PAPR of OFDM waveforms, an additional DFT process and its inverse can be utilised at the transmitter and receiver sides, respectively (Wu et al. 2021), (Berardinelli et al. 2021). The resulting waveform is a low-PAPR SC variant of the OFDM waveform (Wu et al. 2021). However, the practical generation and real-time processing of such a waveform is more complicated than the OFDM waveform.

The research question that reveals itself here is—whether there is a resilient waveform that can meet the design requirements of terahertz communications systems without overwhelming processing at the transmitter and receiver sides. The answer to this question is that, so far, the design requirements of terahertz communications have not been thoroughly investigated. Instead, waveforms previously developed for 5G are directly employed without being adapted to the specific requirements of terahertz communications. It should be highlighted that, these waveforms have been developed to solve key challenges that are specific to microwave and optical 5G communications. Likewise, terahertz communications has its own challenges and requirements (Tarboush et al. 2022), such as the limited computational resources of baseband signal processing equipment as well as the susceptibility to the non-ideal transmission characteristics of terahertz devices. Therefore, understanding these requirements is necessary to the development of waveforms that can fulfil these design challenges (Tarboush et al. 2022), (Nguyen et al. 2022). In relation to this, a few studies called attention to the need for optimal SC waveforms in terahertz communications, especially in the 90–200 GHz band (Corre et al. 2019). However, the design guidelines and techniques for such waveforms have not been initiated.

To address these design challenges, the design (Doré et al. 2018) and prototyping (Gustavsson et al. 2021) of high-speed terahertz links have focused mainly on low-complexity SC waveforms (Li et al. 2019). This is because, basically, MC waveforms can be synthesised using a selected combination of multi-parameter SC waveforms and signals processing techniques. The multiple parameters of SC waveforms form a multi-dimensional hyperspace. Low-complexity SC waveforms are defined in terms of points that represent only the modulation alphabet and orthogonal pulse shapes in this signal space (Yazar & Arslan 2020). Thus, on the most fundamental level, pulse shaping plays a central, if not the most important, role in controlling the temporal and spectral characteristic of OTA emitted waveforms (Yazar & Arslan 2020). Reshaping the spectrum of communications

2.2 Implementation Techniques and Challenges

signals has a non-negligible impact on the performance reliability and spectral efficiency of wireless communications systems. In terahertz communications, the development of a diversity of multi-parameter pulse shaping filters is the key to produce various of waveforms for different purposes (Yazar & Arslan 2020).

In this chapter, we highlight three use cases and design challenges associated with current terahertz communications systems and show how these limitations can be overcome by employing pulse shaping techniques as problem solvers. The rest of this chapter is organised as follows. Section 2.2 overviews current implementation techniques and their associated challenges for terahertz pulse shaping. The same section also highlights the need for low-complexity transceivers architectures for future terahertz wireless communications. Section 2.3 overviews the temporal and spectral characteristics of two Nyquist pulse shapes as potential candidates for terahertz communications. Section 2.4 presents two Nyquist pulse shapes that could be potential contenders for terahertz wireless communications. The potential limitations of these waveforms are also discussed in this section. The same section also shows a preliminary analysis on the design of IEEE 802.15.3d compliant waveforms.

2.2 Implementation Techniques and Challenges

The state-of-the-art experimental demonstrations on terahertz communications can be classified as narrowband or wideband, depending on the generated signals' bandwidths and carrier frequencies. Reshaping the spectra of these signals directly in the passband is not possible due to the unavailability of signal processing building blocks at terahertz frequencies (Zhou et al. 2021). Instead, there are well-established techniques to synthesise arbitrarily shaped terahertz waveforms and precisely reshape their spectra using optical pulse shaping techniques, followed by optical-to-terahertz down-conversion. Initially, these techniques have been implemented using bulky free-space optical components (Park et al. 1999), (Degert et al. 2012), (Sato et al. 2013), (Miyamaru et al. 2014), (Hamraoui et al. 2017), which are impractical for wireless communications applications with possible mobility. As an illustration, Fig. 2.1 shows examples of the experimental setup for terahertz pulse shaping techniques using FSO components. As shown in this figure, these setups are impractical for communications applications where large scale integration of several components is usually desired. More importantly, with these techniques, terahertz waves can be only generated in the form of energy bursts. These energy bursts have extremely large bandwidths compared to the

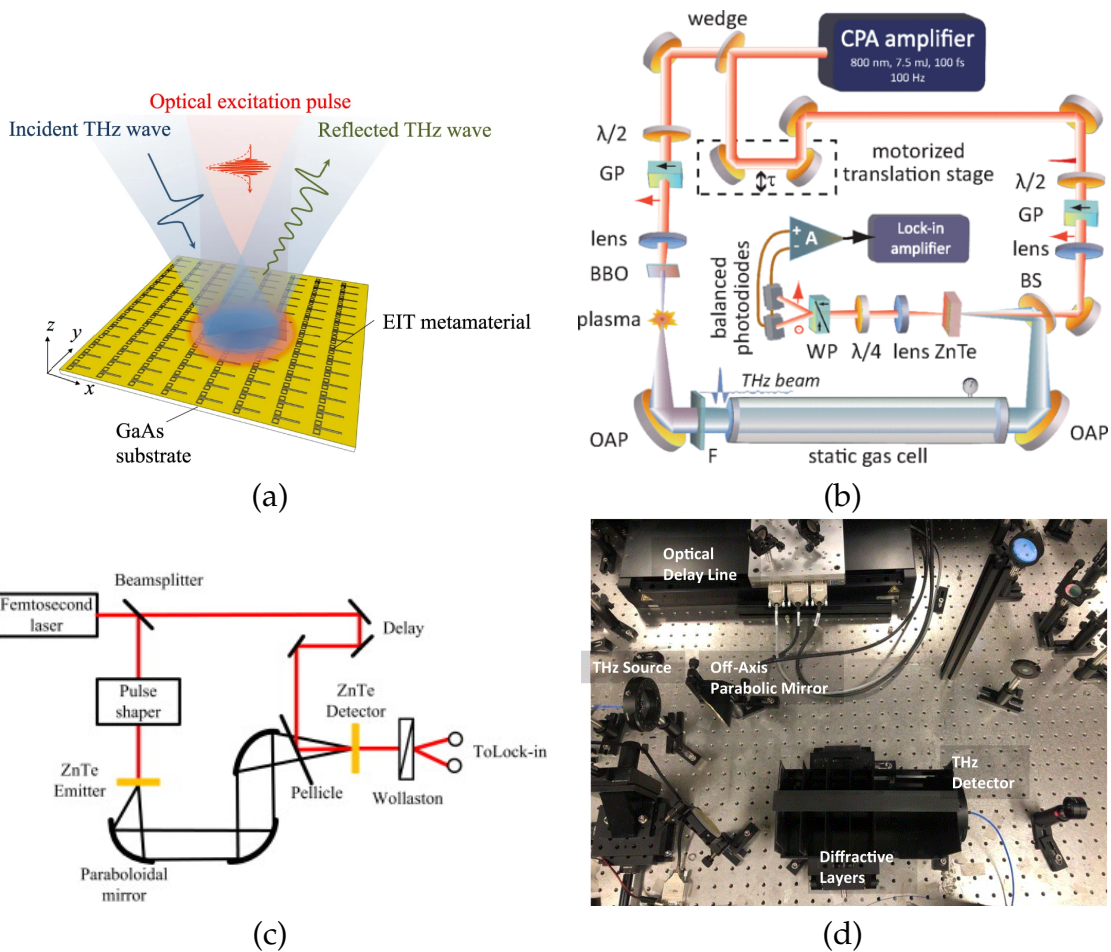


Figure 2.1. Example of terahertz pulse shaping techniques using free-space optics. (a) Schematic diagram showing a narrowband terahertz pulse shaping technique using optical excitation of metasurfaces (Miyamaru et al. 2014) (*Reproduced with permission from Springer Nature under the creative common license*) (View license online). (b) Terahertz pulse shaping through propagation in a gas tube and free-space optical components (Hamraoui et al. 2017) (*Reproduced with permission from the American Physical Society*) (View doi). (c) Experimental setup for the tunable generation and spectral shaping of terahertz pulses from optically shaped femto-second pulses (*Reproduced from (Lu et al. 2014) with permission from Elsevier, Copyright 2014*) (View license online). (d) Experimental setup for amplitude and phase terahertz spectral shaping using passive diffractive devices (*Reproduced from Nature, (Veli et al. 2021) under the creative common license: CC-BY, open access*) (View license online).

typical spectral requirements for terahertz communications applications (IEEE 2017). Further to that, the terahertz wave that propagate through the free-space between these components are prone to transmission impairments, such as the frequency-dependent group delay, exhibited by each individual component.

Integrated microelectronic platforms, such as re-programmable high-speed digital-to-analog converters (DACs), are multi-functional signal processing platforms that can be used to overcome the limitations of FSO-based techniques. However, operating these

2.2 Implementation Techniques and Challenges

platforms at terahertz frequencies exceeds their practically achievable limits (Song & Lee 2022). The problem of reshaping the terahertz signal spectrum can be simplified to reshaping the spectrum of its envelope, which can be flexibly accomplished in the baseband using high-speed DACs as follows. First, the spectrum of the terahertz signal envelope is designed and synthesised in the baseband, using a high-speed DAC. This way, a wide variety of pulse shapes with flexibly controllable temporal and spectral characteristics can be generated. Second, the generated baseband spectrum is up-converted to the terahertz band, using photonic or electronic techniques, to obtain terahertz waveforms with the desired spectral characteristics. This way, it is possible to cope up with the speed demands expected from terahertz communications.

An important challenge in the implementation of pulse shaping for terahertz communications is the need for high-speed DACs and analog-to-digital converters (ADCs) to perform multi-functional processing at the transmitter and receiver sides (Song & Lee 2022). With these platforms, data rates as high as 100 Gbit/s could be achieved during the last decade using a maximum sampling speeds of 100 GS/s (Rodríguez-Vázquez et al. 2020), (Song & Lee 2022). However, still this speed needs to be increased by at least one order of magnitude in order to reach bit rates up to 1 Tbit/s in the next decade (Song & Lee 2022). The effective sampling rate, denoted by f_s , can be calculated as follows:

$$f_s = \left\lfloor \frac{f_{\text{DAC}}}{f_{\text{N}}} \right\rfloor f_{\text{N}}, \quad (2.1)$$

where f_{DAC} is the maximum DAC sampling rate, $f_{\text{N}} = 2\text{BW}_{\text{BB}}$ is the Nyquist sampling rate, BW_{BB} is the baseband signal bandwidth. Table 2.1 shows the sampling rate requirements for various channel bandwidths defined in the IEEE 802.15.3d Standard, considering $f_{\text{DAC}} = 65 \text{ GS/s}$, which is typical for many currently-available DACs. It should be highlighted that, in addition to pulse shaping, digital platforms are also

Table 2.1. Sampling rate requirements for the IEEE 802.15.3d Standard, assuming a maximum sampling rate of 65 GS/s.

Passband Bandwidth (GHz)	Baseband Bandwidth (GHz)	Nyquist Sampling rate (GS/s)	Oversampling factor	Effective Sampling Rate (GS/s)
2.16	1.08	2.16	30	64.80
4.32	2.16	4.32	15	64.80
8.64	4.32	8.64	7	60.48
12.96	6.48	12.96	5	64.80
17.28	8.64	17.28	3	51.84
25.92	12.96	25.92	2	51.84
51.84	25.92	51.84	1	51.84
69.12	34.56	69.12	0	–

required to perform other complicated DSP tasks, such as channel equalisation, non-linearity compensation, matched filtering, sampling as well as error detection and correction. However, the computational resources of currently-available ADCs and DACs are rather limited, making these DSP tasks overwhelming, especially at high baud rates. Therefore, it is reasonable to start the pulse shape design by identifying the needs, limitations and transmission impairments that motivate the design of new pulse shapes for terahertz communications. In the following sections, we highlight three of the challenges and design requirements that have been encountered so far in terahertz communications before pulse shaping solutions are introduced in the next three chapters.

2.3 IEEE 802.15.3d-Compliant Communications

It has been envisaged that the terahertz band can support the demands of the sixth generation (6G) of wireless communications systems for the high-speed transmission of gigantic data volumes. Various communications systems have been reported at terahertz frequencies (Nagatsuma & Carpintero 2015), (Elayan et al. 2020), especially, from 220 GHz to 330 GHz. The majority of these experimental demonstrations have focused on optimising the transmission performance without imposing any constraints on the effective isotropic radiated power (EIRP) of the radiated terahertz signals.

It is important to note that, the technical specifications defined in regulatory standards can be used as guidelines for the design and development of terahertz communications systems. In addition, meeting these regulations as design targets make it possible to assess different implementations within a unified framework. Further to that, complying with globally adopted wireless standards is also crucial to the harmonious interoperability of wireless communications equipment produced by different manufacturers.

In 2017, the IEEE released the first global standard for wireless communications in order to regulate these increasing research interests in the advancement of terahertz communications (IEEE 2017). In this standard, a large bandwidth of 70 GHz, namely, from 252.72 GHz to 321.84 GHz, usually called the low-terahertz band, is dedicated for terahertz communications. This bandwidth is shareable among multiple users based on the principle of frequency division multiplexing. The number of users, and consequently, their bandwidths, are determined by one of eight possible channelisation schemes. The bandwidth of a single user channel ranges from 2.16 GHz to 69 GHz. Due to the inherently weak power of currently available key terahertz devices, no

upper bound on the power spectral density (PSD) transmitted by each channel has been set. However, to ensure an almost interference-free coexistence of terahertz signals, spectral constraints with sharp cutoff frequencies have been imposed to their PSDs at the boundaries of adjacent channels. Therefore, the spectra of terahertz signals should be carefully designed to be fully compliant with the spectral constraints defined by this standard.

Indeed, since its release in 2017, there has been increasing interests in the full or partial compliance with the regulations defined in the IEEE 802.15.3d Standard, e.g. (Chinni et al. 2018*a,b*, Fujishima 2018, Dan et al. 2020). However, only a few of these demonstrations have considered the PHY layer specifications defined by the IEEE 802.15.3d Standard. For instance, in (Chinni et al. 2018*a*), successful wireless transmission of a 100 Gbps 16-quadrature amplitude-modulated (16-QAM) signal at 280 GHz has been experimentally demonstrated based on photomixing, also known as optical heterodyning, using a UTC-PD. The spectrum of the generated terahertz signal was reshaped at the baseband by employing a root-raised cosine pulse shaping filter with a roll-off factor of 0.35. The generated terahertz signal occupied the 69th channel regulated by the IEEE 802.15.3d Standard with a bandwidth of about 69 GHz. The compliance of this signal with the spectral mask dedicated to this channel was not considered. Moreover, the reported transmission bit rates are not compliant with the standard transmission rates designed by the IEEE 802.15.3d Standard for the 69th channel. In (Fujishima 2018), an all-electronic technique based on silicon CMOS integrated circuits was employed to demonstrate the successful generation of a 27 GHz bandwidth terahertz signal in the low-terahertz band. The author consumed 12.5 channels of 2.16 GHz bandwidth to accommodate the spectrum of the generated signal, which does not comply with any of the channelisation schemes defined in the IEEE 802.15.3d Standard. Also, the spectrum of the generated signal was not reported. Similarly, the work provided in (Dan et al. 2020) reported the multi-channel generation and transmission of two terahertz signals in the 300 GHz band, each with a bandwidth of 2.16 GHz. A raised-cosine pulse shaping filter, with a roll-off factor of 0.35, was employed to reshape the spectra of these signals at the baseband without considering the conformity of the generated spectra to the spectral constraints defined in the IEEE 802.15.3d Standard.

It is important to highlight that, most of the channelisation schemes of the IEEE 802.15.3d Standard support multi-user transmission. Therefore, shaping the spectra of the emitted

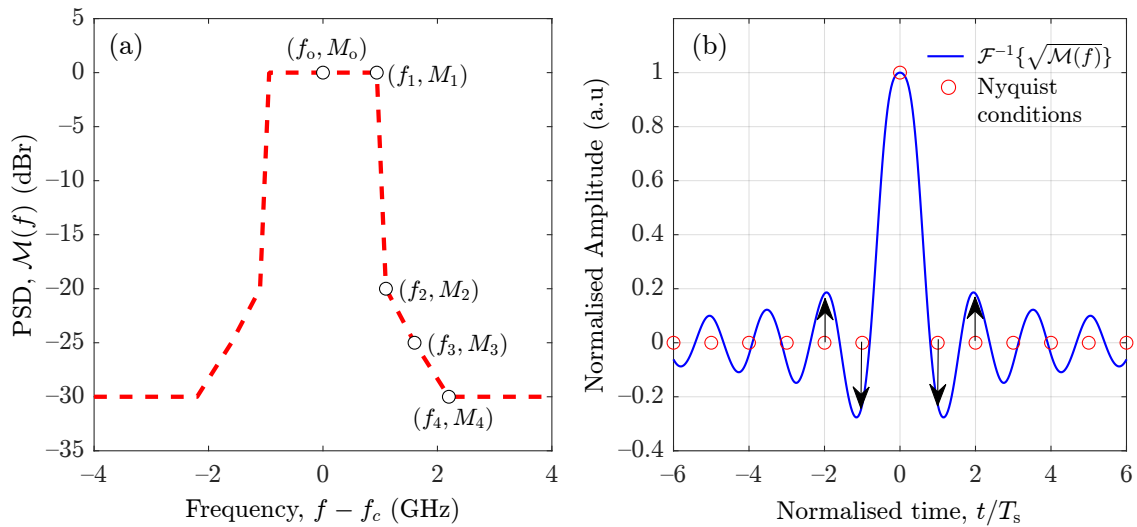


Figure 2.2. The spectral emission mask of the first channelisation scheme in the IEEE 802.15.3d and its inverse Fourier transform. (a) The power spectral density (PSD), $\mathcal{M}(f)$, of the first channelisation scheme in the IEEE 802.15.3d Standard. (b) The inverse Fourier transform of $\mathcal{M}(f)$ in (a). The symbol rate is R_s 1.44 Gbit/s, $T_s = 1/R_s$, and f_c is the terahertz carrier frequency. The numerical values of f_0 to f_4 and M_0 to M_4 are given in Table 2.2.

OTA terahertz waveforms is one of the essential design constraints that should be considered to minimise the mutual cross-talk between adjacent channels. In addition, the terahertz signal must fully comply with the IEEE 802.15.3d spectral emission mask and, at the same time, occupy the maximum possible area under this spectral mask (Shehata et al. 2021) in order to maximise the spectral radiation efficiency of currently available terahertz devices. Figure 2.2(a) shows the IEEE 802.15.3d spectral emission mask for the first channelisation scheme. As shown in this figure, the emission mask is defined in terms of the normalised PSD at four different knee frequencies.

The numerical values of the knee frequencies, i.e., f_0 to f_4 , and the spectral mask at these frequencies, i.e., M_0 to M_4 , are defined in Table 2.2 for the first channelisation scheme. However, the emission masks of other channelisation schemes have the same PSD limits defined at a different set of knee frequencies, depending on each particular scheme. Mathematically, the spectral mask in Fig. 2.2(a) can be expressed in terms of a continuous piece-wise linear function of the frequency, denoted by $\mathcal{M}(f)$.

In principle, a waveform with a PSD of $\mathcal{M}(f)$ is optimal as it fully complies with the IEEE 802.15.3d spectral mask. Assuming a phaseless spectrum, the corresponding time domain waveform can be analytically obtained by applying the inverse Fourier transform directly to $\sqrt{\mathcal{M}(f)}$.

2.4 Existing Pulse Shapes in Terahertz Communications

In the time domain, this waveform can be expressed as follows:

$$m(t) = \mathcal{F}^{-1} \left\{ \sqrt{\mathcal{M}(f)} \right\} = \frac{1}{\pi} \sum_{n=1}^4 \sqrt{\frac{a_n}{k_n^2 + t^2}} \left[\exp(k_n \omega) \cos(\omega t - \phi_n(t)) \right]_{\omega_n}^{\omega_{n+1}}, \quad (2.2)$$

where $\mathcal{F}^{-1} \{ \cdot \}$ is the inverse Fourier transform, $[F(x)]_{x_1}^{x_2} \triangleq F(x_2) - F(x_1)$, $\phi_n(t) = \tan^{-1} \left(\frac{t}{k_n} \right)$, and the constants k_n , a_n and c_n are defined as follows:

$$k_n = \frac{0.1 \ln(10)}{4\pi} \left(\frac{M_n - M_{n-1}}{f_n - f_{n-1}} \right), \quad (2.3a)$$

$$a_n = 10^{0.1c_n}, \quad (2.3b)$$

$$c_n = M_{n-1} - \left(\frac{M_n - M_{n-1}}{f_n - f_{n-1}} \right) f_{n-1}. \quad (2.3c)$$

Figure 2.2(b) plots $m(t)$ for the first channelisation scheme of the IEEE 802.15.3d Standard when the symbol rate is R_s 1.44 Gbit/s. As shown in this figure, $m(t)$ strongly violates the Nyquist criteria for ISI-free signalling, i.e., $m(t = nT_s) \neq 0$, where $T_s = 1/R_s$. This observation is also applicable to all other channelisation schemes. Therefore, designing waveforms that fully comply with the spectral requirements of the IEEE 802.5.13d standard and, at the same time, closely match the Nyquist ISI criteria needs to be investigated more thoroughly, and it is discussed in Chapter 3.

2.4 Existing Pulse Shapes in Terahertz Communications

Typically, binary information signals are generated in the form of the conventional non-return to zero (NRZ) rectangular pulses, which cannot always meet the various design requirements of wireless communications systems. For instance, these pulse shapes are not spectrally efficient and practically un-realisable due to their sharp, i.e., ideally zero, rise and fall times. On the other hand, compared to the conventional rectangular NRZ pulse, Nyquist pulses, such as the raised-cosine (RC) pulse, are practically realisable and

Table 2.2. Spectral limits of the IEEE 802.15.3d emission masks, $\mathcal{M}(f)$, for the first channelisation scheme. The passband bandwidth of this scheme is 2.16 GHz.

Spectral limit, M_n (dBr)	M_0	M_1	M_2	M_3	M_4
Value	0	0	-20	-25	-30
Knee frequency, f_n (GHz)	f_0	f_1	f_2	f_3	f_4
Value	0	0.94	1.1	1.6	2.2

Table 2.3. Commonly used pulse shapes in terahertz communications.

	Modulation Scheme	Carrier frequency (GHz)	Data Rate (GBit/s)	Roll-off factor, α
Nyquist pulses				
(Shams et al. 2016)	QPSK	220–280	100	0.01
(Harter et al. 2019)	QPSK	326	30	0.1
(Gonzalez-Guerrero et al. 2019)	16-QAM	250	20	0.1
(Shams et al. 2016)	16-QAM	350	100	0.1
(Yu et al. 2015a)	QPSK	403	60	0.1
(Pang et al. 2016)	16-QAM	300–500	300	0.15
(Jia et al. 2018a)	16-QAM	400	106	0.15
(Takiguchi 2021)	OOK	300	80	0.3
(Dan et al. 2020)	16-QAM	300	60	0.35
(Chinni et al. 2018a)	16-QAM	280	100	0.35
(Koenig et al. 2013)	16-QAM	237.5	100	0.35
(Moon et al. 2022)	16-QAM	300	100	0.4
(Wang et al. 2014)	16-QAM	340	3	0.4
(Rodriguez-Vazquez et al. 2019)	16-QAM	230	100	0.2–0.7
(Jia et al. 2018b)	16-QAM	370	56	0.8
Non-Nyquist pulses				
(Shrestha et al. 2022)	OOK	197.5	1.12	Rectangular
(Webber et al. 2019)	OOK	350	10	Gaussian
(Shehata et al. 2020)	BPSK	307.8	1.44	Gaussian-Butterworth
(Yu et al. 2015b)	OOK	Carrierless (IR)	640	Gaussian monocycle

more spectrally efficient. Other Nyquist pulse shapes, such as the better-than RC (BTRC) pulse can also be used to improve the tolerance of wireless communications to the time-jittering at the receiver side, especially at high data rates and low signal-to-noise ratio conditions, which is the typical case for terahertz communications. Table 2.3 shows that, in terahertz communications, the RC pulse is the most commonly used pulse shape, whereas other pulse shapes, such as the Gaussian pulse (Shehata et al. 2020) and its derivatives (Shree et al. 2019), and arbitrary pulse shapes have been rarely considered for communications (Chudzik et al. 2014) and channel-analysis applications (Yu et al. 2015b). Therefore, the rest of this section focuses on the temporal and spectral characteristics of Nyquist pulse shapes, specifically, the RC and BTRC pulses, as potential waveform contenders for terahertz communications. The RC pulse shape is a Nyquist pulse that has been widely adopted for signalling over the physical layers of various wireless and optical communications systems. It should be highlighted that, Nyquist pulse shapes, including the RC and BTRC pulses, are inherently descendants of the sinc pulse with different decaying envelope profiles. The sinc pulse has zero-crossings at integer multiples of the symbol duration (Alagha & Kabal 1999). This property satisfies the first Nyquist criterion to minimise the impact of ISI on the BER performance in the

presence of transmitter-receiver synchronisation errors (Nyquist 1928). The envelopes of the mother sinc pulse, on the other hand, are designed to improve the temporal and spectral characteristics of this pulse, especially, the decay rate in the time-domain and the stop-band attenuation in the frequency-domain.

In non-terahertz wireless communications, various Nyquist pulses with different envelope profiles have been proven to outperform, or at least be comparable with, the RC pulse in terms of the transmission performance over band-limited channels. Examples of these pulse shapes include, but are not limited to, the generalised phase-compensated Nyquist pulse (Alagha & Kabal 1999), the flipped hyperbolic-secant (fsech) and the flipped inverse hyperbolic-secant pulses (Assalini & Tonello 2004). Of particular importance is the BTRC pulse owing to its several advantages. For instance, the BTRC is the only pulse shape, other than the RC pulse, that has a closed-form time-domain expression (Beaulieu et al. 2001), which facilitates the theoretical evaluation of the BER performance. Additionally, in (Kumar et al. 2017) it has been proven that, compared with the RC waveform, employing the BTRC waveform in the generalised frequency division multiplexing (GFDM) systems can potentially improve the symbol error rate (SER) performance. In (Haigh et al. 2018), the transmission performance of the BTRC waveform has been experimentally tested using a visible light communication system operating under AWGN channel conditions. It was found that the BTRC pulse shape offers superior bit-error rate (BER) performance and lower computational complexity compared with the RC pulse shape. Throughout this dissertation, the RC and the BTRC pulse shapes are adopted as comparison benchmarks.

The spectrum of a typical RC waveform is given by (Beaulieu et al. 2001):

$$S_{\text{RC}}(f) = \begin{cases} 1, & 0 \leq |f| < B(1 - \alpha) \\ \frac{1}{2} \left\{ 1 + \cos \left(\frac{\pi}{2B\alpha} (|f| - B(1 - \alpha)) \right) \right\}, & B(1 - \alpha) \leq |f| \leq B(1 + \alpha) \\ 0, & B(1 + \alpha) \leq |f|, \end{cases} \quad (2.4)$$

where α is the roll-off factor, T_s is the symbol period, and $B = R_s/2 = 1/(2T_s)$ is the minimum transmission bandwidth, i.e., the Nyquist bandwidth, R_s is the symbol rate and $T_s = 1/R_s$ is the symbol duration. The corresponding time-domain RC waveform is given by (Beaulieu et al. 2001):

$$s_{\text{RC}}(t) = \text{sinc} \left(\frac{t}{T_s} \right) \frac{\cos(\pi\alpha t/T_s)}{1 - 4\alpha^2 t^2/T_s^2}. \quad (2.5)$$

As shown in Eq. (2.4), the RC pulse is a variant of the sinc pulse that fulfils the Nyquist criteria for ISI-free signalling and, at the same time, has an envelope that improves its time and frequency characteristics.

The spectrum of the BTRC pulse shape is defined as follows Beaulieu et al. (2001):

$$S_{\text{BTRC}}(f) = \begin{cases} 1, & 0 \leq |f| < B(1 - \alpha) \\ \exp \left\{ \frac{\ln 2}{\alpha B} |f - B(1 - \alpha)| \right\}, & B(1 - \alpha) \leq |f| < B \\ 1 - \exp \left\{ \frac{\ln 2}{\alpha B} |f - B(1 + \alpha)| \right\}, & B \leq |f| < B(1 + \alpha) \\ 0, & B(1 + \alpha) \leq |f|. \end{cases} \quad (2.6)$$

The corresponding time-domain BTRC pulse is given by (Beaulieu et al. 2001):

$$s_{\text{BTRC}}(t) = 2B \text{sinc}(2Bt) \times \frac{4\beta\pi t \sin(2\pi B\alpha t) + 2\beta^2 \cos(2\pi B\alpha t) - \beta^2}{4\pi^2 t^2 + \beta^2}, \quad (2.7)$$

where $\beta = (\ln 2 / \alpha B)$. It should be pointed out that, practically, the RC and the BTRC pulse shaping are realised using the square root of Eq. (2.4) and Eq. (2.6) at the transmitter and receiver side (Farhang-Boroujeny & Mathew 1996), respectively. To comply with the IEEE 802.15.3d Standard, the value of T_s in Eq. (2.5) and Eq. (2.7) is selected according to the discrete set of the symbol rates defined in (IEEE 2017). However, in this way, α is the only independent parameter that can be used to control the in-band and the out-of-band (OOB) spectral characteristics of the RC and BTRC pulses. In addition, for both pulse shapes, increasing α increases the OOB power at the expense of the in-band power and vice versa.

2.5 Time-Jittering in Terahertz Communications

In practice, the generation and modulation of high carrier frequencies is usually accompanied by a randomly fluctuating phase noise, which becomes noticeable as random timing-jitter in the baseband at the receiver side. Unless precisely estimated and compensated, this timing-jitter gives rise to imperfect synchronisation between the transmitter and the receiver. Such a net non-zero time-varying timing-offset could severely deteriorate the end-to-end bit error rate (BER) performance, especially at high transmission symbol rates (Roumelas et al. 2020).

2.5 Time-Jittering in Terahertz Communications

In the field of terahertz communications, timing-jitter with a remarkable proportion of the symbol period has been frequently observed in many experimental demonstrations (Ducournau et al. 2014, Nagatsuma et al. 2013, 2016a, Webber et al. 2019). For instance, in a typical terahertz electronic receiver, the average timing-jitter was measured to be in the range of 10 ps at 5 Gbit/s to 25 ps at 12 Gbit/s (Webber et al. 2019), which corresponds to about 5% to 30% of the symbol duration, respectively. The impact of this timing-jitter, and consequently, the inter-symbol interference (ISI), on the BER performance was considered insignificant since the received signal exhibited a highly-confined Gaussian-like profile over the allocated symbol duration (Webber et al. 2019). However, for the same symbol rate, the root mean squared (RMS) bandwidth of a typical Gaussian pulse is much higher than the Nyquist bandwidth requirement. Therefore, in most of the previous demonstrations of terahertz communications, e.g., (Chinni et al. 2018a,b, Fujishima 2018, Dan et al. 2020), it has been a common practice to rely on the RC pulse shape with various roll-off factors for bandwidth-efficient signalling.

Although spectrally-efficient, the transmission performance of Nyquist pulses, including the RC pulse, is sensitive to the timing-jitter due to the large overlap between adjacent pulses. The ISI caused by this overlap can severely deteriorate the BER performance unless the detection is performed at the optimum sampling instants at the receiver side. In (Beaulieu 1991), it has been shown that when the timing-offset is 25% of the symbol period, the BER can exceed 10^{-3} , which is much higher than the error-free transmission limit of 10^{-12} .

Admittedly, in most of the previous demonstrations of terahertz communications links, the impact of timing-jitter on the transmission performance of RC pulses has not been considered. This is because that, in these demonstration, offline digital signal processing (DSP) techniques have been employed to jointly compensate for various transmission impairments, including the timing-jitter. Whilst offline DSP techniques are sufficient for proof-of-concept experiments, the timing-jitter estimation and compensation can be a complicated DSP task for receivers with limited computational resources. This issue can be challenging in practical scenarios, especially for real-time applications. A computationally-efficient solution to reduce the severity of the timing-jitter on the receiver error performance is to design Nyquist pulse shapes with rapidly decaying profiles. This way, the power contained in the time-domain sidelobes of these pulse shapes and, consequently, their ISI interaction, can be reduced. As a result, the receiver

error performance can be improved, and the need for high-speed precise timing-control circuitry can be relaxed.

In digital communications, the timing-jitter can typically be modelled as a Gaussian random process that has a mean value equal to the optimum time sampling instant within the symbol period (Roumelas et al. 2020). For symmetric pulse shapes, this sampling instant is located at the pulse centre, i.e., $t = 0$, where the maximum of this pulse is located. In addition, the relationship between this timing-jitter, denoted by δt , and the symbol waveform, denoted by $p(t)$, can be modelled in terms of the modified Cramer-Rao bound (MCRB) as follows (D'Andrea et al. 1994):

$$\mathbf{Var}(\delta t) \geq \sqrt{\frac{\int_{-\infty}^{\infty} |P(f)|^2 df}{4\pi^2 \text{SNR}_{\text{eff}} \int_{-\infty}^{\infty} f^2 |P(f)|^2 df}}, \quad (2.8)$$

where $\mathbf{Var}(\cdot)$ is the statistical variance operator, f is the frequency domain, $P(f)$ is the Fourier transform of $p(t)$, and SNR_{eff} is the effective signal-to-noise ratio after terahertz-to-baseband down-conversion at the receiver side. As can be seen from Eq. (2.8), the effective SNR at the receiver side and, consequently, its error performance, depends on the timing-jitter as well as the selection of a particular symbol waveform, $p(t)$. It should be highlighted that Eq. (2.8) can be reformulated and expressed in terms of the root mean squared (RMS) spectral width of $P(f)$, denoted by σ_f , which is defined as follows (Cohen 1994, Loughlin & Cohen 2004):

$$\sigma_f = \frac{1}{2\pi} \sqrt{\langle \omega^2 \rangle - \langle \omega \rangle^2}, \quad (2.9)$$

where $\omega = 2\pi f$, $\langle \omega \rangle$ and $\langle \omega^2 \rangle$ are first and the second centralised order moments of the pulse spectrum, defined, respectively, as follows:

$$\langle \omega^2 \rangle = \frac{\int_{-\infty}^{\infty} \omega^2 |P(\omega)|^2 d\omega}{\int_{-\infty}^{\infty} |P(\omega)|^2 d\omega}, \quad (2.10a)$$

$$\langle \omega \rangle = \frac{\int_{-\infty}^{\infty} \omega |P(\omega)|^2 d\omega}{\int_{-\infty}^{\infty} |P(\omega)|^2 d\omega}. \quad (2.10b)$$

2.5 Time-Jittering in Terahertz Communications

Since $p(t)$ is real-valued, then $\langle \omega \rangle = 0$. Expressing Eq. (2.8) in terms of Eq. (2.9) yields:

$$\text{SNR}_{\text{eff}} \geq \frac{1}{4\pi^2\sigma_f^2 \text{Var}(\delta t)}. \quad (2.11)$$

It is reasonable to assume that the timing-jitter off the optimum sampling instant, i.e., $\text{Var}(\delta t)$, does not exceed the RMS temporal width of $p(t)$, which is denoted by σ_t .

Such a practically valid assumption makes it possible to simplify Eq. (2.11) to the following form:

$$\text{SNR}_{\text{eff}} \geq \frac{1}{4\pi^2\sigma_f^2\sigma_t^2}, \quad (2.12)$$

where σ_t is defined as follows:

$$\sigma_t = \frac{1}{2\pi} \sqrt{\langle t^2 \rangle - \langle t \rangle^2}, \quad (2.13)$$

and $\langle t \rangle$ and $\langle t^2 \rangle$ are the first and second order moments of $p(t)$, respectively. These moments are defined, respectively, as follows:

$$\langle t^2 \rangle = \frac{\int_{-\infty}^{\infty} t^2 |p(t)|^2 dt}{\int_{-\infty}^{\infty} |p(t)|^2 dt}, \quad (2.14a)$$

$$\langle t \rangle = \frac{\int_{-\infty}^{\infty} t |p(t)|^2 dt}{\int_{-\infty}^{\infty} |p(t)|^2 dt}. \quad (2.14b)$$

The time-jittering range can be expressed in terms of the MCRB inequality in Eq. (2.11) as follows:

$$\sigma_t \geq \sqrt{\frac{1}{4\pi^2\sigma_f^2 \text{SNR}_{\text{eff}}}}. \quad (2.15)$$

The effective SNR can be given by $\text{SNR}_{\text{eff}} \triangleq E_s R_s / (N_o B)$, where E_s is the average received symbol energy, i.e., after terahertz-to-baseband down-conversion, R_s is the symbol rate, B is the signal transmission bandwidth, $N_o = kT$ is the additive white Gaussian noise power spectral density, $k = 1.38 \times 10^{-23}$ J/K is the Boltzmann constant, and $T = 300$ K is the temperature in Kelvin.

Ideally, the signal transmission bandwidth, B , is equal to the Nyquist bandwidth. However, in practice, $p(t)$ is time-limited as it is usually generated by a finite impulse

response (FIR) digital filter. Consequently, $P(f)$ is band-unlimited due to the time-frequency uncertainty principle (Cohen 1994, Loughlin & Cohen 2004). In this case, the spectral spread of $P(f)$ is not limited to the Nyquist bandwidth, and it is more reasonable to assume that the signal transmission bandwidth is equal to its RMS spectral width (Hranilovic 2007), i.e., $B = \sigma_f$.

For a symbol duration of T_s , $E_s \triangleq V_{\text{rms}}^2 T_s$, where V_{rms} is the received RMS voltage after terahertz detection, SNR_{eff} can be expressed as follows:

$$\text{SNR}_{\text{eff}} = \frac{2V_{\text{rms}}^2}{N_0 R_s}. \quad (2.16)$$

Substituting Eq. (2.16) in Eq. (2.15), the MCRB of σ_t , normalised to the symbol duration, T_s , can be expressed as follows:

$$\min\left\{\frac{\sigma_t}{T_s}\right\} = \sqrt{\frac{N_0 R_s}{2\pi^2 V_{\text{rms}}^2}}. \quad (2.17)$$

To estimate the time-jittering range in terahertz communications, it is reasonable to use the wide range of symbol rates defined for all channelisation schemes in the IEEE 802.15.3d Standard (IEEE 2017). Figure 2.3 plots the minimum fractional time-jittering, i.e., $\min\{\sigma_t/T_s\}$, versus the symbol rate, R_s , at three different values of the

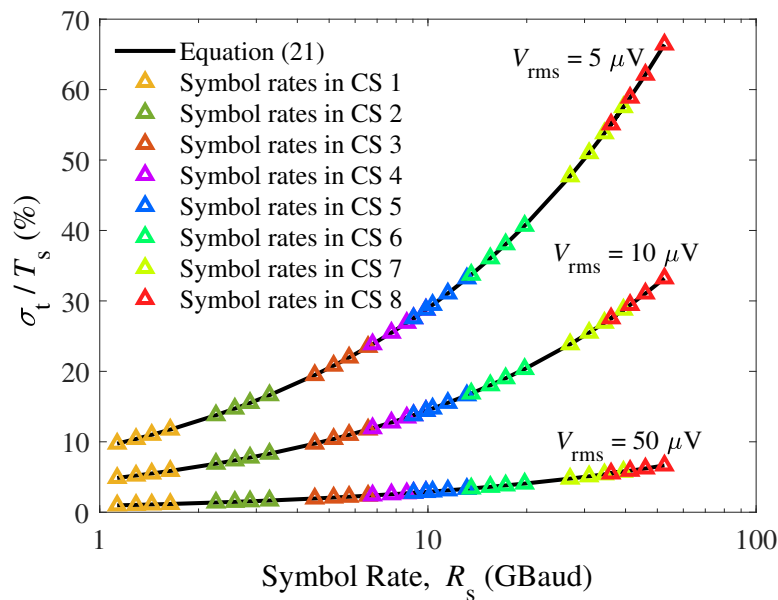


Figure 2.3. Estimated lower bound of the time-jittering range versus the symbol rate. The symbol rates of all channelisation schemes in the IEEE 802.15.3d Standard are included, and three different values of the received root mean squared (rms) voltage are considered. CS: channelisation scheme.

2.6 Overview of Terahertz Transceiver Architectures

received rms voltage, i.e., $V_{\text{rms}} = 5 \mu\text{V}$, $10 \mu\text{V}$, and $50 \mu\text{V}$. As shown in this figure, for all symbol rates, as the rms voltage increases, the corresponding fractional timing-jitter decreases as a result of improving the SNR. Additionally, for all symbol rates defined in this Standard, the timing-jitter can be as low as 0.97% and up to 66.4% of the symbol duration, depending on the particular symbol rate as well as the RMS received voltage at the terahertz receiver output. Such a wide timing-jitter range incorporates the range theorised in (Beaulieu et al. 2001) and the range measured in (Webber et al. 2019). This observation emphasise the role of pulse shaping in mitigating the timing-jitter effects on the BER performance of terahertz communications systems. Chapter 4 presents a proposed pulse shape that is highly tolerant to the timing-jitter.

2.6 Overview of Terahertz Transceiver Architectures

The terahertz band, i.e., 0.1–10 THz, has been envisioned as a promising part of the radio spectrum that can potentially fulfil the increasing demands for short-range high-speed wireless communications services and applications. As a proof-of-concept, a number of system-level experiments have demonstrated the generation and wireless transmission of terahertz signals in the J-band, i.e., from 200 GHz to 400 GHz. Some of these demonstrations have focused on simple modulation schemes, such as the on-off keying (OOK) (Pirrone et al. 2022), (Ducournau et al. 2014) and the pulse amplitude modulation (PAM) schemes (Oshiro et al. 2021). However the maximum speed that can be achieved using these modulation schemes does not exceed 50 Gbit/s, whereas it has been widely acceptable that 100 Gbit/s is the transmission limit targeted by terahertz communications. Therefore, the majority of proof-of-concept terahertz communications experiments focused on the generation of high-throughput terahertz signals (Jia et al. 2018a, Song & Lee 2022, Chinni et al. 2018a,b, Seeds 2014a, Jia et al. 2016a, Dan et al. 2020, Hamada et al. 2018, Rodriguez-Vazquez et al. 2019, Gustavsson et al. 2021). This high throughput is enabled mainly by the spectrally efficient M -ary quadrature amplitude modulation (M -QAM) schemes based on I - Q mixing, together with advanced digital signal processing (DSP) at the transmitter and receiver sides (Jia et al. 2018a, Song & Lee 2022).

Currently, there are two broad categories of direct I - Q mixing techniques to modulate the in-phase (I) and quadrature (Q) components of a baseband signal onto a terahertz carrier. In the first category, namely, direct optical I - Q mixing, the I and Q components are modulated onto a dual-wavelength optical carrier via an optical I - Q modulator (Chinni

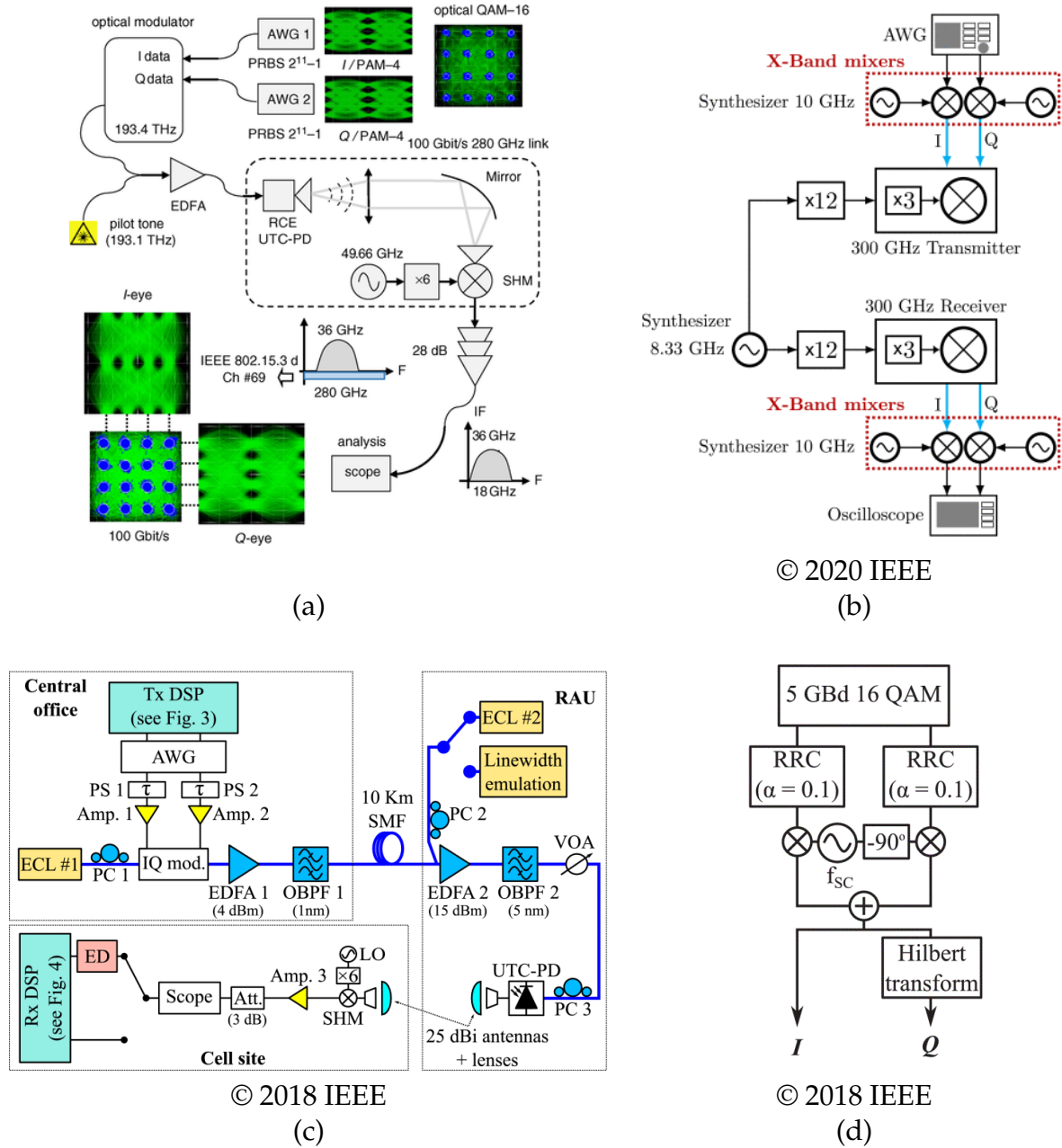


Figure 2.4. Photonics- and electronics-based implementation of terahertz transceiver architectures for the generation of quadrature amplitude modulated (QAM) terahertz signals. (a): Optical *I-Q* mixing (Reproduced from (Chinni et al. 2018a), with permission from John Wiley & Sons). (b) Electronic *I-Q* mixing using the super-heterodyne approach, adapted from (Dan et al. 2020). (c) Optical *I-Q* mixing, together with digital *I-Q* mixing (Gonzalez-Guerrero et al. 2018). (d) Digital *I-Q* mixing using the arbitrary waveform generator (AWG) in (c) (Gonzalez-Guerrero et al. 2018).

et al. 2018a),(Chinni et al. 2018b). Then, the modulated optical signal is down-converted to the terahertz band using a photo-mixer, such as the uni-travelling carrier photodiode (UTC-PD) (Chinni et al. 2018a). Figure 2.4(a) illustrates a sample realisation of this

2.6 Overview of Terahertz Transceiver Architectures

technique. However, a major drawback with this technique is that, unless the photo-mixed carriers are coherent (Seeds 2014a, Jia et al. 2016a), the resulting terahertz QAM signal is often accompanied by a high phase noise, leading to I - Q demodulation errors at the receiver side. In the second category, namely, electronic I - Q mixing, a combination of high-frequency local oscillators (LOs), frequency multipliers, harmonic or sub-harmonic mixers (SHM), and/or filter circuits (Dan et al. 2020) are usually required to I - Q -modulate a terahertz carrier. A sample realisation of this technique is depicted in Fig. 2.4(b). However, electronically-generated terahertz QAM signals usually suffer from the I - Q imbalance, which deteriorates the error performance of these systems (Dan et al. 2020),(Hamada et al. 2018),(Rodriguez-Vazquez et al. 2019). A major drawback that is common to both optical and electronic I - Q mixing-based terahertz transceivers is their highly complicated architectures, especially, involving heterodyne terahertz detection (Gustavsson et al. 2021).

Digital I - Q mixing can be used to reduce the phase noise and I - Q imbalance problems of the optical and electronic-based techniques (Song & Lee 2022). In this technique, highly precise digital-to-analog converters (DACs) are used to generate amplitude-matched and time-synchronous I and Q signals. These signals are modulated onto a quadrature pair of intermediate frequency (IF) sinusoidal carriers, which are synthesised by the same DAC. The resulting IF signal is then modulated onto an optical or a microwave signal, before being down-converted or up-converted, respectively, to a terahertz signal (Fujishima 2018). This way, the I - Q imbalance and phase noise problems can be avoided, and the coherent detection and the phase noise mitigation techniques (Jia et al. 2018a) are no longer required at the receiver side. Figure 2.4(c) shows a sample realisation of the digital I - Q mixing with the optical I - Q mixing techniques combined. Figure 2.4(d) details the implementation of the digital I - Q mixing technique before optical modulation. Although electronic and optical I - Q mixing become more accurate when assisted by digital I - Q mixing, the generation and modulation of high-frequency IF carriers can be an overwhelming DSP task for DACs with limited computational resources, which makes the design of practical terahertz transceivers challenging, especially for real-time applications at high baudrates. The topologies of the photonic-assisted terahertz transmitters in Figs. 2.4(a) and (c) are, so far, the only known optical I - Q mixing techniques in terahertz communications. As shown in both figures, the I and Q components are orthogonally modulated onto an optical carrier using a dual-drive Mach-Zehnder modulator (MZM), without or with digital I - Q mixing, respectively. On the other hand, Fig. 2.4(b) shows an example of many

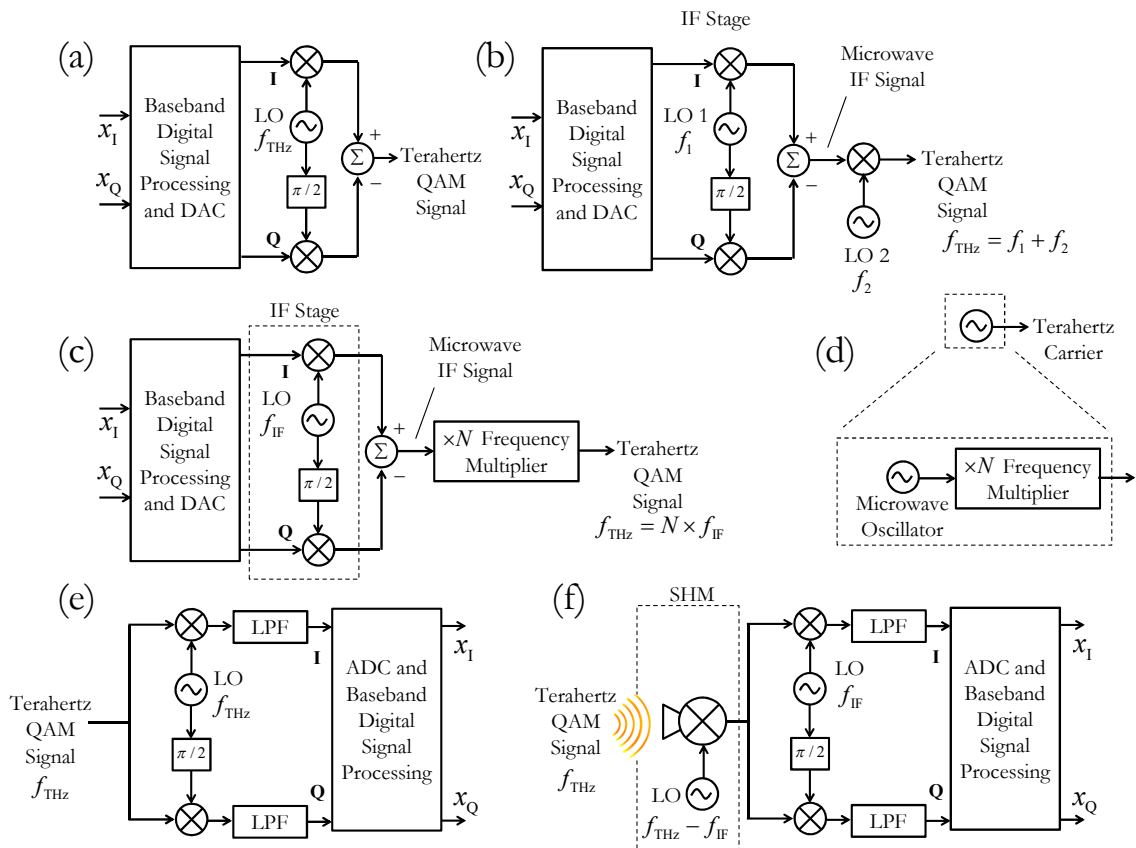


Figure 2.5. Common terahertz transceiver architectures for the generation of quadrature amplitude modulated (QAM) terahertz signals. (a) Homodyne terahertz transmitter architecture based on direct conversion mixer, i.e., zero IF. (b) Heterodyne terahertz transmitter architecture based on a single stage or multi-stage IF-to-terahertz up-conversion. (c) Heterodyne terahertz transmitter architecture based on a single stage or multi-stage IF-to-terahertz up-conversion. (d) Possible implementation of a terahertz frequency oscillator based on a single microwave oscillator and a single-stage or multi-stage frequency multiplier. (e) Architecture of a superheterodyne terahertz receiver. (f) A sub-harmonic mixing (SHM)-based terahertz receiver. LO: Local oscillator. IF: intermediate frequency. I: in-phase. Q: quadrature. LPF: low-pass filter. ADC: analog-to-digital converter. DAC: digital-to-analog converter.

possible implementation topologies for electronics-based terahertz transmitters. For instance, Fig. 2.5(a) shows the functional block diagram of the homodyne terahertz transmitter. As shown in this figure, the I and Q baseband signals are modulated onto the terahertz carrier using a direct converting mixer. Figure 2.5(b) shows a more complicated topology, which is commonly called the heterodyne terahertz transmitter. As shown in this figure, the heterodyne terahertz transmitter is based on a single stage or multi-stage baseband-to-IF up-conversion using microwave LOs and I - Q mixers before IF-to-terahertz up-conversion. The IF-to-terahertz up-conversion can be implemented

2.6 Overview of Terahertz Transceiver Architectures

using frequency mixing, as shown in Fig. 2.5(b), or a single-stage or multi-stage N^{th} -order frequency multiplier as in Fig. 2.5(c), which can destroy the phase information due to its high nonlinearity. Figure 2.5(d) also shows a typical implementation of a terahertz frequency oscillator based on a single microwave oscillator and a single-stage or multi-stage frequency multiplier. This functional block diagram models the terahertz LO in Fig. 2.4(b) at the transmitter and receiver sides. Terahertz LOs are also required for the coherent demodulation of I - Q -modulated terahertz signals at the receiver side, in which the terahertz signal is down-converted directly to the baseband. The architecture of such receiver types, also known as the superheterodyne terahertz receivers, is illustrated in Fig. 2.5(e). Figure 2.5(f) shows a multi-stage terahertz receiver, in which the I - Q terahertz signal is down-converted to an IF stage, also sub-harmonic mixing (SHM), before IF-to-baseband down-conversion. Both receiver types can be used with photonics- and electronics-based terahertz transmitters, regardless of its particular implementation topology.

It is noteworthy that, the generation and demodulation of I - Q -modulated terahertz signals for high-throughput applications requires rather complicated terahertz transceiver architectures. However, currently available terahertz transceiver architectures are still impractical for future 6G communications equipment, which should be compact and less demanding in terms of the design complexity. Therefore, there it is of paramount importance to develop terahertz transceivers that can support high data rates as the I - Q -based transceivers and, at the same time, have a reasonable implementation complexity. Fundamentally, the implementation of the I - Q mixing and demodulation concepts as well as consequential problems originate from the need for physical components to orthogonally combine or demodulate the I and Q baseband signals using two quadrature sinusoids. Importantly, the baseband pulse shaping is an essential DSP task that is independently implemented at the transmitter and receiver sides using two identical Nyquist waveforms for the I and Q baseband signals, regardless of their terahertz transceiver architecture. Therefore, a potential radical solution to these design challenges is to orthogonally combine the I and Q components of the transmitted signal in the baseband using a pair of Hilbert Nyquist waveforms. The DSP modules at the transmitter and receiver sides can be configured to orthogonally combine and demodulate the I and Q signals accurately in the baseband at the transmitter and receiver sides, respectively. This part is discussed in detail in Chapter 5.

2.7 Demonstration of Terahertz Communications

Terahertz wireless communications has been envisaged as a capable carrier of future high data rate applications such as the live streaming of 360° panoramic videos (Du et al. 2020). To realise the long-term vision of integrating 6G wireless networks with the existing optical infrastructure, the concept of combining terahertz wireless communications with optical RoF technologies has been proposed and experimentally demonstrated (Shams et al. 2015). Previous experimental demonstrations on terahertz-over-fibre systems have been primarily based on the high-speed reliable transmission of random binary streams. The reliability of these systems has been achieved by employing offline DSP techniques at the receiver side, which is impractical for many real-world usage scenarios. A few of these demonstrations have been concerned with the real-time distribution of user-interpretable signals, such as 4k videos, over practically deployable terahertz-over-fibre links. For instance, in (Zhen Chen et al. 2013), the wireless transmission of 2.5 Mbit/s and 5 Mbit/s video signals for 2.4 m was experimentally demonstrated using a 3.9 THz carrier. In a more spectrally-efficient demonstration (Moon et al. 2021), two uncompressed full-8K videos of 24 Gbit/s each have been simultaneously transmitted for a distance of 2–3 cm over two independent terahertz channels operating at 324 GHz and 335 GHz. In (Nallappan et al. 2018), a real-time generated 5.5 Gbit/s 4k video was transmitted over a 1 m wireless terahertz link using a 140 GHz carrier. However, these demonstrations have relied on pre-recorded video signals that have been pre-processed offline to minimise the required transmission bandwidth (Shafi et al. 2020). Additionally, the optical transmission have not been considered in these demonstrations. Therefore, these experimental demonstrations do not approach the real capabilities of terahertz communications as a key enabler of 6G hybrid access, i.e., wireless and optical, networks.

In this section, we show that terahertz communications has a potential to deliver user interpretable signals at high speeds in real-time. Additionally, we also show that terahertz wireless communications systems can be readily integrated with the existing optical networks, at least for the last mile point-to-point optical connection before the wireless distribution of terahertz signals to end users. Specifically, we experimentally demonstrate the real-time generation and transmission of a 6 Gbit/s 4k video signal over a highly reliable terahertz-over-fibre communications system. This system is highly reliable and comprises a 30 cm terahertz wireless channel operating at 300 GHz as well as a 5-km single mode optical fibre link.

2.7 Demonstration of Terahertz Communications

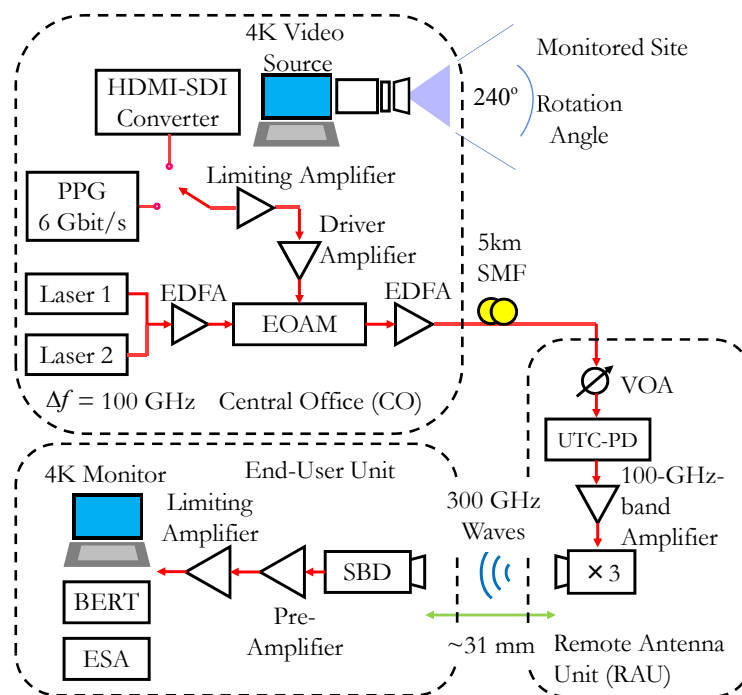


Figure 2.6. Schematic showing the experimental setup of the terahertz over fibre system. B2B: back-to-back. RoF: Radio-over-Fibre. VOA: Variable optical attenuator. EDFA: Erbium doped fibre amplitude. PPG: Pulse pattern generator. UTC-PD: Uni-travelling-photo diode. SBD: Schottky-barrier diode. BERT: Bit error rate tester. ESA: Electrical spectrum analyser. SSMF: Standard single mode fibre.

Figure 2.6 illustrates the block diagram for the experimental setup of a typical terahertz-over-fibre system, which emulates a realistic scenario conceived for future 6G communications. As shown in this figure, the system comprises three main units, namely, a photonics-based central office (CO), a remote antenna unit (RAU) and a wireless end user (EU). The CO is connected to the RAU, which is based on a UTC-PD, via a 5-km single-mode fibre. The RAU wirelessly radiates a terahertz video signal to the EU, which is a low-complexity electronic receiver that relies on an SBD as a non-coherent detector.

At the CO, two independent continuous-wave (CW) tunable laser sources (TLS) with identical optical power of -30 dBm emit two lightwave carriers at a wavelength of 1550.000 nm and 1550.802 nm, leading to a frequency difference of about 100 GHz. The linewidth of the emitted optical carriers is less than 100 kHz.

The pulse-pattern generator (PPG) produces a 6 Gbit/s pseudo-random binary sequence (PRBS) of $2^{12} - 1$ bits length. Meanwhile, the two optical carriers are amplified by the first erbium-doped fibre amplifier (EDFA) and combined via the optical coupler (OC) before being applied to the Mach-Zehnder modulator (MZM), together with the

PPG signal, for electro-optic modulation. The gross line rate of the dual-wavelength modulated signal, i.e., after the OC, is 12 Gbit/s.

The modulated optical signal is then optically amplified using the second EDFA before being launched into the 5-km standard single-mode fibre (SSMF), which connects the CO to the RAU. The optical signal at the SMF output end is applied to the UTC-PD via the variable optical attenuator (VOA) for terahertz signal generation via photo-mixing. The RAU has an electronic front-end, which comprises a 100 GHz terahertz amplifier, followed by a $3\times$ frequency multiplier, which up-converts the generated 100 GHz signal to 300 GHz. The generated terahertz signal is then forwarded to a 25 dBi diagonal horn antenna via a WR-3.4 waveguide before being wirelessly emitted over free-space to an identical antenna at the end-user side.

At the receiver side, i.e., the EU unit, the terahertz signal is envelope-detected and applied to a low-noise amplifier (LNA), which is cascaded by a limiting amplifier, in order to compensate for the free space path loss (FSPL). Subsequently, the amplified signal is forwarded to a BER tester (BERT) for BER evaluation.

We evaluate the transmission performance of this system using two experiments. In the first experiment, the transmission performance is tested with and without the SSMF, i.e., a back-to-back (B2B) configuration. The SNR is controlled by tuning the UTC-PD photo-current in the range from 0.7 mA to 1.2 mA with a step of 0.1 mA. This relatively narrow tuning range reflects the high sensitivity of the terahertz electronic front-end. Figure 2.7(a) plots the measured BER versus the UTC-PD photo-current with and without RoF transmission. In both cases, the BER relationships are logarithmically approximated by first-order polynomials. The approximations are used to estimate the optical power penalty due to SSMF transmission, which is about $20\log(I_{\text{ph},5\text{ km}}/I_{\text{ph},\text{B2B}}) = 1.4$ dB at a BER of 10^{-9} . Additionally, at a photo-current of 1.2 mA, a minimum BER performance of 1.06×10^{-9} and 7.91×10^{-12} is attained with and without SSMF transmission, respectively. Considering on-off keying (OOK) over additive white Gaussian noise (AWGN) channels, these BER limits correspond to signal-to-noise ratio (SNR) upper bounds of about 15.54 dB and 16.57 dB, respectively. Figures 2.7(b)-(e) depict the eye diagrams of the received signal with and without SSMF transmission at a photo-current of 1 mA and 1.2 mA. In terms of the overall shape, the eye diagrams in Figs. 2.7(b) and (d) show similar trends owing to similar transmission conditions, namely, without SMF transmission. Importantly, the eye diagram in Fig. 2.7(b) is evaluated at a photo-current of $I_{\text{ph},1} = 1$ mA, whereas the eye diagram in Fig. 2.7(d) is

2.7 Demonstration of Terahertz Communications

evaluated at a photo-current of $I_{ph,2} = 1.2$ mA. Such a subtle difference between both photo-currents results in an optical signal-to-noise ratio (OSNR) improvement of about $20\log(I_{ph,2}) - 20\log(I_{ph,1}) = 1.58$ dB. This incremental change in the OSNR makes it barely possible to visually assess the corresponding improvement in the performances through only the eye diagrams, specially because both figures are evaluated without SMF transmission. Likewise, Figs. 2.7(c) and (e) show similar trends as they both use an SSMF and have the same difference in their photo-currents. Therefore, the BERs are quantified and plotted in Fig. 2.7(a) for all scenarios. As can be seen in this figure, when the photo-current is beyond 1 mA, the BER is as low as 10^{-9} with and without SSMF transmission. However, it still can be noticed that, the rising and falling edges of the waveforms in Figs. 2.7(c) and (e) are thicker than the corresponding edges in Figs. 2.7(b) and (d), respectively, due to the 1.4 dB optical power penalty introduced by the SSMF. Also, the vertical and horizontal eye openings shown in Figs. 2.7(b) and (d) for B2B transmission are wider than the corresponding eye patterns shown in Fig. 2.7(c) and (e) for the RoF transmission. The widths of these eye patterns are inline with the corresponding BERs depicted in Fig. 2.7(a). However, for the same propagation scenario, no much difference can be observed when the photo-current is 1 mA or 1.2 mA.

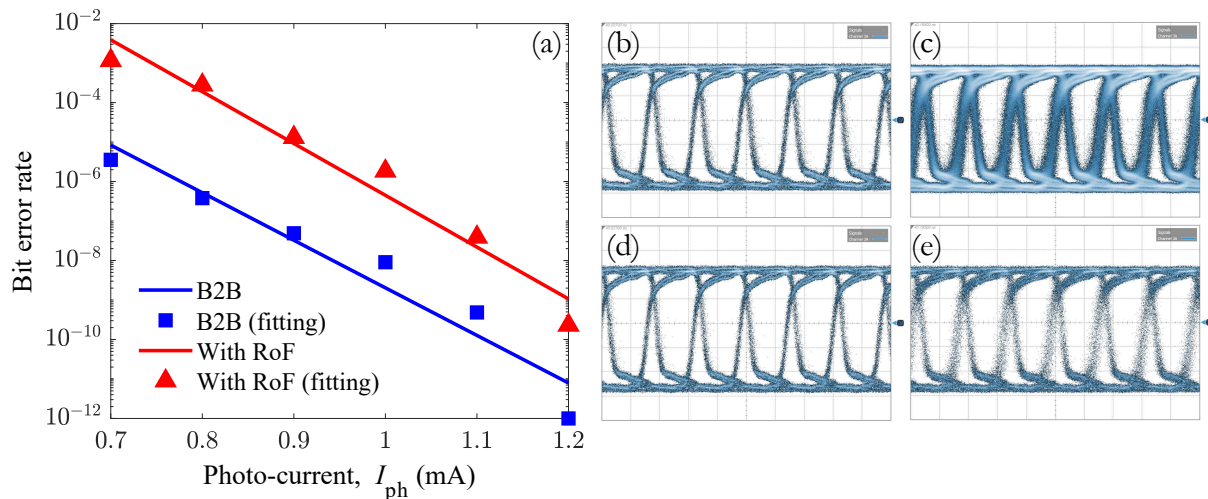


Figure 2.7. Measured error performance with and without single mode fibre transmission. (a) Bit error rate versus the photo-current without radio-over-fibre transmission. (b) Eye diagram of the received waveforms at a photo-current of 1 mA without fibre transmission. (c) Eye diagram of the received waveforms at a photo-current of 1 mA with fibre transmission. (d) Eye diagram of the received waveforms at a photo-current of 1.2 mA without fibre transmission. (e) Eye diagram of the received waveforms at a photo-current of 1.2 mA with fibre transmission. The voltage scale is 100 mV/division and the time base is 100 ps/division. B2B: Back-to-back. RoF: Radio-over-Fibre.

In the second experiment, the PPG is replaced by a 4k video source. This video source is a laptop 4k camera connected to a HDMI-to-SDI video encoder to generate a 6 Gbit/s video signal. At the EU side, this video signal is decoded by an SDI-to-HDMI video converter before being displayed on a 4k monitor. We manually rotate the 4k video source over an angle of 240° and continuously monitor the received video spectrum. Ideally, the spectrogram of the video signal should be continuously monitored to ensure the invariance of the spectral budget required for 4k video transmission. However, since this feature is currently beyond the capabilities of the measurement equipment, the received video spectrum is measured and recorded at different time instants using a 10 GHz electrical spectrum analyser (ESA). Figure 2.8(a) shows the video signal spectrum, recorded at three different view angles of the video source, i.e., 0° , 120° , and 240° , in the B2B configuration and with SSMF transmission. As shown in Fig. 2.8(a), without fibre transmission, the video signal spectrum remains invariant with changing the view angle and the video contents at each angle. A similar observation holds for Fig. 2.8(b) when the video signal is optically transmitted for a 5 km distance. However, a spectral broadening effect is observed with the optically transmitted video compared to the B2B transmission. This spectral re-growth highlights the nonlinearities of the optical fibre, which is likely to be induced by the EDFAs. The photograph in Fig. 2.8(c) shows that, still the transmitted 4k video can be correctly decoded at a high quality at the receiver side, even with combined optical and wireless transmission.

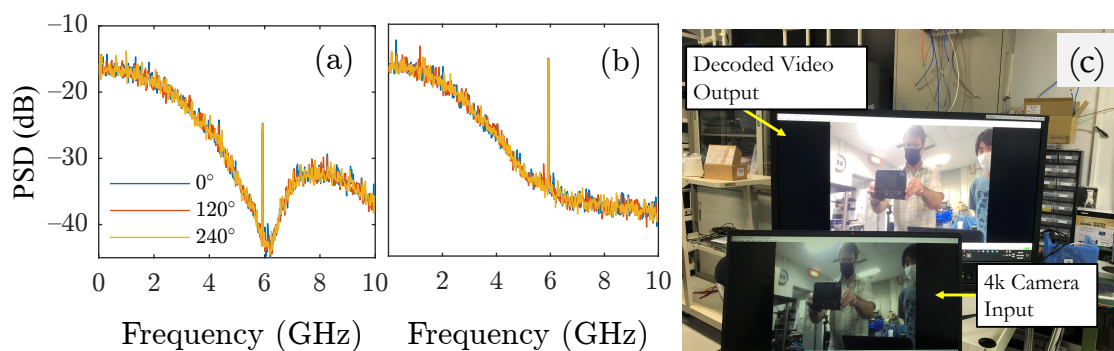



Figure 2.8. Transmission of a 4k video signal over a photonics-based terahertz communications system with combined optical and wireless transmission. (a) Measured electrical spectra of the received 4k video signal without optical fibre transmission. (b) Measured electrical spectra of the received 4k video spectrum after optical transmission over a 5-km standard single mode fibre (SSMF). (c) A photograph of the experiment showing 4k video streaming in real-time. The 4k video signal is wirelessly transmitted over a 31 cm terahertz wireless link operating at 300 GHz.

2.8 Summary

In conclusion, key pulse shaping techniques using digital platforms need to be substantially investigated before being re-introduced to, and potentially incorporated into, the field of terahertz communications. This chapter highlights the need for these techniques to meet design requirements that are specific to terahertz communications. These design requirements include the compliance with the IEEE 802.15.3d Standard as a global wireless standard, high tolerance to time-jittering and ease of transceiver implementation. By considering the design challenges identified in this chapter, terahertz communications systems with low-complexity and improved transmission performance can be realised. The parallel development of computationally-efficient signal processing techniques is crucial to the adoption of these techniques for real-time high-speed terahertz communications. Yet, much work on pulse shaping and computationally-efficient signal processing is to be done in the domain of terahertz communications.

IEEE 802.15.3d-Compliant Pulse Shaping



COMPLYING with globally adopted standards for wireless communications is crucial to the harmonious interoperability of wireless communications equipment produced by different manufacturers. In this chapter, we propose a waveform that shows full compliance with the spectral emission mask imposed by the IEEE Standard for terahertz communications. The designed waveform exploits 99.3% of the total in-band energy admissible by this mask and provides an extra degree of freedom for out-of-band interference management. A proof-of-concept experiment is conducted using a 300 GHz photonics-based terahertz communications link to demonstrate the generation and wireless transmission of the proposed waveform. Experimentally validated bit error rates show that the proposed waveform outperforms the widely adopted raised-cosine waveform as well as the better-than-raised-cosine waveform, even when the Nyquist criterion for inter-symbol interference-free signalling is not satisfied. Moreover, an error-free transmission at an IEEE 802.15.3d Standard-compliant bit rate of 1.44 Gbit/s is achieved without employing complicated digital signal processing at the receiver side.

3.1 Introduction

Continuously increasing demands for short-range high-speed wireless communications have stimulated intensive research interests in innovative solutions towards spectrally efficient communications technologies amid the radio spectrum, which is fully allocated up to 100 GHz. As an unoccupied part in the electromagnetic spectrum, the terahertz band from 100 GHz to 10 THz has emerged as a promising solution to meet these demands (Tekbıyık et al. 2019). To regulate multi-user access to this band and control inter-band interference, the maximum effective isotropic radiated powers (EIRPs) of practical wireless transmitters and their usable bandwidths are regulated by the local regulatory authorities based on the globally-adopted wireless communication standards. To meet the spectral emission requirements of these standards, the over-the-air (OTA) signals' spectra are reshaped at the transmitter side before being wirelessly distributed over free-space channels (R. E. & Spencer 2010, Shin 2013, Gigl et al. 2010, Thomas Gigl & Witrisal 2012, Du et al. 2015, Tuset-Peiró et al. 2019, Dalce et al. 2014, Guglielmo et al. 2016).

In the field of terahertz communications, the first worldwide standard, officially called the IEEE 802.15.3d Standard (IEEE 2017), was released in 2018 to support the operation of high-speed Ethernet wireless links up to 100 Gbit/s. In this standard, a 69 GHz bandwidth is dedicated to terahertz communications in the frequency range from 252 GHz to 321 GHz, commonly called the IEEE terahertz band. It is important to highlight that, as shown in Fig. 2.2, the IEEE 802.15.3d Standard does not specify a pulse shaping filter. Instead, filtering is implied in the spectral emission masks specified by this standard. Despite the broad bandwidth allocated by the IEEE 802.15.3d Standard to terahertz communications, the power levels offered by currently available terahertz wireless transmitters are relatively limited (Song et al. 2012), (Chinni et al. 2018a). The power is further reduced at the receiver side due to the high free-space path loss at terahertz frequencies. Hence, the prudent utilisation of the emission masks admissible by the IEEE 802.15.3d Standard raises a key challenge in the development of future terahertz communications systems. Despite its importance, this challenge remains under-investigated.

In most of the previous demonstrations, the terahertz spectrum has been explored freely without imposing any constraints on the EIRPs, the central frequencies and the bandwidths of the generated terahertz signals (Shams et al. 2016, Koenig et al. 2013, Webber et al. 2019, Jia et al. 2016a, Ducournau et al. 2014).

3.1 Introduction

Only a limited number of the previous demonstrations have partially considered the physical (PHY) layer specifications defined by the IEEE 802.15.3d Standard, including the pulse shaping required to comply with this standard. For instance, in (Chinni et al. 2018a), (Chinni et al. 2018b), the first successful transmission of an IEEE 802.15.3d terahertz signal in the 300 GHz band was reported. An RC pulse shaping filter, with a roll-off factor of 0.35, was employed to reshape the spectrum of a quadrature amplitude modulated (QAM) signal in the baseband before being up-converted and transmitted over the IEEE band at data rates of 56, 80 and 100 Gbit/s. In (Fujishima 2018), an all-electronic transmitter was implemented to demonstrate the generation of a 27 GHz bandwidth signal at 300 GHz. The generated terahertz signal spanned 12.5 single-user channels of 2.16 GHz bandwidth each, which violates the frequency allocation plan defined by the IEEE 802.15.3d Standard for multi-user operation scheme. Moreover, the design criteria of the generated signal spectrum were not reported. In (Dan et al. 2020), a dual-channel generation and transmission of 2.16 GHz bandwidth terahertz signals in the 300 GHz band was reported. An RC pulse shaping filter, with a roll-off factor of 0.35, was employed to reshape the signals spectra in the baseband. The conformity of the generated spectra to the emission mask defined in the IEEE terahertz communications standard was not investigated either. Obviously, a common shortcoming in the aforementioned demonstrations is the lack of compliance to this IEEE Standard.

To address this issue systematically, here we provide an analytical framework for the design and performance assessment of terahertz waveforms developed for IEEE 802.15.3d terahertz communications. Then, we investigate two widely-used waveforms, namely the RC and the better-than raised-cosine (BTRC) waveforms, using the developed analytical framework. Importantly, we propose an alternative waveform for terahertz communications under the most stringent spectral constraints defined by the IEEE 802.16.3d Standard. The transmission performance of the three considered waveforms is experimentally investigated using a photonics-based terahertz communication system, with the bit error rate (BER) as a performance metric. It should be highlighted that, using photonics-based terahertz systems for experimental demonstrations emphasises the possibility of seamless integration of radio-over-fibre (RoF) optical networks to terahertz wireless links as well as the applicability of microwave-photonic (MWP) signal processing techniques, at least conceptually, to terahertz communications (Shams et al. 2016).

The rest of this chapter is organised as follows. Section 3.2 overviews the IEEE 802.15.3d Standard and introduces a relevant analytical framework for the terahertz waveform design. In particular, two metrics are defined to quantify the compliance of terahertz waveforms with the spectral emission mask of the IEEE 802.15.3d Standard. In Section 3.3, the proposed waveform is presented and compared with two of the most commonly used pulse shapes in digital communications. Section 3.4 presents the experimental investigation of the transmission performance of the three considered waveforms using a terahertz photonic system. Section 3.5 discusses the impact of the terahertz system nonlinearity on the compliance of IEEE 802.15.3d signals before the chapter is finally concluded in Section 3.6.

3.2 IEEE 802.15.3d Spectrum Analysis Framework

Since the IEEE 802.15.3d Standard-compliant terahertz waveforms are subject to a set of spectral constraints, designing the targeted waveform in the frequency domain followed by frequency-to-time conversion is a straightforward approach. However, reshaping the spectra of narrow band signals in the terahertz band is not practical when using the currently available all-electronic digital platforms. Therefore, to relax the computational efforts required, we map the IEEE spectral emission mask from the passband to the baseband (Adalan et al. 2009). Then, the baseband spectrum is reshaped using all-electronic-based processing platforms before being up-converted to the passband to produce the spectrally compliant terahertz OTA signal.

Since the IEEE 802.15.3d Standard relies on multi-rate adaptive coding and modulation (ACM) schemes, the proposed design approach can be considered highly adaptive as it allows for a modular transmitter design and implementation using all-electronic platforms, such as high-speed re-programmable digital-to-analog converters (DACs), regardless of the terahertz carrier frequency and/or the generation technique. These platforms are generic as they have the capacity to implement sophisticated communications processing in the baseband, including the pulse shaping (Schmogrow et al. 2011). The implementable modulation schemes can be simple on-off keying (OOK) and binary phase shift keying (BPSK), or higher-order vector modulation formats such as the $\pi/2$ -quadrature phase shift keying ($\pi/2$ -QPSK), 16-quadrature amplitude modulation (16-QAM) and 64-QAM. Moreover, the transmission bit rates supported by all-electronic SDR-driven optical systems can exceed 100 Gbit/s (Schmogrow et al. 2010). All of the

3.2 IEEE 802.15.3d Spectrum Analysis Framework

aforementioned modulation formats and data rates are compatible with the technical requirements defined in the IEEE 802.15.3d Standard.

The IEEE 802.15.3d Standard defines eight different channelisation schemes within the range from 252 GHz to 321 GHz. Each channelisation scheme comprises multiple parallel channels with bandwidths ranging from 2.16 GHz to 69.1 GHz. To limit the mutual inter-band interference (IBI) among the OTA terahertz signals transmitted in adjacent channels, a spectral emission mask is imposed to the EIRP of each signal. The spectral emission mask of the i^{th} channelisation scheme, denoted by $M_i(f)$, can be modelled by a piece-wise linear function when expressed in the dBr unit. This spectral mask is defined by a unique set of four knee frequencies, denoted by $f_{i,k}$, and the corresponding power spectral density (PSD) upper-bounds at these frequencies. Here, $i \in \{1, 2, \dots, 8\}$ denotes the channelisation scheme number and $k \in \{0, 1, 2, 3, 4\}$ is the knee frequency index. This can be formulated mathematically as follows:

$$M_i(f) \text{ (dBr)} = \begin{cases} \left(\frac{M_{i,k} - M_{i,k-1}}{f_{i,k} - f_{i,k-1}} \right) f - \left(\frac{M_{i,k+1} - M_{i,k}}{f_{i,k+1} - f_{i,k}} \right) f_{i,k} + M_{i,k} & ; f_{i,k-1} \leq f < f_{i,k} \\ \leq -30 & ; f \geq f_{i,4} \end{cases} \quad (3.1)$$

where $M_{i,k}$ denotes the maximum admissible PSD at the k^{th} knee frequency of the i^{th} channelisation scheme. Tables 3.1 and 3.2 list the numerical values of the PSD limits and the corresponding knee frequencies for the eight channelisation schemes specified by the IEEE 802.15.3d Standard, respectively. It should be pointed out that the PSD limits are expressed in the dBr unit. This is because the IEEE 802.15.3d standard does not specify the absolute EIRP level as it is dependent on the respective local regulating authorities. In addition, the channel bandwidths listed in Table 3.2 are in the passband. The equivalent baseband bandwidths are 50% of the bandwidths in Table 3.2. The knee frequencies are relative to the terahertz carrier frequency in the passband.

Table 3.1. Spectral limits of the IEEE 802.15.3d emission masks.

Spectral limit, $M_{i,k}$ (dBr)	$M_{i,0}$	$M_{i,1}$	$M_{i,2}$	$M_{i,3}$	$M_{i,4}$
Value	0	0	-20	-25	-30

Table 3.2. Knee Frequencies of the spectral emission masks of the IEEE 802.15.3d Standard. Frequencies are in GHz (IEEE 2017).

Channelisation Scheme ID	Bandwidth (GHz)	$f_{i,1}$	$f_{i,2}$	$f_{i,3}$	$f_{i,4}$
1	2.16	0.94	1.1	1.6	2.20
2	4.32	2.02	2.18	2.68	3.28
3	8.64	4.18	4.34	4.84	5.44
4	12.96	6.34	6.50	7.00	7.60
5	17.28	8.50	8.66	9.16	9.76
6	25.92	12.82	12.98	13.48	14.08
7	51.84	25.78	25.94	26.44	27.04
8	69.12	34.42	34.58	35.08	35.68

3.2.1 Spectral Compliance Metric

In non-terahertz wireless communications, several metrics have been introduced to quantify the compliance of wirelessly radiated signals' spectra with a pre-specified spectral emission mask (Fellows et al. 2015 b,a). For instance, in (Abraha et al. 2011), a frequency-dependent binary compliance metric, denoted by $B_{\Psi}(f) \in \{0, 1\}$, has been proposed to quantify the compliance of ultra-wideband (UWB) signals with the FCC spectral emission mask.

Likewise, this metric can be employed in the context of IEEE 802.15.3d Standard-compliant terahertz communications. The normalised PSD of an arbitrary terahertz signal envelope, denoted by $|\tilde{\Psi}_n(jf)|^2$, is quantified as follows. Firstly, a logarithmic PSD ratio, denoted by $\zeta(f)$ is defined and evaluated as follows:

$$\zeta(f) = 10 \log \left(M_{i,k}(f) / |\tilde{\Psi}_n(jf)|^2 \right). \quad (3.2)$$

Secondly, a frequency-domain binary variable $B_{\Psi}(f)$ is defined as follows:

$$B_{\Psi}(f) = \begin{cases} 1; & \zeta \geq 0 \\ 0; & \zeta < 0. \end{cases} \quad (3.3)$$

where $B_{\Psi}(f) = 1$ indicates that the compliance to the spectral mask $M_{i,k}(f)$ is achieved at f , while $B_{\Psi}(f) = 0$ denotes the violation of this compliance. It should be pointed out that, in contrast to the definition provided in (Abraha et al. 2011), $\zeta(f)$ is defined in the dBr unit, rather than in the linear unit, to capture spectral details at low PSD levels such as the additive white Gaussian noise (AWGN) floor level. Hence, this modified metric can precisely identify the frequencies at which the signal PSD should be particularly considered. Meanwhile, it is also reasonable to define a figure-of-merit (FoM) that

3.2.2 Spectral Radiation Efficiency Metric

quantifies the overall compliance of the signal PSD over an arbitrary bandwidth of interest. We define the average compliance coefficient (CC), denoted by ρ_{Ψ} , as follows:

$$\rho_{\Psi} = \frac{1}{2\Delta f} \int_{f_0-\Delta f}^{f_0+\Delta f} B_{\Psi}(f)df, \quad (3.4)$$

where $0 \leq \rho_{\Psi} \leq 1$, f_0 is the central terahertz carrier frequency of interest, and $2\Delta f$ is the bandwidth over which the CC of $|\tilde{\Psi}_n(jf)|^2$ is calculated. Although the IEEE 802.15.3d Standard limits the operation of a terahertz signal to the passband bandwidths listed in Table 3.2, the value of Δf in Eq. (3.4) can be arbitrarily large ($\Delta f \gg \text{BW}$) to capture the aggregate contributions of the spurious out-of-band (OOB) emissions and the spectral regrowth effects in the overall compliance analysis (Dahlman et al. 2016).

3.2.2 Spectral Radiation Efficiency Metric

The concept of maximising the spectral radiation efficiency (SRE) of an emitted OTA signal, whilst complying with the constraints of a spectral emission mask, has been developed in the context of UWB communications (Abraha et al. 2011). In UWB communications, the SRE has been adopted as a waveform design objective that can be optimised in order to maximise other dependent metrics, such as the wireless reach and channel capacity. Likewise, in this work, we employ this metric to the design of IEEE 802.15.3d-compliant signals for the same considerations that were in UWB communications. Assume that $|\tilde{\Psi}_n(jf)|^2$ is defined over the bandwidth of an IEEE 802.15.3d channel. The SRE of this envelope signal is defined as the ratio of the power contained within its spectrum to the total PSD admissible by the spectral emission mask. This definition is expressed mathematically as follows:

$$\eta = \frac{\int |\tilde{\Psi}_n(jf)|^2 df}{\int_{\text{BW}} M_i(f)df}, \quad (3.5)$$

where η is the SRE of the baseband envelope of the terahertz signal. A number of benefits can be achieved by maximising the SRE of terahertz signals at the receiver front-end, including the improvement of the signal-to-noise plus interference ratio (SNIR) and extending the wireless communications reach. An implicit challenge arises when considering Eq. (3.4) and Eq. (3.5) jointly, where the PSD of an optimal terahertz waveform should be carefully shaped to achieve the maximum SRE, and at the same

time, be subject to the EIRP constraints imposed by the IEEE 802.15.3d spectral regulation mask. This design trade-off leads to the definition of the following non-convex multi-objective optimisation problem:

Problem Statement. *An optimal terahertz signal that fully complies with the spectral emission mask of the IEEE 802.15.3d Standard can be obtained by designing its baseband envelop waveform $\psi(t)$, defined by a complete parameter set of Ξ , such that the following two independent optimisation problems are jointly satisfied:*

$$\underset{\Xi}{\text{maximize}} \left(\int_{\text{BW}} |\tilde{\Psi}_n(jf, \Xi)|^2 df \right) \quad (3.6)$$

such that

$$\max \left\{ |\tilde{\Psi}_n(jf, \Xi)|^2 \right\} \leq M(f) \forall f \text{ or } \rho_{\tilde{\Psi}} = 1. \quad (3.7)$$

The solution of the multi-objective optimisation problem defined in Eq. (3.6) and Eq. (3.7) jointly yields a desired optimal terahertz waveform.

3.3 Proposed Waveform

The proposed waveform is based on the Lorentzian pulse shape, which has been largely overlooked in the context of spectral shaping for digital communications (Farès et al. 2017) despite its unique temporal and spectral features. An amplitude-scaled Lorentzian pulse can be expressed as (Farès et al. 2017):

$$p_L(t) = \frac{A}{1 + \left(\frac{t}{\tau}\right)^2}, \quad (3.8)$$

whereas the Fourier transform of $p_L(t)$ is given by Farès et al. (2017)

$$L(f, \tau) = A\pi\tau \exp\left(-2\pi\tau |f|\right). \quad (3.9)$$

When expressed in the dBr unit, $L(f, \tau)$ follows a triangular-shaped spectrum with a steady spectral roll-off (Pace et al. 2008), which can be controlled via the temporal width τ of the Lorentzian basis pulse. This spectral feature makes it possible to use the Lorentzian pulse to match the spectral mask shape defined in Tables 3.1 and 3.2. In particular, we propose a fully-compliant spectrum based on a linear combination of

3.3 Proposed Waveform

logarithmic double-sided Lorentzian spectra centred at the knee frequencies as follows:

$$\begin{aligned}\mathcal{L}(f) \text{ (dB)} &= \sum_{k=1}^4 A_k \left(L_k^+(f, \tau_k) + L_k^-(f, \tau_k) \right) \\ &= - \sum_{k=1}^4 \left(b_k \left(|f + f_k| + |f - f_k| \right) + 2a_k \right),\end{aligned}\quad (3.10)$$

where $L_k^\pm(f, \tau_k) = 10 \log(L(f \pm f_k, \tau_k))$, $b_k = 10\tau_k \log(e)$, $a_k = 10\tau_k \log(\pi A_k \tau_k)$, and A_k and τ_k denote the amplitude and the temporal width of the corresponding k^{th} time-domain Lorentzian pulse, respectively. Equation (3.10) suggests that the area under $M_i(f)$ can be fully occupied by four overlapping pairs of the triangular logarithmic Lorentzian spectra, corresponding to the four knee frequencies defined in Table 3.2.

To reduce the mathematical complexity associated with applying the inverse Fourier transform directly to the linear form of Eq. (3.10), we inspect the distribution of the emission mask PSD over frequency. The total power contained in a sub-band located between two consecutive knee frequencies is given by:

$$P_{i,k} = \frac{\int_{f_{k-1}}^{f_k} M_i(f) df}{\int_0^{f_4} M_i(f) df}; k \in \{1, 2, 3, 4\}, \quad (3.11)$$

where $f_0 = 0$. Accordingly, the cumulative PSD contribution of $M_i(f)$ at the k^{th} knee frequency can be defined as follows:

$$C_k = \sum_{m=1}^k P_m; k \in \{1, 2, 3, 4\}. \quad (3.12)$$

Figure 3.1 illustrates P_k and C_k versus k for the first channelisation scheme specified in the IEEE 802.15.3d Standard. From this figure, it is observed that, more than 95% of the PSD under the spectral emission mask is concentrated in the frequency range of $-f_2 \leq f \leq f_2$. However, it will be shown that an SRE of about 99% is achieved when only $A_1 L_1^\pm(f, \tau_1)$ is considered in Eq. (3.10). This is because the amount of PSD lost as a result of neglecting $L_2^\pm(f, \tau_2)$, $L_3^\pm(f, \tau_3)$ and $L_4^\pm(f, \tau_4)$ is substituted by $L_1^\pm(f, \tau_1)$, which is non-zero for $|f| \geq f_1$. This property holds for the eight IEEE 802.15.3d channelisation schemes and can be utilised to simplify Eq. (3.10) to the following form:

$$\mathcal{L}(f) \text{ (dB)} \approx L_1^+(f, \tau_1) + L_1^-(f, \tau_1) = 2a_1 - b_1 \left(|f + f_1| + |f - f_1| \right). \quad (3.13)$$

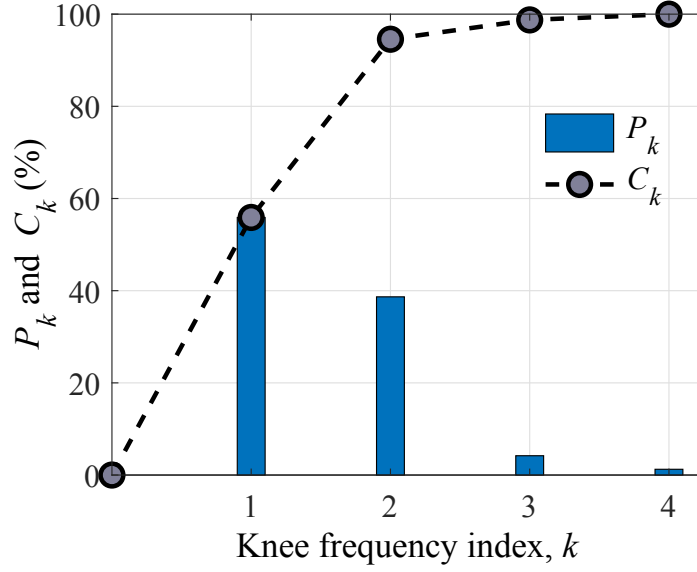


Figure 3.1. Distribution of the PSD over the sub-bands of spectral emission mask defined by the IEEE 802.15.3d Standard for the first channelisation scheme. P_k is for power distribution in each sub-band, whereas C_k is for cumulative power. The dashed line is for visual guidance.

The corresponding PSD, measured in the units of W/Hz, is given by:

$$|\mathcal{L}(f)|^2 = \exp(2\gamma B\bar{\alpha}) \exp\left(-\gamma\left(|f + B\bar{\alpha}| + |f - B\bar{\alpha}|\right)\right), \quad (3.14)$$

where $\gamma = \pi\tau$, and $\bar{\alpha} = 1 - \alpha$, which is defined as the complementary roll-off factor. It should be pointed out that, practically, the pulse shaping and a corresponding matched filtering are applied at the transmitter and the receiver sides, respectively, using the square root of Eq. (3.14). Accordingly, the time-domain waveform corresponding to Eq. (3.14) can be obtained by applying the inverse Fourier transform to the square root of Eq. (3.14), which yields:

$$\begin{aligned} s_{\mathcal{L}}(t) &= \frac{1}{2\pi} \int_{-\infty}^{+\infty} \mathcal{L}(f) \exp(j\omega t) d\omega \\ &= \exp(\gamma B\bar{\alpha}) \pi \exp\left(-\gamma \frac{\bar{\alpha}}{T_s}\right) \\ &\quad \times \left\{ \frac{\bar{\alpha}}{T_s} \operatorname{sinc}\left(\frac{\bar{\alpha}t}{T_s}\right) + \frac{1}{\gamma} \frac{\cos\left(\frac{\pi\bar{\alpha}t}{T_s}\right) - \left(\frac{\pi t}{\gamma}\right) \sin\left(\frac{\pi\bar{\alpha}t}{T_s}\right)}{1 + \left(\frac{\pi t}{\gamma}\right)^2} \right\}. \end{aligned} \quad (3.15)$$

It is noted from Eq. (4.1) that the Nyquist sampling conditions for inter-symbol interference (ISI)-free signalling is not strictly satisfied by $s_{\mathcal{L}}(t)$, i.e., $s_{\mathcal{L}}(t=0) = 1$, whereas $s_{\mathcal{L}}(t = nT_s) \neq 0$ when $n = \{\pm 1, \pm 2, \dots\}$.

3.3.1 Comparison of the Waveforms' Spectra

Alternatively, the ISI performance of $s_{\mathcal{L}}(t)$ can be evaluated based on the relaxed Nyquist condition as follows (Bobula et al. 2010):

$$\text{ISI (dB)} = 10 \log \frac{|s_{\mathcal{L}}(0)|^2}{\left| \sum_{n=-\infty; n \neq 0}^{+\infty} s_{\mathcal{L}}(t - nT_s) \right|^2}. \quad (3.16)$$

This condition considers a signalling waveform to be ISI-free as long as the instantaneous signal-to-ISI power ratio at the optimum sampling time instant is maintained above a pre-specified acceptable threshold. In Section 3.3.2, the condition in Eq. (3.16) is employed to quantify the ISI performance of the proposed waveform after optimising its spectrum.

3.3.1 Comparison of the Waveforms' Spectra

One of the major drawbacks of the RC and BTRC waveforms is that, although their bandwidths can be well-controlled, the amount of power divided between the in-band and the OOB spectra cannot be controlled independently. Instead, the in-band spectral flatness and the IBI that could result from the non-zero OOB spectra are jointly controlled with only a single degree of freedom, which is α . Figure 3.2 compares the impact of reshaping the spectra of the three considered waveforms on their compatibility to the IEEE 802.15.3d spectral requirements. Specifically, Figs. 3.2(a) and 3.2(b) show the RC and the BTRC spectra at different values of α , whereas Fig. 3.2(c) plots the proposed spectrum at $\alpha = 0$ and different values of γ . On the other hand, based on Eq. (3.14), the proposed spectrum possesses two independent degrees of freedom to manage the spectral flatness and the IBI, namely, α and γ . These properties make it possible to manage the SRE and the compliance independently with great flexibility. Additionally, in the proposed waveform, the impact of the complementary roll-off factor, i.e., $\bar{\alpha}$, is the same as the impact of α in the RC and the BTRC waveforms; increasing both parameters increase the transmission bandwidth.

3.3.2 Waveform Design Optimisation

We optimise the design of each waveform to fit the spectral emission mask defined by the IEEE 802.15.3d Standard for the first channelisation scheme, which has the most stringent emission mask with a steady roll-off as large as 20 dB over a transition bandwidth of only 160 MHz. The waveforms considered in this work are optimised to

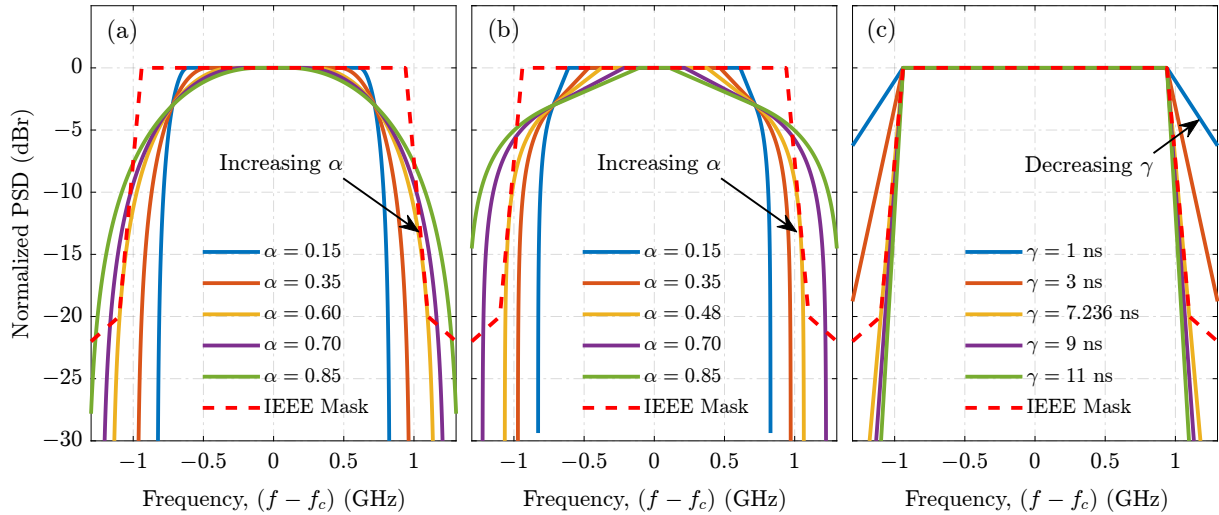


Figure 3.2. Simulated baseband spectra of the three considered waveforms. (a) RC waveform, (b) the BTRC waveform, and (c) the proposed waveform. The roll-off factor is fixed at $\alpha = 0$ for the proposed waveform at all value of γ .

fit the first channelisation spectral mask by setting $B = f_1$ in Eq. (3.14). This implies that the conducted analysis is also applicable to other channelisation schemes by considering the first knee frequency of each particular channelisation scheme listed in Table 3.2.

To ensure that the designed spectrum is compliant with the first emission mask, the involved parameters are optimised for each waveform individually, based on Eq. (3.6) and Eq. (3.7). Moreover, we assume a maximum frequency of 32 GHz to define the spectra of the three spectral shapes. This maximum bandwidth is large enough compared to the baseband equivalent bandwidth of the considered channelisation scheme (1.08 GHz) and, consequently, guarantees aliasing-free spectra. However, for other channelisation schemes, if the bandwidth increases by a factor of n , the maximum frequency should be increased by the same factor in order to capture the same spectral details and avoid low-pass filtering distortions during the waveform design process. For the three spectral shapes, the value of α is changed from 0 to 1 with a step of 10^{-3} . For the RC and the BTRC waveforms, B is set to $R_s/2$, where $R_s = 1.44$ Gbit/s, while for the proposed waveform, B is set to f_0 . Moreover, for the proposed spectrum, since γ relies on the full width at half maximum (FWHM) τ , the value of τ is increased from 0 to $20T_s$ with a resolution of $0.001T_s$. The SRE and CC are evaluated for the three pulse shapes over the considered parameters ranges. Then, the direct search algorithm (DSA) (Abraha et al. 2011) is applied to the calculated SRE and CC to extract the optimum values of α and γ .

Figure 3.3(a) shows the SRE and the CC versus α for the RC and the BTRC waveforms, whereas Fig. 3.3(b) shows the SRE and the CC versus γ for the proposed waveforms

3.3.2 Waveform Design Optimisation

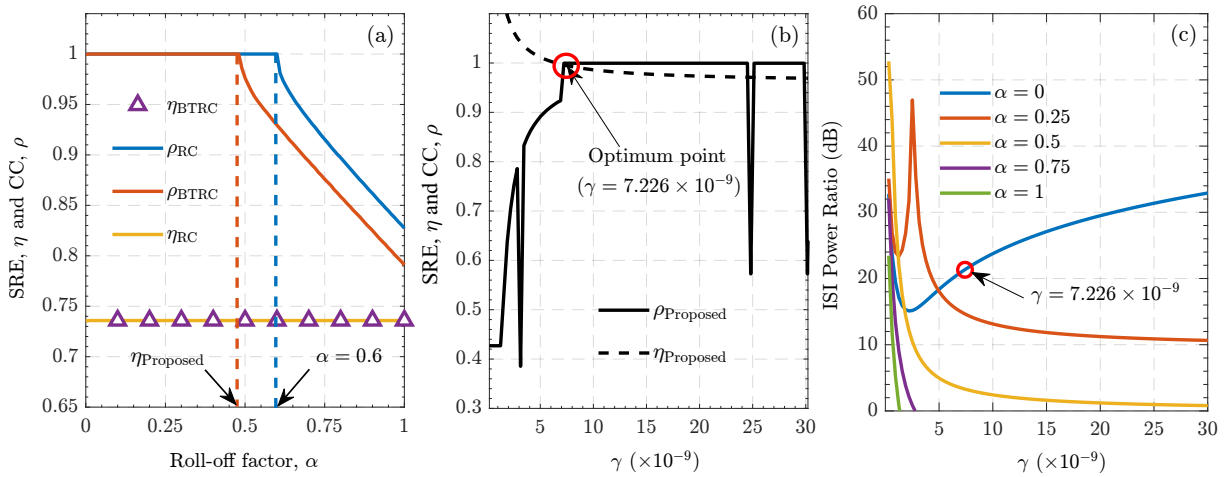


Figure 3.3. Design optimisation metrics of the three considered waveforms. (a) the compliance and spectral radiation efficiency versus α for the RC and BTRC waveforms, (b) the compliance and spectral radiation efficiency versus γ for the proposed waveform at a $\alpha = 0$, and (c) the ISI performance versus γ for the proposed waveform at different values of α .

at the optimised value of α . From Fig. 3.3(a), it can be seen that the RC and the BTRC waveforms fully comply with the IEEE 802.15.3d emission mask constraints with a roll-off factor α up to 0.48 and 0.6, respectively. Beyond these values, the compliance condition is violated, which is strictly prohibited for IBI considerations in multi-user channel access scenarios. The SRE is approximately independent of α with a constant value of 73.58% for both waveforms.

As can be observed from Figs. 3.2(a) and 3.2(b), this independence is a result of substituting the unfilled parts under the emission mask at $|f| < B$ by the spectrally broadening of the PSD for $|f| > B$ and hence; maintaining a constant total power. Therefore, in this work, the roll-off factor is selected at the commonly used value of $\alpha = 0.35$ to define the optimum RC and the BTRC waveforms.

For the proposed waveform, the full compliance is achieved at $\alpha = 0$ and a spectral roll-off control factor, γ , of 7.226×10^{-9} , whereas the corresponding SRE is 99.3% as can be seen from Fig. 3.3(b). The dips observed in the CC are due to the step discontinuity in the Heaviside function used in this metric as well as the non-differentiability of the spectral emission mask at the knee frequencies. This difference between the SRE of the proposed waveform and that of the RC and the BTRC waveforms implies that a virtual increase of about 34.96% in the emitted terahertz power can be achieved at no additional cost. It is noteworthy that, the monolithic integration of two photonic transmitters would be required to increase the power of the emitted terahertz waveform

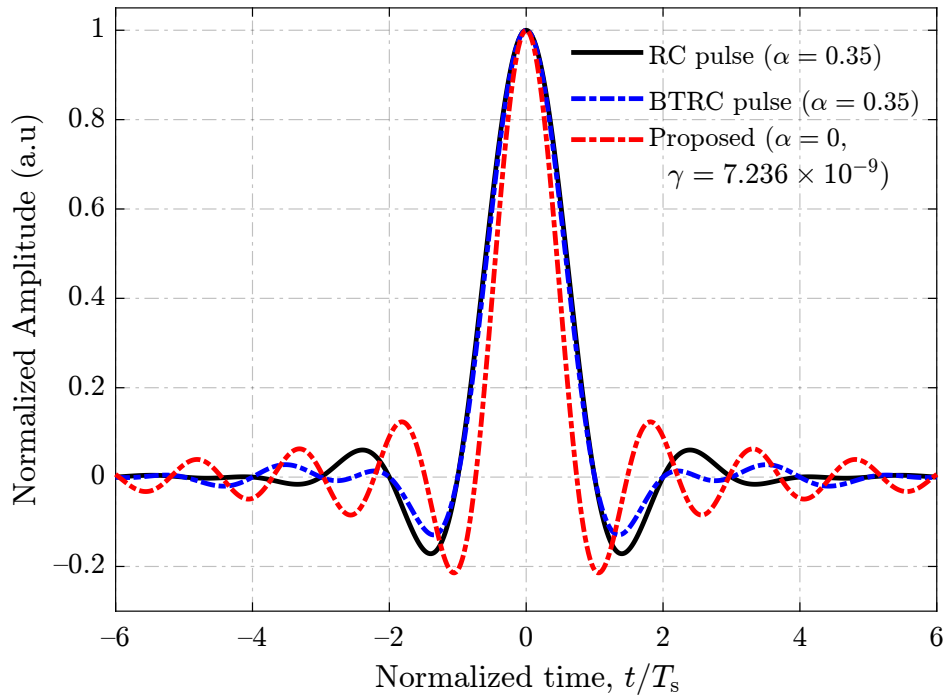


Figure 3.4. Three waveforms obtained from the optimal parameters to comply with the IEEE spectral emission mask. RC: raised-cosine. BTRC: better-than RC.

by 20% (Song et al. 2012). This comparison emphasises the importance of spectral shaping in managing the power budget of currently available terahertz technology.

Since the proposed waveform is not ISI-free, the ISI performance of this waveform is evaluated using 2^{10} pseudo-random BPSK symbols (Beaulieu et al. 2001), which interfere a pulse centred at $t = 0$ with no AWGN. Figure 3.3(c) shows the result of ISI based on Eq. (3.16) of the proposed waveform versus γ at different values of α . At the optimum values of α and γ , the proposed waveforms experiences a signal-to-ISI power ratio of 21.93 dB, which is high enough to ignore its impact during the matched filtering at the receiver side (Bobula et al. 2010). Figure 3.4 shows the three considered waveforms resulting from the optimisation of their respective parameters α and γ .

In practice, the pulse shaping process is implemented in the digital domain using finite impulse response filter (FIRs). Here, a truncated version of the signalling waveform is generated with an adequately finite filter length, denoted by L , to minimise the group delay of the FIR filter. However, this truncation induces undesired side-lobe level (SLL) spectral components beyond the dedicated waveform bandwidth. For an RC waveform with a symbol span of $L = 5$ and a roll-off factor of 0.35, this SLL can be as high -1.5 dB, which strongly violates the maximum stop-band attenuation of -30 dB (Bobula et al. 2010). Figures 3.5(a)-(c) show the impact of hard truncation on the stop-band attenuation

3.4 Experiment and Results

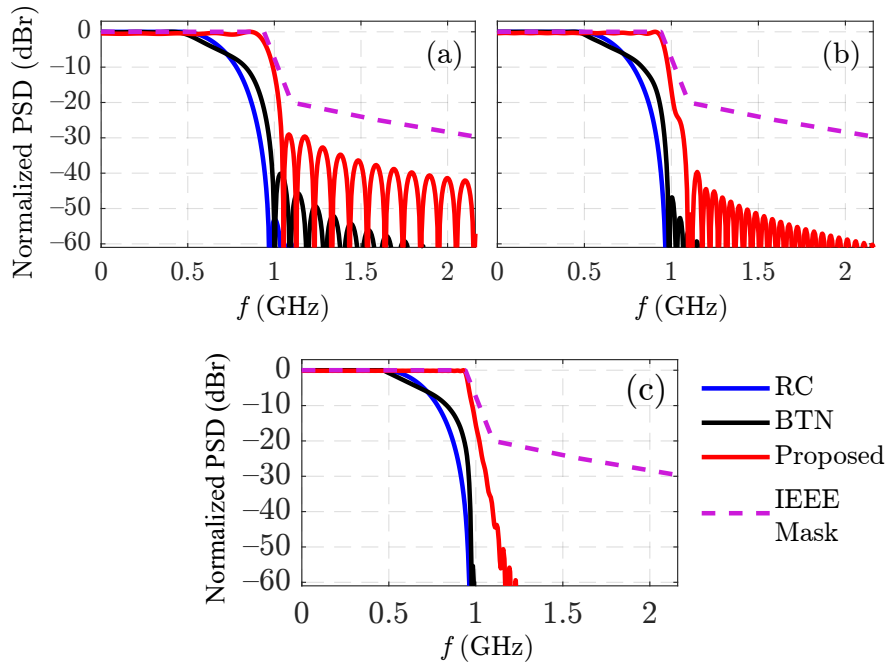


Figure 3.5. Impact of hard truncation on the stop-band attenuation of the RC, BTRC and the proposed waveforms. (a) $L = 7$, (b) $L = 15$, and (c) $L = 41$. The dashed lines represent maximum OOB emission limit allowed by the IEEE 802.15.3d Standard.

of the three considered waveforms for a symbol span of $2L$, where $L = 7, 15$ and 41 , respectively. For the proposed waveform, an almost flat passband response is exhibited up to the first knee frequency, i.e., $f_1 = 0.94$ GHz, while offering a maximum SLL of about -30 dB. Moreover, although the proposed waveform shows SLL that is higher than the RC and the BTRC waveforms, this SLL is still lower than the -30 dBr PSD limit defined in Eq. (3.1) for OOB emissions. By using a sufficiently long symbol span, i.e., $L > 41$, the SLL can be maintained well below this limit and the spectrum can be fit to the emission mask more efficiently.

3.4 Experiment and Results

As a proof-of-concept, the transmission performance of the three considered waveforms is experimentally evaluated using the photonic-terahertz communications system shown in Fig. 3.6. This system is based on the principles of intensity modulation–direct detection (IM-DD) and photo-mixing. In the experiment, the spectrum of a $2^{20} - 1$ pseudo-random OOK or BPSK-modulated binary sequence is reshaped by each of the three considered pulse shapes to generate the baseband signals. A regular pattern of consecutive of "1"s and "0"s, running at a symbol rate of $R_s/4$, is employed as a

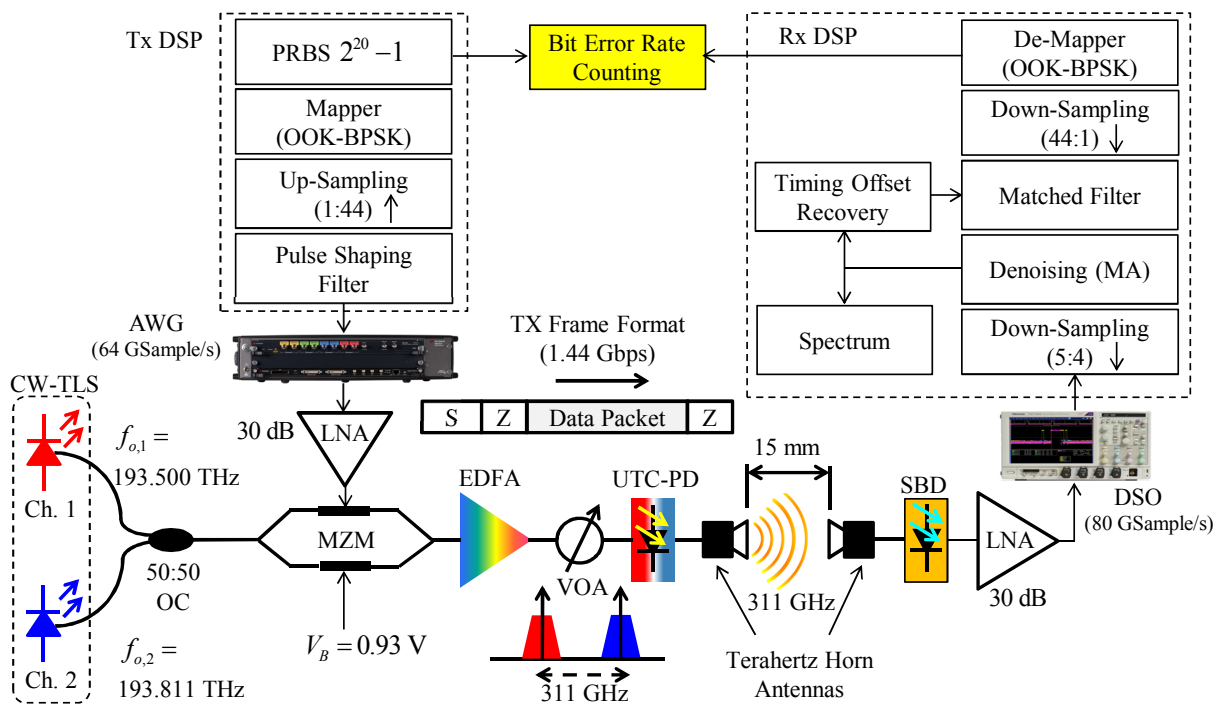


Figure 3.6. Experimental setup of the terahertz photonic communications link based on photomixing. TLS: tunable laser source. AWG: arbitrary waveform generator. LNA: low-noise amplifier. MZM: Mach-Zehnder modulator. EDFA: erbium doped fibre amplifier. VOA: variable optical attenuator. UTC-PD: uni-travelling carrier photodiode. SBD: Schottky barrier diode. LPF: low-pass filter. DSO: digital sampling oscilloscope. MA: moving average. S: synchronisation word. D: data payload. Z: zero-padding sequence. The maximum sampling rate of the AWG is 65 GSamples/s.

synchronisation word. This synchronisation word is interleaved cyclically with the data packets. A guard time interval of 100 zero-valued symbols is inserted between consecutive data packets. It should be mentioned that, the resulting data packet format does not follow the IEEE 802.15.3d Standard frame structure defined in the IEEE 802.15.3d Standard, which allows automatic switching between different modulation schemes by changing the physical layer (PHY) mode options in the relevant field of the frame header. Instead, for proof-of-concept, the OOK and BPSK modulated signals are independently transmitted.

This baseband signal is generated at a peak voltage of $V_p = 300$ mV using an arbitrary waveform generator (AWG) at a sampling rate of 64 GSamples/s. The generated data rate, which is 1.44 Gbit/s, is compatible with the first channelisation scheme specified in the IEEE 802.15.3d Standard. In principle, this data rate can be increased without degrading the system error performance as long as the AWG and DSO sampling rates can be proportionally increased. This is to maintain a constant over-sampling factor that is well-above the Nyquist condition as briefly discussed in Chapter (2) through Table 2.1

3.4 Experiment and Results

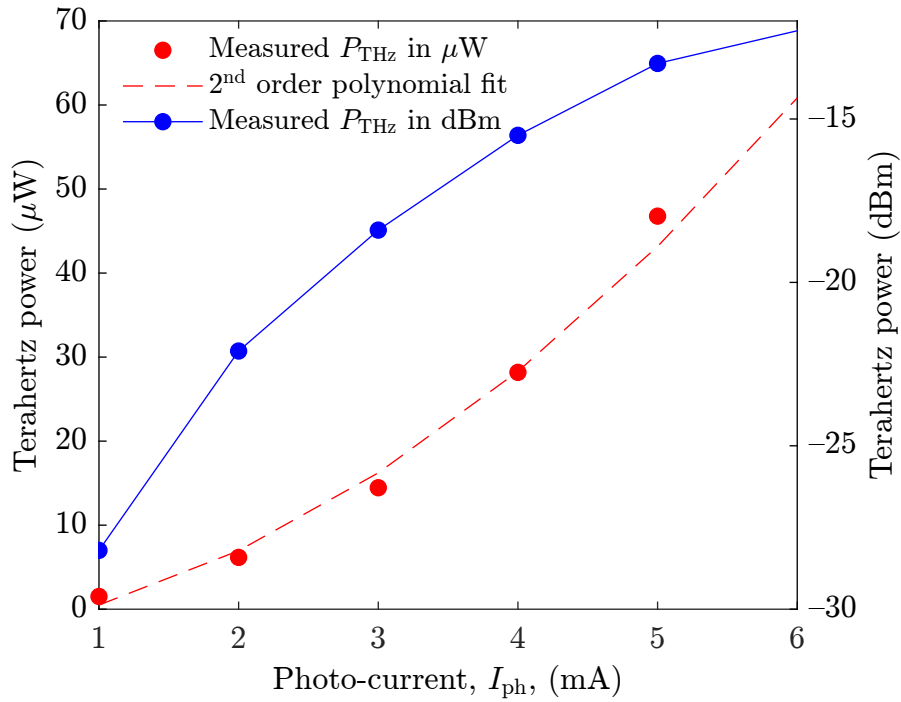


Figure 3.7. The measured UTC-PD terahertz output power versus its photo-current. The fitting error using the second order polynomial is about 0.087.

and Eq. (2.1). However, practical off-the-shelf electronics exhibit non-ideal frequency responses. Therefore, the signal data rate and, consequently, its bandwidth, are limited by the flat bandwidth of all baseband electronic components combined, which depends on a particular system design. Independently, two optical carriers at 193.5000 THz and 193.8100 THz are emitted by a dual-channel continuous wave tunable laser source (CW-TLS) and combined by a 50:50 optical coupler (OC). The linewidth of this CW-TLS is about 100 kHz. The generated baseband signal is then modulated onto the combined optical carriers by a Mach-Zehnder modulator (MZM), operated in the linear region of its electro-optic transfer characteristics. The 3-dB bandwidth of this MZM is about 20 GHz, which guarantees an almost distortion-free electro-optic conversion for the 1.44 Gbit/s signal. After optical amplification, the two optical signals are injected into a UTC-PD for photo-mixing. The terahertz carrier frequency is 311.00 GHz, which corresponds to the 32nd channel defined by the Standard. In the experiment, the photo-current is increased from 1 mA to 6 mA, with a step of 1 mA. Figure 3.7 plots the UTC-PD photo-current, denoted by I_{ph} , and the corresponding measured terahertz output power, denoted by P_{THz} .

The generated terahertz signal then propagates over a wireless channel, which comprised two identical WR-3.4 diagonal horn antennas aligned in the line-of-sight (LoS)

configuration along their directions of maximum emission with an antenna separation of 15 mm. The estimated free-space propagation loss at this distance, using the Friis transmission formula, is -25.83 dB. Moreover, this propagation distance is within the wireless transmission range specified by the IEEE 802.15.3d Standard for close-proximity terahertz wireless links (Kado et al. 2010, Hirata & Hirokawa 2018, Hirata & Hirokawa, Jiro 2018, Nagatsuma et al. 2016b, T. Nagatsuma, K. Oogimoto, Y. Inubushi, and J. Hirokawab 2016, Nishida et al. 2019, Diebold et al. 2016).

The passband bandwidth of the UTC-PD-SBD configuration is determined by the bandwidths of the individual wave-guiding structures attached to the UTC-PD and the SBD. Since the UTC-PD is attached to a WR-3.4 waveguide, its actual bandwidth ranges from 220 GHz to 325 GHz. Moreover, the actual bandwidth of the SBD is from 260 GHz to 400 GHz as it is attached to a WR-2.8 waveguide. As a result, the effective bandwidth of the UTC-PD-SBD configuration is from 260 GHz to 325 GHz. Within this band, the entire UTC-PD-SBD configuration is operated near its frequency of maximum emission. The end-to-end system frequency response possesses low-pass characteristics with a baseband bandwidth of 20 GHz and a cut-off frequency of 10 GHz.

At the receiver side, the baseband envelope of the received terahertz signal is detected via the SBD and the free space path loss is compensated by a 30 dB low-noise amplifier (LNA). The amplified signal is then sampled by a 80 GSample/s digital storage oscilloscope (DSO) for offline digital signal processing (DSP) using MATLAB as illustrated in Fig. 3.6.

To match the sampling rate at the transmitter side, the recorded data is down-sampled from 80 GSample/s to 64 GSample/s using a down-sampling ratio of 5:4 to remove the redundant samples. To mitigate the AWGN, a 44-taps moving average (MA) filter is applied to the received signal as a denoising filter. This filter length is equivalent to a sliding window width of the symbol duration, measured in samples, to ensure that the AWGN is averaged over the symbol duration without influencing the information content in adjacent symbols. The synchronisation word is then extracted from the denoised signal for timing offset estimation and compensation. The sliding window approach (Massey 1972) is also adopted for frame-level synchronisation (Pfletschinger et al. 2015), which is achieved by estimating the optimum delay that maximises the cross-correlation of the received sequence and the synchronisation word. Figures 3.8(a) and 3.9(a) confirm the accuracy of the timing offset estimation and recovery using this algorithm at the receive side. It is noteworthy that, the experimental setup results in

3.4 Experiment and Results

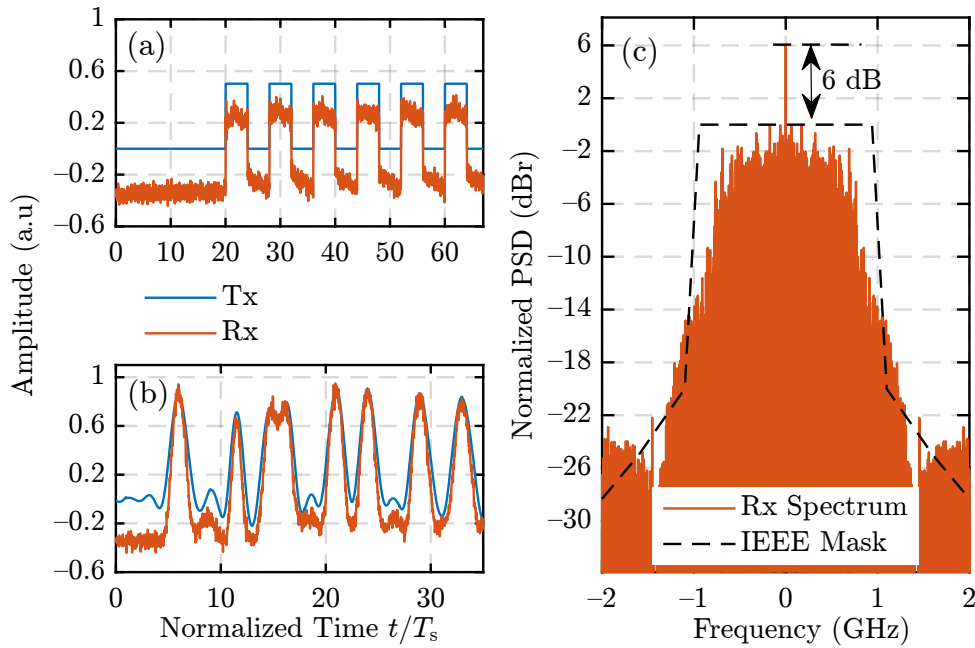


Figure 3.8. Signals and spectra at the receiver side for OOK modulation. (a) Segment of the synchronisation word, (b) segment of the data payload, and (c) spectrum of the received signal after de-noising. The UTC-PD photo-current is 3 mA.

a non-coherent terahertz communications link as it relies on IM-DD. However, since a constant bias voltage is applied to the MZM, an optical double-side band envelope modulated signal is produced at the MZM output. Correspondingly, this results in a DSB terahertz signal with a positive envelope emitted by the UTC-PD. The phase of the emitted terahertz signal is not modulated by the baseband information. At the receiver side, having a terahertz carrier with a positive envelope makes it possible to employ a simple envelope detector, such as the Schottky-barrier diode, to extract the baseband information signal from the terahertz carrier envelope. After that, the BPSK demodulation can be applied by relying on the polarity of the detected baseband signal. Therefore, the Kramer-Krönig algorithm is not required to reconstruct the signal phase at the receiver side. Further to that, the synchronisation word in the baseband data packet enables the correct identification of each symbol boundaries.

Figures 3.8(b) and 3.9(b) also show the received baseband waveforms after denoising and synchronisation, at a UTC-PD photo-current of 3 mA for OOK and BPSK modulation schemes, respectively. Figures 3.8(c) and 3.9(c) plot the spectra of these two signals at the same value of the UTC-PD photo-current. For the OOK spectrum in Fig. 3.8(c), a 6-dBr carrier component is detected at $f = f_c$ due to the non-zero net DC component of the transmitted OOK signal. This relative power level is much lower than

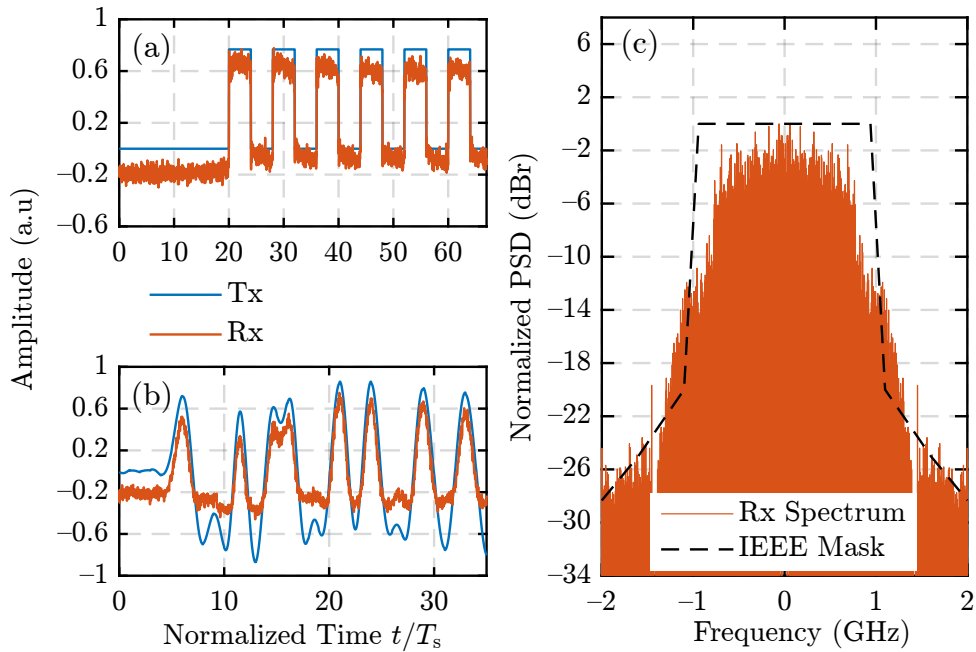


Figure 3.9. Signals and spectra at the receiver side for BPSK modulation. (a) Segment of the synchronisation word, (b) segment of the data payload, and (c) spectrum of the received signal after denoising. The UTC-PD photo-current is 3 mA.

the 40-dBr carrier-to-signal power margin allowed by the IEEE 802.15.3d Standard for the un-modulated carrier component in the OOK terahertz signalling mode.

The received signals comply with the IEEE spectral mask over most of the channelisation scheme bandwidth as shown in Figs. 3.8(c) and 3.9(c), which illustrate the spectra of the OOK and BPSK signals, respectively, at $I_{ph} = 3$ mA. It should be pointed out that, although the compliance requirements is achieved throughout the waveform design phase, this requirement is partially violated by the received signal spectrum. This partial violation is mainly attributed to the SBD nonlinearities (Harter et al. 2020), which induces the spectral regrowth effects in the received envelope. This observation applies at all considered values of the photo-current. However, the full-compliance of the emitted terahertz signal should not be affected by these nonlinear distortions, which occur at the receiver, i.e., after the SBD. The impact of the SBD nonlinearities on the compliance of the received IEEE 802.15.3d is detailed in Section 3.5. Figure 3.10 shows the measured UTC-PD power response as well as the overall end-to-end amplitude response of the terahertz link, i.e., from the AWG output at the transmitter side to the LNA output at the receiver side. As shown in Fig. 3.10(a), the UTC-PD exhibits a quasi-linear response, which guarantees the linearity of the entire photonic-terahertz transmitter. However, the overall end-to-end amplitude response of the terahertz

3.4 Experiment and Results

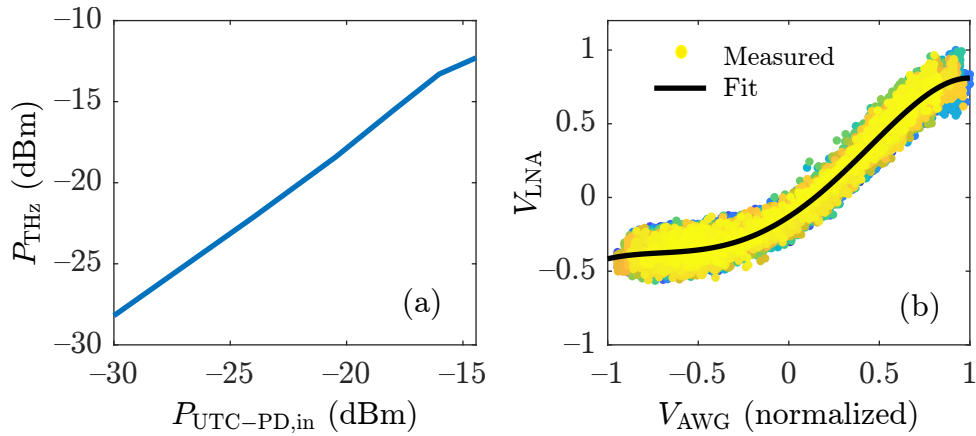


Figure 3.10. Measured optical-terahertz response of the UTC-PD and the end-to-end response of the photonic-terahertz system. (a) input-output power response of the photonic-terahertz transmitter. (b) transceiver end-to-end normalised voltage response. P_{THz} (dBm): terahertz output of the uni-travelling carrier photo-diode (UTC-PD), measured in the dBm units. $P_{\text{UTC-PD,in}}$ (dBm): is the input optical power at the UTC-PD input, also measured in the dBm units. V_{LNA} : normalised voltage at the low-noise amplifier output. V_{AWG} : normalised arbitrary waveform generator voltage. In (a), $P_{\text{UTC-PD,in}} = I_{\text{ph}}^2 R_{\text{in}}$, where $0 \leq I_{\text{ph}} \leq 6$ mA and $R_{\text{in}} = 1 \Omega$ denotes the normalised input resistance of the UTC-PD.

link shown in Fig. 3.10(b) is remarkably nonlinear, which identifies the SBD as the main source of this nonlinearity. This observation agrees with the measured voltage-current response and the associated nonlinear SBD model detailed in the supplementary material of (Harter et al. 2020). Nonetheless, the nonlinear response of SBD-based receivers can be mitigated by employing Kramer–Krönig (KK) post-processing at the receiver to improve its decoding capabilities (Harter et al. 2020, Ecozzi 2019, An et al. 2019, Li et al. 2017a,b).

The BER performance of the RC, BTRC and proposed Lorentzian-based pulse shapes are also evaluated under the OOK and BPSK modulation formats, without applying forward error correction (FEC) techniques. The results, which are plotted in Figs. 3.11(a) and (b), show that the lowest BER performance is achieved by the proposed waveform, regardless of the modulation format. It is worth mentioning that, the BERs in Figs. 3.11(a) and (b) are evaluated using offline DSP. The minimum BER that can be evaluated using this technique is impacted by the maximum number of bits that can be practically generated and collected at the transmitter and receiver sides, respectively. To put into perspective, achieving bit error rates (BERs) below 10^{-5} generally requires a minimum of 10^6 transmitted/received bits so that the counted bit errors converge. In the experiment, 10^5 bits were transmitted. This means that, the BERs in Figs. 3.11(a) and (b) are accurate to about 10^{-4} , and more transmitted/received bits would be required to observe more

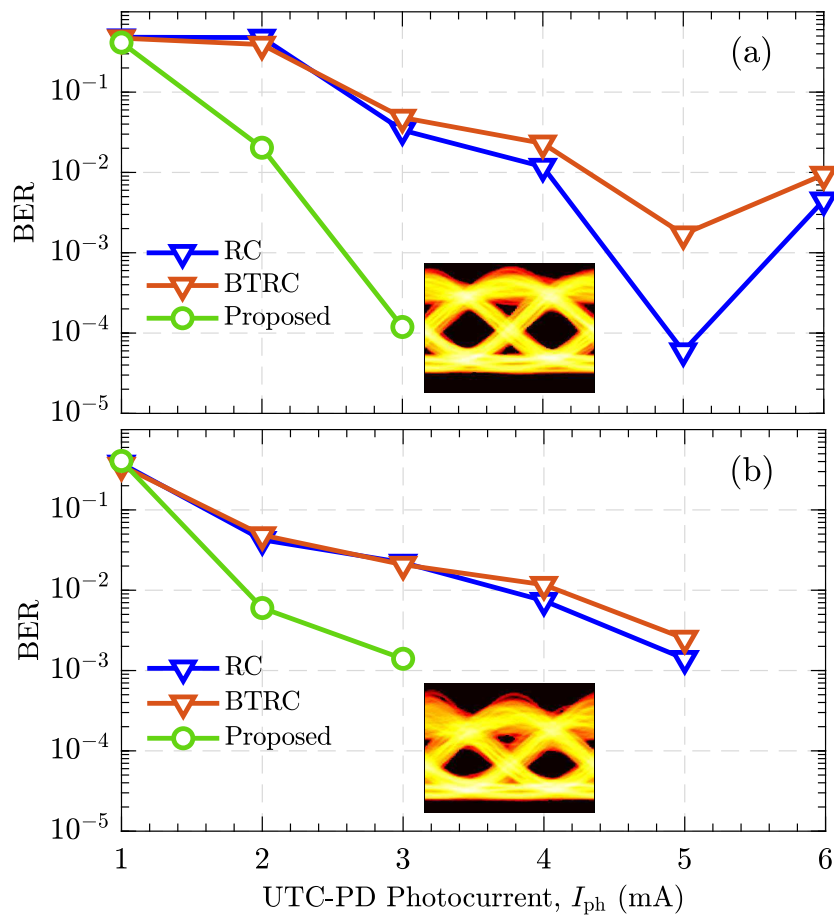


Figure 3.11. Measured bit error rate performance of the proposed waveforms as compared to the RC and the BTRC waveforms. (a) OOK and (b) BPSK modulation schemes. The eye diagrams are plotted for the proposed waveform obtained at a photo-current of 3 mA. The line plots are terminated at the points after which the error-free transmission limit is achieved. BER: bit error rate. RC: raised-cosine. BTRC: better-than RC.

errors. In Fig. 3.11(a), the OOK-modulated RC and BTRC waveforms show similar BER trends for $1 \text{ mA} \leq I_{ph} \leq 6 \text{ mA}$ with a minimum BER of 5.952×10^{-5} and 1.7×10^{-3} , respectively, achieved at $I_{ph} = 5 \text{ mA}$. However, increasing the photo-current I_{ph} beyond 5 mA deteriorates the BER of both waveforms. This effect is attributed to the nonlinearity of the terahertz link (Harter et al. 2020), (Ecozzi 2019), which induces harmonic and inter-modulation distortion components that grow with increasing photo-current and hence dominate the desired signal. Figure 3.11(b) shows that the BPSK-modulated RC and BTRC waveforms also follow similar BER trends for $1 \text{ mA} \leq I_{ph} \leq 5 \text{ mA}$ with a minimum BER of 1.4×10^{-3} and 2.5×10^{-3} , respectively, both achieved at $I_{ph} = 5 \text{ mA}$. An error-free transmission is observed for both waveforms when I_{ph} is increased beyond 5 mA.

3.5 Impact of Receiver Nonlinearity

On the other hand, for the proposed waveform, the BER decreases monotonically with increasing the photo-current from 1 mA to 3 mA for both OOK and BPSK modulation formats. A minimum BER of about 10^{-4} and 10^{-3} is achieved by this waveform at $I_{\text{ph}} = 3$ mA with OOK and the BPSK modulations, respectively. The error-free transmission limit of 10^{-12} is observed when I_{ph} is increased beyond 3 mA. From the aforementioned observations, it can be concluded that the transmission performance is more sensitive to the SRE rather than the ISI.

3.5 Impact of Receiver Nonlinearity

As discussed in Section 3.4, the compliance of the proposed IEEE 802.15.3d waveform is mainly impacted by the nonlinearities introduced by the SBD at the receiver side. In this section, we further elaborate on the compliance-linearity trade-off by using an independent experimental setup similar to that in Fig. 3.6. It should be highlighted that the experimental setup used in this investigation is similar to that used in Section 3.4, as here we intend to verify the origin of spectrum regrowth, regardless of the particular system implementation.

In the new experimental setup, the system comprises the same equipment as the system in Fig. 3.6, except for the low-noise amplifier at the transmitter side before the MZM. This is due to the lack of this amplifier in the new setup. However, the EDFA optical pump current is increased to its maximum value such that the output terahertz power is -10 dBm, which is higher than the maximum terahertz power in the original setup as shown in Fig. 3.7, i.e., -12.3 dBm. It should be noted that, typically, the close-to-saturation power limit of SBDs is about -10 dBm (Hesler et al. 2007). Additionally, The MZM is biased at its quadrature point, which is 1.3 V, and the optical carrier frequencies are fixed at 193.000 THz and 193.253 THz. The difference between these two frequencies, i.e., 253 GHz, is the maximum emission terahertz frequency, which is required to strongly stimulate the system nonlinearities.

To confirm that the spectral regrowth is dominated by the SBD nonlinearity, we consider the transmitter side in more detail. We experimentally measure the MZM electro-optic transmittance over a sufficiently wide range of the input voltage as well as the corresponding optical dynamic range at the EDFA output. The MZM characteristics can be approximated by a quasi-linear input/output relationship over the narrow voltage swing around its operating point. Figures 3.12 (a) and (b) show the MZM electro-optic transmittance, i.e., from the AWG electrical output to the MZM optical output as well as

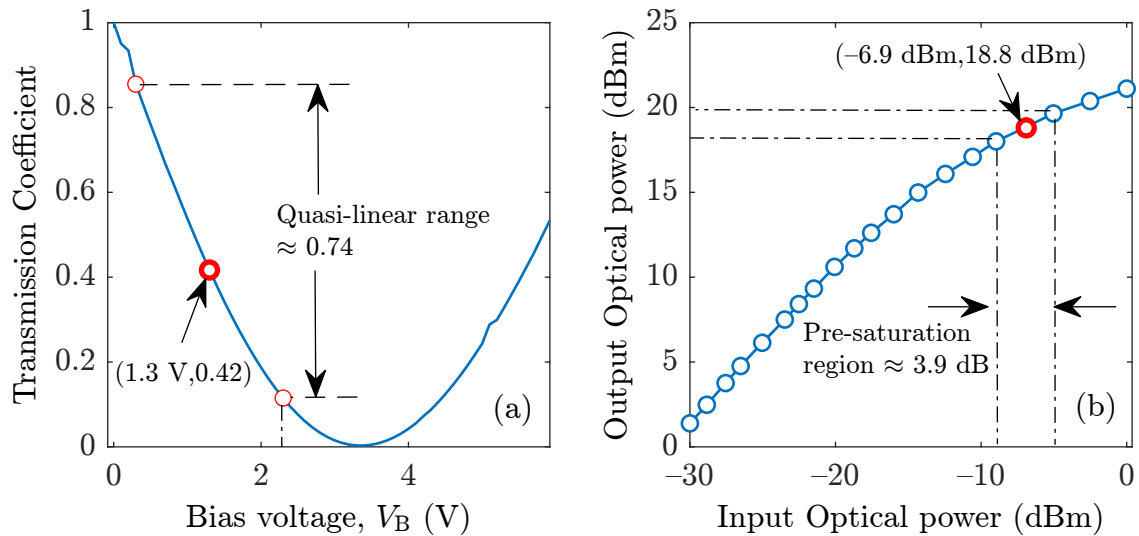


Figure 3.12. Measured input-output response of the photonic-terahertz transmitter active and passive components. (a) MZM electro-optic response. (b) Input-output power response of the Erbium doped fibre amplifier. The thick red markers denote the operating points.

the corresponding EDFA power response, respectively. As can be seen in both figures, a quasi-linear narrow dynamic range of each device is exploited, reflecting the high linearity of the transmitter. Additionally, this range is relatively linear compared to the overall nonlinear system response depicted in Fig. 3.10(b).

To further confirm the dominance of the SBD nonlinear effects, a new experimental approach is proposed. This approach can be explained as follows. At high photo-currents and short Tx-Rx antenna separation, high terahertz power levels are detected at the receiver side. This high power level should be sufficient to stimulate the receiver nonlinearities. However, when the Tx-Rx antenna separation is increased, the received terahertz power is reduced, and only a limited range of the SBD response is exploited, which makes it possible to approximate the SBD response by a quasi-linear input-output relationship. It is noted that, although the system we use for this experiment is slightly different from that used in Section 3.4, due to system availability, the architecture is exactly the same from a functional viewpoint. To stimulate strong SBD nonlinearities, the photo-current is set to 5 mA. The transmission distance is set to 2, 4, 5, and 6 cm. At each transmission distance, the waveform spectra is sampled and recorded using a 25 GSample/s RTO. After that, the waveform is denoised using a MA filter. Subsequently, the waveform spectrum is evaluated using the fast Fourier transform (FFT) technique without applying spectral windowing.

Figure 3.13 shows the received terahertz envelope spectra measured at a Tx-Rx antenna separation of 2, 4, 5, and 6 cm, respectively. As can be seen in these figure, different

3.6 Conclusion

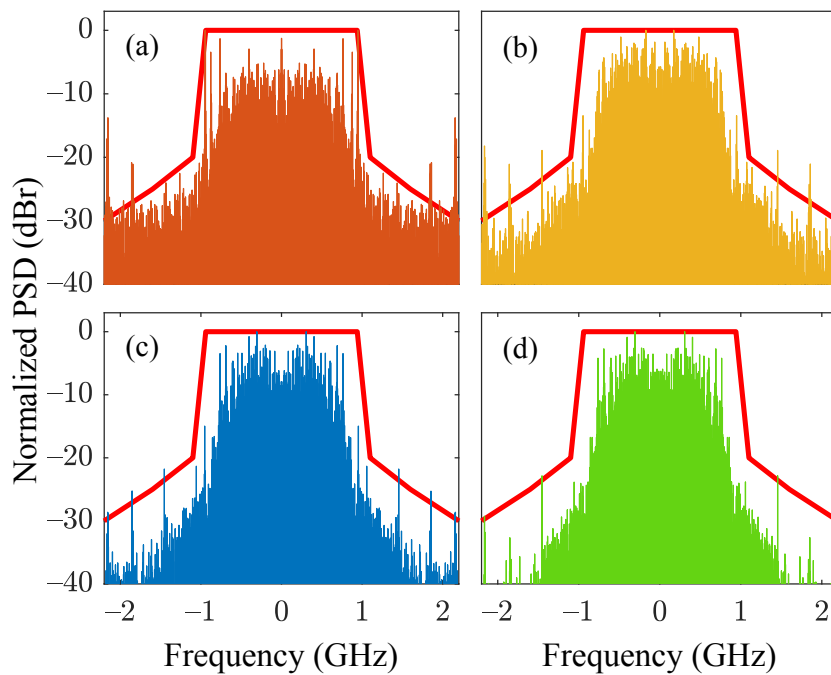


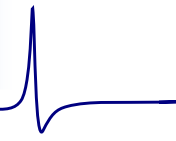
Figure 3.13. Evolution of the received IEEE 802.15.3d signal spectrum with the transmitter-receiver antenna separation. (a) 2 cm. (b) 4 cm. (c) 5 cm. (d) 6 cm. In all figures, the solid red line represents the IEEE 802.15.3d spectral emission mask.

distances stimulate different levels of the spectral broadening effect. As shown in Fig. 3.13(a), the received envelope spectrum exceeds the spectral mask at a distance of 2 cm. However, as the distance is increased to 4, 5, and 6 cm, the compliance with the IEEE 802.15.3d mask is fulfilled as shown in Figs. 3.13(b), (c), and (d), respectively. These observations confirm that SBD is mainly responsible for the spectral regrowth effects.

3.6 Conclusion

In this chapter, we establish the context of pulse shaping for terahertz communications networks that comply with the technical specifications defined in the IEEE 802.15.3d Standard. An analytical framework is formulated for the design of optimal terahertz envelope waveforms, with an aim to maximise the spectral radiation efficiency under the spectral emission constraints defined in this Standard. Importantly, a new waveform is proposed and compared to the RC and BTRC waveforms via numerical analysis and experiments. The proposed waveform shows full compliance with the most stringent spectral mask defined by the IEEE 802.15.3d Standard, where the largest number of densely packed channels can be found. Additionally, this waveform utilises more than

99% of the power spectral density admissible by this spectral mask and outperforms the conventional RC and the BTRC waveforms by about 35% in terms of the radiation efficiency, leading to an improvement of, at least, one order of magnitude in the BER performance. Moreover, experimental results show that, using the experimental setup reported in this work, the transmission error-free limit of 10^{-12} defined by the IEEE 802.15.3d Standard can be achieved using the proposed waveform without employing FEC codes. Additionally, since the bandwidths of all IEEE 802.15.3d emission masks are integer multiples of 2.16 GHz, the proposed waveform presented in this work is applicable to the design and development of standard-compliant terahertz communications systems considering the higher-order channelisation schemes. The matched-filter implementation of the proposed waveform is beneficial for noise shaping as it results in the maximum possible signal-to-noise ratio (SNR) at the receiver side, and consequently, reduces the bit error rate to the minimum possible levels. Therefore, this issue is also open for further investigation in future work.



Timing-Jitter Tolerant Nyquist Pulse for Terahertz Communications

SEAMLESS integration of terahertz wireless communications with existing optical access networks can potentially offer tens of gigahertz of channel bandwidth. However, the timing-jitter exhibited by the electronics-based transceivers is a key transmission impairment that tends to ceil the performance of these hybrid access networks, especially at high transmission baud rates. In this chapter, we propose a sinc-Lorentzian Nyquist pulse shape that outperforms the conventional raised-cosine and the better-than raised-cosine pulse shapes under the influence of timing-jitter of up to 35% of the symbol duration. Experimental demonstrations are carried out using a 311 GHz photonic-terahertz system operating at a standard bit rate of 1.44 Gbit/s to investigate the robustness of the three pulse shapes against timing-jitter. It is confirmed that the proposed pulse shape is highly-tolerant to timing-jitter as well as the nonlinearity exhibited by terahertz systems, and hence, can improve the bit error rate performance by an order of magnitude when the average timing-jitter is as large as 0.24 ns. The proposed pulse shape is a critical step for designing ultra-high-speed terahertz communications links with improved robustness to timing-jitter.

4.1 Introduction

Day-by-day increasing demands for reliable high-speed wireless services are expected to rapidly approach and exceed the capacity of fifth-generation (5G) communications networks. These demands are unlikely to be fulfilled without ongoing vigorous research on next-generation wireless communications, namely, 6G. Terahertz technology is a key enabler for 6G communications as it makes it possible to access ample spectral resources for point-to-point wireless systems (Petrov et al. 2020) in the terahertz band. Numerous advantages are expected from pushing the carrier frequencies towards the terahertz band (100 GHz to 10 THz), such as increased channel capacities with much lower latency and increased user activities on the network. In practice, the generation and modulation of such high carrier frequencies is usually accompanied by a randomly fluctuating phase noise, which becomes noticeable as random timing-jitter in the baseband modulated signal. Unless precisely estimated and compensated, this timing-jitter gives rise to imperfect synchronisation, i.e., a net timing-offset, between the transmitter and the receiver, which could severely deteriorate the end-to-end bit error rate (BER) performance, especially when increasing the system data rate (Roumelas et al. 2020).

In the field of terahertz communications, timing-jitter with a remarkable proportion of the symbol period has been frequently observed in many experimental demonstrations (Ducournau et al. 2014, Nagatsuma et al. 2013, 2016a, Webber et al. 2019). For instance, in a typical terahertz electronic receiver, the average timing-jitter was measured to be in the range of 10 ps at 5 Gbit/s to 25 ps at 12 Gbit/s (Webber et al. 2019), which corresponds to about 5% to 30% of the symbol duration. The impact of this timing-jitter, and consequently, the inter-symbol interference (ISI), on the BER performance was considered insignificant since the received signal exhibited a highly-localised Gaussian-like profile over the allocated symbol duration (Webber et al. 2019). However, for the same symbol rate, the root mean squared (RMS) bandwidth of a typical Gaussian pulse is much higher than the Nyquist bandwidth requirement. Therefore, in most of the previous demonstrations of terahertz communications, e.g., (Chinni et al. 2018a,b, Fujishima 2018, Dan et al. 2020), it has been a common practice to rely on the raised-cosine (RC) pulse shape with various roll-off factors for bandwidth-efficient signalling.

Although spectrally-efficient, the transmission performance of Nyquist pulses, including the RC pulse, is sensitive to the timing-jitter due to the large overlap between adjacent symbols. Unless the detection is performed at the optimum sampling instants

4.1 Introduction

at the receiver side, the ISI caused by this overlap can severely deteriorate the BER performance. In (Beaulieu 1991), it has been shown that, typically, the BER of Nyquist pulses can exceed 10^{-3} when the timing-offset is 25% of the symbol period. It is important to minimise the gap between such a relatively high BER and the error-free transmission limit of 10^{-12} in terahertz communications.

Admittedly, in most of the previous demonstrations of terahertz communications links, the impact of timing-jitter on the transmission performance of RC pulses has not been considered since offline digital signal processing (DSP) techniques have been employed to compensate for various transmission impairments, including the timing-jitter. Whilst offline DSP techniques are sufficient for proof-of-concept experiments, the timing-jitter estimation and compensation can be a complicated DSP task for receivers with limited computational resources. This issue can be challenging in practical scenarios, especially for real-time applications.

A spectrally-efficient solution to reduce the severity of the timing-jitter on the transmission performance of Nyquist pulses is to design pulse shapes with rapidly decaying profiles in order to reduce the power contained in time-domain sidelobes and, consequently, the resulting ISI. This way, the BER of these pulses can be improved and the requirement for high-speed precise timing-control circuitry at the receiver side can be relaxed.

To this end, we propose and experimentally demonstrate a sinc-Lorentzian Nyquist pulse shape that is highly-tolerant to timing-jitter exhibited by photonic-terahertz systems. The proposed pulse shape possesses two independent degrees of freedom, which allow for flexible control of its temporal and spectral characteristics. We further investigate the impact of timing-offsets on the transmission and detection performance of the proposed waveform in comparison to the other two common waveforms using a photo-mixing-based terahertz communications link. It should be highlighted that, unlike the waveform presented in Chapter 3, the Nyquist condition for ISI-free signalling is considered for the proposed sinc-Lorentzian.

The rest of this chapter is organised as follows. The proposed Nyquist pulse is presented in Section 4.2. Here, an ISI analysis is carried out for the three considered pulse shapes in Section 4.3. Section 4.4 presents an experimental investigation of the transmission performance of these pulse shapes before this chapter is finally concluded in Section 4.5.

4.2 Proposed Nyquist Pulse Shape

The proposed pulse shape, referred as the sinc-Lorentzian pulse, is defined mathematically as follows:

$$p_{\text{SL}}(t) = \frac{\gamma T_s E(t)}{\gamma \alpha^- + T_s} \text{sinc}\left(\frac{t}{T_s}\right), \quad (4.1)$$

where $\gamma = \zeta T_s$ is a parameter that controls the time-domain decay rate as well as the spectral distribution of $p_{\text{SL}}(t)$, ζ is a dimensionless parameter, and $E(t)$ is defined as follows:

$$E(t) = \frac{\alpha^- \text{sinc}\left(\frac{\alpha^- t}{T_s}\right)}{T_s} + \frac{\cos\left(\frac{\pi \alpha^- t}{T_s}\right) - \left(\frac{\pi t}{\gamma}\right) \sin\left(\frac{\pi \alpha^- t}{T_s}\right)}{\gamma + \left(\frac{\pi^2 t^2}{\gamma}\right)}. \quad (4.2)$$

The two-parameters in Eq. (4.1), i.e., α^- and γ , make it possible to flexibly control the temporal and the spectral characteristics of the sinc-Lorentzian pulse (Assimonis et al. 2008).

The spectrum of Eq. (4.1) is numerically evaluated using the fast Fourier transform (FFT) technique with 2^{18} points. Figure 4.1 shows the spectrum of the proposed waveform. The RC and BTRC spectra are also shown for comparison. In this figure, the spectra of the three waveforms are evaluated at the same roll-off factor of $\alpha = 0.35$. For the sinc-Lorentzian pulse, ζ is set to 10.47 unit-less for reasons to be discussed in detail in Section 4.4. It should be highlighted that, in contrast to the RC and BTRC pulses, the proposed SL pulse shape is band-unlimited. Therefore, we apply the concept

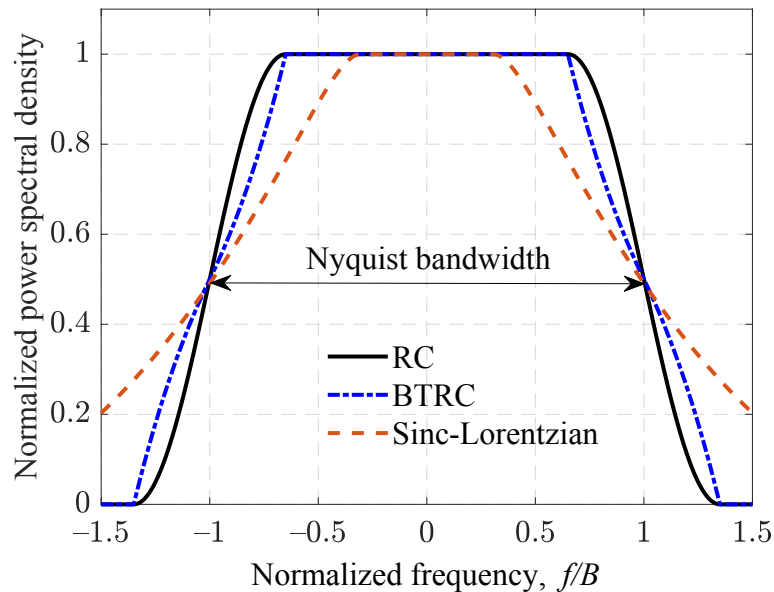


Figure 4.1. Simulated baseband spectra of the three considered waveforms. All spectra are evaluated at a roll-off factor of $\alpha = 0.35$. For the sinc-Lorentzian pulse, $\zeta = 10.47$.

4.2 Proposed Nyquist Pulse Shape

of -10 dB bandwidth in order to evaluate the excess bandwidth required beyond the Nyquist bandwidth. Consequently, the excess bandwidth of the proposed pulse is $0.77B$, compared to $0.35B$ in the RC and BTRC pulses.

Figure 4.2 shows the eye diagrams of the three considered waveforms evaluated using 2^{10} BPSK symbols at $\alpha = 0.35$. The proposed waveform has much smaller amplitude distortions, i.e., lower sidelobe energy, and a much wider horizontal eye opening at the receiver side than the eye diagrams of the classical RC and BTRC Nyquist pulses. This implies that the proposed pulse can tolerate a larger timing deviation around the optimum sampling instant without experiencing significant ISI. This behaviour is attributed to the pulse decay rate in the time domain, which we discuss in details below.

In (Assalini & Tonello 2004), it has been shown that the decay rate of a Nyquist waveform depends on the overall waveform design, i.e., considering the mother sinc together with its envelope, rather than the particular envelope decay order. For instance, analytically, Eq. (2.5) and Eq. (2.7) show that the envelopes of the RC and the BTRC pulses decay as $|t|^{-3}$ and t^{-2} , respectively. Also, the two pulse shapes presented in (Assalini & Tonello 2004) show an analytical envelope decay rate of $|t|^{-3}$ and t^{-2} . However, the overall waveform amplitude of the main sidelobes with the t^{-2} envelope decay rate are smaller than those of the pulse shapes with the $|t|^{-3}$ envelope decay rate. Likewise, although Eq. (4.1) shows that the proposed pulse shape has an envelope asymptotic decay of t^{-2} . Figures 4.3(a) and (b) show that this decay rate is larger than the RC

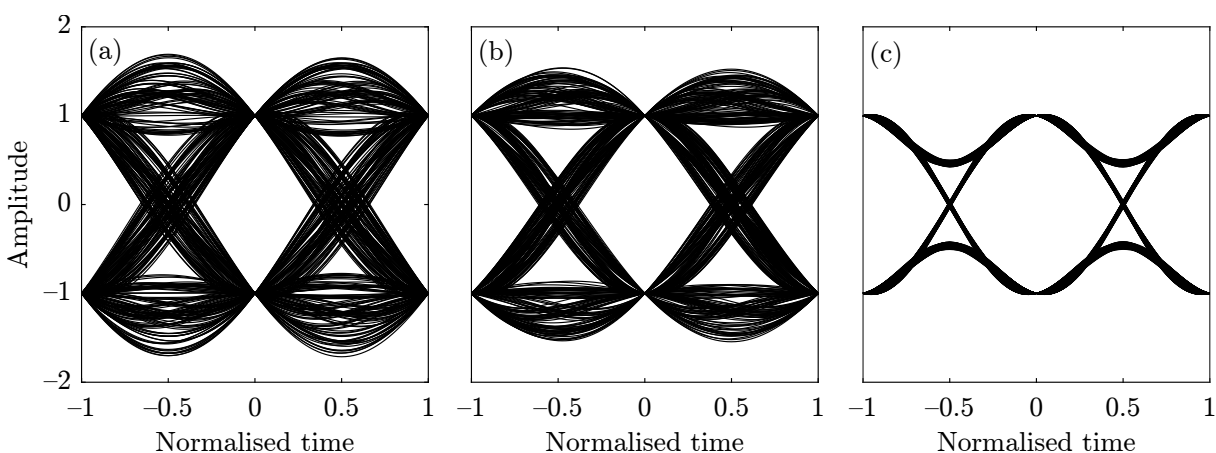


Figure 4.2. Eye diagrams of a binary-phase modulated sequence of 2^{10} symbols length. (a) Raised-cosine pulse with $\alpha = 0.35$, (b) better-than raised-cosine pulse with $\alpha = 0.35$, and (c) proposed sinc-Lorentzian pulse shape with $\alpha = 0.35$ and $\gamma = 7.226 \times 10^{-9}$. Time is normalised to one symbol duration.

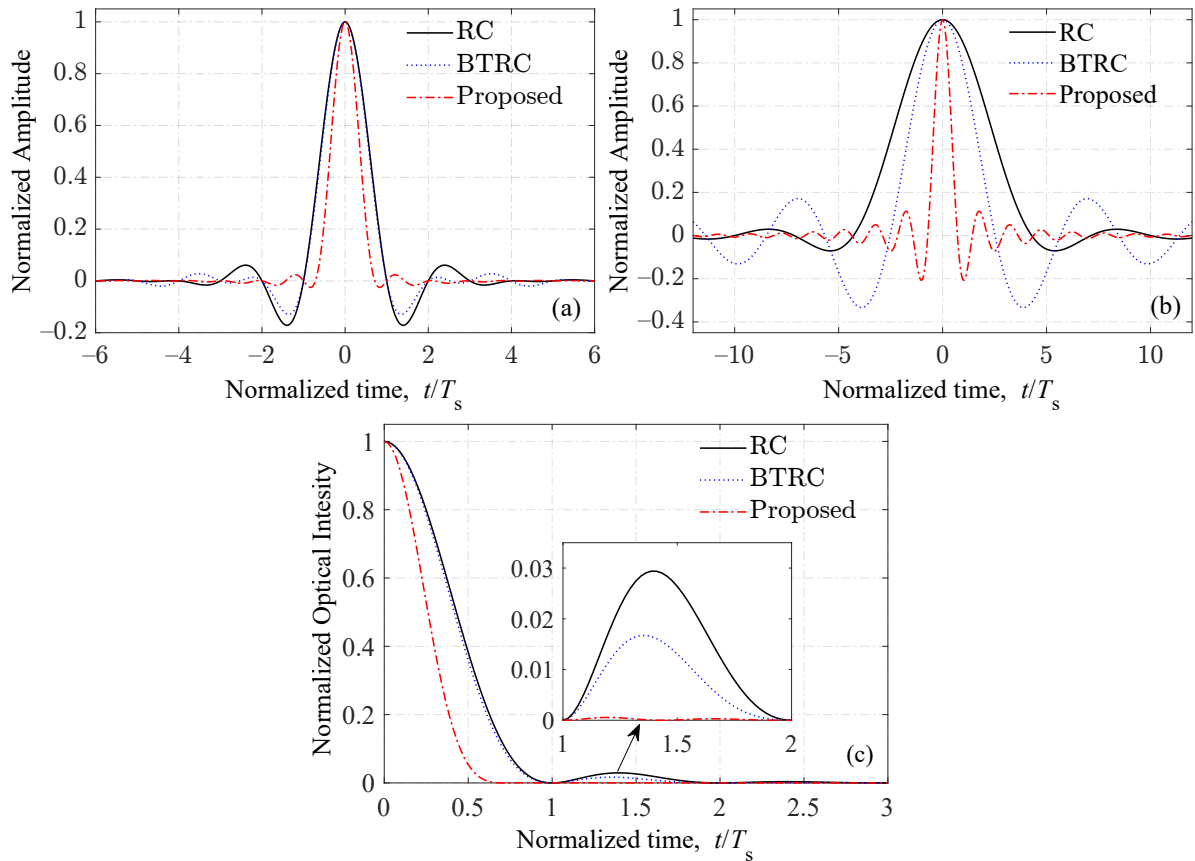


Figure 4.3. Simulated time domain baseband waveforms. (a) Electrical baseband waveforms, (b) envelopes of the electrical baseband waveforms, and (c) optical intensity waveforms. The roll-off factor is fixed at $\alpha = 0.35$ for the raised-cosine and the BTRC waveforms, whereas, for the proposed waveform, $\alpha = 0$ and $\zeta = 10.47$.

and the BTRC pulses. Further to that, since we employ a photonics-based terahertz communications system in this work, the impact of the electro-optic (EO) modulation nonlinearity on the three waveforms is considered. In this work, we employ a Mach-Zehnder modulator (MZM) as an EO modulator. However, it is noteworthy that other types of nonlinearities can also be exhibited by several components other than the MZM, such as the erbium doped fibre amplifier (EDFA) at the transmitter side, and the Schottky-barrier diode (SBD) at the receiver side. Since, the EO modulation is essentially a voltage-to-optical intensity conversion process, the optical waveforms are proportional to the squared amplitude of the electrical waveforms. Figure 4.3(c) compares the squared magnitude of the three considered waveforms corresponding to the electrical waveforms in Fig. 4.3(a) for $0 \leq t \leq 3T_s$. As shown in Fig. 4.3(c), the three optical waveforms decay more rapidly compared to the corresponding electrical waveforms in Fig. 4.3(a). In particular, the decay rate is doubled due to the EO modulation. Additionally, the inset of Fig. 4.3(c) shows that the maximum sidelobe level

4.3 Inter-Symbol Interference Analysis

of the proposed waveform, i.e., for $T_s \leq t \leq 2T_s$, is much lower than the RC and the BTRC waveforms. To put into perspective, the maximum sidelobe optical intensity of the proposed pulse is lower than the corresponding levels of the RC and the BTRC pulses by 17 dB and 15 dB, respectively. At the high transmission speeds of terahertz communications, it is desirable to minimise the overlap between adjacent symbols, which increases in the presence of time-jittering. Therefore, the low sidelobe level of the proposed waveform beyond the symbol duration, $-T_s/2 \leq t \leq T_s/2$, has a clear advantage.

4.3 Inter-Symbol Interference Analysis

Assuming ideal sampling and binary phase shift keying (BPSK) modulation, the received symbol sequence is ISI-free and the probability of bit error is theoretically given by $P_\varepsilon = Q(\sqrt{2\text{SNR}})$, where SNR is the signal-to-noise ratio (SNR), and $Q(\cdot)$ is the complementary cumulative distribution function of a standard zero-mean unit-variance Gaussian distribution. At an SNR of 15 dB, $P_\varepsilon = 9.124 \times 10^{-16}$, which is much lower than the standard error-free transmission limit of 10^{-12} . In the presence of timing-jitter, the semi-analytical method proposed in (Beaulieu 1991) can be used to evaluate the ISI performance of an arbitrary Nyquist pulse. Here, to avoid the impact of the residual errors associated with the approach in (Beaulieu 1991), we employ a more straightforward semi-analytical approach to quantify the impact of the timing-jitter on the probability of symbol error for the considered pulse shapes. First, we formulate the received symbol sequence, denoted by $y(t)$, in the presence of timing-jitter and the additive white Gaussian noise (AWGN), as follows:

$$y(t) = \sum_{k=-N^-}^{N^+} b_k p(t \pm \Delta t_k - kT_s) + n(t), \quad (4.3)$$

where $k \in \{0, \pm 1, \pm 2, \pm 3, \dots\}$ is the symbol index, N^- is the number of interfering symbols that precedes the central data symbol located at $t = 0$, and N^+ denotes the number of symbols that follow this central symbol. Moreover, $b_k \in \{\pm 1\}$ is the k^{th} BPSK information symbol, and $n(t)$ is the AWGN. The pulse shape $p(t)$ denotes one of the three candidate pulses considered here: $p_{\text{RC}}(t)$, $p_{\text{BTRC}}(t)$ or $p_{\text{SL}}(t)$ and Δt_k denotes the timing-jitter introduced to the k^{th} symbol. A \pm sign is introduced to Δt_k in Eq. (4.3) in order to account for positive and negative timing deviations around the optimum sampling instant of the k^{th} symbol. Secondly, we assume that $y(t)$ is forwarded to a

timing-jitter estimator and compensator. The compensated received symbol is denoted by $\hat{y}(t) = y(t \mp \widehat{\Delta t}_k)$, where $\widehat{\Delta t}_k$ is the estimated timing-jitter. At the optimum sampling instants, i.e., $t = kT_s$, $\hat{y}(t)$ is given by

$$\hat{y}(kT_s) = p(\pm\delta t_k)b_k + I_k(\delta t_m) + n_k, \quad (4.4)$$

where $p(\pm\delta t_k)$ accounts for the reduction in the desired symbol amplitude, and $I_k(\delta t_m)$ is the adjacent ISI, defined as follows:

$$I_k(\delta t_m) \triangleq \sum_{m=-N^-}^{N^+} b_m p(\pm\delta t_m + (k - m)T_s); m \neq k. \quad (4.5)$$

Moreover, $\delta t_k = |\widehat{\Delta t}_k - \Delta t_k|$ is the timing-jitter estimation error, while n_k is the AWGN at the k^{th} symbol. A decision variable, denoted by z_k , is formed as follows:

$$z_k = \begin{cases} +1; & \hat{y}(kT_s) \geq 0 \\ -1; & \hat{y}(kT_s) < 0. \end{cases} \quad (4.6)$$

It should be highlighted that, $p(\pm\delta t_k) = 1$ and $I_k(\pm\delta t_m) = 0$ when $\delta t_k = 0$, whereas for $\delta t_k \neq 0$, the values of $p(\pm\delta t_k)$ and $I_k(\pm\delta t_m)$ depend on the particular choice of the pulse shape, $p(t)$. Thirdly, the probability of symbol error, denoted by P_ε , is numerically evaluated by calculating $\Pr\{z_k \neq b_k\}$ using the Monte-Carlo numerical simulation technique. It is noteworthy that, the proposed approach results in the same error performance as the earlier approach (Beaulieu 1991) when used to evaluate time unlimited waveforms (Beaulieu et al. 2001),(Assalini & Tonello 2004), while it can avoid the mathematical complexity associated with the approach in (Beaulieu 1991).

Table 4.1 lists the simulation parameters used to evaluate the BER performance of the three considered waveforms in the presence of timing-jitter. The symbol rate, R_s , corresponds to a symbol rate of 1.44 Gbit/s based on the IEEE standard for terahertz communications. Additionally, in practice, $p(t)$ is the impulse response of a digital FIR filter, which is implemented using a finite number of symmetric taps to avoid long processing delays (Koike-Akino et al. 2018a). Therefore, the impact of ISI introduced by a finite number of interfering symbols before and after the desired symbol is considered in Eq. (4.3). The number of interfering symbols listed in Table I is in line with the typical filter half-length required for a $(2L + 1)$ -tap symmetric FIR filter (Koike-Akino et al. 2018a), where $L \leq 31$.

4.3 Inter-Symbol Interference Analysis

Table 4.1. Simulation Parameters for the inter-symbol interference analysis of the raised-cosine better-than raised-cosine and proposed pulse shapes.

Parameter	Value	Unit
Roll-off factor, α	0.25, 0.35, 0.45	—
Symbol rate, R_s	1.44	Gbit/s
Symbol period, T_s	0.694	ns
$\zeta = \gamma/T_s$	10.47	—
Normalised timing-offset, $\delta t_k/T_s$	$\pm\{0.2, 0.25, 0.3, 0.35\}$	—
Number of ISI symbols, N^+, N^-	40	—

Figure 4.4 plots the simulated BER performance of the three considered waveforms in the presence of timing-offsets at a signal-to-noise ratio of 15 dB. For a given pulse shape with a fixed roll-off factor, the BER deteriorates with an increase in the timing-offset. Moreover, for the RC and BTRC pulse shapes and fixed timing-offset, increasing the roll-off factor improves the BER performance. This is because increasing the roll-off factor increases the bandwidth beyond the Nyquist bandwidth and hence, reduces the time-domain sidelobes, which in turn reduces the ISI. On the other hand, for the proposed sinc-Lorentzian pulse, increasing the roll-off factor degrades the BER performance. This is because the sinc pulse envelope in Eq. (4.1) depends on α^- rather than α . Nevertheless, among the three pulse shapes, the BER performance of the sinc-Lorentzian pulse is least sensitive to the roll-off factor as well as the most tolerant to the timing-offsets. The differences in the BER performances exhibited by the three pulse shapes can be explained in terms of the effective SNR of the signal in Eq. (4.4) as follows.

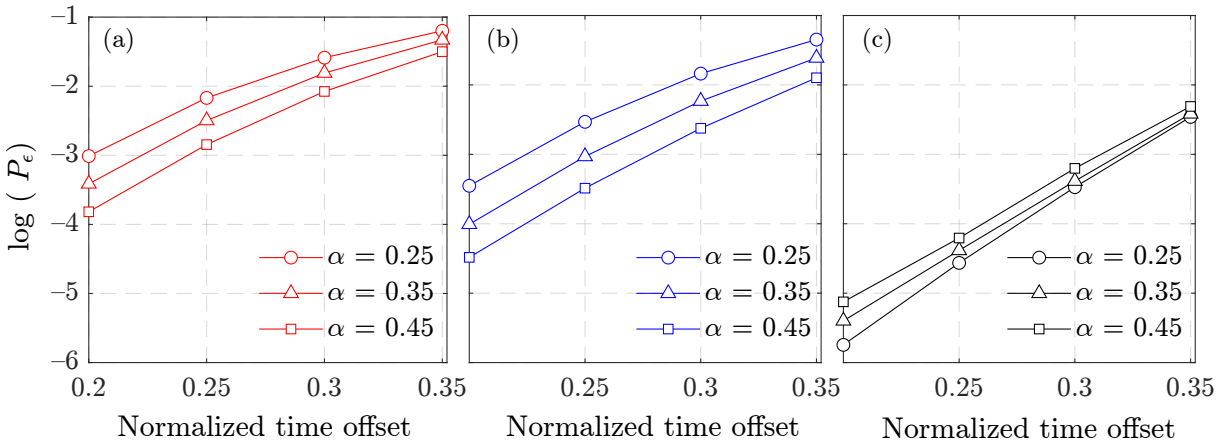


Figure 4.4. Probability of bit error performance resulting from the timing-offset-induced inter-symbol interference. (a) Raised-cosine pulse. (b) Better-than raised-cosine pulse. (c) Proposed sinc-Lorentzian pulse. For the proposed waveform, $\gamma = 7.226 \times 10^{-9}$. For all waveforms, the roll-off factor, α , is 0.25, 0.35, and 0.45, and the signal-to-noise ratio is 15 dB.

Assuming a Gaussian distribution for the ISI in Eq. (4.4), the effective SNR becomes equal to the signal-to-interference plus noise ratio. In this case, the non-zero error performance of timing-offset estimators, i.e., when $\delta t_k \neq 0$, in the presence of AWGN is lower-bounded by the modified Cramer-Rao bound (MCRB) (D'Andrea et al. 1994) and can be formulated in terms of the effective SNR derived in Chapter 2 as follows:

$$\text{SNR}_{\text{eff}} \geq \frac{1}{4\pi^2\sigma_f^2\sigma_t^2}, \quad (4.7)$$

where SNR_{eff} is the effective SNR of the timing-offset-compensated signal, while σ_f and σ_t are the root mean squared (RMS) spectral width and temporal width, respectively. As can be seen from Eq. (4.7), the effective SNR of a signalling waveform, and its corresponding BER performance, depends on the distribution of its energy in the time and the frequency domains. Figure 4.5 illustrates the normalised time-bandwidth product (TBP), defined as $\sigma_t\sigma_f/(BT_s)$, for the three considered waveforms when $0 \leq \alpha \leq 1$. Figure 4.5 also plots the corresponding SNR_{eff} over the same range of α based on Eq. (4.7). In both plots, the sinc-Lorentzian pulse is calculated at $\zeta = 10.47$. In terms of the SNR, the three pulse shapes are equivalent when α is about 0.8. On one hand, decreasing α below 0.8 improves the SNR of the sinc-Lorentzian pulse compared to the RC and the BTRC pulses. This improvement attains its maximum, which is about 23 dB,

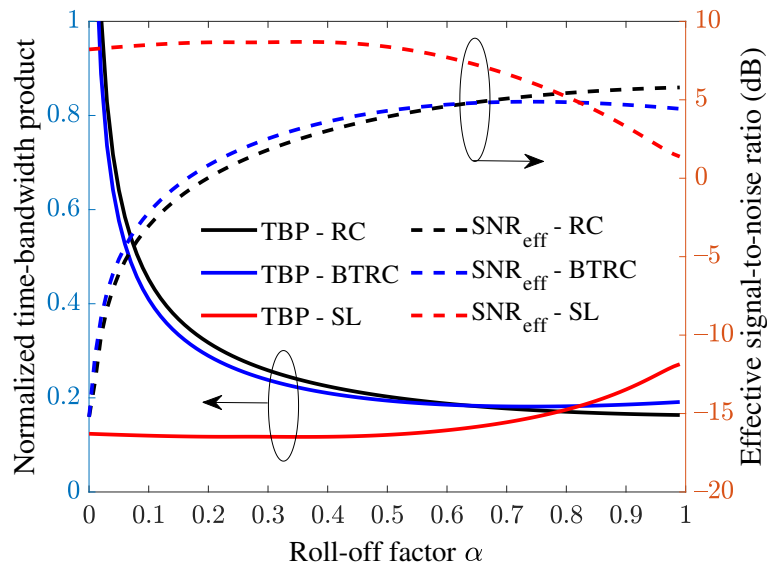


Figure 4.5. Time-bandwidth product and effective signal-to-noise ratio versus the roll-off factor, α . The time-bandwidth product is normalised to the Nyquist bandwidth multiplied by the symbol duration. TBP: time-bandwidth product. RC: raised-cosine. BTRC: better-than raised-cosine. SL: sinc-Lorentzian. The SL spectrum is evaluated at $\zeta = 10.47$.

4.4 Experimental Results and Analysis

at $\alpha = 0$. On the other hand, increasing α beyond 0.8 reverses the situation as the SNR of the sinc-Lorentzian pulse becomes lower than that of the RC or the BTRC pulse, with a maximum SNR degradation of 4.41 dB compared to the RC pulse.

4.4 Experimental Results and Analysis

To assess the transmission performance of the three considered pulse shapes, we conduct experimental investigations using the same experimental setup, together with the DSP at the transmitter side, as that reported in Chapter 3. Figure 4.6 shows this experimental setup as well as the post-detection DSP at the receiver side for this work.

In the experiment, α is set to 0.35 for the RC and BTRC waveforms. This value is frequently reported in the literature on terahertz communications, e.g., (Koenig et al. 2013, 2014, Chinni et al. 2018a), and other forms of communications, e.g., (Alagha & Kabal 1999), (Beaulieu et al. 2001), (Assimonis et al. 2008). In addition, setting the same roll-off factor for both waveform guarantees fair comparisons as in (Beaulieu et al. 2001). For the proposed waveform, as shown in Fig. 4.5, the effective signal-to-noise ratio and the time-bandwidth product are almost independent of α in the range $0 \leq \alpha \leq 0.5$. Therefore, in the experiments, α is set to zero to simplify the analysis without significantly affecting the results. Additionally, further reduction of ζ below 10.47 does not improve the effective signal-to-noise ratio nor reduce the time-bandwidth product. Also, at the transmitter side, the AWG in Fig. 4.6 is programmed to generate the three considered waveforms at a data rate as low as 1.44 Gbit/s to ensure that the signal bandwidth is well-below the flat bandwidth of all baseband electronic equipment.

At the receiver side, the baseband envelope of the received terahertz signal is detected via the SBD and the free space path loss is compensated by a 30 dB low-noise amplifier (LNA). The amplified signal is then sampled by a 80 GSample/s real-time oscilloscope (RTO) for offline DSP as illustrated in Fig. 4.6. To match the sampling rate at the transmitter side, the recorded data is down-sampled from 80 GSample/s to 64 GSample/s using a down-sampling ratio of 5:4 to remove the redundant samples. To mitigate the AWGN, a 44-taps moving average (MA) filter is applied to the received signal as a denoising filter. This filter length is equivalent to the width of the symbol duration, measured in samples, to ensure that the AWGN is averaged over the symbol duration without influencing adjacent symbols. The Tx-Rx synchronisation is recovered by estimating the

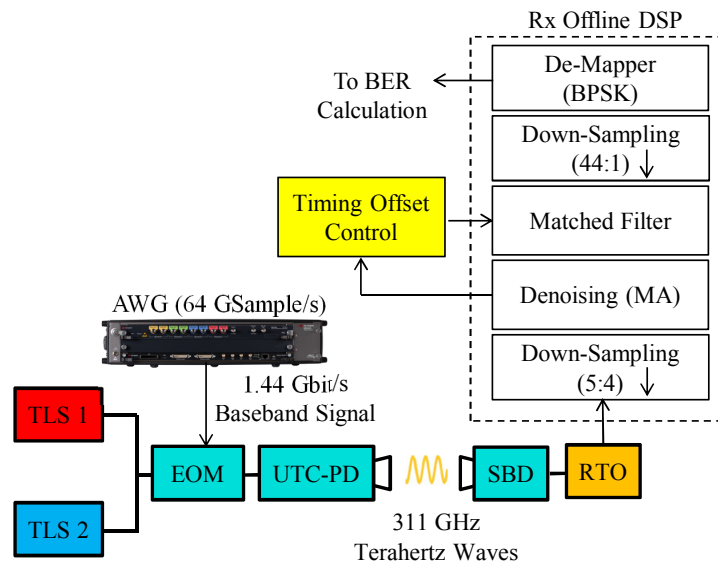


Figure 4.6. Block diagram of the experimental setup including the receiver processing. TLS: tunable laser source. AWG: arbitrary waveform generator. EOM: electro-optic modulator. SBD: Schottky-barrier diode. UTC-PD: uni-travelling carrier photo-diode. RTO: real-time oscilloscope. MA: moving average. Rx DSP: receiver digital signal processing. The maximum sampling rate of the AWG is 65 GS/s.

optimum delay that maximises the cross-correlation of the transmitted and the received sequences.

It should be highlighted that, this experimental setup relies on optical intensity modulation at the transmitter side and direct terahertz envelope detection (IM-DD) at the receiver side. The constant voltage at the MZM bias input results in a double-side band (DSB) envelope-modulated optical signal with a carrier component. After photo-mixing, this DSB signal is down-converted to a corresponding DSB terahertz signal with a non-negative envelope at the uni-travelling carrier photo-diode (UTC-PD) output. Since the phase of the emitted terahertz signal is not modulated by the baseband signal, the phase noise does not impose a strong effect on the detector side.

The timing-offset process is imitated offline by introducing an integer delay of $[\delta t/T_s]$ samples to the time-corrected signal before matched filtering, where $[\cdot]$ is the rounding operator. Figures 4.7(a) and (b) plot the BER performance of the three considered pulse shapes versus the sampling time-offset, δt , at a photo-current of $I_{ph} = 3$ mA or 5 mA, which corresponds to an emitted terahertz power of $P_{THZ} = -18.4$ dBm or -13.3 dBm, respectively. The eye diagrams are plotted for the three waveforms at $\delta t = 0.05T_s$. As shown in the BER plots, for the three pulse shapes, the BER increases monotonically with increasing the timing-offset. This BER deterioration is a result of

4.4 Experimental Results and Analysis

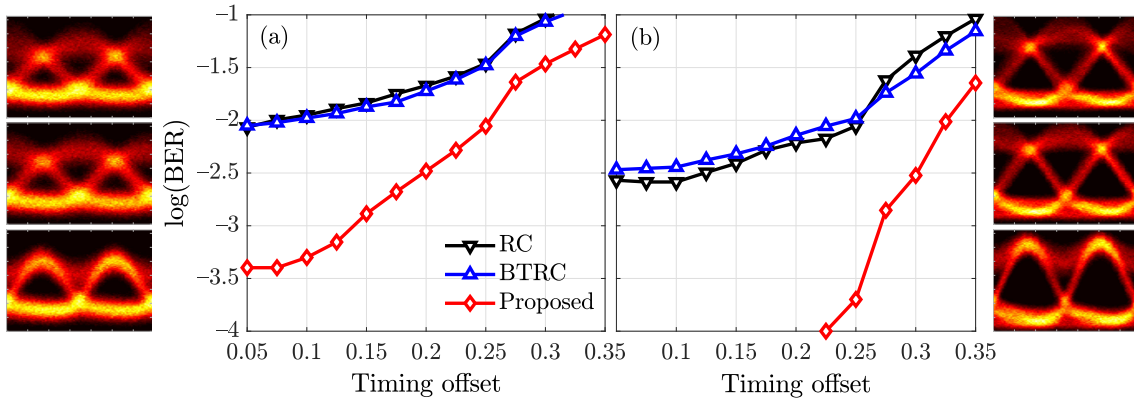


Figure 4.7. Bit error rate performance versus the normalised timing-offset of the received waveforms at two different values of the emitted terahertz power. (a) $P_{\text{THz}} = -18.4$ dBm. (b) $P_{\text{THz}} = -13.3$ dBm. The eye diagrams are plotted for the RC, BTRC, and the proposed waveforms from top to bottom, respectively, at a normalised timing-offset of 0.05.

the reduction in the desired symbol amplitude and an accompanying increase in the sidelobe level introduced by the adjacent symbols as the sampling instant is displaced further from the optimum sampling instant. Figure 4.7(a) shows that, at $\delta t = 0.35T_s$, the BER performance of the terahertz link is improved by a factor of 50% when the RC and BTRC pulses are replaced by the sinc-Lorentzian pulse. This improvement confirms the gain observed in the effective SNR as shown in Fig. 4.5. When δt is reduced to $0.05T_s$, an improvement of about 95% in the BER can be achieved. Additionally, in Fig. 4.7(b), at $\delta t = 0.35T_s$, the BER performance of the sinc-Lorentzian pulse is further improved by about an order of magnitude compared to the RC and the BTRC pulses. Whilst the RC and the BTRC pulses show a minimum BER of 3.2×10^{-3} at $\delta t = 0.05T_s$, the sinc-Lorentzian pulse shows error-free transmission, i.e., zero BER, for $0 \leq \delta t < 0.225T_s$. The eye diagrams in Figs. 4.7(a) and 4.7(b) confirm the transmission performance of the three pulse shapes. From these diagrams, the sinc-Lorentzian pulse has the widest eye opening as well as the minimum sidelobe distortion. The superior BER performance exhibited by the proposed pulse is attributed to its low time-domain sidelobe, which is further suppressed by the system nonlinearities, including the EO modulation nonlinearity as discussed in Section 4.3, and, hence, reduces the nonlinear interaction between adjacent symbols as illustrated in Fig. 4.3(c).

It is noteworthy that, in contrast to the simulated BER performance shown in Fig. 4.4, the experimentally evaluated BER performances for the RC and the BTRC pulse shapes are very close over the entire range of δt . This discrepancy between the simulated and measured BER performances can be explained as follows. In electrical channels, the

ISI is the result of linear interaction between adjacent symbols, i.e., the superposition of the accumulating ISI contributed by all symbols that precede or follow the desired symbol. In optical channels, however, this interaction is affected by the EO conversion nonlinearity. Additionally, the SBD is one of the highly-nonlinear elements in terahertz wireless links, which further strengthens the nonlinear interactions between adjacent symbols (Harter et al. 2020). At the receiver side, matched filtering is applied to $|p(t)|^2$ rather than $p(t)$, which does not result in the maximum SNR, even if the symbols are sampled at the optimum sampling instants. However, such nonlinear interaction does not significantly impact the BER of the proposed waveform due to its rapidly decaying profile.

4.5 Conclusion

This chapter presents a timing-jitter-tolerant pulse shape for photonically-enabled terahertz communications. The bit error rate performance of the proposed sinc-Lorentzian waveform is numerically and experimentally investigated. Numerical and experimental results show that the proposed pulse shape is more robust than the conventional RC and BTRC waveforms against the time sampling errors caused by the timing-jitter. The results reported in this work serve as a starting point as well as a guideline for further research on waveform designs that are more robust to the time sampling errors in high-speed photonically-enabled terahertz communications. Furthermore, the proposed waveform can be considered as a guideline towards the design of spectrally efficient Nyquist waveforms for multi-user IEEE 802.15.3d-compliant terahertz communications systems.

Carrierless Terahertz Amplitude and Phase Modulation

TERAHERTZ communications has been foreseen as a key enabler to the sixth generation (6G) of wireless communications systems. However, the design of spectrally-efficient waveforms and modulation schemes is an ongoing challenge in this regime. In this chapter, we propose and experimentally demonstrate the transmission of M -ary carrierless amplitude and phase (CAP) modulated signals using a 253 GHz photomixing-based terahertz wireless communications system combined with the optical transmission over a 10-km standard single mode fibre (SSMF). Experimental results show that the CAP modulation technique has the capability to support the high-speed transmission of terahertz signals over a wide range of data rates from 4 Gbit/s to 96 Gbit/s based solely on optical intensity modulation at the transmitter side and terahertz envelope detection at the receiver side. Consequently, M -ary CAP can potentially be adopted as a low-complexity waveform and modulation contender to simplify the transceivers architectures for the sixth generation (6G) terahertz communications systems, without sacrificing the high throughput targeted by these systems.

5.1 Introduction

During the last two decades, a number of system-level experiments have demonstrated the generation and wireless transmission of high-throughput terahertz signals in the J-band, i.e., from 200 GHz to 400 GHz (Jia et al. 2018a, Song & Lee 2022, Chinni et al. 2018a,b, Seeds 2014a, Jia et al. 2016a, Dan et al. 2020, Hamada et al. 2018, Rodriguez-Vazquez et al. 2019, Gustavsson et al. 2021). This high throughput is enabled mainly by the spectrally efficient M -ary quadrature amplitude modulation (M -QAM) schemes, together with advanced baseband digital signal processing (DSP) at the transmitter and receiver sides (Jia et al. 2018a, Song & Lee 2022).

The generation of QAM-modulated signals is based on the concept of I - Q mixing, in which the I and Q baseband components of these signals are modulated onto two quadrature sinusoids with the desired carrier frequency before being combined to form the passband QAM signal. The straightforward implementation of the I - Q mixing technique, which is technically called the super-heterodyne approach, is relatively complicated as it requires quadrature oscillators, frequency mixers and 90° phase shifters.

In terahertz communications, implementing super-heterodyne transmitters using electronic components is difficult owing to a number of issues that also result in decoding errors at the receiver side. For instance, terahertz oscillators, such as the resonant tunnelling diodes (RTDs), suffer from the frequency-instability and nonlinearity problems. To avoid these issues, terahertz oscillators are usually substituted by microwave oscillators, followed by N^{th} order frequency multipliers, to generate a desired terahertz carrier frequency. However, the phase noise of these microwave oscillators increases with the frequency multiplication factor, N . Additionally, terahertz frequency mixers suffer from the I - Q imbalance problem (Dan et al. 2020), which significantly deteriorates the error performance of terahertz transceivers.

Terahertz QAM-modulated signals can also be generated using two-stage heterodyne transmitters. First, the baseband I and Q components are modulated onto an intermediate frequency (IF) carrier using an all-microwave super-heterodyne transmitter. Second, the resulting IF QAM signal is up-converted to the terahertz band using single- or multi-stage IF-to-terahertz up-converters, which comprise frequency multipliers and/or frequency mixers. However, the terahertz QAM signals resulting from this technique also suffer from the high phase noise as well as inter-modulation distortion due to the nonlinearities of the frequency multipliers and/or frequency mixers.

5.1 Introduction

Compared to the electronic I - Q mixing, the optical I - Q mixing technique is a less complicated alternative as it employs a dual-drive Mach-Zehnder modulator to modulate the I and Q baseband components onto an optical carrier. The modulated optical carrier is then down-converted to the terahertz band via photo-mixing. Nonetheless, still photonically generated terahertz QAM signals suffer from the same I - Q imbalance and the phase noise problems, which impact their error rate performance and hence, increase the processing demand at the receiver side, as with their electronics-based counterparts.

It should be highlighted that, the role of I - Q mixing is to orthogonally combine the I and Q components of QAM signals after baseband-to-passband up-conversion. Fundamentally, the I and Q components are the output of the baseband DSP at the transmitter side. To date, the main role of DSP in terahertz transmitters is limited to the spectral shaping of these components using two identical Nyquist filters. Therefore, a potential radical solution to the design challenges associated with the conventional I - Q mixing is to combine the I and Q components in the baseband using a digitally synthesised pair of Hilbert filters. Such an approach is called carrierless amplitude and phase (CAP) modulation, which was originally developed to replace the optical I - Q mixing in optical communications (Abdolhamid & Johns 1998).

The adoption of this modulation technique to terahertz communications yields several advantages. First, this approach makes it possible to eliminate the physical or software-based I - Q mixing stages at the terahertz transmitter side, leading to a significant reduction in its implementation complexity. Second, unlike QAM signals, as an amplitude-only modulated signal, the I - Q imbalance and phase noise problems are undefined, at least in principle, for a CAP-modulated signals. Third, the I and Q components can be reconstructed at the receiver side based solely on terahertz envelope detection, i.e., without using down-converting mixers. To this end, we propose to apply the CAP modulation technique (Zhong et al. 2018) to terahertz communications as a low-complexity surrogate that can replace conventional I - Q mixing techniques. To prove the concept, we provide a preliminary investigation of this technique in (Shehata et al. 2022b). Here, we present a thorough analysis and experimentally demonstrate the generation of CAP-modulated terahertz signals at 253.0 GHz and an effective data rate up to 96 Gbit/s. The generated terahertz CAP signals are transmitted over a photonically-assisted terahertz communications system with combined optical and wireless transmission. The detailed experimental result presented in this chapter shows

that, indeed, it is possible to achieve high-speed data transmission rates that are competitive to the conventional QAM-based transceivers within reasonable performance limit, namely, around the 10^{-3} bit error rate limit. Consequently, the CAP modulation technique can be considered as a practically feasible pulse shaping and a modulation contender that has a capacity to transmit massive data using low-complexity terahertz transceivers, offering a clear advantage for future 6G communications.

The remainder of this chapter is organised as follows. Section 5.2 highlights the key differences between the carrier-based versus CAP modulation and outlines the analytical framework of the proposed CAP terahertz system. The experimental setup of the proposed M -ary CAP terahertz system is presented in Section 5.3. The transmission performance of this system is discussed and analysed in Section 5.4. Section 5.5 concludes this chapter.

5.2 CAP Modulation versus I-Q Mixing

In this section, we briefly discuss the key differences between the QAM and CAP modulation techniques in the context of terahertz communications. Figures 5.1(a) and (b) show typical block diagrams of the transmitters based on both techniques from a functional viewpoint (Abdolhamid & Johns 1998). Regardless of a particular I - Q mixing implementation, a M -ary QAM signal can be expressed mathematically as follows:

$$x_{\text{QAM}}(t) = \sum_{k=-\infty}^{+\infty} \left(x_k^I g(t - kT_s) \cos(2\pi f_{\text{LO}} t) - x_k^Q g(t - kT_s) \sin(2\pi f_{\text{LO}} t) \right), \quad (5.1)$$

where $g(t)$ is an arbitrary Nyquist pulse, k is the time-domain symbol index, T_s is the symbol duration, f_{LO} is the LO frequency, and x_k^I and x_k^Q are the in-phase and quadrature components of the k^{th} M -ary QAM symbol, respectively. Likewise, the x_k^I and x_k^Q symbols can also be used to form a M -ary CAP signal, denoted by $x_{\text{CAP}}(t)$, as follows (Chvojka et al. 2017):

$$x_{\text{CAP}}(t) = \sum_{k=-\infty}^{+\infty} \left(x_k^I \phi_I^m(t - kT_s) - x_k^Q \phi_Q^m(t - kT_s) \right), \quad (5.2)$$

where $\phi_I^m(t)$ and $\phi_Q^m(t)$ form an orthogonal Hilbert-transform filter pair, and $m \in \{1, 2, 3, \dots\}$ is the filter order. The filters $\phi_I^m(t)$ and $\phi_Q^m(t)$ are usually called the in-phase and quadrature filters, respectively.

5.2 CAP Modulation versus I-Q Mixing

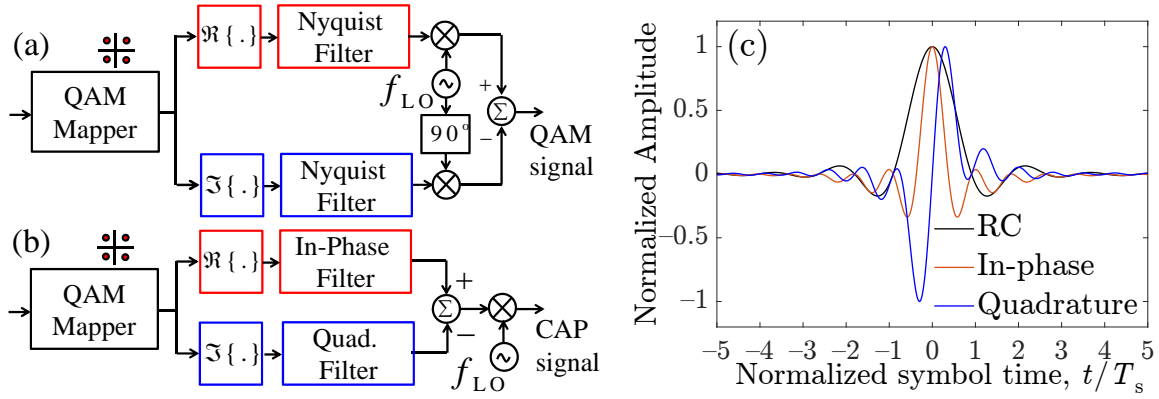


Figure 5.1. Comparison of sinusoidal carrier-based versus carrierless I-Q mixing. (a) Block diagram of the conventional I-Q mixing for quadrature amplitude modulation (QAM). (b) Block diagram of a carrierless amplitude and phase (CAP) modulation-based transmitter. (c) Impulse responses of the raised-cosine (RC) filter and the CAP modulation Nyquist filters. For both signals, the roll-off factor is 0.35. LO: local oscillator.

The impulse responses of the in-phase and quadrature filters are given, respectively, by (Chvojka et al. 2017):

$$\phi_I^m(t) = g(t) \cos(\gamma(2m-1)\delta), \quad (5.3)$$

$$\phi_Q^m(t) = g(t) \sin(\gamma(2m-1)\delta), \quad (5.4)$$

where $\gamma = \pi t/T_s$, $\delta = (1 + \beta)$, and β is the roll-off factor. Here, we choose $g(t)$ as the conventional square-root raised-cosine (SRRC) pulse, defined as follows (Chvojka et al. 2017):

$$g(t) = \frac{\sin(\gamma(1-\beta)) + 4\beta \frac{t}{T_s} \cos(\gamma\delta)}{\gamma \left[1 - \left(4\beta \frac{t}{T_s} \right)^2 \right]}. \quad (5.5)$$

It should be highlighted that, Nyquist pulses other than the SRRC pulse, such as the better-than raised-cosine and Xia pulses (Haigh et al. 2018), can also be used as $g(t)$ to implement the CAP modulation.

Figure 5.1(c) shows the impulse responses of the first order Hilbert-Nyquist pulse pair $\{\phi_I^1(t), \phi_Q^1(t)\}$ compared with the SRRC pulse, evaluated at a symbol rate of $R_s = 1/T_s = 1$ GBaud and a roll-off factor β of 0.35. This roll-off factor has been commonly used in previous experimental demonstrations on terahertz QAM modulation schemes (Koenig et al. 2013, 2014, Chinni et al. 2018a). As shown in Fig. 5.1(c), at the optimum sampling instants, i.e., at $t = kT_s$, the zero locations of $\phi_I^m(t)$ and $\phi_Q^m(t)$ are the same as those of $g(t)$. This means that, despite the multiplication by the terms $\cos(\gamma(2m-1)\delta)$ and $\sin(\gamma(2m-1)\delta)$ in Eq. (5.3) and Eq. (5.4), respectively, still

$\phi_I^m(t)$ and $\phi_Q^m(t)$ can satisfy the Nyquist criteria for zero inter-symbol interference after matched filtering at the receiver side.

In terahertz QAM modulation, the pulse shaping is always implemented digitally in the baseband (Koenig et al. 2013, 2014, Chinni et al. 2018a). After pulse shaping, the QAM pair $(x_k^I, x_k^Q) \cdot g(t)$ is modulated onto the quadrature pair $(\cos(\omega_{LO}t), \sin(\omega_{LO}t))$ for I - Q mixing as illustrated in Eq. (5.1) and Fig. 5.1(a). The I - Q mixing can be implemented either digitally, or using external physical I - Q mixers. In this case, the LO frequency should be at least equal to the baseband signal bandwidth to achieve aliasing-free I - Q mixing. When implemented digitally, IF I - Q mixing and IF-to-baseband down-conversion increase the computational burden at the transmitter and receiver sides, respectively.

In contrast to this, Eq. (5.2) and Fig. 5.1(b) show that the pulse shaped I and Q pairs $(x_k^I \phi_I^m(t), x_k^Q \phi_Q^m(t))$ can be combined directly in the baseband to form the M -ary CAP symbol. The additional IF stage for I - Q mixing in Fig. 5.1(a) and the 90° phase shifter can be eliminated as the orthogonality of the I and Q components is already inherent in the baseband Hilbert filters. In addition, since in terahertz communications the pulse shaping is often required and always implemented digitally, the taps of the two SRRC digital filters in Fig. 5.1(a) can be re-programmed to produce $\phi_I^m(t)$ and $\phi_Q^m(t)$, instead of $g(t)$ at no additional cost as shown in Fig. 5.1(b).

At the receiver side, the QAM-modulated terahertz signals can be detected coherently, using harmonic or sub-harmonic mixing (SHM). The coherent detection of a QAM-modulated terahertz signal using harmonic mixing, also called direct down-conversion, is almost equivalent to its generation in terms of the implementation complexity. In this technique, extracting the I and Q baseband components from a QAM-modulated terahertz signal is a single-step down-conversion process that requires a high frequency LO and a frequency mixer for each component. The LO frequency is equal to the terahertz signal frequency. In SHM, extracting the I and Q baseband components from a QAM-modulated terahertz signal is a two step process. First, the QAM terahertz signal is down-converted to an IF frequency using a single LO and a frequency mixer. Second, the IF signal is further down-converted to the baseband using two IF LOs and two frequency mixers for the I and Q components. This step is usually accomplished offline using DSP. In both techniques, using LOs at the receiver side is essential and enhances the receiver sensitivity due to the power contributed by the LOs. It should be highlighted that, in practice, these demodulation techniques could be implemented

5.3 Experimental Setup

using more complicated transceiver architectures as outlined in Fig. 2.5. The non-ideal characteristics of the LOs and frequency mixers that comprise these architectures also contribute to the I - Q imbalance, high phase noise and nonlinearity experienced by the terahertz signal. To reduce these impacts and, at the same time, simplify the terahertz receiver architecture, QAM-modulated terahertz signals can also be demodulated using digitally-assisted non-coherent demodulation techniques. In these techniques, the QAM terahertz signal is non-coherently detected using terahertz envelope detectors, such as the Schottky-barrier diode (SBD). After that, the QAM signal envelope is forwarded to a digital coherent receiver, such as the generalised Kramer-Krönig receiver (Harter et al. 2020) to extract the baseband I and Q components.

On the contrary, since the CAP-modulation is essentially a variant of the amplitude modulation scheme, the terahertz CAP signals can be only envelope detected, i.e., non-coherently, at the receiver side. After that, the baseband I and Q components can be extracted from the envelope CAP signal using a Hilbert filter pair that are matched to the corresponding filters at the transmitter side as detailed in the next section. In this way, as an envelope detector, the terahertz CAP receiver is similar to the digitally-assisted non-coherent QAM demodulator in terms of the power requirements and physical implementation complexity. This is because both receiver types employ envelope detectors, together with post-detection DSP, to extract the I and Q components, and do not employ neither LOs nor frequency mixers. However, being a non-coherent technique, the CAP demodulation sensitivity is lower than that of the coherent QAM demodulation techniques. Therefore, the implementation of the CAP modulation/demodulation technique should be considered when the terahertz transceiver complexity is the primary design concern, whereas the QAM modulation/demodulation technique is when the receiver sensitivity is the main design consideration.

5.3 Experimental Setup

To experimentally demonstrate the transmission performance of the M -ary CAP terahertz system, we use the setup depicted in Figs. 5.2(a) and (b). As shown in Fig. 5.2(a), the transmitter is based on optical IM using the Mach-Zehnder modulator (MZM), and photo-mixing using the UTC-PD, whereas the receiver front-end is the zero-biased Schottky-barrier diode (SBD), which is a non-coherent terahertz envelope detector. As shown in this figure, a $2^{12} - 1$ pseudo-random binary sequence (PRBS) is generated and

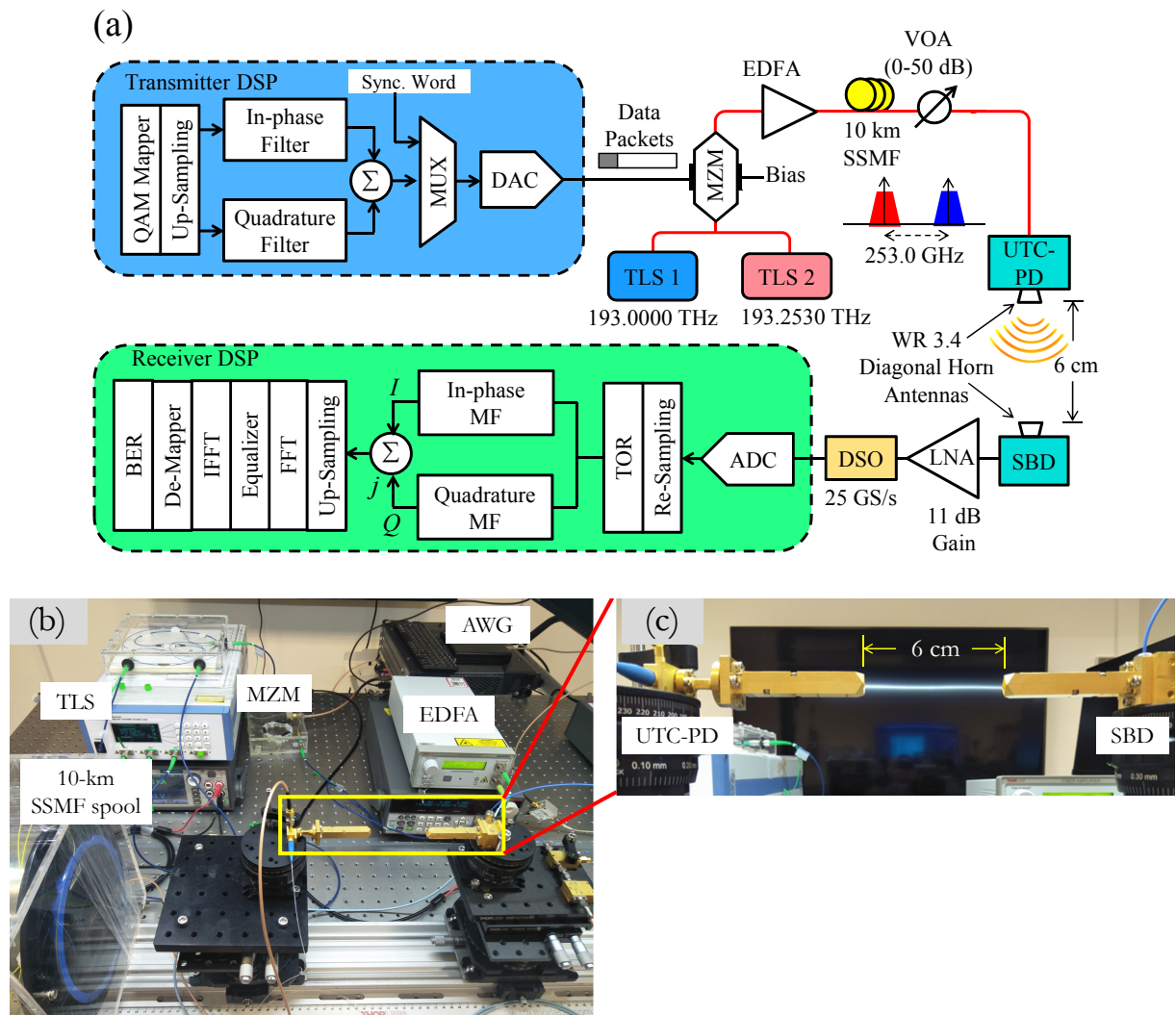


Figure 5.2. Experimental setup of the M -ary CAP photonics-terahertz system. (a) System block diagram. (b) Photo for the experimental setup. (c) Photo for the UTC-PD transmitter and the SBD receiver, including the WR-3.4 waveguides and diagonal horn antennas. QAM: quadrature amplitude modulation. Sync.: synchronisation. DAC: digital-to-analog conversion. ADC: analog-to-digital conversion. TOR: timing-offset recovery. MF: matched filter. FFT: fast Fourier transform. IFFT: inverse FFT. BER: bit error rate. TLS: tunable laser source. AWG: arbitrary waveform generator. MZM: Mach–Zehnder modulator. EDFA: erbium doped fibre amplifier. SSMF: standard single-mode fibre. VOA: Variable optical attenuator. SBD: Schottky-barrier diode. UTC-PD: uni-travelling carrier photo-diode. DSO: digital-storage oscilloscope. DSP: digital signal processing. The maximum sampling rate of the AWG is 65 GS/s.

applied to a M -ary CAP constellation. Each CAP symbol is then up-sampled before being split into its I and Q components, which are applied to the in-phase and quadrature filters, respectively, for pulse shaping. To minimise the bandwidth, the transmitter I and Q Hilbert filters are designed to have a close-to-Nyquist transmission bandwidth by using a roll-off factor of $\beta = 0.1$. The I and Q pulse shaped symbols are combined

5.3 Experimental Setup

to form the CAP signal, which we refer to as the 4-, 16-, or 64-CAP signal. These CAP modulation schemes are equivalent to the $\pi/2$ -quadrature phase shift keying ($\pi/2$ -QPSK), 16-QAM, and 64-QAM, respectively, which are commonly used in terahertz communications (Shams et al. 2017).

Each group of L CAP symbols are multiplexed with the synchronisation word to form a data payload packet. Additionally, each data packet is preceded and succeeded by 100 zero-valued symbols to simplify the identification of the data packet boundaries and hence, precisely recover the transmitter-receiver timing-offset at the receiver side. The AWG generates these encapsulated data packets in real-time at a fixed sampling rate of $f_s = 64$ GS/s. The effective transmission bit rate, denoted by R_b , depends on the symbol rate and the CAP modulation order, denoted by M , as follows: $R_b = R_s \log_2(M)$. Here, three different symbol rates, namely, $R_s = 2, 8,$ and 16 GBaud are employed. Consequently, the CAP signal can be generated at a wide range of data rates, from a minimum of 4 Gbit/s, corresponding to the 4-CAP modulation at a symbol rate of 2 GBaud, and up to a maximum of 96 Gbit/s for the 64-CAP modulation at a symbol rate of 16 GBaud. However, since the AWG sampling rate is fixed, increasing the symbol rate comes at the expense of the number of samples per CAP symbol, f_s/R_s .

In the experiment, two independent lightwave carriers at frequencies of 193.0000 THz and 193.2530 THz, or equivalently, wavelengths of 1553.33 nm and 1551.295 nm, respectively, with an optical power of 35 mW each, are emitted by a tunable laser source (TLS) before being combined via a 50:50 optical coupler. The linewidth of the TLS is less than 100 kHz, which guarantees a high spectral purity in the generated optical carriers. It should be highlighted that, the frequency drifting of the TLS in Fig. 5.2 impacts the frequency and phase stability of the generated terahertz signals. These impacts would be salient if the generated terahertz signal was amplitude and phase-modulated, such as in QAM modulation schemes, or phase-only modulated, such as in the QPSK modulation scheme. In such cases, phase noise mitigation techniques are usually employed at the receiver side (Gonzalez-Guerrero et al. 2018). However, with the CAP modulation technique, the generated terahertz CAP signals are amplitude-only modulated, which makes these signals almost insensitive of the frequency and phase stability problems associated the terahertz carrier. The generated baseband M -ary CAP signal is intensity-modulated onto the combined optical carriers by a single-drive Mach-Zehnder modulator (MZM), which is biased at its $-Q$ point to minimise the electro-optic conversion nonlinearity. After that, the modulated optical carrier is amplified using the erbium

doped fiber amplifier (EDFA) before being launched into the 10-km standard single mode fibre (SSMF). At the SSMF output end, the optical signal is applied to the variable optical attenuator (VOA), which controls the optical power injected into the UTC-PD for photo-mixing. The photo-mixing results in the CAP-modulated terahertz signal at 253.0 GHz. This frequency is the difference between the two TLS optical frequencies and also the maximum emission power of this particular UTC-PD module. To increase the emitted terahertz power and consequently, the signal-to-noise ratio (SNR) at the receiver side, the UTC-PD photo-current is increased from 1 mA to 3.5 mA, with a step of 0.5 mA.

The wireless terahertz channel comprises two identical WR-3.4 diagonal horn antennas aligned in a face-to-face configuration and separated by a distance of 6 cm. Each antenna has a gain of 25 dBi. Although small, the 6-cm antenna separation is within the range recommended by the IEEE 802.15.3d-2017 Standard for device-to-device (D2D) terahertz communications (IEEE 2017), (Kim & Zajic 2016). Nonetheless, this distance can be further extended by using terahertz lenses for beam collimation. However, increasing the wireless reach of the generated terahertz CAP signal does not affect neither the main purpose of using the CAP modulation technique to reduce the terahertz transceiver complexity nor the overall system error performance, especially because the received terahertz power comes only from the line-of-sight (LoS) path. After wireless transmission, the received terahertz signal is then envelope-detected via the SBD. The detected signal is amplified by a 40 GHz low-noise amplifier (LNA), which amplifies the detected signal power by about 11 dB before being sampled and recorded in real-time using a 25 GS/s digital-sampling oscilloscope (DSO) for further offline DSP.

Figure 5.2(a) also shows the functional block diagram customised for the receiver DSP. As shown in this diagram, the received signal is fractionally up-sampled from 25 GSa/s to 64 GSa/s using a sinc-interpolation filter to match the AWG sampling rate. The up-sampled signal is then forwarded to the timing offset recovery (TOR) stage for synchronisation correction and data payload extraction. After that, the extracted CAP signal is forwarded to the Hilbert Nyquist filters, which match the corresponding filter pair $\{\phi_I(t), \phi_Q(t)\}$ at the transmitter side. The outputs from the matched filters are sampled at the symbol rate, and the resulting I and Q sample pairs are then combined via the $j = \sqrt{-1}$ operator to form QAM symbols. Each L symbols are forwarded to the L -tap frequency domain equaliser (FDE) on a frame-by-frame basis. The equalised symbols are applied to the M -ary QAM demapper to estimate the transmitted bit

5.4 System Performance and Analyses

sequence and evaluate the BER performance. Here, we employ a modified form of the FDE in the TeraNova testbed (Sen & Jornet 2019). Specifically, we assume that the end-to-end system transfer function, denoted by $H(k)$, can be estimated as $H(k) = Y(k)/X(k)$, where $X(k)$ and $Y(k)$ are the fast Fourier transform (FFT) of the baseband QAM signal at the transmitter and receiver, respectively, and $k \in \{0, 1, 2, \dots, L-1\}$ is the frequency domain index. The FDE transfer function can be given by:

$$W(k)|_l = \begin{cases} H^{-1}(k), & 0 \leq k \leq l \\ 1, & l < k \leq L, \end{cases} \quad (5.6)$$

where $l \in \{0, 1, 2, \dots, L\}$ is defined as the number of perfectly estimated and equalised channel taps. Assuming that the FDE taps are separated by Δf Hz in the frequency domain, $B_f \triangleq \Delta f l / \Delta f L$ can be defined as the fractional equalisation bandwidth over which the signal is fully compensated for the transmission impairments. In this case, l determines the equalisation bandwidth as well as the spectral resolution of the FDE. When $l = 0$, the received signal is un-equalized, i.e., $B_f = 0$, whereas when $l = L$, $W(k)$ operates over the full signal bandwidth and $B_f = 1$. When $0 < l < L$, or equivalently, $0 < B_f < 1$, the signal is partially equalised.

5.4 System Performance and Analyses

5.4.1 System Performance

Figure 5.3 shows the BER performance of the 4-CAP, 16-CAP and 64-CAP modulation schemes as a function of the fractional equalisation bandwidth, $B_f(\%)$, at different photo-currents. In this figure, each row compares the BER performances of the three modulation schemes at the same symbol rate, whereas each column presents the BER of a single modulation scheme at different symbol rates. As can be seen in Fig. 5.3, for all modulation schemes and symbol rates, the BER decreases monotonically with increasing the fractional equalisation bandwidth, regardless of the photo-current. In addition, for all modulation schemes, symbol rates and photo-currents, the minimum non-zero BER is attained at $B_f \approx 90\%$. When the CAP signals are equalised over $B_f \gtrsim 90\%$ of their bandwidths, no bit errors are observed so they are not shown in the figure. For each modulation scheme and symbol rate combination, two constellation diagrams are evaluated at two values of $B_f(\%)$, namely, $B_f = 95\%$ and $B_f = 99.6\%$. These constellation diagrams show that the density of the received noisy CAP symbols

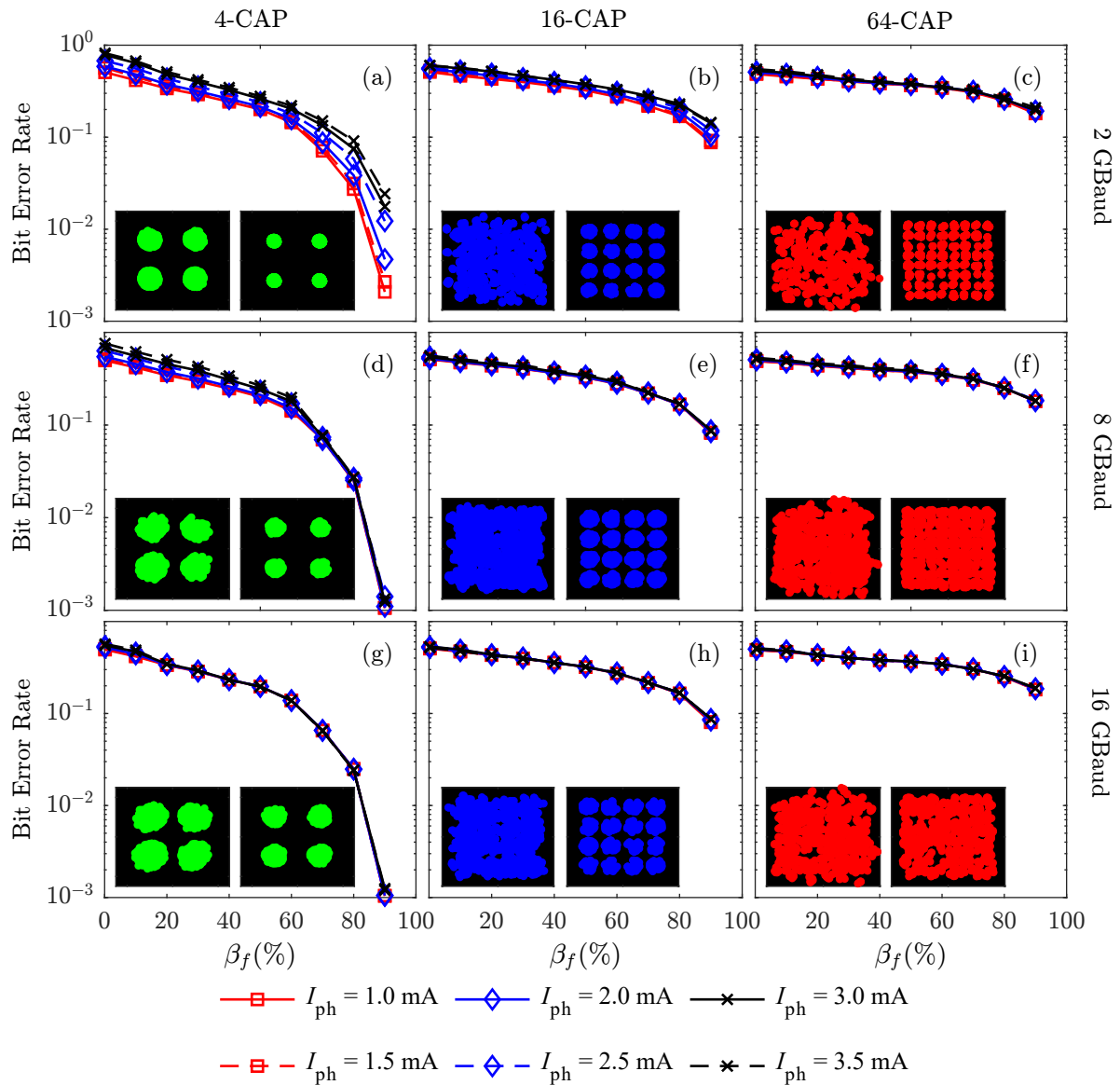


Figure 5.3. Measured bit error rate performance of three QAM-equivalent CAP modulation schemes. Each column represents a modulation scheme and each row represents a different symbol rate. (a) 4-CAP at 2 GBaud. (b) 16-CAP at 2 GBaud. (c) 64-CAP at 2 GBaud. (d) 4-CAP at 8 GBaud. (e) 16-CAP at 8 GBaud. (f) 64-CAP at 8 GBaud. (g) 4-CAP at 16 GBaud. (h) 16-CAP at 16 GBaud. (i) 64-CAP at 16 GBaud. For $90\% < \beta_f \leq 100\%$, no bit errors can be observed in all scenarios. Therefore, the results are not shown in the figures for this range. Instead, insets present constellation diagrams evaluated at a photo-current of 3.5 mA and $\beta_f = 95\%$ and 99.6% .

around their ideal positions decreases with increasing the equalisation bandwidth, which is in line with the BER trends for $B_f < 90\%$. In each row of Fig. 5.3, i.e., for same symbol rate, increasing the modulation order deteriorates the BER performance. This is because that the M -ary amplitude levels in the 16- and 64-CAP signals are closer, making these signals more prone to the de-mapping errors than the 4-CAP signal. On the other hand, in each column, i.e., for the same modulation scheme, the BER deteriorates when

5.4.2 Linear and Nonlinear Impairments

the symbol rate increases. Apparently, for the 4-CAP signal, the 8 GBaud and 16 GBaud signals outperform the 2 GBaud signal in terms of the BER at $\beta = 90\%$. This is because that, numerically, the 2 GBaud signal achieves a zero BER when $\beta > 90\%$, whereas the BER of the 8 GBaud and 16 GBaud signals is about 10^{-3} at $\beta \approx 90.1\%$. The deterioration of the BER at higher symbol rates is because that increasing the symbol rate of the CAP signal leads to a proportional increase in its bandwidth, making the transmitted symbols susceptible to frequency-dependent distortion and noise. Meanwhile, since the AWG sampling rate is fixed, the symbol rate increases at the expense of a lower number of samples per symbol and hence, less energy is carried by higher-speed symbols. Together, the symbol energy, distortions on the pulse shape level as well as superimposed noise reduce the per-symbol signal-to-noise ratio (SNR).

The dependence of the BER performance on the photo-current is also illustrated in Figure 5.3 for the three considered modulation schemes. As an example, in Fig. 5.3(a), the minimum non-zero BER of the 2 GBaud 4-CAP signal deteriorates by about one order of magnitude when the photo-current increases from 1.0 mA to 3.5 mA. Such an anomalous deterioration in the BER performance is because increasing the photo-current induces higher nonlinearity in the SBD (Harter et al. 2020), (Shehata et al. 2021). Figures 5.3(b) and (c) show that the 16-CAP and 64-CAP signals, respectively, also exhibit the same BER trends at the same symbol rate. However, unlike the 4-CAP modulation, the BERs of these two modulation schemes are less sensitive to the photo-current, or equivalently, the system nonlinearities, regardless of B_f . When the symbol rate increases to 8 GBaud and 16 GBaud, Figs. 5.3(d)-(i) show that the BERs of all modulation schemes become less sensitive to the photo-current. The impact of increasing the symbol rate and system nonlinearity on the system transmission performance is detailed in the following sub-section.

5.4.2 Linear and Nonlinear Impairments

There are several linear and nonlinear transmission impairments exhibited by various components in this particular terahertz-photonic system. The nonlinearity is mainly introduced by the SBD to the CAP signal in the terahertz domain (Harter et al. 2020),(Shehata et al. 2021). The linear dispersive effects are caused by the chromatic dispersion (CD) introduced by the SSMF to the CAP-modulated optical signal. It should be highlighted that, practically, there are two optical CAP signals at closely-spaced optical frequencies due to the dual-wavelength modulation as shown in Fig. 5.2. Both signals are simultaneously transmitted over the SSMF. Consequently, the optical signals are

more susceptible to the fibre CD. At sufficiently low symbol rates, these dispersive and nonlinear effects are nearly independent. However, when the symbol rate and/or the photo-current increase, the interplay between the dispersion and nonlinearity can no longer be neglected. Such interaction can be analyzed using highly complicated models, such as the nonlinear Schrödinger equation (Shah et al. 2020), and equalised using sophisticated DSP compensation techniques, such as the back-propagation method (Essiambre et al. 2010). Additionally, the non-ideal baseband frequency responses of the DAC and ADC at the transmitter and receiver sides, respectively, also introduce non-negligible impacts on the end-to-end error performance of terahertz communications systems (Dan et al. 2020). With these considerations in mind, the BERs in Fig. 5.3 can be regarded as reasonable.

Here, we experimentally evaluate these transmission impairments by performing two independent experiments. In the first experiment, we measure the frequency response of the AWG-DSO when connected in a back-to-back configuration. The main purpose of this measurement is to evaluate the non-negligible impact of the DAC and ADC at the transmitter and receiver sides, respectively, on the overall BER performance without considering the impact of the terahertz communications system (Dan et al. 2020). Figure 5.4(a) shows the measured AWG-DSO frequency response to a 100 equal-amplitude sum-of-sinusoids (SoS) test signal. This frequency comb signal spans the frequency range from 100 MHz, and up to 10 GHz with a uniform frequency resolution as low as 10 MHz. The measurement bandwidth covers the bandwidth of the highest baudrate CAP signal considered in this work, i.e., ≈ 8.8 GHz at 16 GBaud. The frequency response of the AWG-DSO configuration is highly distorted over the bandwidth of the CAP signals considered in this work. Importantly, this frequency response exhibits several ripples that are randomly distributed across different spectral bins in the passband and can be as high as 3 dB. In the second experiment, the quasi-stationary time-domain magnitude response of the photonic-terahertz system is measured using a 500 MHz triangular waveform. Using such a low frequency makes it possible to highlight the effect from the SBD nonlinearity without interference from the fiber CD and the AWG-DSO frequency response. Figure 5.4(b) shows the measured magnitude response and a 5-th order polynomial fitting, which is used to estimate the ideally noiseless magnitude response from the measured response. The estimated magnitude response reveals that the system is highly nonlinear and asymmetric, depending on the signal polarity. Figure 5.4(c) shows the impact of the combined linear and nonlinear transmission impairments on the spectrum of the received 4-CAP signal. As can be

5.4.3 Signal-to-Noise Ratio Analysis

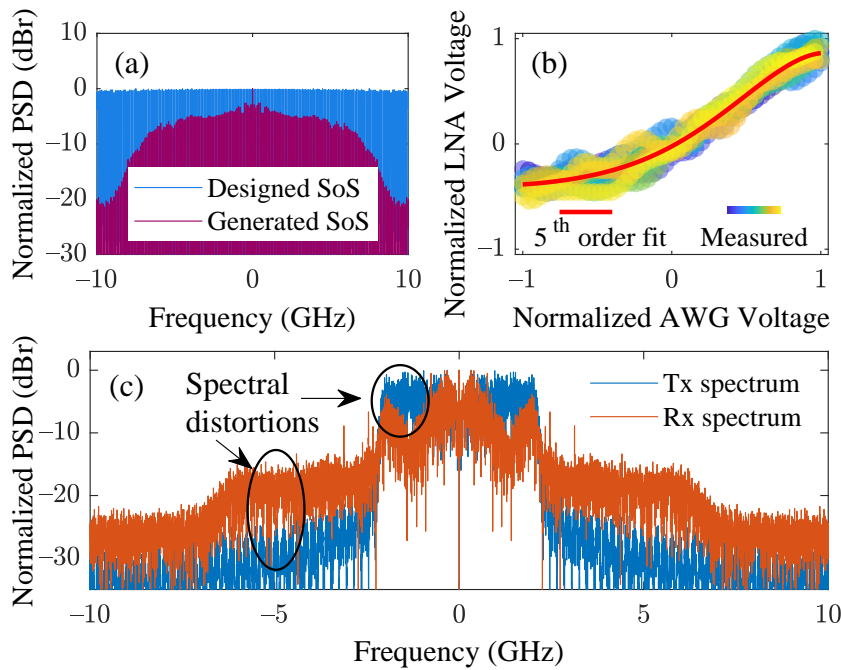


Figure 5.4. Linear and nonlinear distortions of the terahertz photonic system. (a) Combined frequency response of the arbitrary waveform generator and the digital storage oscilloscope. (b) End-to-end magnitude response of the terahertz photonic system. (c) Transmitted and received spectra of the 4-CAP signal at 2 GBaud. SoS: sum-of-sinusoids.

seen in this figure, these interactions cause in-band spectral distortions as well as out-of-band spectral regrowth effects. As a consequence, these spectral distortions result in non-matched filtering by the receiver Hilbert filters and hence, reduces the SNR and hence deteriorates the BER performance.

5.4.3 Signal-to-Noise Ratio Analysis

In addition to the aforementioned linear and nonlinear distortions, the signal-to-noise ratio (SNR) at the SBD front-end is another key factor that limits the BER performance shown in Fig. 5.3. This SNR in turn depends on the maximum terahertz output power of our UTC-PD. Based on the manufacturers' specifications, the relationship between the UTC-PD input photo-current and its terahertz output power can be approximated by a quadratic fitting polynomial, i.e., $P_{\text{THz}} \approx 4I_{\text{ph}}^2$. Without the SSMF, the UTC-PD photo-current can be increased to $I_{\text{ph,B2B}} = 5 \text{ mA}$, resulting in a terahertz output power of about -10 dBm . However, the optical power penalty due to SSMF transmission limits this photo-current to about $I_{\text{ph,SSMF}} = 3.5 \text{ mA}$. Thus, the terahertz power lost due

to SSMF transmission can be estimated as follows:

$$\Delta P_{\text{SMF}}(\text{dB}) = 20 \log \left(\frac{I_{\text{ph,B2B}}}{I_{\text{ph,SSMF}}} \right) = 3.1 \text{ dB}. \quad (5.7)$$

This power loss is consistent with the measured end-to-end optical power loss of the SSMF, which is about 5 dB, including the connector loss at both fibre ends. The free-space path loss (FSPL) also limits the received SNR at the SBD front-end. This FSPL can be calculated using the modified Friis equation as follows (Oshima et al. 2017):

$$\text{FSPL (dB)} = -7.56 - G_{\text{Tx}}(\text{dBi}) - G_{\text{Rx}}(\text{dBi}) + 20 \log(f_{\text{GHz}}) + 20 \log(d_{\text{cm}}), \quad (5.8)$$

where f_{GHz} is the frequency in GHz, d_{cm} is the Tx-Rx antenna separation in cm, and $G_{\text{Tx}}(\text{dBi})$ and $G_{\text{Rx}}(\text{dBi})$ are the transmitter and receiver antenna gain, respectively, measured in the dBi units. The emitted UTC-PD terahertz power and the FSPL in Eq. (5.8) are used to evaluate the received terahertz power at the SBD front-end, which can be expressed mathematically as follows:

$$P_{\text{Rx}}(\text{dB}) \approx 10 \log(4I_{\text{ph}}^2) + G_{\text{Tx}}(\text{dBi}) + G_{\text{Rx}}(\text{dBi}) - \text{FSPL}(d)(\text{dB}), \quad (5.9)$$

where P_{Rx} is the received terahertz power, measured in the dB units. Figure 5.5 plots P_{Rx} in Eq. (5.9) versus d at different values of the photo-current, I_{ph} , where $0 \leq I_{\text{ph}} \leq 3.5$ mA and $1 \text{ cm} \leq d \leq 6 \text{ cm}$ as listed in Table 5.1. Assuming transmission over an additive white Gaussian noise (AWGN) channel, the SNR at the LNA output can be expressed as follows (Oshima et al. 2017):

$$\text{SNR}_{\text{Rx}}(\text{dB}) \approx P_{\text{Rx}}(\text{dB}) + G_{\text{LNA}}(\text{dB}) - 10 \log(N_0 \cdot \text{BW}_{\text{LNA}}) - 10 \log(\text{NEP}_{\text{avg}}), \\ - \text{NF}(\text{dB}) \quad (5.10)$$

where $\text{SNR}_{\text{Rx}}(\text{dB})$, is the received SNR at the LNA output, measured in dB, $N_0 = kT$ is the additive white Gaussian noise (AWGN) power spectral density, $k = 1.38 \times 10^{-23}$ J/K is the Boltzmann constant, and $T = 300$ K is the room temperature in Kelvin. The rest of the parameters in Eq. (5.10), together with their numerical values, are defined in Table 5.1. Based on these parameters, the estimated SNR at the LNA output ranges from about -1.84 dB to 9.05 dB. Such a low SNR range is far below the minimum SNR required for similar terahertz communications systems, which is least 20 dB (Pirrone et al. 2022). Nevertheless, the BERs in Fig. 5.3 are within the typical

5.4.3 Signal-to-Noise Ratio Analysis

limits attained by similar terahertz communications systems with optical and electronic-based I - Q mixing techniques. We also use the estimated SNR obtained from Eq. (5.10) to evaluate the BER performance of the three considered CAP modulation schemes via

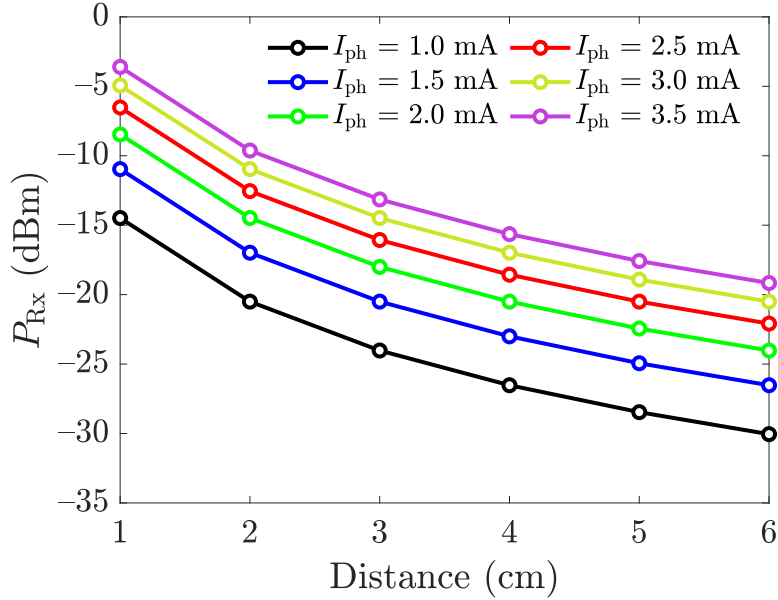


Figure 5.5. Received terahertz power as a function of distance at different photo-currents based on Eq. (5.9). The transmitter and receiver antenna gains are 25 dBi.

Table 5.1. Link-level simulation parameters for the bit error rate comparison of the M -ary CAP and QAM modulation scheme. An AWGN channel is assumed.

Parameter and Symbol	Value	Unit
Roll-off factor, α	0.1	—
Symbol rate, R_s	2, 8, 16	GBaud
Sampling rate, f_s	64	GS/s
Modulation	4-, 16-, 64-CAP & 4-, 16-, 64-QAM	—
UTC-PD photo-current, I_{ph}	1.0–3.5	mA
Terahertz frequency, f_{GHz}	253.0	GHz
Antenna gains, G_{Tx}, G_{Rx}	25	dBi
Antenna separation, d_{cm}	6	cm
SBD noise-equivalent power, NEP	17	pW/ \sqrt{Hz}
SBD bandwidth, BW_{SBD}	110 (220–330)	GHz
LNA gain, G_{LNA}	11	dB
LNA bandwidth, BW_{LNA}	40	GHz
LNA noise figure, NF	5	dB
LNA input return loss, RL_{in}	13	dB
LNA output return loss, RL_{out}	13	dB

numerical simulations. The same SNR range is also used to evaluate the BER of the QAM-equivalent modulations, namely, the QPSK, 16-QAM and 64-QAM modulations. In the simulations, we assume the transmission of both modulation schemes over an AWGN channel without the linear and nonlinear distortions discussed earlier in this section. The purpose of these simulations is to assess the BER performance of the CAP modulation schemes under ideal transmission conditions and compare this performance with the experimentally obtained BER ranges. Another purpose is to compare the CAP modulation schemes with their QAM-equivalent modulations in terms of the BER performance. In the simulations, we also assume that the terahertz up- and down-conversion of both signals are transparent, i.e., without I - Q imbalance and phase noise, and distortion-less.

Figure 5.6 compares the BER performances of the 4-, 16-, 64-CAP modulation schemes with their QAM-equivalent schemes, namely, the QPSK, 16-QAM and 64-QAM modulations, respectively. Each row compares the BER performances of two equivalent modulation schemes at the same symbol rate, whereas each column presents the BER of a single modulation order at different symbol rates. As can be seen in Fig. 5.6, for all modulation schemes, the BER decreases monotonically with increasing the SNR. Importantly, the M -ary QAM signal always outperforms its corresponding M -CAP equivalence in terms of the BER, regardless of the modulation order, symbol rate and SNR. This can be interpreted as follows. In Fig. 5.1(c), it can be seen that the impulse responses of the two Hilbert filters show a relatively rapid ringing in their side-lobes compared with the SRRC filter. This increased ringing is attributed to the $\cos(\cdot)$ and $\sin(\cdot)$ terms in Eq. (5.3) and Eq. (5.4), respectively. The symbol rates of both signals are increased at a fixed sampling rate. As a result, the quadrature filters are relatively under-sampled, which in turn reduces the energy per symbol and deteriorates the overall BER performance. Practically, the BER performance depends on the particular channel estimation, equalisation and nonlinearity compensation techniques. Here, we assume that the FDE transfer function, $W(k)|_l$, in Eq.(5.6) is based on the perfect estimation of the end-to-end channel response, $H(k)$. Therefore, the BER limits in Fig. 5.3 can be considered as performance indicators of the CAP modulation technique in photonics-based terahertz communications systems operated over a wide range of baud rates.

It should be highlighted that, in terms of the equalisation complexity, both the CAP and QAM techniques are equivalent as the equalisation is required to compensate for the transmission impairments and channel non-ideal device characteristics. Another

5.4.3 Signal-to-Noise Ratio Analysis

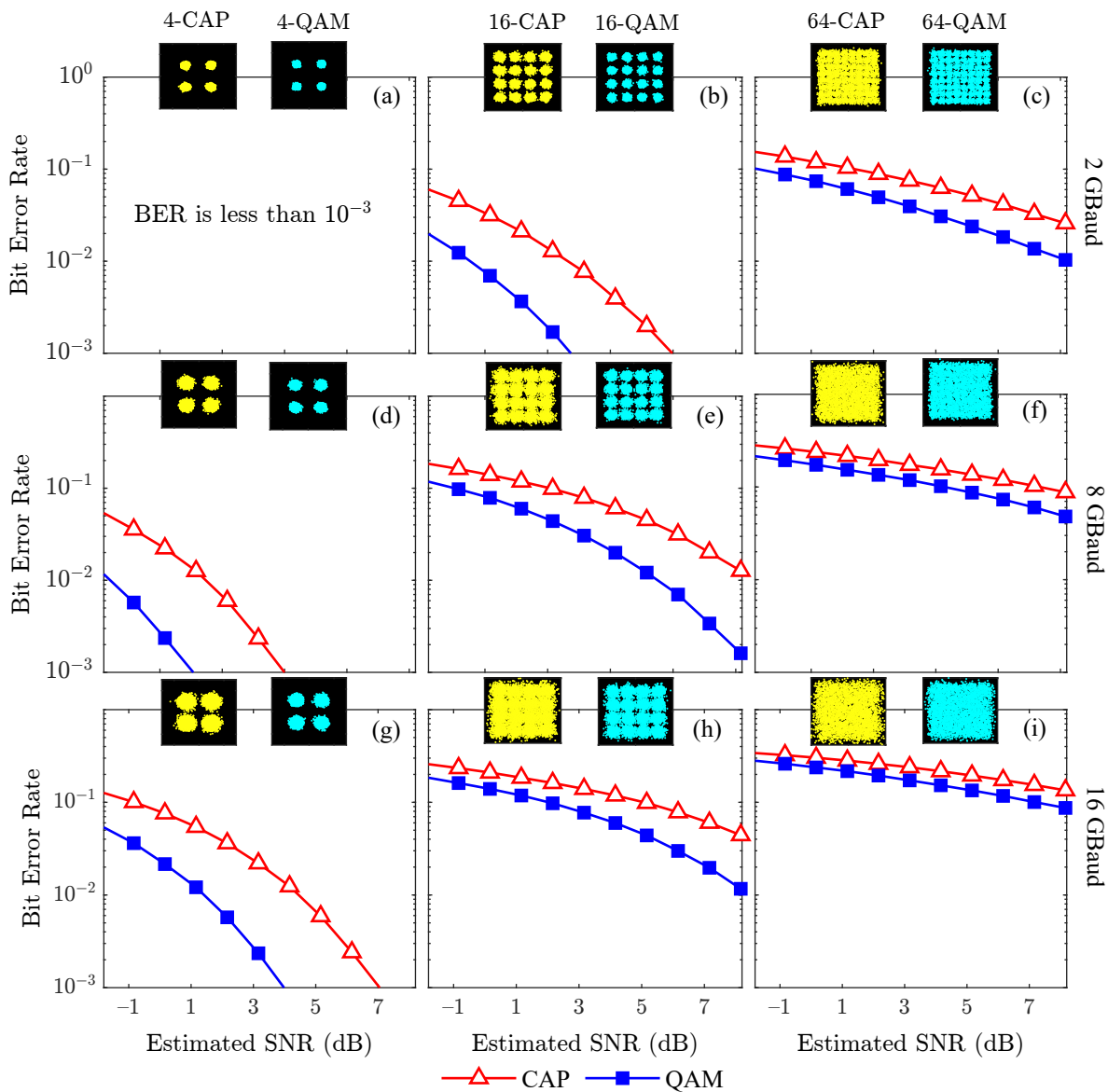


Figure 5.6. Simulated bit error rate performance of CAP and QAM modulation schemes in an AWGN channel. Each column represents a modulation scheme and each row represents a different symbol rate. (a) 4-CAP, QPSK at 2 GBaud. (b) 16-CAP and 16-QAM at 2 GBaud. (c) 64-CAP and 64-QAM at 2 GBaud. (d) 4-CAP and QPSK at 8 GBaud. (e) 16-CAP and 16-QAM at 8 GBaud. (f) 64-CAP and 64-QAM at 8 GBaud. (g) 4-CAP and QPSK at 16 GBaud. (h) 16-CAP and 16-QAM at 16 GBaud. (i) 64-CAP and 64-QAM at 16 GBaud. Insets are constellation diagrams evaluated at a signal-to-noise ratio of 9 dB.

fundamental difference between the CAP and QAM modulation techniques is the sensitivity to the phase noise effects. In QAM modulation, both the amplitude and the phase of the generated terahertz signal are modulated by the I and Q components of the baseband signal. This way, the phase noise generated by the TLSs unavoidably impacts the phase component of the demodulated QAM signal at the receiver side. Therefore, DSP techniques for phase noise mitigation (Gonzalez-Guerrero et al. 2018) are

usually employed. In contrast to this, the CAP modulation is based only on amplitude modulation, and the I and Q components can both be extracted from the amplitude of the envelope-detected CAP signal. In this way, in principle, the phase noise has no impact on the demodulated CAP signal.

5.4.4 Transceiver Complexity Analysis

Table 5.2 compares the proposed CAP terahertz system with the state-of-the-art terahertz experimental demonstrations, with a focus on their transceivers architectures. As shown in this table, the architectures of low-complexity terahertz transceivers are based on optical intensity modulation (OIM) and envelope detection at the transmitter and receiver sides, respectively. These transceivers can be used to implement simple modulation schemes, such as the on-off keying (OOK) and the 4-level pulse amplitude modulation (4-PAM). However, with these modulation schemes, the maximum data rate that can be achieved is so far limited to 48 Gbit/s, which is less than 50% of the average data rate required for future terahertz communications, namely, 100 Gbit/s (Pirrone et al. 2022).

Table 5.2 also shows that, to increase the data rate towards or beyond 100 Gbit/s, the use of the high-order QAM modulation schemes, such as the 16-QAM, is commonly implemented. Remarkably, supporting the generation and detection of such a high-order modulation scheme complicates the terahertz transceiver architecture. As an example, in (Gonzalez-Guerrero et al. 2018) and (Gonzalez-Guerrero et al. 2019), the transmitters are based on digital as well as optical I - Q mixing to generate 16-QAM signals. At the receiver side, the 16-QAM terahertz signals are down-converted to the IF band using SHM. In addition, in SHM-based terahertz receivers, still the IF signal needs to be I - Q -demodulated using baseband offline DSP. Although highly complicated, these transceivers can support a data rate of only 20 Gbit/s. Furthermore, in the majority of the state-of-the-art experimental demonstrations, pulse shaping and matched filtering at the transmitter and receiver sides, respectively, are indispensable for spectrally efficient QAM terahertz signals. These functionalities contribute to the overall computational burden of DSP-assisted terahertz transceivers. In contrast to this, the proposed terahertz CAP system combines several advantages of previous terahertz transceivers. These advantages can be summarised as follows:

5.4.4 Transceiver Complexity Analysis

Table 5.2. Comparison of the proposed CAP terahertz system with the state-of-the art terahertz experimental demonstrations.

Reference	Transmitter Topology	Receiver Topology	Modulation Scheme	Maximum Data Rate (Gbit/s)	Optical Transmission	Wireless Distance
(Pirrone et al. 2022)	OIM (single-drive MZM)	Envelope detection	OOK	14	No	50 cm
(Ducourneau et al. 2014)	OIM (single-drive MZM)	Sub-harmonic mixing	OOK	40	No	2 m (with lens)
(Oshiro et al. 2021)	OIM (single-drive MZM)	Envelope detection	4-PAM	48	No	5 cm
(Pirrone et al. 2022)	Direct optical I - Q mixing	Sub-harmonic mixing	16-QAM	104	No	50 cm (with lens)
(Chinni et al. 2018a)	Direct optical I - Q mixing	Sub-harmonic mixing	16-QAM	100	No	50 cm
(Koenig et al. 2013)	Direct optical I - Q mixing	Sub-harmonic mixing	16-QAM	100	No	40 m (with lens)
(Gonzalez-Guerrero et al. 2018)	Digital IF + Optical I - Q mixing	Sub-harmonic mixing	16-QAM	20	10-km SSMF	30 cm
(Gonzalez-Guerrero et al. 2019)	Digital IF + Optical I - Q mixing	Sub-harmonic mixing	16-QAM	20	No	10 cm
(Rodriguez-Vazquez et al. 2020)	Direct electronic I - Q mixing	Harmonic mixing (I, Q)	16-QAM	80	No	1 m (with lens)
(Rodriguez-Vazquez et al. 2019)	Direct electronic I - Q mixing	Harmonic mixing (I, Q)	16-QAM	100	No	1 m (with lens)
(Dan et al. 2020)	Analog IFs (I, Q) + electronic I - Q mixing	Two-stage down-converting mixers	16-QAM	60	No	50 cm
(Hamada et al. 2018)	Digital IF + electronic up-converting mixer	Sub-harmonic mixing	16-QAM	100	No	2.2 m
This work	Digital CAP + OIM (single-drive MZM)	Envelope detection	4-CAP	4,16,32	10-km SSMF	6 cm
This work	Digital CAP + OIM (single-drive MZM)	Envelope detection	16-CAP	16,32,64	10-km SSMF	6 cm
This work	Digital CAP + OIM (single-drive MZM)	Envelope detection	64-CAP	32,64,96	10-km SSMF	6 cm

- In terms of the transmitter complexity, this system is based on OIM as the I and Q components of the CAP signal are orthogonally combined via pulse shaping.
- At the receiver side, the system is based on terahertz envelope detection, which makes it possible to eliminate terahertz-to-IF down-conversion stages and hence, reduce the overall transceiver implementation complexity.
- The elimination of the IF-based I - Q demodulation at the receiver side also makes it possible to rely solely on Hilbert matched filtering to extract the I and Q components. That said, still such a low-complexity CAP transceiver can support the transmission of QAM-equivalent signals over a wide range of data rates, up to 96 Gbit/s.

In addition to the aforementioned advantages, Table 5.2 also shows that, unlike most of the previous demonstrations on terahertz communications, the proposed terahertz CAP system can support optical transmission to distances up to 10 km. Supporting the proposed system by SSMF transmission is highly desirable and in line with the foreseen seamless integration of terahertz wireless communications with existing and future optical access networks (Shams et al. 2016).

5.5 Conclusion

We introduce the CAP modulation to terahertz communications as a spectrally-efficient low-complexity alternative to the conventional sinusoidal-based QAM modulation schemes. Up to 96 Gbit/s, optical intensity-modulated CAP signals are generated and transmitted over 10-km single mode optical fibre before being down-converted to 253 GHz using a UTC-PD photo-mixer. After wireless transmission, this terahertz CAP-modulated signal is envelope detected using an SBD. Experimental results show that, employing the CAP modulation technique to terahertz communications makes it possible to rely on low-complexity terahertz transceivers and, at the same time, achieve high-speed data transmission rates that are competitive to the conventional QAM-based transceivers with bit error rates lower than 10^{-3} . Therefore, CAP modulation can be considered as both a promising pulse shaping and a modulation contender that has a capacity to transmit gigantic data volumes using low-complexity terahertz transceivers, which is highly desirable for future 6G communications.

As an extension, multi-band CAP modulation is available to support multi-user transmission with manageable inter-band interference. Although applied to a single-drive electro-optic modulator in this work, we also foresee that the CAP modulation technique could potentially be used with electronic-based key terahertz devices that have a single IF input port, such as resonant tunnelling diodes (RTDs) and quantum-cascade lasers (QCLs).

Signal Generation and Processing in Terahertz Communications

DESPITE the maturity of the terahertz signal generation and detection techniques, still the functionality and reliability of these techniques are rather limited on the device- and system-levels. Therefore, photonics-based signal processing techniques is foreseen as a potential opportunity that can be used to overcome the functionality limitations of terahertz communications systems. Additionally, to increase the reliability of these systems, conventional signal processing techniques are applied to the baseband signal. In this chapter, we propose two all-optical signal processing techniques that are called-for in terahertz communications, namely, frequency tuneability and multi-band spectral shaping. These two functionalities are essential for the development of frequency-division multiplexed terahertz communications, where the dynamic frequency allocation and multi-band processing are essential requirements. We also show that some already in-use baseband signal-processing techniques should be revised before being applied to terahertz communications. Particularly, we optimise two typical linear and nonlinear equalisation techniques, with a focus on the accuracy and computational complexity metrics, which are of a paramount importance for the high-speed processing of massive data in real-time.

6.1 Introduction

The advancement of terahertz communications has been relying on the development of terahertz signal generation, transmission and processing techniques. Employing signal processing techniques to terahertz communications has two vital roles. First, with these techniques the temporal and spectral characteristics of terahertz signals can be flexibly controlled. Second, the reliability of most terahertz communications systems crucially depends on the mitigation of practical transmission impairments using these techniques. Despite the growing interests in terahertz communications, terahertz signal processing techniques are relatively under-investigated compared with the generation techniques. To date, still the major contributions to terahertz communications are largely at the device level rather than the system level (Tarboush et al. 2022).

Whilst terahertz signals can be processed in the passband in real-time using photonic (Yoo et al. 2012) or terahertz (Ma et al. 2017) techniques, so far, still the processing of these signals is often implemented offline in the baseband using high-speed electronically programmable platforms (Song & Lee 2022), (Tarboush et al. 2022). This is because baseband processing offers a variety of well-established techniques that have been widely adopted for years in optical and microwave communications before being transferred to terahertz communications. Adapting these techniques to the requirements of terahertz communications systems will significantly enhance the performance of these systems and extend their capabilities. In terahertz communications, signal processing techniques are employed for various purposes, such as spectral shaping, phase noise mitigation (Gonzalez-Guerrero et al. 2018), linear (Schram et al. 2020) and nonlinear (Qiao et al. 2021) equalisation, to name a few. In this chapter, we present four different electrical and optical signal processing techniques that aim to extend the capabilities of existing terahertz communications systems. It should be highlighted that, this chapter presents preliminary analysis and results for the proposed techniques, which require further investigations in future work.

The remainder of this chapter deals with all-optical as well as baseband signal processing techniques and comprises five sections, which are organised as follows. Sections 6.2 and 6.3 present two all-optical techniques that can be used to control the spectrum of terahertz signals. Sections 6.4 and 6.5 focus on the highly precise and computationally-efficient implementation of linear and nonlinear baseband equalisation techniques, which are viable requirements for the reliability and real-time operation of terahertz communications.

6.2 Optical Frequency Tuning of Terahertz Signals

Specifically, in Section 6.2, we propose a photonic generation technique of sub-terahertz signals based on the Kerr effect in highly nonlinear optical fibres. We show via simulations that this technique can be used to generate on-off keying (OOK) modulated terahertz signals with electrically tunable frequency. In Section 6.3, we propose an all-optical multi-band raised-cosine filter with tunable bandwidth for multi-channel IEEE 802.15.3d Standard-compliant terahertz communications using only a single-tap microwave photonic filter. The functionality of the proposed filter is modelled, simulated and experimentally demonstrated. In Section 6.4, we experimentally demonstrate a highly-precise equalisation technique based on a Volterra nonlinear filter for highly nonlinear terahertz communications systems. This technique is experimentally demonstrated using a 253 GHz photonics-based terahertz system with 10-km radio-over-fibre link. In Section 6.5, we propose a low-complexity implementation for the zero-forcing (ZF) equaliser in single-carrier frequency domain multiple access (SC-FDMA) MIMO terahertz communications systems. The proposed method is based on restructuring the MIMO channel matrix to reduce the computational complexity of the conventional ZF equaliser. Simulation results show that the proposed equaliser is comparable to the conventional ZF equaliser in terms of the bit error rate (BER), with a much lower computational complexity. The proposed equalisation technique can be considered as a potentially significant step towards the implementation of real-time terahertz communications applications. Section 6.6 concludes this chapter.

6.2 Optical Frequency Tuning of Terahertz Signals

Terahertz signal generation based on the photo-mixing of two independent optical signals is a well-established technique in terahertz communications (Shams & Seeds 2017). However, since independent optical sources (Jia et al. 2016b) are uncorrelated and non-coherent, terahertz signals resulting from this technique are usually accompanied with a highly random phase noise. Additionally, in terms of the practical implementation requirements, the monolithic integration of semiconductor laser structures with different wavelengths on the same chip is relatively complicated (Jia et al. 2016b). Importantly, terahertz frequencies resulting from this technique are tuned manually by controlling the optical frequencies. This tuning mechanism is not practical for dynamic frequency allocation, which is essential for efficient spectral sharing in future multi-user terahertz wireless communications. To overcome these tunability and phase noise limitations, another category of techniques have been developed to generate low-phase noise frequency-tunable terahertz signals from an optical frequency comb (OFC).

In these techniques, a single laser source with a fixed optical frequency is applied to an optical phase modulator, together with frequency-tuneable radio frequency (RF) oscillator (Nagatsuma & Carpintero 2015). The optical phase modulator generates an OFC with multiple uniformly spaced optical tones. Two optical comb lines with the desired terahertz frequency spacing are selected for terahertz signal generation via photo-mixing. The frequency of the resulting terahertz signal can be continuously tuned by varying the RF oscillator frequency, which changes the spacing between the optical comb tones. However, only two out of N OFC lines are usable for frequency mixing, which limits the power efficiency to only $2/N$. In this section, we propose a simple technique that relies on optical wavelength conversion in highly nonlinear fibre (HNLF) to generate continuously tunable terahertz signals from a single optical source. In contrast to OFC-based techniques, the generated sub-terahertz frequency can be continuously tuned by controlling the amplitude of the modulating baseband signal rather than the frequency of an independent RF oscillator. This capability has a clear practical advantage for frequency division multiplexed terahertz communications, which often require dynamic frequency allocations for efficient spectral sharing.

6.2.1 Principle of Operation

The proposed technique relies on a single wavelength optical source, from which a second optical tone is generated via optical wavelength conversion. The optical wavelength conversion is based on the frequency chirp resulting from the self-phase modulation (SPM) of the first optical frequency based on the the Kerr effect in a HNLF. The chirped and non-chirped optical signals has a frequency spacing equal to the desired terahertz frequency and are forwarded to a photo-mixer for terahertz signal generation. The schematic diagram in Fig. 6.1 illustrates this principle. The continuous wave (CW) laser source generates an optical carrier with a power of P_o and a frequency of f_o . The power of this optical carrier is equally split into two identical optical paths using a 50:50 optical splitter (OS). The first optical signal, referred to as the reference frequency, is forwarded directly to the high-speed PD. The optical electric fields of these signals can be expressed in the phasor form as follows:

$$\tilde{E}_1(t) = \sqrt{\frac{P_o}{2}} \cdot \exp(j\omega_o t) \quad (6.1)$$

$$\tilde{E}_2(t) = \sqrt{\frac{P_o}{2}} \cdot \exp(j\omega_o t), \quad (6.2)$$

where $\omega_o = 2\pi f_o$, and $\tilde{E}_1(t)$ and $\tilde{E}_2(t)$ are the complex baseband optical electric fields.

6.2.1 Principle of Operation

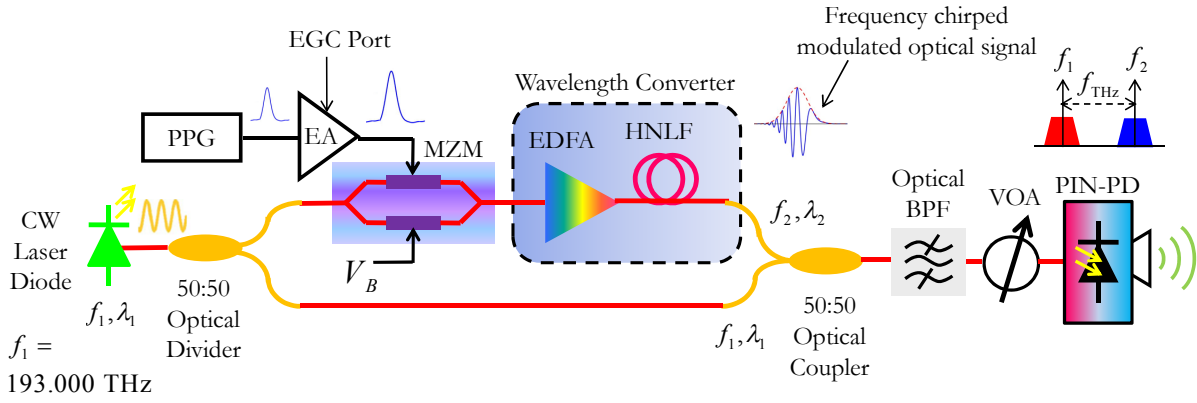


Figure 6.1. Schematic diagram of the proposed photonics-based terahertz voltage controlled oscillator. CW: continuous wave. PPG: pulse pattern generator. EA: electrical amplifier. EGC: electrical gain control. MZM: Mach-Zehnder modulator. EDFA: erbium doped fibre amplifier. HNLF: highly nonlinear fibre. OC: optical coupler. BPF: bandpass filter. PIN-PD: positive-intrinsic-negative photo-detector. Black lines represent electrical paths, whereas red lines represent optical paths.

The second optical signal, i.e., $\tilde{E}_2(t)$, is forwarded to the Mach-Zehnder modulator (MZM) for electro-optic modulation. Meanwhile, a signal source generates an on-off keying (OOK) non-return-to-zero (NRZ) baseband signal, denoted by $v_{in}(t)$. This signal is applied to an electrical amplifier (EA), which has a voltage gain of G_{elec} . The EA output voltage is given by $v_m(t) = G_{elec}v_{in}(t)$. The electrically amplified voltage signal is modulated onto the second optical carrier using the MZM. The optical intensity at the MZM output is given by:

$$I_{MZM}(t) = \frac{P_o}{2} \cos^2 \left(\frac{\pi}{2V_\pi} (V_B + v_m(t)) \right), \quad (6.3)$$

where V_π is the MZM half-wave voltage, i.e., the voltage required to introduce a phase shift of $\pi/2$ to the optical carrier, and V_B is its DC bias voltage. Assuming that the MZM is biased at the negative quadrature point of its transfer characteristics and operates over its quasi-linear range, i.e., $v_m(t) \ll V_\pi$, the output optical intensity in Eq. (6.3) can be amplitude-modulated and approximated as follows:

$$I_{MZM}(t) \approx \frac{P_o}{2} (A - Bv_m(t)), \quad (6.4)$$

where A and B are defined as follows:

$$A \triangleq \frac{1}{2} + \frac{1}{2} \cos \left(\frac{\pi V_B}{V_\pi} \right), \quad (6.5a)$$

$$B \triangleq \frac{\pi}{2V_\pi} \sin \left(\frac{\pi V_B}{V_\pi} \right). \quad (6.5b)$$

The MZM output optical intensity in Eq. (6.4) is amplified by the erbium doped fibre amplifier (EDFA), which has an optical gain of G_{EDFA} , before being coupled to the HNLF. In the HNLF, the modulated optical carrier experiences a self-phase modulation (SPM) due to the Kerr-based nonlinearity (Zadok et al. 2010). The optical electric field at the HNLF output, denoted by $E'_2(t)$, can be expressed as follows:

$$\tilde{E}'_2(t) = \sqrt{\frac{P_o G_{\text{EDFA}} I_{\text{MZM}}(t)}{2}} \cdot \exp(j\omega_o t + j\varphi(t)), \quad (6.6)$$

where $\varphi(t) = n_2 G_{\text{EDFA}} I_{\text{MZM}}(t)$, $n_2 = \gamma L_{\text{HNLF}}$ is the second-order refractive index of the HNLF, γ is the nonlinearity coefficient of the this fibre, measured in $(\text{m.W})^{-1}$, and L_{HNLF} is the fibre length. A time varying optical frequency chirp, denoted by Δf_o , results from $\varphi(t)$ and can be calculated as follows:

$$\Delta f_o = \frac{1}{2\pi} \frac{d\varphi(t)}{dt} = \left(\frac{\gamma L_{\text{HNLF}} P_o G_{\text{elec}} G_{\text{EDFA}}}{8V_\pi} \right) \sin\left(\frac{\pi V_B}{V_\pi}\right) \frac{dv_{\text{in}}(t)}{dt}. \quad (6.7)$$

It should be highlighted that, practically generated OOK-NRZ signal possess non-zero rise and fall times, denoted by τ_r and τ_f , respectively, due to capacitive effects in electronic platforms, specially at high switching speeds. Considering an individual OOK-NRZ pulse with a peak voltage of V_p and equal rise and fall times, i.e., $\tau_r = \tau_f = \tau$, the derivative in Eq. (6.7) can be approximated as follows:

$$\frac{dv_{\text{in}}(t)}{dt} \approx \begin{cases} +\frac{V_p}{\tau}; & \text{for the rising edge} \\ -\frac{V_p}{\tau}; & \text{for the falling edge} \\ 0; & \text{otherwise.} \end{cases} \quad (6.8)$$

After the HNLF, the reference and the chirped optical signals are combined via the 50:50 optical coupler (OC) and applied to the optical bandpass filter (OBPF). The OBPF removes the excess amplified spontaneous emission (ASE) noise resulting from the EDFA. The filtered optical signal is forwarded to the positive-intrinsic-negative PD (PIN-PD) for photo-mixing. For photo-mixing, the PIN-PD operates as a square-law optical detector, and the electric field at its output, denoted by $E_{\text{PIN-PD}}(t)$, can be related to the optical electric fields at its input as follows:

$$E_{\text{PIN-PD}}(t) \propto \left(\text{Re}\{\tilde{E}_1(t)\} + \text{Re}\{\tilde{E}'_2(t)\} \right)^2. \quad (6.9)$$

6.2.1 Principle of Operation

In practical terahertz communications systems, the photo-mixing PD is coupled to a terahertz antenna via a terahertz waveguide that supports only one dominant mode. Consequently, this waveguide can be modelled as a bandpass filter that bypasses only the terahertz component of the electric field in Eq. (6.9). The radiated terahertz field can be expressed as follows:

$$E_{\text{THz}}(t) \propto \cos(2\pi|\Delta f_o|t) = \cos(2\pi KV_p t) = \cos(2\pi f_{\text{THz}}t), \quad (6.10)$$

where $KV_p \triangleq f_{\text{THz}}$ is the resulting terahertz frequency and K is defined as the frequency tuning sensitivity, measured in Hz/V, and expressed as follows:

$$K \triangleq \frac{\gamma L_{\text{HNLF}} P_o G_{\text{elec}} G_{\text{EDFA}} V_p}{8V_\pi \tau} \sin\left(\frac{\pi V_B}{V_\pi}\right). \quad (6.11)$$

Equation (6.11) suggests that the generated terahertz frequency can be tuned either electrically by controlling the parameter set $\{V_B, V_p, G_{\text{elec}}, \tau\}$, or optically via the parameter set $\{P_o, G_{\text{EDFA}}, \gamma, L_{\text{HNLF}}\}$. We focus on the electrical tuning of the parameter K via the peak input voltage, V_p , so that the resulting frequency, f_{THz} , is in the terahertz band. In this way, the proposed system can be regarded as a photonic-assisted terahertz voltage controlled oscillator (VCO). The tuning sensitivity of this VCO can be controlled via the parameters $\{V_B, G_{\text{elec}}, P_o, G_{\text{EDFA}}, \gamma, L_{\text{HNLF}}\}$. We evaluate K and the resulting absolute frequency chirp $|\Delta f_o|$, which is also the terahertz frequency f_{THz} , at different values of the EA gain, G_{elec} based on the parameters listed in Table 6.1. These parameters are exhibited by typical practical equipment so that the results are close-to-realistic. The input voltage, $v_{\text{in}}(t)$, is modelled as a super Gaussian pulse with non-zero rise and fall times to emulate practically generated OOK-NRZ signals.

Table 6.1. Simulation parameters to evaluate the tuning sensitivity, K , based on Eq. (6.11).

Parameter and Symbol	Value and Unit
Input voltage amplitude, V_p	0–800 mV
Rise/fall time, τ	18 ps
Electrical amplifier gain, G_{elec}	0, 3, 10 dB
Input optical power, P_o	20 dBm
MZM halfwave voltage, V_π	1 V
MZM DC bias voltage, V_B	0.5 V
Optical amplifier gain, G_{EDFA}	19 dB
Fibre length, L_{HNLF}	200 m
Nonlinear fibre coefficient, γ	31.4 (W.km)^{-1}

Figure 6.2(a) shows a typical amplitude-normalised input voltage, $v_{in}(t)$, over a single “1” OOK-NRZ symbol duration, together with its amplitude-normalised derivative. As shown in this figure, based on Eq. (6.7), the derivative of each “1” OOK-NRZ symbol, i.e., $v_{in}(t)$, comprises two impulse-like waveforms with opposite polarities, corresponding to the rising and falling edges of $v_{in}(t)$ at the symbol boundaries. These two impulse-like waveforms result in a positive and negative optical frequency chirp with respect to the reference optical frequency, f_o . The amount of this frequency chirp, and consequently, the generated terahertz frequency, depends on the steepness of $v_{in}(t)$, i.e., the ratio of V_p to τ .

Figure 6.2(b) shows the impact of the peak input voltage on the resulting terahertz frequency. As shown in this figure, regardless of the electrical gain, G_{elec} , the generated terahertz frequency, f_{THz} depends linearly on the peak input voltage V_p , and the slope is equal to the tuning sensitivity, K , defined in Eq. (6.11). The tuning sensitivity can be enhanced by increasing the electrical gain, G_{elec} . As an example, a terahertz frequency of 220 GHz can be generated without using the EA, i.e., $G_{elec} = 0$ dB, when the peak voltage is about 630 mV, whereas the same frequency can be generated when the peak voltage is reduced to 160 mV at $G_{elec} = 10$ dB. It is also noteworthy that, the maximum of V_p is 800 mV, which can be generated by currently available waveform generators.

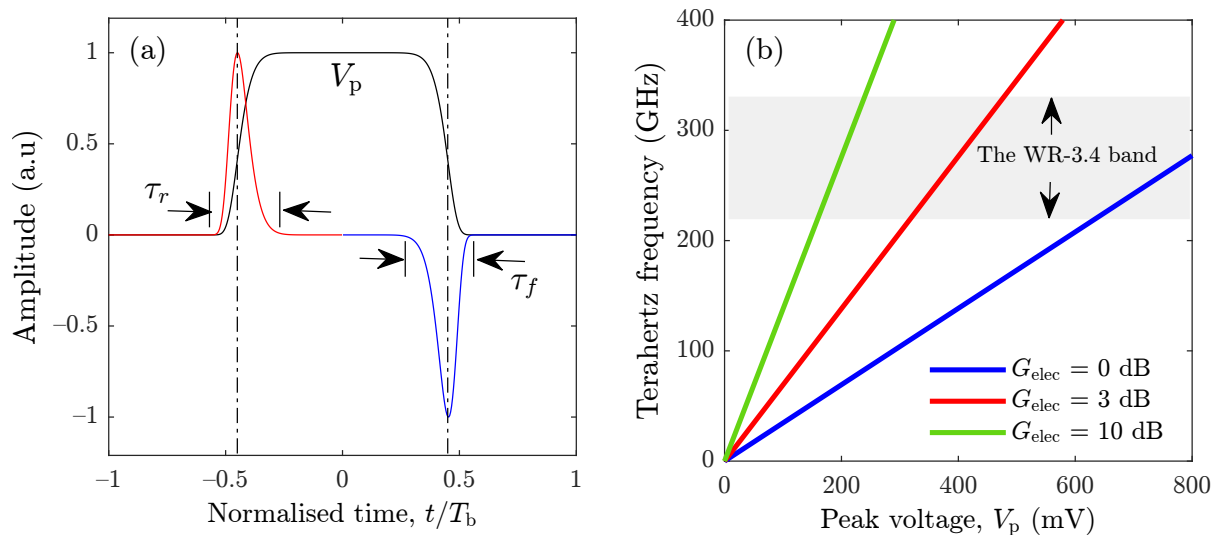


Figure 6.2. Performance of the system proposed in Fig. 6.1. (a) Positive and negative frequency chirps in response to the input voltage. (b) Generated terahertz frequency at different values of the tuning sensitivity, K . V_p : peak input voltage. τ_r : pulse rise time. τ_f : pulse fall time. T_b : symbol duration. G_{elec} : electrical amplifier gain. The WR-3.4 band extends from 220 GHz to 330 GHz.

6.2.2 Simulation Results and Analysis

Additionally, this voltage range is sufficient to generate terahertz frequencies in the WR-3.4 band, i.e., from 220 GHz to 330 GHz, which is in line with most of the experimental demonstrations on terahertz devices and communications systems.

6.2.2 Simulation Results and Analysis

The performance of the proposed terahertz generator is simulated based on the finite-difference time-domain (FDTD) technique using VPI Transmission Maker. We use the simulation parameters listed in Table 6.2. Each “1” OOK-NRZ symbol is a super-Gaussian pulse with a 95% duty cycle, i.e, 5% rise and fall times. We also use a sampling rate of 1 TS/s. Such a high sampling rate is required in order to capture the details of the super-Gaussian pulse at the rise and fall times. The length of the HNLF is 200 m.

Table 6.2. Link-level simulation parameters for the photonic-terahertz system shown in Fig. 6.1. Simulations are carried out using VPI Photonics.

Parameter	Value and Unit
Pulse pattern generator	
Modulation	OOK-NRZ
Waveform profile	Super-Gaussian
Voltage amplitude, V_p	1 V
Rise/fall time, τ	20% – 80%
Data rate, R_b	20 Gbit/s
Sampling rate	1 Tbit/s
Electrical gain, G_{elec}	0 dB
Tunable laser source	
Optical frequency	193.000 THz
Line width	100 kHz
Optical Power	15 dBm
Mach-Zehnder modulator	
Null voltage, V_π	1 V
Bias voltage, V_B	0.5 V
Erbium doped fibre amplifier	
Optical gain, G_{EDFA}	10 dB
Highly nonlinear fibre	
Type	single mode fibre
Length, L_{HNLF}	100 m
Nonlinear coefficient, γ	31.4 (W.km)^{-1}
Optical bandpass filter	
Type	Super-Gaussian, 5 th order
Centre frequency	193.000 THz
Bandwidth	200 GHz

Such a relatively short length is suitable mainly for optical signal processing. However, for broadcasting application scenarios, longer HNLF sections with different nonlinear coefficients can be used (Zadok et al. 2010).

Figure 6.3 shows the time and frequency domain performance of the proposed sub-terahertz photonic signal generator. Figure 6.3(a) shows a segment of the transmitted OOK-NRZ waveform, i.e., before electro-optic modulation. Figures 6.3(b) and (c) show the envelope of the terahertz signal generated at the PD output before and after post-processing, respectively. As shown in Fig. 6.3(b), the terahertz signal envelope has a non-zero net DC component due to the MZM bias. The post-processing comprises a DC level shifter, followed by a 11-tap moving average (MA) filter. Figure 6.3(d) shows the optical spectrum of the TLS. Figure 6.3(e) shows the optical spectrum at the OBPF output and before being applied to the PD. As shown in this figure, this composite optical spectrum comprises two dominant optical tones at 193.000 THz and 193.150 THz as well as multiple low-power discrete comb lines separated by 20 GHz. The difference between the two dominant optical frequencies is equal to the generated terahertz signal frequency, whereas the comb line spacing is equal to the baseband data

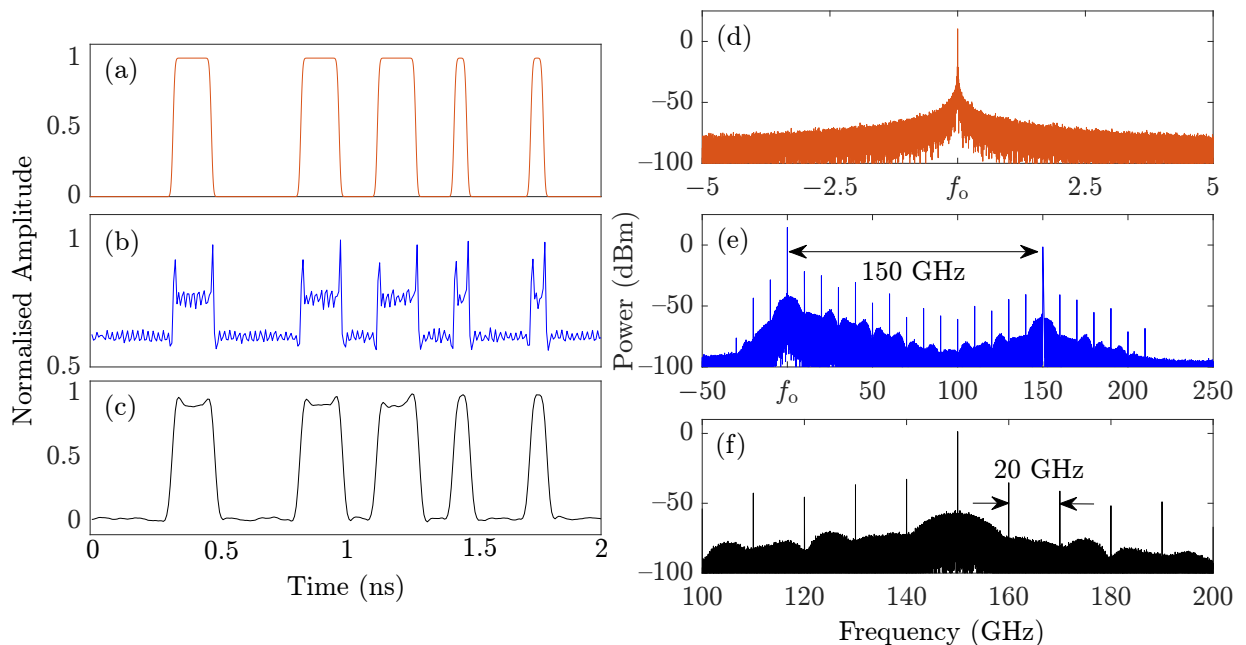


Figure 6.3. Time and frequency domain performance of the proposed sub-terahertz photonic signal generator. (a) Transmitted OOK-NRZ waveform. (b) Received terahertz signal envelope before post-processing. (c) Received OOK-NRZ waveform after post-processing. (d) Optical spectrum of the tunable laser source (TLS). (e) Combined optical spectra of the TLS and the chirped modulated optical signal before photo-mixing. In (d) and (e), f_0 is 193.000 THz (f) Terahertz spectrum at the PIN PD output.

6.3 Terahertz Pulse Shaping using Microwave-Photonics

rate, i.e., 20 GBit/s. The 150 GHz frequency spacing results in the OOK-modulated sub-terahertz signal at 150 GHz after photo-mixing as shown in Fig. 6.3(f). It should be highlighted that, a major limitation of the proposed approach is that higher order modulation schemes, such as the quadrature phase shift keying (QPSK) scheme, are not supported (Zadok et al. 2010).

6.3 Terahertz Pulse Shaping using Microwave-Photonics

The implementation of the technical specifications defined in the IEEE 802.15.3d Standard calls for high-speed low-complexity signal generation concepts and system-level demonstrations. In particular, considering the first channelisation scheme in the IEEE 802.15.3d Standard, a typical multi-user transmitter must apply spectral shaping filters to the 32 wireless channels in the 252–321 GHz band. Traditionally, this requires a raised-cosine (RC) filter bank for 32 users to reshape their spectra in the baseband before up-conversion to the terahertz frequencies. It should be highlighted that, in multi-band terahertz communications systems, the processing of multiple frequency division multiplexed signals could be prohibitively complicated when implemented in the baseband using digital platforms. In this section, we propose to overcome this implementation complexity by employing MWP filters (Yao 2009) as a low-complexity all-optical processing solution. The technique can also potentially contribute to the implementation of IEEE 802.15.3d Standard-compliant terahertz transmitters with high-speed centralised multi-user processing. Experimental and simulation results show that a typical single-tap MWP filter can be employed as a tunable all-optical multi-band RC pulse shaper for terahertz communications.

6.3.1 Principle of Operation

The IEEE 802.15.3d Standard defines eight channelisation schemes within the range from 252 GHz to 321 GHz. Six of these channelisation schemes are dedicated to multi-user signalling. To fully comply with this standard, the terahertz signal spectrum must be carefully reshaped before being emitted by each user. In a typical terahertz downlink, a computationally-powerful central station (CS), equipped with a digital pulse shaping filter bank, is required to implement this task. Table (6.3) shows the maximum per-user symbol rates as well as the total number of users defined in each channelisation scheme, which should be simultaneously handled by a fully-loaded CS. As shown in this table,

Table 6.3. Multi-user specifications of the IEEE 802.15.3d Standard (IEEE 2017).

Channelisation scheme ID	1	2	3	4	5	6
Number of users	32	16	8	5	4	2
Maximum symbol rate (GBaud)	1.64	3.29	6.57	9.86	13.14	19.71

the per-user symbol rate decrease with increasing the number of users to limit the overall terahertz channel bandwidth to the 252–321 GHz band. Additionally, for the first channelisation scheme, a maximum overall symbol rate of 52.48 GBaud is required to process all users' signals. Assuming a practical over-sampling factor of 21 Koike-Akino et al. (2018b), an overall sampling rate of 1 TSample/s is required by the CS in order to process these signals. Such a high sampling rate is overwhelming and power-inefficient for currently available electronic-platforms. To overcome this implementation complexity, we propose to employ microwave photonic (MWP) filters (Yao 2009) to terahertz communications as a low-complexity multi-band pulse shaping solution. Figure 6.4 illustrates the schematic diagram of a typical photonic-enabled terahertz transmitter, with a first-order MWP filter incorporated into to this transmitter. As shown in this figure, the multi-band intermediate frequency (IF) IEEE 802.15.3d signal modulates an optical carrier, which has a frequency of f_1 , using the Mach-Zehnder modulator (MZM). The modulated optical signal is then applied to the single-tap MWP filter for optical spectral shaping. After that, the filtered optical signal is combined with an un-modulated optical carrier, which has a different frequency of f_2 , using an optical power coupler. The resulting dual-wavelength optical signal is then forwarded to the unit-travelling photo-diode (UTC-PD) for photo-mixing, which results in the spectrally-reshaped terahertz signal.

The MWP filter comprises a power divider with a splitting ratio of α , a tunable optical time delay line (OTDL), which introduces a time delay of τ , and a power combiner with a power coupling ratio of κ . Mathematically, the baseband-equivalent frequency response of this filter, denoted by $H_{\text{MWP}}(j\omega)$, can be expressed as follows Yao (2009):

$$H_{\text{MWP}}(j\omega) = \alpha + \kappa \exp(-j\omega\tau), \quad (6.12)$$

where ω is the angular frequency. Assuming an equal-ratio power divider and coupler, i.e., $\alpha = \kappa = 1$, the squared-magnitude frequency response of this filter can be expressed as follows Yao (2009):

$$|H_{\text{MWP}}(j\omega)|^2 = 2(1 + \cos(2\omega\tau)). \quad (6.13)$$

6.3.1 Principle of Operation

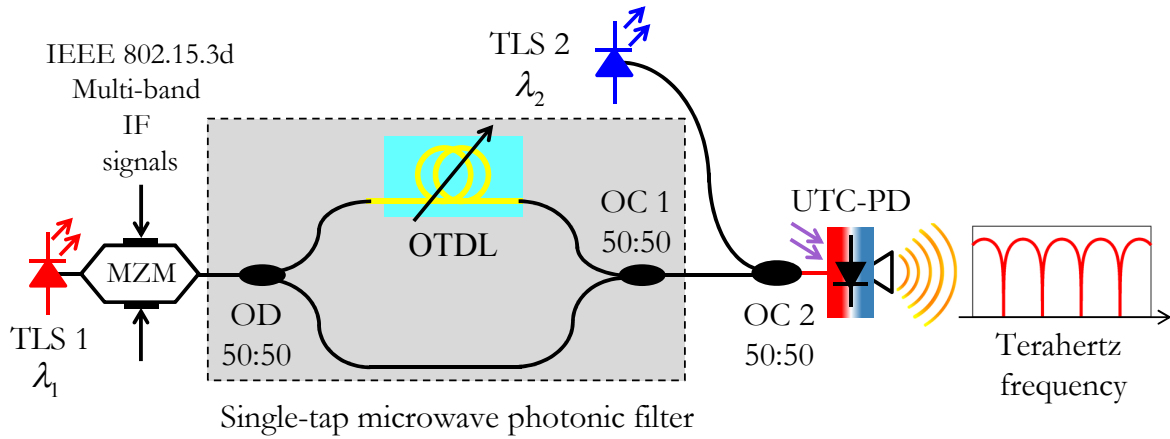


Figure 6.4. Schematic diagram of the proposed microwave photonic-assisted multi-band terahertz filter. TLS: tunable laser diode. MZM: Mach-Zehnder modulator. IF: intermediate frequency. OD: optical divider. OTDL: optical time-delay line. OC: optical coupler. UTC-PD: uni-travelling carrier photo-diode.

Figure 6.5(a) plots this squared-magnitude response at three different values of τ . As shown in this figure and Eq. (6.13), the optical delay, τ , is the key parameter that controls the overall filter response. In addition, the frequency response of the MWP filter in Eq. (6.13) is periodic with uniformly-spaced nulls. The null-to-null (N2N) bandwidth, denoted by BW_{N2N} , is given by $BW_{N2N} = 1/(4\tau)$.

Importantly, for $|f| \leq BW_{N2N}/2$, this frequency response is identical to the frequency response of a typical baseband raised-cosine (RC) filter with a unity roll-off factor. Whilst the MWP filter frequency response is periodic, the frequency response of a baseband RC filter is equal to zero, for $|f| > BW_{N2N}/2$.

The optical time delay, τ , is numerically optimised to minimise the mean-squared error (MSE) between the MWP filter response and the frequency response of an RC pulse shaping filter at different values of the roll-off factor, denoted by β . Figure 6.5(b) shows the normalised MSE as a function of the optical time delay. In all cases of the roll-off factor β , a minimum MSE of about 10^{-2} is obtained at an optical time delay of 0.6944 ns, which is half the symbol duration required for an equivalent RC filter with a unity roll-off factor and a standard symbol rate of 1.44 GBaud IEEE (2017).

It should be highlighted that, matching the spectral emission masks defined by the IEEE 802.15.3d Standard using the proposed MWP filter is a two-step process that can be performed as follows. First, the OTDL is tuned so that the N2N bandwidth of the MWP filter is equal to the bandwidth of the desired IEEE 802.15.3d channelisation scheme. This can be done regardless of the optical frequency of the first TLS in Fig. 6.4.

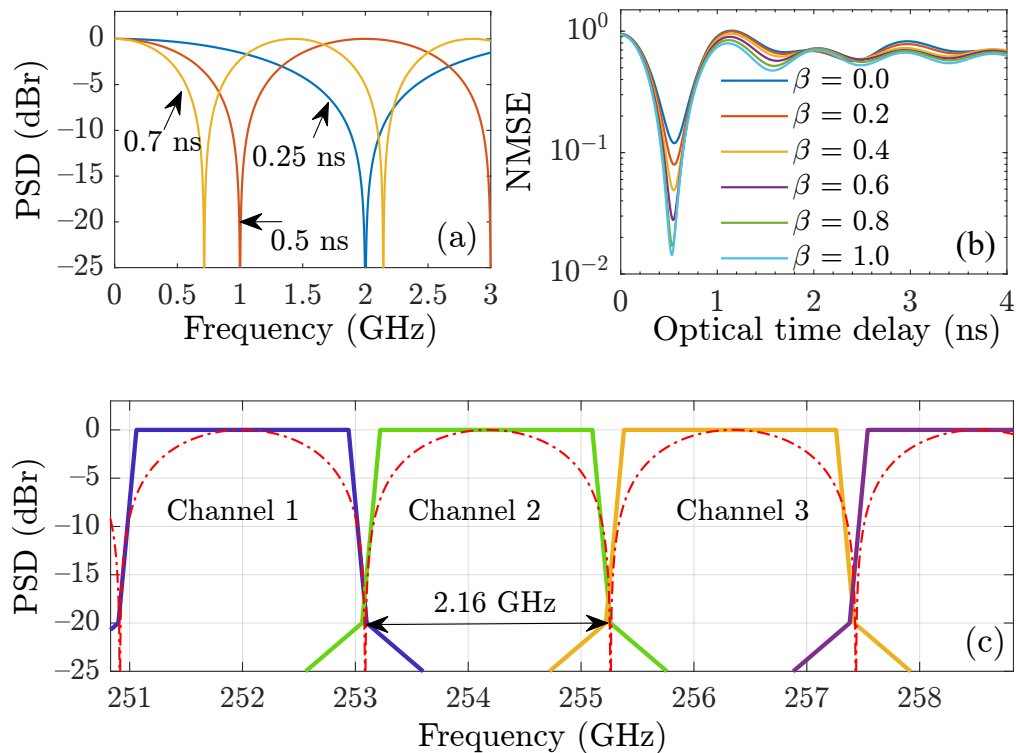


Figure 6.5. Design and optimisation of the microwave photonic filter frequency response. (a) Impact of tuning the optical delay on the MWP filter frequency response. (b) Normalised mean-squared error (NMSE) between the MWP and the raised-cosine frequency responses versus the optical time-delay. (c) Periodic frequency response of the MWP filter (red dashed line) and the IEEE 802.15.3d spectral emission masks of the first channelisation scheme at terahertz frequencies (solid lines).

Second, the optical frequency of the second TLS must be chosen precisely so that the generated terahertz signal at the UTC-PD output are located at the centre frequencies of the desired IEEE 802.15.3d channelisation scheme. Fig. 6.5(c) illustrates this principle, where the terahertz frequency response is designed to match the spectral emission masks defined by the IEEE 802.15.3d Standard for the first channelisation scheme.

The OTDL can also be tuned, together with the optical frequency of the second TLS, so that the resulting terahertz frequency response matches other IEEE 802.15.3d Standard channelisation schemes with different bandwidths and centre frequencies. Such a parallel tuneability mechanism could be potentially useful for the centralised processing of multi-rate multi-user terahertz signals.

6.3.2 Experiment

We experimentally measure the optical frequency response of the proposed multi-band optical filter using the setup shown Fig. 6.6(a) and (b). As shown in Fig. 6.6(a), the

6.3.2 Experiment

MWP filter is constructed using two OTDLs instead of a single OTDL as in Fig. 6.4. This is because, practically, the OTDL introduces a non-zero delay offset due to the fibres pigtailed at its input and output ports. To compensate for this delay, the second OTDL, which has an almost identical characteristics, is used in the second tap so that the net relative delay between both filter arms is zero.

Both OTDLs operate at a wavelength of 1550 nm and are mechanically tunable, with a maximum time delay of 500 ps. The 1550 nm erbium doped fibre amplifier (EDFA) is used as source of broadband optical noise. This broadband noise is the amplified spontaneous emission (ASE) emitted by the EDFA when operated in the free running mode, i.e., without an optical signal at its input. When the EDFA optical pump current is 450 mA, the measured ASE power is -8.14 dBm.

The MWP output response is measured using an optical spectrum analyser (OSA) in the optical wavelength range from 1540 nm to 1560 nm. The OSA spectral measurement window is centred at 1550 nm and has a spectral resolution of 0.05 nm. These measurement settings correspond to an electrical bandwidth of 2.5 THz and a frequency resolution of 6.24 GHz. Figure 6.6(c) and (d) show the optical frequency response at the MWP filter output at optical time delays of about 4 ps and 8 ps, respectively. Figure 6.6(c) shows that the N2N bandwidth is about 250 GHz, whereas in Fig. 6.6(d) the N2N bandwidth is about 125 GHz. These bandwidths are in precise agreement with the analytical relationship between the OTDL delay and the N2N bandwidth, i.e., $BW_{N2N} = 1/(4\tau)$. Conceptually, these bandwidths can be further reduced by increasing the time delay to match the IEEE 802.15.3d bandwidths. However, practically, the measurement of the resulting optical bandwidth is lower bounded by the OSA optical measurement resolution, which limits the sufficient number of optical frequency bins required to represent the optical frequency response. Nonetheless, these experimental results prove the feasibility of using the proposed MWP filter for the optical pulse shaping of multi-band terahertz signals.

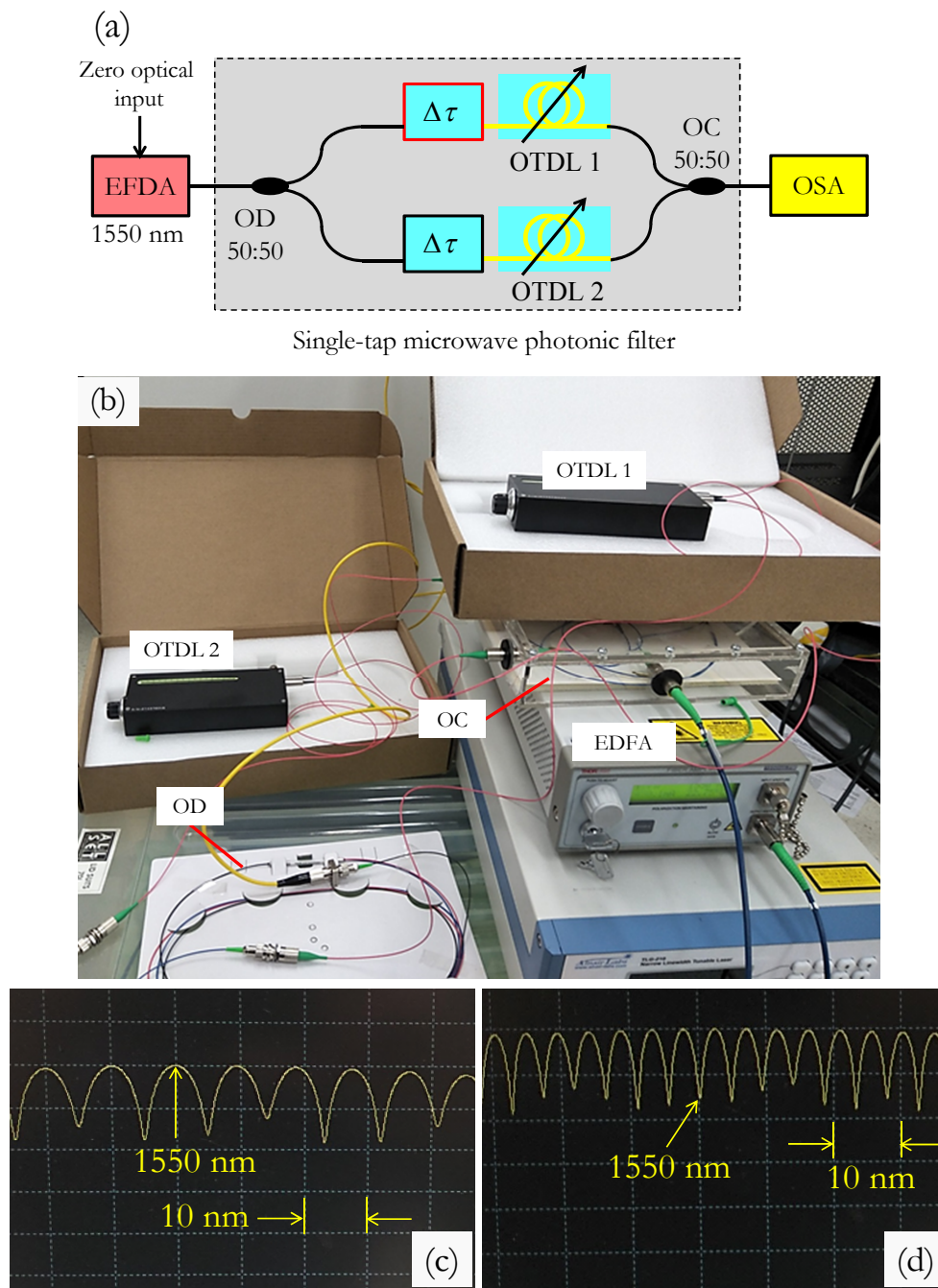


Figure 6.6. Experimental setup and measurement of the photonics-based multi-band terahertz filter. (a): Schematic of a practical photonic filter. (b): Photo of the MWP experimental setup. OD: optical divider. OC: optical coupler. EDFA: erbium doped fibre amplifier. OSA: optical spectrum analyser. $\Delta\tau$: optical time offset due to fibre pigtail. (c) Optical filter frequency response for an optical bandwidth of 10 nm, or equivalently, 1.25 THz. (d) Optical filter frequency response for an optical bandwidth of 5 nm, or equivalently, 624 GHz.

6.4 Low-Complexity Equalisation for MIMO SC-FDMA

Multiple input-multiple output (MIMO) transmission diversity has proven to be a spectrally-efficient technique that increases the capacities of band-limited wireless channels. Employing this technique to the inherently bandwidth-generous terahertz technologies results in massive data volumes, which calls for computationally-affordable signal processing techniques.

Single-carrier frequency division multiple access (SC-FDMA) transmission technique is an example of many concepts and experimental demonstrations that have been inspired after proven practically feasible during the development of the 5G wireless networks. Recently, this concept has been suggested as a potential multi-carrier air interface for terahertz wireless communications (Schram et al. 2020). Specifically, the transmission performance of a 2×2 MIMO SC-FDMA system was numerically evaluated over a channel bandwidth as large as 900 GHz, ranging from 100 GHz to 1 THz (Schram et al. 2020). Moreover, two frequency domain equalisation (FDE) techniques; the zero-forcing (ZF) equaliser and the minimum mean squared error (MMSE) equaliser, were employed to mitigate the inter-symbol interference (ISI) and the inter-antenna interference (IAI) effects in frequency-selective MIMO channels (Singh et al. 2020).

Conceptually, the ZF-FDE technique can be considered as potential contender that can be adapted to meet the technical requirements of the terahertz wireless communications networks. Typically, this equaliser is implemented by direct inversion of the full MIMO channel matrix. The effective number of floating-point operations (flops) required for matrix inversion is proportional to the number of non-zero entries in this matrix. However, in practical FDMA systems, the number of sub-carriers, and consequently, the MIMO channel matrix dimensions, can be as large as 2048 (Schram et al. 2020), (IEEE 2004). Such a large number of sub-carriers calls for prohibitively complex computational efforts and impractical processing speeds at the receiver side to implement the ZF equaliser using the full matrix inversion (FMI) approach, especially at high data rates. It should be highlighted that, until now, the vast majority of the experimental demonstrations of terahertz transceivers designs still relying on offline digital signal processing (DSP), including channel equalisation techniques (Harter et al. n.d., Koenig et al. 2013, Gonzalez-Guerrero et al. 2018). Therefore, in parallel to these experimental demonstrations, the development of powerful terahertz-specific DSP algorithms is crucial to the realisation of real-time high-speed applications promised by terahertz technology.

To address this issue, we focus on reducing complexity of the conventional ZF-FDE (Wen et al. 2013) for MIMO terahertz wireless communications. Particularly, we show that, by exploiting the sparseness of the MIMO channel matrix, the computational complexity of this equaliser can be significantly reduced to yield a benefit for future terahertz wireless links. The remainder of this section is structured as follows. The analytical model of a typical 2×2 MIMO SC-FDMA system is reviewed in Section 6.4.1. In Section 6.4.2, the proposed equaliser is analytically derived and a complexity analysis is presented. Simulation results are presented in Section 6.4.3 to verify the analysis. Also, throughout the rest of this section, boldface letters and symbols designate both vectors and matrices, whereas $(\cdot)^{-1}$ and $(\cdot)^H$ denote the matrix inversion and the Hermitian operators, respectively.

6.4.1 MIMO SC-FDMA: System Model Review

We consider the 2×2 MIMO SC-FDMA system depicted in Fig. 6.7. Throughout the analysis, a perfect transmitter-receiver (Tx-Rx) timing synchronisation is assumed. At the transmitter side, the binary data emitted by the information source is forwarded to a convolutional encoder with a coding rate of r_c . The encoded bits are then applied to a baseband mapper, which groups each k bits into a single complex-valued symbol $\mathbf{s} \in \mathbb{C}^{2N \times 1}$. Afterwards, the modulated symbols are demultiplexed into two independent parallel sequences $\mathbf{s}_j \in \mathbb{C}^{N \times 1}$, where $j = 1$ and 2 , corresponding to the first and the second Tx antennas, respectively. Each N samples are grouped and applied to an N -points discrete Fourier transform (DFT) $\mathbf{S}_D = \mathbf{F}_N \mathbf{s}_j$, where $\mathbf{F}_N \in \mathbb{C}^{N \times N}$ and $\mathbf{F}_N(k, n) = \exp(j2\pi kn/N)$; $k, n = 0, 1, \dots, N - 1$. It should be highlighted that \mathbf{F}_N is a unitary matrix, i.e., $\mathbf{F}_N \mathbf{F}_N^H = \mathbf{F}_N \mathbf{F}_N^{-1} = \mathbf{I}_N$. The resulting N frequency-domain samples are mapped onto a number of M sub-carriers, where $M > N$. As a result, the bandwidth of the frequency domain symbol expands by a factor of $Q = M/N$. The frequency domain vector is converted to the time domain via an M -points inverse DFT (IDFT) module. The resulting SC-FDMA symbol can be expressed as follows:

$$\tilde{\mathbf{s}}_j = \mathbf{F}_M^{-1} \mathbf{M}_T \mathbf{F}_N \mathbf{s}_j, \quad (6.14)$$

where \mathbf{M}_T is the sub-carriers mapping matrix. The structure of \mathbf{M}_T depends on whether the distribution of the N sub-carriers over the M frequency bins is localised Song et al. (2011) or interleaved Sridharan & Lim (2012). A cyclic prefix (CP) vector of N_{CP}

6.4.1 MIMO SC-FDMA: System Model Review

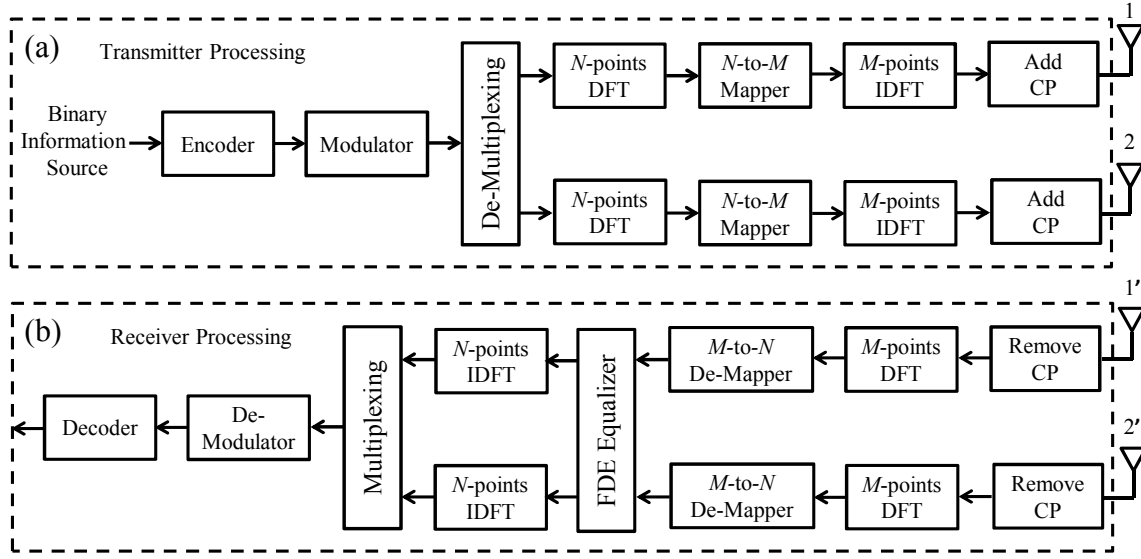


Figure 6.7. Block diagram of a typical 2×2 MIMO SC-FDMA system. CP: cyclic prefix. DFT: discrete Fourier transform. IDFT: inverse DFT. FDE: frequency domain equalisation.

samples length is added to the header of each SC-FDMA symbol. The cyclic prefixed SC-FDMA symbols are then forwarded to a dual-channel terahertz transmitter before being synchronously emitted to free space by the Tx antennas. In the absence of IAI, each symbol is received by the relevant Rx antenna. However, in practice, this requires highly directional terahertz antennas at the Tx and the Rx sides. In practice, the cross coupling between the two single input - single output (SISO) channels is usually caused by the misalignment and/or the beam spreading of the corresponding Tx and Rx antenna elements Kokkonniemi et al. (2020). As a result, both transmitted signals are likely to interfere at each Rx antenna. After the CP removal, the received SC-FDMA vectors can be expressed mathematically as follows:

$$\mathbf{R}_{M_1} = \Phi_{M_{11}} \mathbf{S}_{M_1} + \Phi_{M_{12}} \mathbf{S}_{M_2} + \mathbf{N}_{M_1} \quad (6.15)$$

$$\mathbf{R}_{M_2} = \Phi_{M_{21}} \mathbf{S}_{M_1} + \Phi_{M_{22}} \mathbf{S}_{M_2} + \mathbf{N}_{M_2}, \quad (6.16)$$

where $\Phi_{M_{ij}} \in \mathbb{C}^{M \times M}$ is a diagonal matrix that represents the channel frequency response between the j^{th} transmit antenna and the i^{th} receive antenna as illustrated in Fig. 6.7, whereas $\mathbf{S}_{M_i} = \mathbf{F}_M \tilde{\mathbf{s}}_j \in \mathbb{C}^{M \times 1}$ and $\mathbf{N}_{M_i} \in \mathbb{C}^{M \times 1}$ are the frequency domain received vector and the noise vector observed at the the i^{th} receive antenna, respectively. The entries of the noise vector, \mathbf{N}_{M_i} , follow a zero-mean complex-valued Gaussian random process $\sim \mathcal{CN}(0, \sigma_n^2)$, where σ_n^2 is the noise variance.

Within each receiver, the received signal is processed on a symbol-by-symbol basis and can be modelled as follows:

$$\mathbf{R}_{D_1} = \Phi_{D_{11}} \mathbf{S}_{D_1} + \Phi_{D_{12}} \mathbf{S}_{D_2} + \mathbf{N}_{D_1} \quad (6.17)$$

$$\mathbf{R}_{D_2} = \Phi_{D_{21}} \mathbf{S}_{D_1} + \Phi_{D_{22}} \mathbf{S}_{D_2} + \mathbf{N}_{D_2}, \quad (6.18)$$

where $\mathbf{R}_{D_i} = \mathbf{M}_R \mathbf{R}_{M_i}$ is the i^{th} received frequency-domain SC-FDMA symbol after applying the demapping process, $\mathbf{M}_R \mathbf{M}_T = \mathbf{I}_N$, $\Phi_{D_{ij}} = \mathbf{M}_R \Phi_{M_{ij}} \mathbf{M}_T$, $\mathbf{S}_{D_i} = \mathbf{M}_R \mathbf{S}_{M_i}$ and $\mathbf{N}_{D_i} = \mathbf{M}_R \mathbf{N}_{M_i}$. It should be highlighted that, since $N < M$, the FDE process is applied after de-mapping to avoid the high complexity associated with processing a large number of sub-carriers. The equalised SC-FDMA symbol is expressed as follows:

$$\mathbf{Y} = \mathbf{W}_{\text{FDE}} \Phi_D \mathbf{S} + \mathbf{W}_{\text{FDE}} \mathbf{N}, \quad (6.19)$$

where $\mathbf{Y} \in \mathbb{C}^{2N \times 1}$ is the equalised frequency-domain vector, $\mathbf{W}_{\text{FDE}} \in \mathbb{C}^{2N \times 2N}$ is the FDE matrix, $\mathbf{Y} = [\mathbf{Y}_1^T \quad \mathbf{Y}_2^T]^T$, $\mathbf{S} \in \mathbb{C}^{2N \times 1}$, $\mathbf{S} = [\mathbf{S}_{D_1}^T \quad \mathbf{S}_{D_2}^T]^T$, $\mathbf{N} \in \mathbb{C}^{2N \times 1}$, $\mathbf{N} = [\mathbf{N}_{D_1}^T \quad \mathbf{N}_{D_2}^T]^T$ and $\Phi_D \in \mathbb{C}^{2N \times 2N}$ is the demapped MIMO channel matrix, defined as follows:

$$\Phi_D = \begin{bmatrix} \Phi_{D_{11}} & \Phi_{D_{12}} \\ \Phi_{D_{21}} & \Phi_{D_{22}} \end{bmatrix} \quad (6.20)$$

It should be highlighted that $\Phi_{D_{11}}$ and $\Phi_{D_{22}}$ model the ISI effects, whereas $\Phi_{D_{12}}$ and $\Phi_{D_{21}}$ model the IAI effects. Moreover, each of the aforementioned matrices include the impact of the inter-carrier interference (ICI) in mobility-induced carrier frequency offset (CFO) channels. Since $\Phi_{M_{ij}}$ is diagonal in the absence of CFO, $\Phi_{D_{ij}}$ is also diagonal. At the receiver side, the symbols after FDE are then transformed back to the time domain via an N -point IDFT matrix before being multiplexed, detected and decoded for subsequent BER calculation.

6.4.2 Proposed FDE-ZF Algorithm

The FMI-ZF equaliser is given by direct inversion of the full MIMO channel matrix, i.e., $\mathbf{W}_{\text{FDE}} = \Phi_D^{-1}$, so that the effective MIMO channel matrix can be fully equalised as follows:

$$\Phi_e = \left(\Phi_D^{-1} \Phi_D \right) = \begin{bmatrix} \mathbf{I}_{N \times N} & \mathbf{0}_{N \times N} \\ \mathbf{0}_{N \times N} & \mathbf{I}_{N \times N} \end{bmatrix}. \quad (6.21)$$

Since the dimensions of the MIMO channel matrix Φ_D is $2N \times 2N$, the FMI-ZF equalisation matrix inversion costs $\mathcal{O}(8N^3)$ flops (Cao et al. 2007). The proposed equalisation

6.4.2 Proposed FDE-ZF Algorithm

approach is based on the successive elimination of the ISI and the IAI, respectively. To do so, we assume that the FDE matrix can be decomposed into a product of two matrices; an ISI mitigation matrix, denoted by \mathbf{W}_{ISI} , and an IAI mitigation matrix, denoted by \mathbf{W}_{IAI} , i.e., $\mathbf{W}_{\text{FDE}} = \mathbf{W}_{\text{IAI}} \mathbf{W}_{\text{ISI}}$. In the absence of IAI, $\mathbf{W}_{\text{IAI}} = \mathbf{I}_N$ and \mathbf{W}_{ISI} can be expressed as follows:

$$\mathbf{W}_{\text{ISI}} = \begin{bmatrix} \Phi_{D11}^{-1} & \mathbf{0}_{N \times N} \\ \mathbf{0}_{N \times N} & \Phi_{D22}^{-1} \end{bmatrix}. \quad (6.22)$$

The necessary and sufficient condition to obtain a jointly ISI- and IAI-free effective channel matrix can be written as follows:

$$\Phi_e = \mathbf{W}_{\text{IAI}} (\mathbf{W}_{\text{ISI}} \Phi_D) = \begin{bmatrix} \mathbf{I}_{N \times N} & \mathbf{0}_{N \times N} \\ \mathbf{0}_{N \times N} & \mathbf{I}_{N \times N} \end{bmatrix}. \quad (6.23)$$

Here, we assume that the IAI cancellation matrix can be structured as follows:

$$\mathbf{W}_{\text{IAI}} = \begin{bmatrix} \mathbf{W}_{\text{IAI}11} & \mathbf{W}_{\text{IAI}12} \\ \mathbf{W}_{\text{IAI}21} & \mathbf{W}_{\text{IAI}22} \end{bmatrix}. \quad (6.24)$$

Substituting Eq. (6.24) in Eq. (6.23) and solving for $\mathbf{W}_{\text{IAI}ij}$ yields:

$$\mathbf{W}_{\text{IAI}12} = \Phi_{D11}^{-1} \Phi_{D12} \left(\Phi_{D22}^{-1} \Phi_{D21} \Phi_{D11}^{-1} \Phi_{D12} - \mathbf{I}_N \right)^{-1} \quad (6.25a)$$

$$\mathbf{W}_{\text{IAI}11} = \mathbf{I}_N - \mathbf{W}_{\text{IAI}12} \Phi_{D22}^{-1} \Phi_{D21} \quad (6.25b)$$

$$\mathbf{W}_{\text{IAI}21} = \Phi_{D22}^{-1} \Phi_{D21} \left(\Phi_{D11}^{-1} \Phi_{D12} \Phi_{D22}^{-1} \Phi_{D21} - \mathbf{I}_N \right)^{-1} \quad (6.25c)$$

$$\mathbf{W}_{\text{IAI}11} = \mathbf{I}_N - \mathbf{W}_{\text{IAI}21} \Phi_{D11}^{-1} \Phi_{D12}. \quad (6.25d)$$

Although the equalisation matrices in Eq. (6.25) are designed to equalise 2×2 MIMO channels, the condition in Eq. (6.23) can be reformulated and applied to square MIMO channels with square diversity orders higher than the second order.

As can be seen from Eq. (6.22) and Eq. (6.25), the proposed technique relies on the inversion of the individual SISO channel matrices. Therefore, throughout the rest of this section, we refer to the proposed technique as the sub-matrix inversion ZF (SMI-ZF) technique. Since Φ_{Dij} is diagonal, establishing the matrices \mathbf{W}_{ISI} and \mathbf{W}_{IAI} costs $\mathcal{O}(N)$ flops per matrix inversion. Accordingly, an overall complexity of only $54N$ flops is required to establish the SMI-ZF equalisation matrix, which significantly reduces the computational efforts, and correspondingly, the sampling speed and the power consumption requirements, at the receiver side. Particularly, a complexity reduction

ratio of $8N^2/54$ is achieved by the SMI-ZF compared to the FMI-ZF technique. It should be noted that, in previous MIMO SC-FDMA equalisation approaches that rely on individual sub-carriers equalisation, the computational complexity is governed by the number of SC-FDMA sub-carriers as well as the number of iterations required to refine the equalisation coefficients (Dang et al. 2011). In contrast to these approaches, the proposed equalisation technique is a single-shot process.

6.4.3 Simulation Results and Analysis

In this section, we compare the performance of the proposed equalisation technique with the conventional ZF equaliser in the presence of ISI and IAI. The encoder is a convolutional encoder with a coding rate of $1/2$ and an octal generating polynomial of $(133,177)$. The binary phase shift keying (BPSK) and quadrature phase-shift keying (QPSK) modulation formats are employed to modulate the generated SC-FDMA symbols. The number of sub-carriers N is set to $\{32, 64, 128, 256, 512, 1024, 2048\}$, with $M = 2N$. Moreover, throughout the simulations, we employ the statistical 2×2 MIMO terahertz channel model provided in Cheng et al. (2019), which is proven to be accurate over the 200–300 GHz frequency band Singh et al. (2020). The SNR is varied from 0 dB to 30 dB and the BER performance is averaged over 10^5 Monte Carlo iterations. To evaluate the accuracy of the proposed SMI-ZF technique, we employ the normalised mean squared error (NMSE) definition in (Cao et al. 2007) to measure the accuracy of reconstructing the transmitted SC-FDMA symbols using the corresponding noise-free symbols after demapping at the receiver side. Figure (6.8) shows the NMSE performance and the computational complexity of the proposed FDE and the conventional ZF equaliser for the considered values of N . As can be seen in this figure, the NMSE of both FDE techniques are very close to each other for all values of N . The subtle differences between the corresponding NMSEs of both techniques are negligible for practical implementation. The maximum and the minimum NMSE achievable by both techniques is about 2.3×10^{-3} and 1.55×10^{-30} at $N = 32$ and 64 , respectively. Importantly, the computational complexity of the proposed SMI-ZF technique is exceptionally low compared with the conventional FMI-ZF equaliser. The BER performance metric is adopted to evaluate the performance of both techniques in the presence of AWGN. Figures 6.9 (a) and (b) show the BER performance of BPSK modulation without and with the convolutional code, respectively. Also, Figs. 6.9 (c) and (d) show the BER performance of QPSK modulation without and with the convolutional code, respectively.

6.4.3 Simulation Results and Analysis

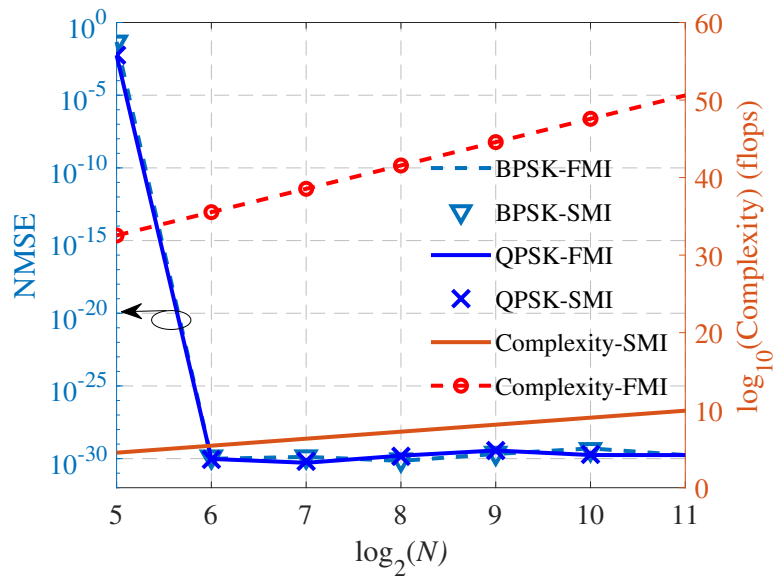


Figure 6.8. Comparison of the accuracy and complexity of the ZF and the proposed equalisers in noiseless channels. FMI: full matrix inversion. SMI: sub-matrix inversion.

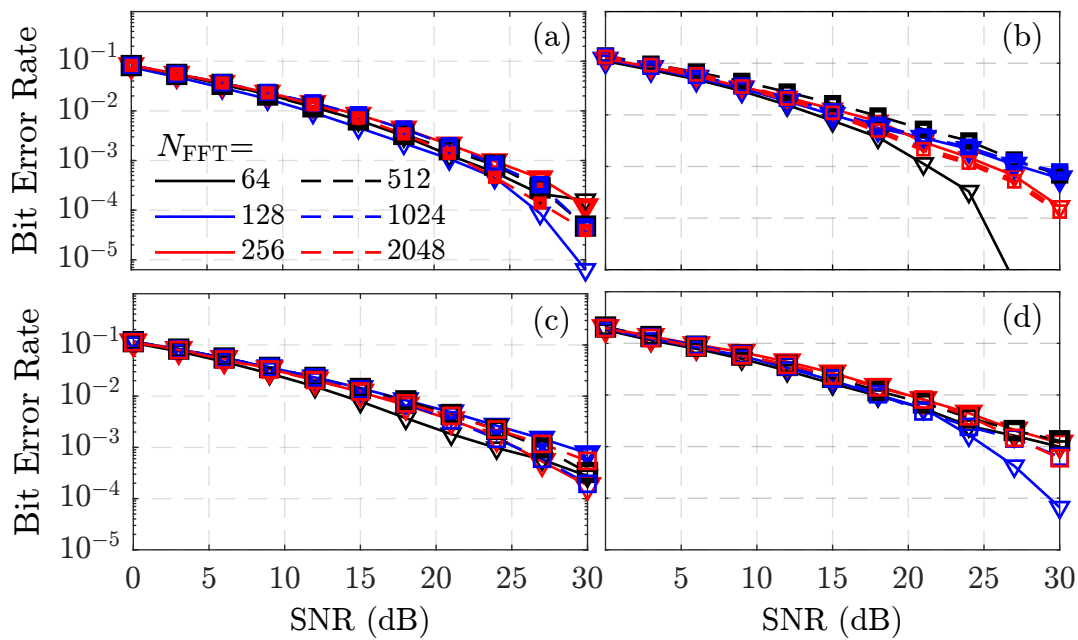


Figure 6.9. Bit error rate performance of the 2×2 MIMO SC-FDMA system. (a) Un-coded BPSK modulation scheme. (b) Coded BPSK modulation scheme. (c) Un-coded QPSK modulation scheme, and (d) the coded QPSK modulation scheme. Solid lines represent the FMI-ZF performance, whereas markers represent the SMI-ZF performance.

Each figure includes the performance of the FMI-based and the SMI-based ZF algorithms. Moreover, the dependence of the BER on the number of sub-carriers, N , is also shown in each figure. Clearly, the BER performances of both equalisation techniques are almost identical, despite the low-complexity of the proposed SMI-ZF algorithm.

This similarity follows from Eq. (6.21) as it is the equalisation condition from which both techniques are derived. It is noteworthy that, for the considered equalisation techniques and modulation types, the SNR after which the coding gain can be achieved is determined by the particular number of sub-carriers.

6.5 Volterra Filters for Nonlinearity Mitigation

Terahertz communications systems are usually prone to power penalties due to their nonlinear response, which is introduced by various electrical, optical and terahertz components such as the low-noise amplifiers (LNA), electro-optic modulators (EOM), optical amplifiers, and Schottky-barrier diode (SBD). So far, three techniques have been proposed to mitigate these nonlinear transmission impairments at the receiver side, namely, the Kramer-Körnig receiver (Ecozzi 2019), the generalised Kramer-Krönig (GKK) receiver (Harter et al. 2020), and the Volterra-series based nonlinear filter (VNLF) (Qiao et al. 2021). The VNLF can be considered as an adaptive and generic form of the KK and GKK receivers as it relies on polynomial basis functions with time-varying coefficients. Hence, the VNLF can capture both the dispersive and nonlinear effects in terahertz-photonic systems, where the response is crucially dependent on the particular system architecture, its peripherals as well as the operating conditions (Harter et al. 2020). In (Qiao et al. 2021), the VNLF was employed to mitigate only the signal-to-signal beating interference (SSBI), i.e., without investigating its applicability to the system and channel responses. Therefore, in this work we employ the VLNF to jointly compensate for the dispersion and nonlinearities introduced by a typical 253 GHz photonic-terahertz communications system.

6.5.1 Experimental Setup and Results

Figure 6.10 illustrates the schematic diagram of the experimental setup we use in this work to characterise the magnitude response of the photonic-terahertz system. The arbitrary waveform generator (AWG) generates a triangular waveform at 500 MHz. Meanwhile, a tunable laser source (TLS) generates two optical continuous waves at 193.000 THz and 193.253 THz before being combined via an optical coupler. The resulting optical signal is then applied to the Mach-Zehnder modulator (MZM), together with the triangular waveform, for electro-optic (EO) modulation. After that, the modulated optical signal is transmitted over a 10-km single mode fibre (SMF). The measured SMF loss, including the connectors at both fibre ends, is about 5 dB. To compensate

6.5.1 Experimental Setup and Results

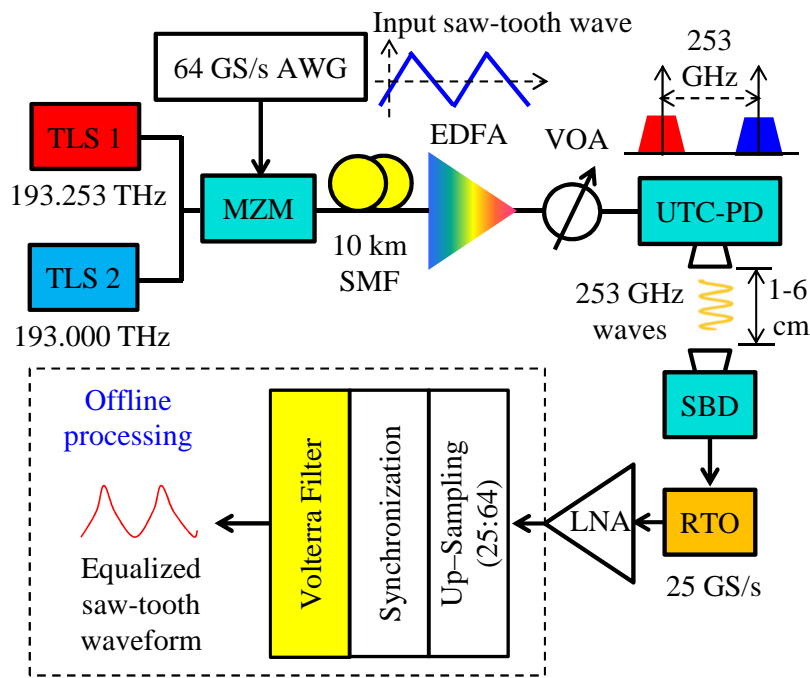


Figure 6.10. Schematic diagram of the nonlinear photonic-terahertz system. TLS: tunable laser source. AWG: arbitrary waveform generator. MZM: Mach-Zehnder modulator. SMF: single mode fibre. EDFA: erbium doped fibre amplifier. VOA: variable optical attenuator. UTC-PD: uni-travelling carrier photo-diode. SBD: Schottky-barrier diode. RTO: real-time oscilloscope. LNA: Low-noise amplifier. MSE: mean squared-error.

for this loss, the signal at the SMF output is optically amplified by the erbium doped fibre amplifier (EDFA) before being applied to the uni-travelling carrier photo-diode (UTC-PD), via a variable optical attenuator (VOA), for photo-mixing. The UTC-PD generates a 253 GHz terahertz signal, which is the difference between the TLS optical frequencies. This terahertz signal is then radiated to free space via a WR-3.4 diagonal horn antenna.

At the receiver side, the terahertz signal is collected by another WR-3.4 horn antenna attached to the SBD for envelope detection. After that, the envelope-detected signal is sampled and recorded by a 25 GS/s real-time oscilloscope (RTO) for post-processing. The processing comprises fractional up-sampling by a factor of 25:64 using a sinc interpolating filter and synchronisation with the AWG signal. After that, the synchronised and transmitted waveforms are applied to a third order VNLFF (Guo et al. 2018), which has an update factor of $\mu = 10^{-2}$.

We consider the system nonlinear response at two considerably different states of the signal-to-noise plus distortion ratio (SNDR). In the low-SNDR state, the photo-current is 1 mA, and the Tx-Rx distance is 6 cm, whereas in the high-SNDR state, the photo-current

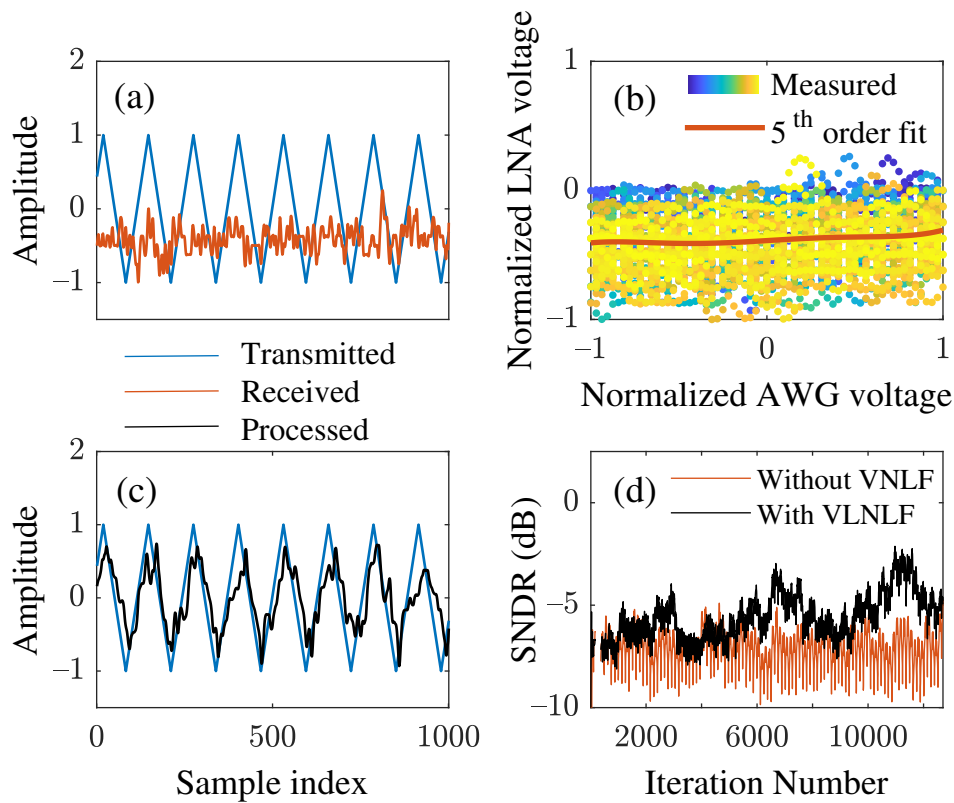


Figure 6.11. Nonlinear distortion and memory effects introduced by the terahertz-photonic system in Fig. 6.10 at a photo-current of 1 mA and a Tx-Rx antenna separation of 6 cm. (a) Segment of the transmitted waveform and the corresponding received waveform versus the time-domain index. (b) Input-output magnitude response. (c) Transmitted and equalised waveforms versus the time-domain index. (d) Signal-to-noise plus distortion ratio before and after applying the Volterra nonlinear filter (VNLF).

is increased to 3 mA, and the distance is reduced to 1 cm. Figures 6.11(a) and 6.11(b) show the transmitted and received waveforms together with the input-output (I/O) magnitude response under the low-SNDR setting, respectively. Figure 6.11(b) also shows a 5th order fitting polynomial, which is used to estimate the ideally noiseless I/O magnitude response. Figures 6.11(c) and 6.11(d) illustrate the equalised waveform, whereas Fig. 6.11(d) shows the evolution of the SNDR, measured in decibels, before and after the VNLF. Figures 6.12(a)-(d) show a set of measurements corresponding to Figures 6.11(a)-(d), respectively, for the high-SNDR state.

As Fig. 6.11(a) shows, there is a high discrepancy between the transmitted and received waveforms. However, after the VNLF, there is a remarkable similarity between the transmitted and equalised waveforms as shown in Fig. 6.11(c). This similarity is attributed to the evolutionary improvement in the SNDR plotted in Fig. 6.11(d), which is iteratively convergent. The speed of this convergence is inversely proportional to the number of

6.5.1 Experimental Setup and Results

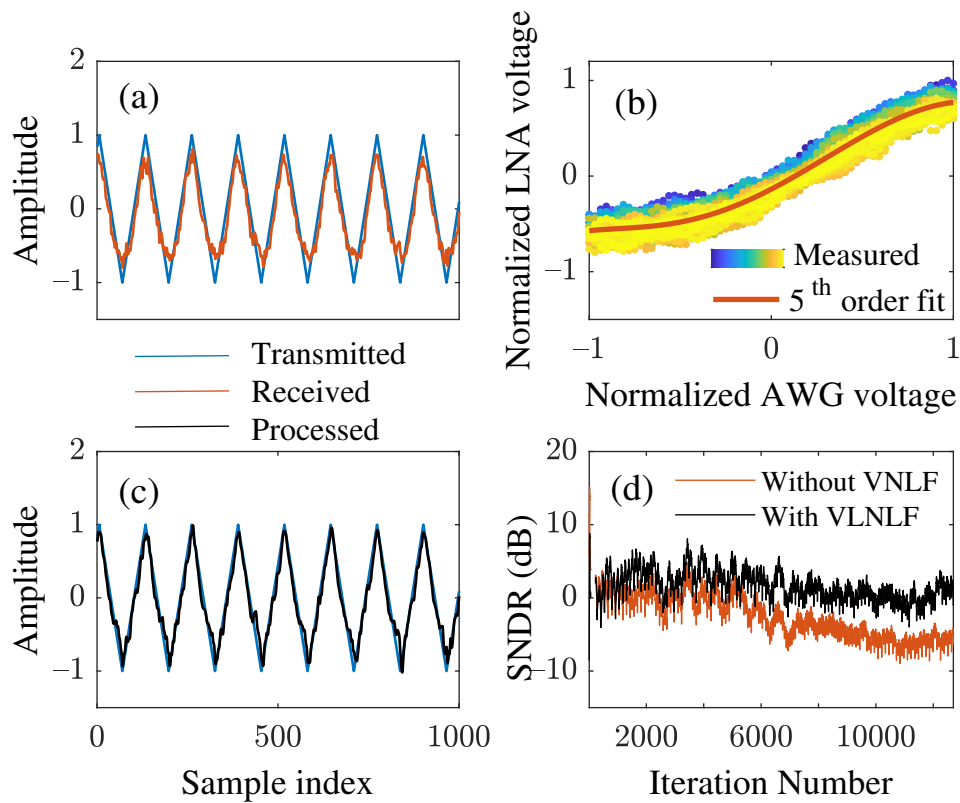


Figure 6.12. Nonlinear distortion and memory effects introduced by the terahertz-photonic system in Fig. 6.10 at a photo-current of 3 mA and a Tx-Rx antenna separation of 1 cm. (a) Segment of the transmitted waveform and the corresponding received waveform versus the time-domain index. (b) Input-output magnitude response. (c) Transmitted and equalised waveforms versus the time-domain index. (d) Signal-to-noise plus distortion ratio before and after applying the Volterra nonlinear filter (VNLf).

waveform samples simultaneously processed by the VNLf and the accuracy update factor, μ . The average improvement in the SNDR, calculated by averaging the SNDR over all iterations, is about 3.38 dB and 4.16 dB for the low-SNDR and high-SNDR states, respectively. It is noteworthy that, Fig. 6.11(b) and Fig. 6.12(b) show that there is a remarkable dissimilarity in the nonlinearities of the high- and low-SNDR states. This dissimilarity is mainly caused by the difference in power loss between the two states, which is estimated to be about 25.01 dB. Despite this large difference, the performance gap between the average improvement in SNDRs of the two states is only 0.78 dB. This observation indicates that, the VNLf could reduce the LNA gain requirements at the receiver side, especially when the received terahertz power is severely low. Nonetheless, future research can focus on further improvement of the SNDR performance by optimising the VNLf parameters, such as the order and the basis functions, prolonging the training period, and/or increasing the number of iterations.

6.6 Conclusion

In this chapter, we propose two all-optical signal processing techniques to extend the capabilities of existing terahertz communications systems. The first technique employs the self-phase modulation introduced by the nonlinear Kerr effect in highly nonlinear fibres to generate a wavelength converted optical signal from a single optical carrier. Analysis and simulation results show that frequency tunable sub-terahertz signals can be generated by electrically tuning the amplitude of the wavelength converted signal and photo-mixing with the un-modulated optical carrier. The second technique is an all-optical multi-band raised-cosine filter based on the periodic frequency response of a single-tap microwave-photonic filter. The underlying theoretical basis of this technique is presented and its optical frequency response is simulated and experimentally verified. Simulation and experimental results show that the proposed technique is bandwidth tunable and hence, is useful for photonic-assisted multi-band terahertz communications systems, where the processing of multiple frequency division multiplexed signals could be prohibitively complicated.

We also present two baseband signal processing techniques to increase the reliability of terahertz communications. The first technique is a frequency-domain linear equalisation technique with an exceptionally-low computational complexity for 2×2 MIMO SC-FDMA terahertz communications systems. Simulation results show that, the proposed equaliser is equivalent to the conventional ZF equaliser in terms of the bit error rate performance and has a lower computational complexity by about two orders of magnitude. Therefore, the proposed equaliser is promising for real-time high-speed terahertz communications applications. Also, the proposed technique can be considered as a potential solution to the mutual cross-talk in other types of frequency-selective MIMO channels, such as polarisation division multiplexing. Additionally, the application of the proposed equalisation technique can be extended to large-scale MIMO terahertz systems with arbitrary high diversity orders. The second technique is a highly-precise nonlinear Volterra equaliser, which is experimentally demonstrated using highly nonlinear terahertz photonic system operating under severely low-signal-to-noise ratio. Experimental results show that, Volterra equaliser can be optimised and used for highly precise recovery of signal patterns that are known at the transmitter and receiver sides.

Summary and Outlook

THIS Dissertation showcased several original contributions to the field of narrowband pulse shaping and signal processing in terahertz communications. The short-term goal of these contributions is to cope up with the current demands of terahertz communications systems. On the long-term, further developments can be introduced based on the techniques and approaches presented in this dissertation. This chapter concludes the work presented throughout this dissertation and foresees possible further research directions.

7.1 Conclusion

The main topic of this dissertation is to investigate terahertz communications systems that can sustain the limitations and non-idealities of their constituting key components. To this end, spectrally efficient pulse shapes and computationally efficient signal processing techniques are showcased. The main goal of the presented contributions is to increase the reliability of terahertz communications systems and, at the same time, simplify their architecture. Based on well-established analytical frameworks and in-depth analysis, two waveforms have been proposed and compared to typical candidate waveforms for terahertz communications. The transmission performance of the proposed waveforms have been experimentally demonstrated using photonics-based terahertz communications systems, with and without optical fibre transmission. Experimental results show that the proposed waveforms can improve the spectral efficiency and reliability of terahertz communications systems. Both factors are essential for the operation of future 6G wireless systems. Also, in this dissertation, it has been shown that, pulse shaping can simplify the architecture of terahertz communications systems without sacrificing their high throughput. In addition, the electrical and optical signal processing techniques presented in this dissertation are developed with the real-time implementation in mind. This section summarises the original contributions presented in this dissertation.

Pulse shaping for standard compliant terahertz communications: This concept and its relevant contribution is presented through Chapter 3. This chapter presents a waveform that fully complies with the spectral constraints imposed by the IEEE 802.15.3d Standard. An analytical framework for the design of IEEE 802.15.3d-compliant waveforms is developed. This framework is then used to design a non-Nyquist waveform that fully complies with the spectral constraints defined in the IEEE 802.15.3d Standard with a close-to-100% spectral power efficiency. The proposed waveform can utilise about 99.3% of the total power admissible by the spectral mask defined by this standard, outperforming the conventional raised-cosine (RC) waveform by more 33% in terms of the radiation power. Additionally, the proposed waveform possesses two degrees of freedom that can be used to control its temporal and spectral properties for flexible spectral interference management. To the best of our knowledge, there has been no other pulse shape designs for the IEEE 802/15.3d Standard. This design would be an asset in terahertz communications, particularly for wireless-channel multiplexing.

7.2 Future Outlook

Pulse shaping for time-jittering tolerant terahertz communications: This concept along with relevant contribution is presented through Chapter 4. This chapter presents a Nyquist pulse that is highly tolerant to the timing-jitter. The proposed pulse shape, which is a modified form of the pulse shape presented in Chapter 3, satisfies the Nyquist criterion for inter-symbol interference (ISI)-free signalling. In addition, experimental results show that the transmission performance of this pulse shape outperforms the conventional RC pulse as well as the BTRC pulses.

Pulse shaping to simplify terahertz transceivers architectures: This concept and its relevant contribution is presented through Chapter 5. This chapter introduces the concept of carrierless amplitude and phase modulation to terahertz communications for the first time, to the best of our knowledge. This modulation technique is experimentally demonstrated using a photonic-based terahertz communications system with combined optical and wireless transmission.

Signal generation and processing techniques for terahertz communications: The contributions related to this area are presented in Chapter 6. These techniques presented in this chapter aim at the generation, processing and pulse shaping of terahertz signals in the optical and the baseband domains. The proposed techniques are computationally-efficient and their implementation is potentially simple and hence, are particularly useful for further development of terahertz communications systems.

7.2 Future Outlook

This dissertation established a context for further developments in the field of pulse shaping and signal processing in terahertz communications. Other advanced pulse shapes can be conceptualised and developed by following the concepts, analytical guidelines and achievements presented in this dissertation. In particular, this section suggests two potentially feasible directions, which can be followed to further advance these concepts.

- First, it is of paramount importance to identify the key limitations and imperfections of existing and emerging terahertz devices as well as the impact of these devices on the transmission performance of the entire terahertz communications

systems. The non-ideal characteristics of these devices give rise to a number of challenges for which waveforms can be specifically designed as potentially feasible solutions.

- Second, it is also important to realise that, the non-idealities of terahertz devices and/or systems can also be mitigated using signal processing techniques. There exist various signal processing techniques that have been originally developed for non-terahertz communications. The major limitation associated with transferring these techniques to terahertz is their computational complexity arising from anticipated data rates beyond 100 Gbit/s. This makes their real-time implementation prohibitively complex and challenging. However, with the necessary adaptation, computationally efficient versions of these techniques can be reproduced.

Bibliography

- Abdolhamid, A. H. & Johns, D. A. (1998), A comparison of CAP/QAM architectures, in '1998 IEEE International Symposium on Circuits and Systems (ISCAS)', Vol. 4, pp. 316–316.
- Abraha, S. T., Okonkwo, C., Yang, H., Visani, D., Shi, Y., Jung, H. D., Tangdiongga, E. & Koonen, T. (2011), 'Performance evaluation of IR-UWB in short-range fiber communication using linear combination of monocycles', *IEEE/OSA Journal of Lightwave Technology* **29**(8), 1143–1151.
- Adalan, A., Fischer, M., Gigl, T., Witrisal, K., Scholtz, A. L. & Mecklenbr, C. F. (2009), Ultra-wideband radio pulse shaping filter design for IEEE 802.15.4a transmitter, in '2009 IEEE Wireless Communications and Networking Conference', pp. 1–6.
- Alagha, N. S. & Kabal, P. (1999), 'Generalized raised-cosine filters', *IEEE Transactions on Communications* **47**(7), 989–997.
- Ali, M., Nellen, S. & Carpintero, G. (2020), 'High-speed terahertz pin photodiode with WR-3 rectangular waveguide output', pp. 2020–2021.
- An, S., Zhu, Q., Li, J., Ling, Y. & Su, Y. (2019), '112-Gb/s SSB 16-QAM signal transmission over 120-km smf with direct detection using a mimo-ann nonlinear equalizer', *Optics Express* **27**(9), 12794–12805.
- Asada, M. & Suzuki, S. (2021), 'Terahertz emitter using resonant-tunneling diode and applications', *Sensors* **21**(4), 1–19. art. no. 1384.
- Assalini, A. & Tonello, A. M. (2004), 'Improved Nyquist pulses', *IEEE Communications Letters* **8**(2), 87–89.
- Assimonis, S. D., Matthaiou, M. & Karagiannidis, G. K. (2008), 'Two-parameter Nyquist pulses with better performance', *IEEE Communications Letters* **12**(11), 807–809.
- Bacon, D. R., Madéo, J. & Dani, K. M. (2021), 'Photoconductive emitters for pulsed terahertz generation', *Journal of Optics* **23**(6), 064001–064029.

BIBLIOGRAPHY

- Baker, K. (2007), 'Torque kills! future control of the ambient electromagnetic spectrum', *IEEE MultiMedia* **14**(1), 4–8.
- Beaulieu, N. C. (1991), 'The evaluation of error probabilities for intersymbol and cochannel interference', *IEEE Transactions on Communications* **39**(12), 1740–1749.
- Beaulieu, N. C., Tan, C. C. & Damen, M. O. (2001), 'A "better than" Nyquist pulse', *IEEE Communications Letters* **5**(9), 367–368.
- Berardinelli, G., Baracca, P., Adeogun, R. O., Khosravirad, S. R., Schaich, F., Upadhyay, K., Li, D., Tao, T., Viswanathan, H. & Mogensen, P. (2021), 'Extreme communication in 6G: vision and challenges for 'in-X' subnetworks', *IEEE Open Journal of the Communications Society* **2**(November), 2516–2535.
- Bobula, M., Prokeš, A. & Daněk, K. (2010), 'Nyquist filters with alternative balance between time- and frequency-domain parameters', *Eurasip Journal on Advances in Signal Processing* **2010**, 8–10. art. no. 903980.
- Borges, R. M., de Souza Lopes, C. H., Lima, E. S., de Oliveira, M. A., Cunha, M. S. B., Alexandre, L. C., da Silva, L. G., Pereira, L. A. M., Spadoti, D. H., Romero, M. A. & Sodr  Junior, A. C. (2021), 'Integrating optical and wireless techniques towards novel fronthaul and access architectures in a 5G NR framework', *Applied Sciences*. art. no. 5048.
- Cao, Z., Tureli, U. & Yao, Y. (2007), 'Low-complexity orthogonal spectral signal construction for generalized OFDMA uplink with frequency synchronization errors', *IEEE Transactions on Vehicular Technology* **56**(3), 1143–1154.
- Castro, C., Elschner, R., Merkle, T., Schubert, C. & Freund, R. (2020), 'Long-range High-Speed THz-Wireless Transmission in the 300 GHz Band', *2020 3rd International Workshop on Mobile Terahertz Systems, IWMTS 2020* pp. 16–19.
- Castro, C., Nellen, S., Elschner, R., Sackey, I., Emmerich, R., Merkle, T., Globisch, B., de Felipe, D. & Schubert, C. (2019), '32 GBd 16qam wireless transmission in the 300 GHz band using a PIN diode for THz upconversion', *Optics InfoBase Conference Papers Part F160-OFC 2019*, 4–6.
- Cheng, C. L., Sangodoyin, S. & Zajic, A. (2019), 'THz MIMO channel characterization for wireless data center-like environment', *2019 IEEE International Symposium on Antennas*

- and Propagation and USNC-URSI Radio Science Meeting, APSURSI 2019 - Proceedings* **2**, 2145–2146.
- Cherry, S. (2004), 'Edholm's law of bandwidth', *IEEE Spectrum* **41**(7), 58–60.
- Chinni, V. K., Latzel, P., Zégaoui, M., Coinon, C., Wallart, X., Peytavit, E., Lampin, J. F., Engenhardt, K., Szriftgiser, P., Zaknoune, M. & Ducournau, G. (2018a), 'Single-channel 100 Gbit/s transmission using III-V UTC-PDs for future IEEE 802.15.3d wireless links in the 300 GHz band', *Electronics Letters* **54**(10), 638–640.
- Chinni, V. K., Zezaoui, M., Coinon, C., Wallart, X., Pevtavit, E., Lampin, J. F., Szriftgiser, P., Zaknoune, M. & Ducournau, G. (2018b), 'Indoor 100 Gbit/s THz data link in the 300 GHz band using fast photodiodes', *2018 25th International Conference on Telecommunications, ICT 2018* pp. 288–290.
- Choi, K. (2021), 'Waveform design for 5G and beyond systems', *Electronics (Switzerland)* **10**(17), 3–5.
- Chowdhury, M. Z., Shahjalal, M., Ahmed, S. & Jang, Y. M. (2020), '6G wireless communication systems: applications, requirements, technologies, challenges, and research directions', *IEEE Open Journal of the Communications Society* **1**, 957–975.
- Chudzik, M., Arnedo, I., Arregui, I., Teberio, F., Lujambio, A., Lopetegi, T., Laso, M. A., Yu, Q., Barker, N. S., Ghaddar, A., Chahadih, A., Ducournau, G., Lampin, J. F. & Akalin, T. (2014), 'Pulse shaping for millimeter-wave and terahertz applications in coplanar technology', *European Microwave Week 2014: Connecting the Future, EuMW 2014 - Conference Proceedings; EuMC 2014: 44th European Microwave Conference (October)*, 818–821.
- Chvojka, P., Werfli, K., Zvanovec, S., Haigh, P. A., Vacek, V. H., Dvorak, P., Pesek, P. & Ghassemlooy, Z. (2017), 'On the m-CAP performance with different pulse shaping filters parameters for visible light communications', *IEEE Photonics Journal*. art. no. 7906712.
- Cisco & its Affiliates (2015), 'Cisco visual networking index: global mobile data traffic forecast update, 2014–2019', *Cisco* pp. 1–42.
- Cohen, L. (1994), The uncertainty principle in signal analysis, *in* 'Proceedings of IEEE-SP International Symposium on Time-Frequency and Time-Scale Analysis', pp. 182–185.

BIBLIOGRAPHY

- Corre, Y., Gougeon, G., Doré, J.-B., Bicaïs, S., Miscopein, B., Saad, M., Palicot, J., Bader, F. & Faussurier, E. (2019), 'Sub-THz spectrum as enabler for 6G wireless communications up to 1 Tbit/s', *Proceedings of the 6G Wireless Summit* **95**(8), 1–17.
- Dahlman, E., Parkvall, S. & Sköld, J. (2016), Chapter 22 - spectrum and RF characteristics, in E. Dahlman, S. Parkvall & J. Sköld, eds, '4G LTE-Advanced Pro and The Road to 5G', third edn, Academic Press, pp. 487–526.
- Dalce, R., Bossche, A. V. D., Val, T., Dalce, R., Bossche, A. V. D. & Val, T. (2014), An experimental performance study of an original ranging protocol based on an IEEE 802.15.4a UWB testbed, in '2014 IEEE International Conference on Ultra-WideBand (ICUWB)', pp. 7–12.
- Dan, I., Ducournau, G., Hisatake, S., Szriftgiser, P., Braun, R. P. & Kallfass, I. (2020), 'A terahertz wireless communication link using a superheterodyne approach', *IEEE Transactions on Terahertz Science and Technology* **10**(1), 32–43.
- D'Andrea, A. N., Mengali, U. & Reggiannini, R. (1994), 'The modified Cramer-Rao bound and its application to synchronization problems', *IEEE Transactions on Communications* **42**(234), 1391–1399.
- Dang, U. L., Ruder, M. A., Schober, R. & Gerstacker, W. H. (2011), 'MMSE beamforming for SC-FDMA transmission over MIMO ISI channels', *EURASIP Journal on Advances in Signal Processing* **2011**(614571), 1–11.
- Degert, J., Vidal, S., Tondusson, M., Amico, C. D., Oberlé, J. & Freysz, É. (2012), 'Generation of Tunable THz Pulses', *Laser Pulses – Theory, Technology, and Applications* pp. 1–26.
- Dhillon, S. S., Vitiello, M. S., Linfield, E. H., Davies, A. G., Hoffmann, M. C., Booske, J., Paoloni, C., Gensch, M., Weightman, P., Williams, G. P., Castro-Camus, E., Cumming, D. R., Simoens, F., Escorcia-Carranza, I., Grant, J., Lucyszyn, S., Kuwata-Gonokami, M., Konishi, K., Koch, M., Schmuttenmaer, C. A., Cocker, T. L., Huber, R., Markelz, A. G., Taylor, Z. D., Wallace, V. P., Axel Zeitler, J., Sibik, J., Korter, T. M., Ellison, B., Rea, S., Goldsmith, P., Cooper, K. B., Appleby, R., Pardo, D., Huggard, P. G., Krozer, V., Shams, H., Fice, M., Renaud, C., Seeds, A., Stöhr, A., Naftaly, M., Ridler, N., Clarke, R., Cunningham, J. E. & Johnston, M. B. (2017), 'The 2017 terahertz science and technology roadmap', *Journal of Physics D: Applied Physics*. art. no. 043001.

- Diebold, S., Nishio, K., Nishida, Y., Kim, J. Y., Tsuruda, K., Mukai, T., Fujita, M. & Nagatsuma, T. (2016), 'High-speed error-free wireless data transmission using a terahertz resonant tunneling diode transmitter and receiver', *Electronics Letters* **52**(24), 1999–2001.
- Doré, J.-B., Corre, Y., Bicaïs, S., Palicot, J., Faussurier, E., Ktenas, D. & Bader, F. (2018), Above-90 GHz spectrum and single-carrier waveform as enablers for efficient Tbit/s wireless communications, in '2018 25th International Conference on Telecommunications (ICT)', pp. 274–278.
- Du, J., Yu, F. R., Lu, G., Wang, J., Jiang, J. & Chu, X. (2020), 'Mec-assisted immersive VR video streaming over terahertz wireless networks: a deep reinforcement learning approach', *IEEE Internet of Things Journal* **7**(10), 9517–9529.
- Du, W., Navarro, D. & Mieleveville, F. (2015), 'Performance evaluation of IEEE 802.5.4 sensor networks in industrial applications', *International Journal of Communication Systems* **28**(10), 1657–1674.
- Ducournau, G., Szriftgiser, P., Beck, A., Bacquet, D., Pavanello, F., Peytavit, E., Zaknoune, M., Akalin, T. & Lampin, J. F. (2014), 'Ultrawide-bandwidth single-channel 0.4-THz wireless link combining broadband quasi-optic photomixer and coherent detection', *IEEE Transactions on Terahertz Science and Technology* **4**(3), 328–337.
- Ducournau, G., Szriftgiser, P., Pavanello, F., Peytavit, E., Zaknoune, M., Bacquet, D., Beck, A., Akalin, T., Lampin, J. F. & Lampin, J. F. (2015), 'THz Communications using Photonics and Electronic Devices: the Race to Data-Rate', *Journal of Infrared, Millimeter, and Terahertz Waves* **36**(2), 198–220.
- Ecozzi, A. N. M. (2019), 'Kramers – Krönig receivers', *Advances in Optics and Photonics* **11**(3), 480–517.
- Elayan, H., Amin, O., Shihada, B., Shubair, R. M. & Alouini, M.-S. (2020), 'Terahertz band: the last piece of RF spectrum puzzle for communication systems', *IEEE Open Journal of the Communications Society* **1**, 1–32. 19294851.
- Essiambre, R. J., Foschini, G. J., Winzer, P. J., Kramer, G. & Goebel, B. (2010), 'Capacity limits of optical fiber networks', *Journal of Lightwave Technology* **28**(4), 662–701.
- Farès, H., Glattli, D., Louët, Y., Palicot, J., Roulleau, P., Farès, H., Glattli, D., Louët, Y., Palicot, J., Roulleau, P. & Spectrum, P. (2017), 'Power spectrum density of single side

BIBLIOGRAPHY

- band CPM using Lorentzian frequency pulses', *IEEE Wireless Communications Letters* **6**(6), 786–789.
- Farhang-Boroujeny, B. & Mathew, G. (1996), Nyquist filters with robust performance against timing jitter, in 'Proceedings of GLOBECOM'96. 1996 IEEE Global Telecommunications Conference', Vol. 2, pp. 1335–1339.
- FCC (2019), 'FCC Opens Spectrum Horizons for New Services and Technologies - First Report and Order 02', *Federal Communications Commission Bureau of Engineering and Technology* pp. 1–45.
- Fellows, M., Barlow, J., Baylis, C., Barkate, J. & Marks, R. J. (2015a), Designing power amplifiers for spectral compliance using spectral mask load-pull measurements, in 'Proceedings, IEEE Topical Conference on Power Amplifiers for Wireless and Radio Applications', pp. 1–3.
- Fellows, M., Baylis, C., Cohen, L. & Marks, R. J. (2015b), 'Real-time load impedance optimization for radar spectral mask compliance and power efficiency', *IEEE Transactions on Aerospace and Electronic Systems* **51**(1), 591–599.
- Fitzgerald, A. J., Berry, E., Zinovev, N. N., Walker, G. C., Smith, M. A. & Chamberlain, J. M. (2002), 'An introduction to medical imaging with coherent terahertz frequency radiation', *Physics in Medicine and Biology* **47**(7), 67–84.
- Fujishima, M. (2018), 'Key technologies for THz wireless link by silicon CMOS integrated circuits', *Photonics* **5**(4), 1–17.
- Gigl, T., Troesch, F., Preishuber-pfluegl, J. & Witrisal, K. (2010), Maximal operating distance estimation for ranging in IEEE 802.15.4a ultra wideband, in 'The 7th Workshop on Positioning, Navigation and Communication, Dresden, Germany', pp. 10–18.
- Gonzalez-Guerrero, L., Shams, H., Fatadin, I., Fice, M. J., Naftaly, M., Seeds, A. J. & Renaud, C. C. (2018), 'Single sideband signals for phase noise mitigation in wireless THz-over-fibre systems', *IEEE/OSA Journal of Lightwave Technology* **36**(19), 4527–4534.
- Gonzalez-Guerrero, L., Shams, H., Fatadin, I., Fice, M. J., Naftaly, M., Seeds, A. J. & Renaud, C. C. (2019), 'Comparison of optical single sideband techniques for thz-over-fiber systems', *IEEE Transactions on Terahertz Science and Technology* **9**(1), 98–105.

- Guglielmo, D. D., Nahas, B. A., Duquennoy, S., Voigt, T. & Anastasi, G. (2016), 'Analysis and experimental evaluation of IEEE802.15.4e TSCH CSMA-CA algorithm', *IEEE Transactions on Vehicular Technology* **66**(2), 1573–1588.
- Guo, X., Li, Y., Jiang, J., Dong, C., Du, S. & Tan, L. (2018), 'Sparse modeling of nonlinear secondary path for nonlinear active noise control', *IEEE Transactions on Instrumentation and Measurement* **67**(3), 482–496.
- Gustavsson, U., Frenger, P., Fager, C., Eriksson, T., Zirath, H., Dielacher, F., Studer, C., Parssinen, A., Correia, R., Matos, J. N., Belo, D. & Carvalho, N. B. (2021), 'Implementation challenges and opportunities in beyond-5G and 6G communication', *IEEE Journal of Microwaves* **1**(1), 86–100.
- Haigh, P. A., Chvojka, P., Zvánovec, S., Ghassemlooy, Z. & Darwazeh, I. (2018), 'Analysis of Nyquist pulse shapes for carrierless amplitude and phase modulation in visible light communications', *IEEE/OSA Journal of Lightwave Technology* **36**(20), 5023–5029.
- Hamada, H., Fujimura, T., Abdo, I., Okada, K., Song, H. J., Sugiyama, H., Matsuzaki, H. & Nosaka, H. (2018), '300-GHz 100-Gb/s InP-HEMT wireless transceiver using a 300-GHz fundamental mixer', *IEEE MTT-S International Microwave Symposium Digest 2018-June*, 1480–1483.
- Hamraoui, K., Babilotte, P., Billard, F., Hertz, E., Faucher, O., Coudert, L. H., Sugny, D. & Lavorel, B. (2017), 'Terahertz pulse shaping through propagation in a gas of symmetric top molecules', *Physical Review A* **96**(4), 1–8.
- Harter, T., Füllner, C., Kemal, J. N., Ummethala, S., Brosi, M., Bründermann, E., Freude, W., Randel, S. & Koos, C. (n.d.), '110-m THz wireless transmission at 100 Gbit/s using a Kramers-Krönig Schottky', *European Conference on Optical Communication (ECOC)* **9**(1), 4–6.
- Harter, T., Füllner, C., Kemal, J. N., Ummethala, S., Steinmann, J. L., Brosi, M., Hesler, J. L., Bründermann, E., Müller, A. S., Freude, W., Randel, S. & Koos, C. (2020), 'Generalized Kramers-Krönig receiver for coherent terahertz communications', *Nature Photonics* **14**(10), 601–606.
- Harter, T., Ummethala, S., Blaicher, M., Muehlbrandt, S., Wolf, S., Weber, M., Adib, M. M. H., Kemal, J. N., Merboldt, M., Boes, F., Nellen, S., Tessmann, A., Walther, M., Globisch, B., Zwick, T., Freude, W., Randel, S. & Koos, C. (2019), 'Wireless THz link with optoelectronic transmitter and receiver', *Optica* **6**(8), 1063.

BIBLIOGRAPHY

- Hermelo, M. F., Shih, P.-T. B., Steeg, M., Ng'oma, A. & Stöhr, A. (2017), 'Spectral efficient 64-QAM-OFDM terahertz communication link', *Optics Express*. art. no. 19360.
- Hesler, J. L., Crowe, T. W. & Diodes, V. (2007), Schottky-diode Detector (WR2.8ZBD), in '18-th International Symposium on Space Terahertz Technology', pp. 0–3.
- Hirata, A. & Hirokawa, J. (2018), 'Absorber integrated planar slot array antenna for suppression of multiple reflection in 120-GHz-band close-proximity wireless system', *2017 International Symposium on Antennas and Propagation (ISAP) E101C(10)*, 791–800.
- Hirata, A. & Hirokawa, Jiro (2018), Terahertz absorber technologies for close-proximity wireless system, in '2018 Asia-Pacific Microwave Conference (APMC)', pp. 434–436.
- Hranilovic, S. (2007), 'Minimum-bandwidth optical intensity Nyquist pulses', *IEEE Transactions on Communications* **55**(3), 574–583.
- IEEE (2004), 'IEEE Std 802.16-2004 (revision of IEEE Std 802.16-2001)', *IEEE Standards Association, the IEEE standard for local and metropolitan area networks part 16: air interface for fixed broadband wireless access systems* pp. 1–857.
- IEEE (2017), 'IEEE Standard for High Data Rate Wireless Multi-Media Networks—Amendment 2: 100 Gb/s Wireless Switched Point-to-Point Physical Layer', *IEEE Standards Association, IEEE Std 802.15.3d-2017 (Amendment to IEEE Std 802.15.3-2016 as amended by IEEE Std 802.15.3e-2017)* pp. 1–55.
- Ito, H. & Ishibashi, T. (2018), 'Low-noise heterodyne detection of terahertz waves at room temperature using zero-biased Fermi-level managed barrier diode', *Electronics Letters* **54**(18), 1080–1082.
- Ito, H., Furuta, T., Nakajima, F., Yoshino, K. & Ishibashi, T. (2004), 'Continuous THz-wave generation using uni-traveling-carrier photodiode', *15th International Symposium on Space Terahertz Technology* pp. 143–150.
- Ji, B., Han, Y., Liu, S., Tao, F., Zhang, G., Fu, Z. & Li, C. (2021), 'Several key technologies for 6G: challenges and opportunities', *IEEE Communications Standards Magazine* **5**(2), 44–51.
- Jia, S., Pang, X., Ozolins, O., Yu, X., Hu, H., Yu, J., Guan, P., Da Ros, F., Popov, S., Jacobsen, G., Galili, M., Morioka, T., Zibar, D. & Oxenlowe, L. K. (2018a), '0.4 THz photonic-wireless link with 106 Gb/s single channel bitrate', *IEEE/OSA Journal of Lightwave Technology* **36**(2), 610–616.

- Jia, S., Wang, S., Liu, K., Pang, X., Zhang, H., Jin, X., Zheng, S., Chi, H., Zhang, X. & Yu, X. (2018b), 'A unified system with integrated generation of high-speed communication and high-resolution sensing signals based on THz photonics', *IEEE/OSA Journal of Lightwave Technology* **36**(19), 4549–4556.
- Jia, S., Yu, X., Hu, H., Yu, J., Guan, P., Da Ros, F., Galili, M., Morioka, T. & Oxenløwe, L. K. (2016a), 'THz photonic wireless links with 16-QAM modulation in the 375-450 GHz band', *Optics Express* **24**(21), 23777–23783.
- Jia, S., Yu, X., Hu, H., Yu, J., Morioka, T., Jepsen, P. U. & Oxenløwe, L. K. (2016b), 'Thz wireless transmission systems based on photonic generation of highly pure beat-notes', *IEEE Photonics Journal* **8**(5), 1–8.
- Kado, Y., Shinagawa, M., Song, H. J. & Nagatsuma, T. (2010), 'Close proximity wireless communication technologies using shortwaves, microwaves, and sub-terahertz waves', *Progress in Electromagnetics Research Symposium* **1**, 767–772.
- Kallfass, I., Boes, F., Messinger, T., Antes, J., Inam, A., Lewark, U., Tessmann, A. & Henneberger, R. (2015), '64 Gbit/s transmission over 850 m fixed wireless link at 240 GHz carrier frequency', *Journal of Infrared, Millimeter, and Terahertz Waves* **36**(2), 221–233.
- Kanda, N., Konishi, K., Nemoto, N., Midorikawa, K. & Kuwata-Gonokami, M. (2017), 'Real-time broadband terahertz spectroscopic imaging by using a high-sensitivity terahertz camera', *Scientific Reports*. art. no. 42540.
- Kim, S. & Zajic, A. (2016), 'Statistical modeling and simulation of short-range device-to-device communication channels at sub-THz frequencies', *IEEE Transactions on Wireless Communications* **15**(9), 6423–6433.
- Kitagawa, S., Suzuki, S. & Asada, M. (2016), 'Wide frequency-tunable resonant tunnelling diode terahertz oscillators using varactor diodes', *Electronics Letters* **52**(6), 479–481.
- Koenig, S., Lopez-Diaz, D., Antes, J., Boes, F., Henneberger, R., Leuther, A., Tessmann, A., Schmogrow, R., Hillerkuss, D., Palmer, R., Zwick, T., Koos, C., Freude, W., Ambacher, O., Leuthold, J. & Kallfass, I. (2013), 'Wireless sub-THz communication system with high data rate', *Nature Photonics* **7**(12), 977–981.

BIBLIOGRAPHY

- Koenig, S., Lopez Diaz, D., Antes, J., Boes, F., Henneberger, R., Leuther, A., Tessmann, A., Schmogrow, R., Hillerkuss, D., Palmer, R., Zwick, T., Koos, C., Freude, W., Ambacher, O., Leuthold, J. & Kallfass, I. (2014), 'Wireless sub-THz communication system with high data rate enabled by RF photonics and active mmic technology', *2014 IEEE Photonics Conference, IPC 2014* **3**, 414–415.
- Koike-Akino, T., Millar, D. S., Parsons, K. & Kojima, K. (2018a), Evolutionary design of pulse-shaping FIR filter to mitigate fiber nonlinearity, *in* 'Advanced Photonics 2018 (BGPP, IPR, NP, NOMA, Sensors, Networks, SPPCom, SOF)', Vol. Part F112-SPPCom 2018, pp. 1–2.
- Koike-Akino, T., Millar, D. S., Parsons, K. & Kojima, K. (2018b), Evolutionary design of pulse-shaping fir filter to mitigate fiber nonlinearity, *in* 'Advanced Photonics 2018 (BGPP, IPR, NP, NOMA, Sensors, Networks, SPPCom, SOF)', p. SpM4G.4.
- Kokkonniemi, J., Boulogeorgos, A. A. A., Aminu, M., Lehtomäki, J., Alexiou, A. & Juntti, M. (2020), 'Impact of beam misalignment on THz wireless systems', *Nano Communication Networks*. art. no. 100302.
- Kumar, A., Magarini, M. & Bregni, S. (2017), 'Improving GFDM symbol error rate performance using better than Nyquist pulse shaping filters', *IEEE Latin America Transactions* **15**(7), 1244–1249.
- Lee, Y. L., Qin, D., Wang, L.-c., Hong, G. & Sim, A. (2020), '6G massive radio access networks : key applications, requirements', *IEEE Open Journal of Vehicular Technology* **2**, 1–12. 20254132.
- Li, X., Yu, J., Zhao, L., Zhou, W., Wang, K., Kong, M., Chang, G.-K., Zhang, Y., Pan, X. & Xin, X. (2019), 132-Gb/s photonics-aided single-carrier wireless terahertz-wave signal transmission at 450 GHz enabled by 64 qam modulation and probabilistic shaping, *in* '2019 Optical Fiber Communications Conference and Exhibition (OFC)', pp. 1–3.
- Li, Z., Erkiling, M. S., Shi, K., Sillekens, E., Galdino, L., Thomsen, B. C., Bayvel, P. & Killey, R. I. (2017a), '168 Gb/s/ λ direct-detection 64-QAM SSB Nyquist-SCM transmission over 80 km uncompensated ssmf at 4.54 b/s/hz net isd using a Kramers-Krönig receiver', *European Conference on Optical Communication, ECOC 2017-Sept.*, 1–3.

- Li, Z., Erkilinc, M. S., Shi, K., Sillekens, E., Galdino, L., Thomsen, B. C., Bayvel, P. & Killey, R. I. (2017b), 'SSBI mitigation and the Kramers-Krönig scheme in single-sideband direct-detection transmission with receiver-based electronic dispersion compensation', *IEEE/OSA Journal of Lightwave Technology* **35**(10), 1887–1893.
- Liu, Y., Zhang, B., Feng, Y., Niu, Z., Qiao, C., Shen, F., Dai, B., Zhang, Y. & Fan, Y. (2021), '10-Gbps real-time wireless link over 1.5 km at 220-GHz band based on Schottky-diode transceiver and 16-QAM modulation', *AEU - International Journal of Electronics and Communications*. 153874.
- Loughlin, P. J. & Cohen, L. (2004), 'The uncertainty principle: Global, local, or both?', *IEEE Transactions on Signal Processing* **52**(5), 1218–1227.
- Lu, C., Zhang, S., Jia, T., Qiu, J. & Sun, Z. (2014), 'Manipulation of terahertz pulse generation in znte crystal by shaping femtosecond laser pulses with a square phase modulation', *Optics Communications* **310**, 90–93.
- Ma, J., Shrestha, R., Moeller, L. & Mittleman, D. M. (2018), 'Invited article: Channel performance for indoor and outdoor terahertz wireless links', *APL Photonics*. art. no. 051601.
- Ma, T., Nallapan, K., Guerboukha, H. & Skorobogatiy, M. (2017), 'Analog signal processing in the terahertz communication links using waveguide Bragg gratings: example of dispersion compensation', *Optics Express*. art. no. 11009.
- Mackay, M., Raschella, A. & Toma, O. (2022), 'Modelling and analysis of performance characteristics in a 60 GHz 802.11ad wireless mesh backhaul network for an urban 5G deployment', *Future Internet*. art. no. 34.
- Mao, T., Chen, J., Wang, Q., Han, C., Wang, Z. & Karagiannidis, G. K. (2021), 'Waveform design for joint sensing and communications in the terahertz band', *arXiv* pp. 1–30. art. id. 2106.01549.
- Massey, J. L. (1972), 'Optimum frame synchronization', *IEEE Transactions on Communications* **20**(2), 115–119.
- Mingming, Z., Kaihui, W., Jimmy, Y., Can, W., Jiangnan, X., Li, Z., Miao, K. & Jianjun, Y. (2019), RoF-OFDM system within terahertz-wave frequency range from 350 GHz to 510 GHz, in 'Metro and Data Center Optical Networks and Short-Reach Links II', Vol. 10946, pp. 1–13.

BIBLIOGRAPHY

- Minoofar, A., Su, X., Zhou, H., Alishahi, F., Pang, K., Zou, K., Zhang, R., Zach, S., Tur, M., Molisch, A. F., Sasaki, H., Lee, D. & Willner, A. E. (2021), 'Experimental demonstration of free-space sub-THz communications link using multiplexing of beams having two different lg modal indices', *2021 European Conference on Optical Communication, ECOC 2021* (1), 2–5.
- Miyamaru, F., Morita, H., Nishiyama, Y., Nishida, T., Nakanishi, T., Kitano, M. & Takeda, M. W. (2014), 'Ultrafast optical control of group delay of narrow-band terahertz waves', *Scientific Reports* **4**, 1–5.
- Moon, S.-R., Kim, E.-S., Sung, M., Kim, J., Lee, J. K. & Cho, S.-H. (2021), 'Experimental investigations on upstream transmission performances in future-proof THz-band indoor network based on photonics', *Optical Fiber Technology*. art. no. 102622.
- Moon, S. R., Kim, E. S., Sung, M., Rha, H. Y., Lee, E. S., Lee, I. M., Park, K. H., Lee, J. K. & Cho, S. H. (2022), '6G indoor network enabled by photonics- and electronics-based sub-THz technology', *IEEE Journal of Lightwave Technology* **40**(2), 499–510.
- Moriwaki, A., Okano, M. & Watanabe, S. (2017), 'Internal triaxial strain imaging of visibly opaque black rubbers with terahertz polarization spectroscopy', *APL Photonics*. art. no. 106101.
- Naftaly, M. & Miles, R. E. (2007), 'Terahertz time-domain spectroscopy for material characterization', *Proceedings of the IEEE* **95**(8), 1658–1665.
- Nagatsuma, T. & Carpintero, G. (2015), 'Recent progress and future prospect of photonics-enabled terahertz communications research', *IEICE Transactions on Electronics* **E98C**(12), 1060–1070.
- Nagatsuma, T., Fujita, Y., Yasuda, Y., Kanai, Y., Hisatake, S., Fujiwara, M. & Kani, J. (2016a), 'Real-time 100-Gbit/s QPSK transmission using photonics-based 300-GHz-band wireless link', *International Topical Meeting on Microwave Photonics (MWP)* **1**, 27–30.
- Nagatsuma, T., Horiguchi, S., Minamikata, Y., Yoshimizu, Y., Hisatake, S., Kuwano, S., Yoshimoto, N., Terada, J. & Takahashi, H. (2013), 'Terahertz wireless communications based on photonics technologies', *Optics Express* **21**(20), 23736–23747.

- Nagatsuma, T., Oogimoto, K., Inubushi, Y. & Hirokawa, J. (2016b), Ultra-stable near-field terahertz communications, *in* '2016 Progress in Electromagnetic Research Symposium (PIERS), Shanghai, China', pp. 3916–3916.
- Nagatsuma, T., Sonoda, M., Higashimoto, T., Kimura, R., Yi, L. & Ito, H. (2019), 300-GHz-band wireless communication using Fermi-level managed barrier diode receiver, *in* '2019 IEEE MTT-S International Microwave Symposium (IMS)', pp. 762–765.
- Nallappan, K., Guerboukha, H., Nerguizian, C. & Skorobogatiy, M. (2018), 'Live streaming of uncompressed HD and 4K videos using terahertz wireless links', *IEEE Access* **6**, 58030–58042. 18188850.
- Nellen, S., Ishibashi, T., Schwenson, L. M., Kohlhaas, R. B., Liebermeister, L., Breuer, S., Deninger, A., Schell, M. & Globisch, B. (2019), 'Direct comparison of PIN and UTC photodiodes for continuous-wave terahertz emission', *International Conference on Infrared, Millimeter, and Terahertz Waves, IRMMW-THz 2019-September*(6), 3544.
- Nguyen, L. H., Braun, V., Halbauer, H. & Wild, T. (2022), 'Waveform comparison under hardware limitations for 6G sub-THz communications', *Zenodo* pp. 1–6. art. no. 5905809.
- Nishida, Y., Nishigami, N., Diebold, S., Kim, J., Fujita, M. & Nagatsuma, T. (2019), 'Terahertz coherent receiver using a single resonant tunneling diode', *Scientific Reports* **9**(1), 1–3.
- Nyquist, H. (1928), 'Abridgment of certain topics in telegraph transmission theory', *Journal of the American Institute of Electrical Engineers* **47**(3), 214–217.
- Oshima, N., Hashimoto, K., Suzuki, S. & Asada, M. (2017), 'Terahertz wireless data transmission with frequency and polarization division multiplexing using resonant-tunneling-diode oscillators', **7**(5), 593–598.
- Oshiro, A., Nishigami, N., Yamamoto, T., Nishida, Y., Webber, J., Fujita, M. & Nagatsuma, T. (2021), 'PAM4 48-Gbit/s wireless communication using a resonant tunneling diode in the 300-GHz band', *IEICE Electronics Express*. art. no. 20210494.
- Pace, D. C., Shi, M., Maggs, J. E., Morales, G. J. & Carter, T. A. (2008), 'Exponential frequency spectrum and Lorentzian pulses in magnetized plasmas', *Physics of Plasmas* **15**(12), 1–13.

BIBLIOGRAPHY

- Pang, X., Jia, S., Ozolins, O., Yu, X., Hu, H., Marcon, L., Guan, P., Ros, F. D., Popov, S., Jacobsen, G., Galili, M., Morioka, T., Zibar, D. & Oxenkwe, L. K. (2016), 260 Gbit/s photonic-wireless link in the THz band, *in* '2016 IEEE Photonics Conference (IPC)', pp. 1–2.
- Park, S. G., Melloch, M. R. & Weiner, A. M. (1999), 'Analysis of terahertz waveforms measured by photoconductive and electrooptic sampling', *IEEE Journal of Quantum Electronics* **35**(5), 810–819.
- Petrov, V., Kokkonen, J., Moltchanov, D., Lehtomaki, J., Koucheryavy, Y. & Juntti, M. (2018), 'Last meter indoor terahertz wireless access: Performance insights and implementation roadmap', *IEEE Communications Magazine* **56**(6), 158–165.
- Petrov, V., Kurner, T. & Hosako, I. (2020), 'IEEE802.15.3d: first standardization efforts for sub-terahertz band communications toward 6G', *IEEE Communications Magazine* **58**(11), 28–33.
- Pfletschinger, S., Navarro, M. & Closas, P. (2015), Frame synchronization for next generation uplink coding in deep space communications, *in* '2015 IEEE Global Communications Conference (GLOBECOM)', pp. 1–6.
- Piels, M. & Bowers, J. E. (2014), '40 GHz si/ge uni-traveling carrier waveguide photodiode', *IEEE/OSA Journal of Lightwave Technology* **32**(20), 3502–3508.
- Pirrone, D., Ferraro, A., Zografopoulos, D. C., Fuscaldo, W. & Szriftgiserand, P. (2022), 'Metasurface-based filters for high data rate THz wireless communication: experimental validation of a 14 Gbps OOK and 104 Gbps QAM-16 wireless link in the 300 GHz band', *IEEE Transactions on Wireless Communications* **21**(10), 8688–8697.
- Qiao, M., Zhang, L., Wang, S., Li, W., Lu, Z., Pang, X., Zhang, L., Zheng, S., Jin, X., Zhang, X. & Yu, X. (2021), '60 Gbit/s PAM-4 wireless transmission in the 310 GHz band with nonlinearity tolerant signal processing', *Optics Communications*. art. no. 126988.
- R. E., F. & Spencer, R. H. (2010), 'But will they buy it?', *IEEE Potentials* **29**(5), 14–15.
- Rodriguez-Vazquez, P., Grzyb, J., Heinemann, B. & Pfeiffer, U. R. (2019), 'A 16-QAM 100-Gb/s 1-M wireless link with an evm of 17% at 230 GHz in an SiGe technology', *IEEE Microwave and Wireless Components Letters* **29**(4), 297–299.

- Rodríguez-Vázquez, P., Leinonen, M. E., Grzyb, J., Tervo, N., Parssinen, A. & Pfeiffer, U. R. (2020), 'Signal-processing challenges in leveraging 100 Gb/s wireless THz', *2nd 6G Wireless Summit 2020: Gain Edge for the 6G Era, 6G SUMMIT 2020*.
- Rodríguez-Vázquez, P., Leinonen, M. E., Grzyb, J., Tervo, N., Parssinen, A. & Pfeiffer, U. R. (2020), Signal-processing challenges in leveraging 100 Gb/s wireless THz, in '2020 2nd 6G Wireless Summit (6G SUMMIT)', pp. 1–5.
- Rogalski, A. & Sizov, F. (2011), 'Terahertz detectors and focal plane arrays', *Opto-Electronics Review* **19**(3), 346–404.
- Roser, H. P., Crowe, T. W., Mattauch, R. J., Bishop, W. L., Peatman, W. C. & Liu, X. (1992), 'GaAs Schottky diodes for THz mixing applications', *Proceedings of the IEEE* **80**(11), 1827–1841.
- Roumelas, G. D., Nistazakis, H. E., Leitgeb, E., Stassinakis, A. N. & Tombras, G. S. (2020), 'On the performance of optical wireless communication links impaired by time jitter, m-turbulence and pointing errors', *Optics Communications* **472**, 1–8.
- Sato, M., Higuchi, T., Kanda, N., Konishi, K., Yoshioka, K., Suzuki, T., Misawa, K. & Kuwata-Gonokami, M. (2013), 'Terahertz polarization pulse shaping with arbitrary field control', *Nature Photonics* **7**(9), 724–731.
- Schmogrow, R., Hillerkuss, D., Dreschmann, M., Huebner, M., Winter, M., Meyer, J., Nebendahl, B., Koos, C., Becker, J., Freude, W. & Leuthold, J. (2010), 'Real-time software-defined multiformat transmitter generating 64QAM at 28 GBd', *IEEE Photonics Technology Letters* **22**(21), 1601–1603.
- Schmogrow, R., Winter, M., Meyer, M., Hillerkuss, D., Nebendahl, B., Meyer, J., Dreschmann, M., Huebner, M., Becker, J., Koos, C., Freude, W. & Leuthold, J. (2011), 'Real-time Nyquist pulse modulation transmitter generating rectangular shaped spectra of 112 Gbit/s 16QAM signals', *Advanced Photonics, OSA Technical Digest (CD)* **1**(I), 15–16.
- Schneider, T., Wiatrek, A., Preussler, S., Grigat, M. & Braun, R. P. (2012), 'Link budget analysis for terahertz fixed wireless links', *IEEE Transactions on Terahertz Science and Technology* **2**(2), 250–256.

BIBLIOGRAPHY

- Schram, V., Wu, Y., Kolleshi, M. & Gerstacker, W. (2020), Comparison of transmission concepts for indoor THz communication systems, in '2020 Third International Workshop on Mobile Terahertz Systems (IWMTS)', pp. 1–5.
- Seddon, J. P., Natrella, M., Lin, X., Graham, C., Renaud, C. C. & Seeds, A. J. (2022), 'Photodiodes for terahertz applications', *IEEE Journal of Selected Topics in Quantum Electronics* **28**(2), 1–12.
- Seeds, A. J. (2014a), 'Terahertz photonics for communications', *Optics InfoBase Conference Papers* **33**(3), 579–587.
- Seeds, A. J. (2014b), 'Terahertz photonics for wireless communications', *Optics InfoBase Conference Papers* **33**(3), 579–587.
- Sen, P. & Jornet, J. M. (2019), 'Experimental demonstration of ultra-broadband wireless communications at true terahertz frequencies', *IEEE Workshop on Signal Processing Advances in Wireless Communications, SPAWC*.
- Shafi, R., Shuai, W. & Younus, M. U. (2020), '360-degree video streaming: a survey of the state of the art', *Symmetry* **12**(9), 1–31.
- Shah, N. A., Agarwal, P., Chung, J. D., El-Zahar, E. R. & Hamed, Y. S. (2020), 'Analysis of optical solitons for nonlinear Schrödinger equation with detuning term by iterative transform method', *Symmetry*. art. no. 1850.
- Shams, H. & Seeds, A. (2017), 'Photonics, fiber and THz wireless communication', *Optics and Photonics News* **28**(3), 24–31.
- Shams, H., Fice, M. J., Gonzalez-Guerrero, L., Renaud, C. C., Van Dijk, F. & Seeds, A. J. (2016), 'Sub-THz wireless over fiber for frequency band 220-280 GHz', *IEEE/OSA Journal of Lightwave Technology* **34**(20), 4786–4793.
- Shams, H., Gonzalez-Guerrero, L., Fice, M., Yang, Z., Renaud, C. & Seeds, A. (2017), 'Distribution of multiband THz wireless signals over fiber', *Broadband Access Communication Technologies XI* **10128**, 101280G.
- Shams, H., Shao, T., Fice, M. J., Anandarajah, P. M., Renaud, C. C., Van Dijk, F., Barry, L. P. & Seeds, A. J. (2015), '100 Gb/s multicarrier THz wireless transmission system with high frequency stability based on a gain-switched laser comb source', *IEEE Photonics Journal*. 7902011.

- Shannon, C. E. (1948), 'A mathematical theory of communication', *The Bell System Technical Journal* **27**(3), 379–423.
- Shehata, M., Wang, K. & Withayachumnankul, W. (2022a), 'Carrierless amplitude and phase modulation for terahertz communications', *IEEE TechRxiv* pp. 1–10. art. id. 20349312.v1.
- Shehata, M., Wang, K. & Withayachumnankul, W. (2022b), Carrierless i-q mixing for terahertz communications, in '2022 47th International Conference on Infrared, Millimeter and Terahertz Waves (IRMMW-THz)', pp. 1–2. access. no.: 22092768.
- Shehata, M., Wang, K., Webber, J., Fujita, M., Nagatsuma, T. & Withayachumnankul, W. (2021), 'IEEE 802.15.3d-compliant waveforms for terahertz wireless communications', *IEEE Journal of Lightwave Technology* **39**(24), 7748–7760.
- Shehata, M., Wang, K., Webber, J., Fujita, M., Nagatsuma, T. & Withayachumnankul, W. (2022c), 'Timing-jitter tolerant Nyquist pulse for terahertz communications', *IEEE Journal of Lightwave Technology* **40**(2), 557–564.
- Shehata, M., Wang, K., Webber, J., Masayuki, F., Nagatsuma, T. & Withayachumnankul, W. (2020), Pulse shaping for IEEE 802.15.3d standard compliant terahertz communications, in '2020 Third International Workshop on Mobile Terahertz Systems (IWMTS)', pp. 1–5.
- Sheikh, F., Gao, Y. & Kaiser, T. (2020), 'A study of diffuse scattering in massive mimo channels at terahertz frequencies', *IEEE Transactions on Antennas and Propagation* **68**(2), 997–1008.
- Shin, S. Y. (2013), 'Throughput analysis of IEEE 802.15.4 network under IEEE 802.11 network interference', *AEU - International Journal of Electronics and Communications* **67**(8), 686–689.
- Shiode, T., Mukai, T., Kawamura, M. & Nagatsuma, T. (2011), 'Giga-bit wireless communication at 300 GHz using resonant tunneling diode detector', *Asia-Pacific Microwave Conference Proceedings, APMC* (1), 1122–1125.
- Shree, P. M., Panigrahi, T. & Hassan, M. (2019), 'Classifying the order of higher derivative gaussian pulses in terahertz wireless communications', *2018 IEEE Globecom Workshops, GC Wkshps 2018 - Proceedings* pp. 1–6.

BIBLIOGRAPHY

- Shrestha, R., Guerboukha, H., Fang, Z., Knightly, E. & Mittleman, D. M. (2022), 'Jamming a terahertz wireless link', *13*, 1–9. art. no. 3045.
- Singh, S., Le, T. & Tran, H. (2020), in 'Measurement of 2×2 los terahertz MIMO channel', Vol. 2020, pp. 1–5.
- Song, H. J. (2019), 'Preliminary study on terahertz channel response for wireless communications applications', *Asia-Pacific Microwave Conference Proceedings, APMC 2018-November*, 432–433.
- Song, H. J. & Lee, N. (2022), 'Terahertz communications: Challenges in the next decade', *IEEE Transactions on Terahertz Science and Technology* **12**(2), 105–117.
- Song, H. J. & Nagatsuma, T. (2011), 'Present and future of terahertz communications', *IEEE Transactions on Terahertz Science and Technology* **1**(1), 256–263.
- Song, H. J., Ajito, K., Muramoto, Y., Wakatsuki, A., Nagatsuma, T. & Kukutsu, N. (2012), 'Uni-travelling-carrier photodiode module generating 300 GHz power greater than 1 mW', *IEEE Microwave and Wireless Components Letters* **22**(7), 363–365.
- Song, S. H., Chen, G. L. & Letaief, K. B. (2011), 'Localized or interleaved? a tradeoff between diversity and cfo interference in multipath channels', *IEEE Transactions on Wireless Communications* **10**(9), 2829–2834.
- Sridharan, G. & Lim, T. J. (2012), 'Performance analysis of sc-fdma in the presence of receiver phase noise', *IEEE Transactions on Communications* **60**(12), 3876–3885.
- Suzuki, D., Oda, S. & Kawano, Y. (2016), 'A flexible and wearable terahertz scanner', *Nature Photonics* **10**, 809–813.
- Systems, M. (2022), 'Fiber coupled THz antennas for 1560 nm'. tera15-tx-fc specifications, advanced features and benefits.
- T. Nagatsuma, K. Oogimoto, Y. Inubushi, and J. Hirokawab (2016), 'Practical considerations of terahertz communications for short distance applications', *Nano Communication Networks* **10**, 1–12.
- Takiguchi, K. (2017a), 'Demultiplexing method of terahertz-wave OFDM sub-carrier channels using integrated-optic DFT circuit', *Terahertz, RF, Millimeter, and Submillimeter-Wave Technology and Applications X* **10103**(February 2017), 101031D.

- Takiguchi, K. (2017b), 'Sub-carrier channel demultiplexing of THz-wave OFDM signal assisted by optical technology', *Electronics Letters* **53**(16), 1123–1125.
- Takiguchi, K. (2021), 'Terahertz-wave Nyquist wavelength division multiplexing communication utilizing integrated-optic spectrum synthesizer', *Terahertz, RF, Millimeter, and Submillimeter-Wave Technology and Applications XIV* **11685**(March 2021), 19.
- Tarboush, S., Sareddeen, H., Alouini, M.-S. & Al-Naffouri, T. Y. (2022), 'Single-versus multi-carrier terahertz-band communications: a comparative study', *arXiv* pp. 1–18. art. no. 2111.07398.
- Tekbıyık, K., Ekti, A. R., Kurt, G. K. & Görçin, A. (2019), 'Terahertz band communication systems: challenges, novelties and standardization efforts', *Physical Communication* **35**, 1–18.
- Thomas Gigl, Florian Troesch, J. P.-P. & Witrisal, K. (2012), 'Ranging performance of the IEEE 802.15.4a UWB standard under FCC/CEPT regulations', *Journal of Electrical and Computer Engineering* **2012**, 1–9.
- Tuset-Peiró, P., Vázquez-Gallego, F., Muñoz, J., Watteyne, T., Alonso-Zarate, J. & Vilajosana, X. (2019), 'Experimental interference robustness evaluation of SUN-OFDM physical layers', *Electronics* **8**(9), 1–16. art. no. 1045.
- Vatansever, F. & Hamblin, M. R. (2012), 'Far infrared radiation (FIR): Its biological effects and medical applications', *Photonics and Lasers in Medicine* **4**, 255–266.
- Veli, M., Mengu, D., Yardimci, N. T., Luo, Y., Li, J., Rivenson, Y., Jarrahi, M. & Ozcan, A. (2021), 'Terahertz pulse shaping using diffractive surfaces', *Nature Communications* **12**(1), 1–13.
- Wang, C., Lu, B., Lin, C., Chen, Q., Miao, L., Deng, X. & Zhang, J. (2014), '0.34-THz wireless link based on high-order modulation for future wireless local area network applications', *IEEE Transactions on Terahertz Science and Technology* **4**(1), 75–85.
- Webber, J., Nishigami, N., Kim, J. Y., Fujita, M. & Nagatsuma, T. (2019), 'Terahertz wireless communications using resonant tunnelling diodes with radio-over-fibre', *Electronics Letters* **55**(17), 949–951.
- Wen, M., Cheng, X., Yin, X., Yang, L. & Jiao, B. (2013), 'A general framework for BER analysis of OFDMA and zero-forcing interleaved SC-FDMA over Nakagami- m fading channels with arbitrary m ', *IEEE Wireless Communications Letters* **2**(4), 395–398.

BIBLIOGRAPHY

- Wild, T., Braun, V. & Viswanathan, H. (2021), 'Joint design of communication and sensing for beyond 5G and 6G systems', *IEEE Access* **9**, 30845–30857.
- Wiltse, J. C. (1984), 'History of millimeter and submillimeter waves', *IEEE Transactions on Microwave Theory and Techniques* **32**(9), 1118–1127.
- Withayachumnankul, W., Fujita, M. & Nagatsuma, T. (2018), 'Integrated silicon photonic crystals toward terahertz communications', *Advanced Optical Materials* **6**(16), 1800401.
- Withayachumnankul, W., Png, G. M., Yin, X., Atakaramians, S., Jones, I., Lin, H., Ung, B. S. Y., Balakrishnan, J., Ng, B. W.-H., Ferguson, B., Micken, S. P., Fischer, B. M. & Abbott, D. (2007), 'T-ray sensing and imaging', *Proceedings of the IEEE* **95**(8), 1528–1558.
- Wu, Y., Koch, J., Vossiek, M. & Gerstacker, W. (2021), Hierarchical beam alignment in single-user mimo single-carrier frequency division multiple access terahertz communication systems, in '2021 IEEE International Conference on Communications Workshops (ICC Workshops)', pp. 1–7.
- Xin, Y., Bao, T., Hua, J. & Yu, G. H. (2021), 'A novel waveform scheme for THz communications', *2021 IEEE 94th Vehicular Technology Conference (VTC2021-Fall)* **2021**, 1–6.
- Yao, J. (2009), 'Microwave photonics', *IEEE/OSA Journal of Lightwave Technology* **27**(3), 314–335.
- Yazar, A. & Arslan, H. (2019), 'Selection of waveform parameters using machine learning for 5G and beyond', *IEEE International Symposium on Personal, Indoor and Mobile Radio Communications, PIMRC*.
- Yazar, A. & Arslan, H. (2020), 'A waveform parameter assignment framework for 6G with the role of machine learning', *IEEE Open Journal of Vehicular Technology* **1**, 156–172. 19660316.
- Yoo, S. J., Scott, R. P., Geisler, D. J., Fontaine, N. K. & Soares, F. M. (2012), 'Terahertz information and signal processing by RF-photonics', *IEEE Transactions on Terahertz Science and Technology* **2**(2), 167–176.
- Yu, X., Asif, R., Piels, M., Zibar, D., Galili, M., Morioka, T., Jepsen, P. U. & Oxenløwe, L. K. (2015a), 60 Gbit/s 400 GHz wireless transmission, in '2015 International Conference on Photonics in Switching (PS)', pp. 4–6.

- Yu, X., Galili, M., Morioka, T., Jepsen, P. U. & Oxenlowe, L. K. (2015b), 'Towards ultrahigh speed impulse radio THz wireless communications', *2015 17th International Conference on Transparent Optical Networks (ICTON) 2015*, 1–4. We.D2.3.
- Yu, X., Ohira, T., Kim, J. Y., Fujita, M. & Nagatsuma, T. (2020), 'Waveguide-input resonant tunnelling diode mixer for THz communications', *Electronics Letters* **56**(7), 342–344.
- Zadok, A., Wu, X., Sendowski, J., Yariv, A. & Willner, A. E. (2010), 'Reconfigurable generation of high-order ultra-wideband waveforms using edge detection', *IEEE/OSA Journal of Lightwave Technology* **28**(16), 2207–2212.
- Zhang, L., Pang, X., Jia, S., Wang, S. & Yu, X. (2020), 'Beyond 100 Gb/s optoelectronic terahertz communications: key technologies and directions', *IEEE Communications Magazine* **58**(11), 34–40.
- Zhen Chen, Z. C., Li Gu, L. G., Zhiyong Tan, Z. T., Chang Wang, C. W. & Juncheng Cao, J. C. (2013), 'Real-time video signal transmission over a terahertz communication link', *Chinese Optics Letters* **11**(11), 112001–112003.
- Zhong, K., Zhou, X., Huo, J., Yu, C., Lu, C. & Lau, A. P. T. (2018), 'Digital signal processing for short-reach optical communications: a review of current technologies and future trends', *IEEE/OSA Journal of Lightwave Technology* **36**(2), 377–400.
- Zhou, S., Tu, X., Wu, Q., Liu, M., Zhang, Y., Chen, P., Wang, W., Xu, Y., Deng, J., Zhao, Q., Jia, X., Zhang, L., Kang, L., Chen, J. & Wu, P. (2021), 'Photonics-inspired terahertz whispering gallery mode resonator waveguide on silicon platform', *Applied Physics Letters*. art. no. 171103.

Biography



Mohamed Shehata was born in Cairo, Egypt in 1984. He received his B.Sc. and M.Sc. degrees in Electronics and Communications Engineering from Al-Azhar University, Cairo, Egypt, in 2006 and 2012, respectively. From 2016 to 2018, he worked as a Research Assistant with the Opto-Nano Electronics Laboratory (ONE-Lab) in the Department of Electronics and Communications, Cairo University, Egypt.

As a recipient of an Adelaide International Scholarship (ASI) in 2018, he joined the School of Electrical and Electronic Engineering at The University of Adelaide, South Australia, where he commenced his Ph.D. degree in Terahertz Communications under the supervision of Prof. Withawat Withayachumnankul and A/Prof. Ke (Desmond) Wang. During his Ph.D. candidature, he received a number of prestigious internal and external scholarships, such as the Faculty of ECMS Travelling Scholarship, Frank Perry Travelling Scholarship, the Faculty of ECMS Dependant Travel Fund as well as a Smart-SAT top-up Scholarship from the SmartSAT Cooperative Research Centre (CRC). In 2021, his research work was selected as a Keynote talk in the IRMMW-THz conference, and in 2022, he received an Adelaide Graduate Award from the University of Adelaide.

Mohamed has been a Senior Member of the IEEE since 2018. He authored and co-authored more than 35 journal and conference publications in Q1 and Q2 journals as well as international flagship conferences. In 2018, he has been recognised as an outstanding reviewer by the *Journal of Optical Fiber Technology*. Currently, he serves as an Active Reviewer for a number of Q1 journals and top international conferences in relevant research fields, including the *IEEE/OSA Journal of Lightwave Technology*, *IEEE Communications Letters*, *IEEE Systems Journals*, *IEEE Transactions on Terahertz Science and Technology*, and *Nature Communications*.

His current research interests include, but are not limited to, digital signal processing,

Biography

microwave photonics, radio-over-fibre (RoF) technologies, terahertz communications and terahertz photonics.

Mohamed Shehata
m.shehata.uoa@gmail.com